

H. G. Schuster and W. Just
Deterministic Chaos

An Introduction

Heinz Georg Schuster and Wolfram Just

Deterministic Chaos

An Introduction

Fourth, Revised and Enlarged Edition



**WILEY-
VCH**

WILEY-VCH Verlag GmbH & Co. KGaA

Authors

Prof. Dr. H. G. Schuster

Christian Albrecht University Kiel, Germany

Department of Theoretical Physics

Lecturer Wolfram Just

Queen Mary / University of London, United Kingdom

School of Mathematical Sciences

Cover Picture

Detail of the “tail” in Plate IX (after Peitgen and Richter)

All books published by Wiley-VCH are carefully produced. Nevertheless, authors, editors, and publisher do not warrant the information contained in these books, including this book, to be free of errors.

Readers are advised to keep in mind that statements, data, illustrations, procedural details or other items may inadvertently be inaccurate.

Library of Congress Card No.: applied for British Library Cataloging-in-Publication Data:

A catalogue record for this book is available from the British Library

Bibliographic information published by Die Deutsche Bibliothek

Die Deutsche Bibliothek lists this publication in the Deutsche Nationalbibliografie; detailed bibliographic data is available in the Internet at <<http://dnb.ddb.de>>.

© 2005 WILEY-VCH Verlag GmbH & Co. KGaA,
Weinheim

All rights reserved (including those of translation into other languages). No part of this book may be reproduced in any form – nor transmitted or translated into machine language without written permission from the publishers. Registered names, trademarks, etc. used in this book, even when not specifically marked as such, are not to be considered unprotected by law.

Printed in the Federal Republic of Germany
Printed on acid-free paper

Composition Michael Bär, Wiesloch

Printing Strauss GmbH, Mörlenbach

Bookbinding Litges & Dopf Buchbinderei GmbH,
Heppenheim

ISBN-13: 978-3-527-40415-5

ISBN-10: 3-527-40415-5

Contents

Table of Contents	v
Preface	ix
Color Plates	xiii
1 Introduction	1
2 Experiments and Simple Models	7
2.1 Experimental Detection of Deterministic Chaos	7
2.1.1 Driven Pendulum	7
2.1.2 Rayleigh–Bénard System in a Box	9
2.1.3 Stirred Chemical Reactions	11
2.1.4 Hénon–Heiles System	12
2.2 The Periodically Kicked Rotator	16
2.2.1 Logistic Map	17
2.2.2 Hénon Map	17
2.2.3 Chirikov Map	18
3 Piecewise Linear Maps and Deterministic Chaos	19
3.1 The Bernoulli Shift	19
3.2 Characterization of Chaotic Motion	21
3.2.1 Liapunov Exponent	21
3.2.2 Invariant Measure	25
3.2.3 Correlation Function	27
3.3 Deterministic Diffusion	29
4 Universal Behavior of Quadratic Maps	33
4.1 Parameter Dependence of the Iterates	35
4.2 Pitchfork Bifurcation and the Doubling Transformation	37
4.2.1 Pitchfork Bifurcations	37
4.2.2 Supercycles	40
4.2.3 Doubling Transformation and α	41
4.2.4 Linearized Doubling Transformation and δ	43

4.3	Self-Similarity, Universal Power Spectrum, and the Influence of External Noise	46
4.3.1	Self-Similarity in the Positions of the Cycle Elements	46
4.3.2	Hausdorff Dimension	48
4.3.3	Power Spectrum	50
4.3.4	Influence of External Noise	52
4.4	Behavior of the Logistic Map for $r_\infty \leq r$	55
4.4.1	Sensitive Dependence on Parameters	55
4.4.2	Structural Universality	57
4.4.3	Chaotic Bands and Scaling	59
4.5	Parallels between Period Doubling and Phase Transitions	61
4.6	Experimental Support for the Bifurcation Route	64
5	The Intermittency Route to Chaos	69
5.1	Mechanisms for Intermittency	69
5.1.1	Type-I Intermittency	70
5.1.2	Length of the Laminar Region	73
5.2	Renormalization-Group Treatment of Intermittency	75
5.3	Intermittency and $1/f$ -Noise	79
5.4	Experimental Observation of the Intermittency Route	84
5.4.1	Distribution of Laminar Lengths	84
5.4.2	Type-I Intermittency	86
5.4.3	Type-III Intermittency	86
6	Strange Attractors in Dissipative Dynamical Systems	89
6.1	Introduction and Definition of Strange Attractors	89
6.1.1	Baker's Transformation	92
6.1.2	Dissipative Hénon Map	94
6.2	The Kolmogorov Entropy	96
6.2.1	Definition of K	96
6.2.2	Connection of K to the Liapunov Exponents	97
6.2.3	Average Time over which the State of a Chaotic System can be Predicted	100
6.3	Characterization of the Attractor by a Measured Signal	102
6.3.1	Reconstruction of the Attractor from a Time Series	103
6.3.2	Generalized Dimensions and Distribution of Singularities in the Invariant Density	106
6.3.3	Generalized Entropies and Fluctuations around the K -Entropy	115
6.3.4	Kaplan–Yorke Conjecture	120
6.4	Pictures of Strange Attractors and Fractal Boundaries	122
7	The Transition from Quasiperiodicity to Chaos	127
7.1	Strange Attractors and the Onset of Turbulence	127
7.1.1	Hopf Bifurcation	127
7.1.2	Landau's Route to Turbulence	128
7.1.3	Ruelle–Takens–Newhouse Route to Chaos	129
7.1.4	Possibility of Three-Frequency Quasiperiodic Orbits	131
7.1.5	Break-up of a Two-Torus	133

7.2	Universal Properties of the Transition from Quasiperiodicity to Chaos	136
7.2.1	Mode Locking and the Farey Tree	139
7.2.2	Local Universality	141
7.2.3	Global Universality	146
7.3	Experiments and Circle Maps	150
7.3.1	Driven Pendulum	151
7.3.2	Electrical Conductivity in Barium Sodium Niobate	153
7.3.3	Dynamics of Cardiac Cells	154
7.3.4	Forced Rayleigh–Bénard Experiment	156
7.4	Routes to Chaos	157
7.4.1	Crises	158
8	Regular and Irregular Motion in Conservative Systems	161
8.1	Coexistence of Regular and Irregular Motion	163
8.1.1	Integrable Systems	163
8.1.2	Perturbation Theory and Vanishing Denominators	165
8.1.3	Stable Tori and KAM Theorem	166
8.1.4	Unstable Tori and Poincaré–Birkhoff Theorem	167
8.1.5	Homoclinic Points and Chaos	170
8.1.6	Arnold Diffusion	171
8.1.7	Examples of Classical Chaos	172
8.2	Strongly Irregular Motion and Ergodicity	174
8.2.1	Cat Map	174
8.2.2	Hierarchy of Classical Chaos	176
8.2.3	Three Classical K -Systems	180
9	Chaos in Quantum Systems?	183
9.1	The Quantum Cat Map	184
9.2	A Quantum Particle in a Stadium	186
9.3	The Kicked Quantum Rotator	187
10	Controlling Chaos	193
10.1	Stabilization of Unstable Orbits	194
10.2	The OGY Method	197
10.3	Time-Delayed Feedback Control	199
10.3.1	Rhythmic Control	200
10.3.2	Extended Time-Delayed Feedback Control	201
10.3.3	Experimental Realization of Time-Delayed Feedback Control	202
10.4	Parametric Resonance from Unstable Periodic Orbits	203
11	Synchronization of Chaotic Systems	207
11.1	Identical Systems with Symmetric Coupling	207
11.1.1	On–Off Intermittency	208
11.1.2	Strong vs. Weak Synchronization	209
11.2	Master–Slave Configurations	210

11.3	Generalized Synchronization	212
11.3.1	Strange Nonchaotic Attractors	212
11.4	Phase Synchronization of Chaotic Systems	213
12	Spatiotemporal Chaos	217
12.1	Models for Space–Time Chaos	217
12.1.1	Coupled Map Lattices	217
12.1.2	Coupled Oscillator Models	218
12.1.3	Complex Ginzburg–Landau Equation	220
12.1.4	Kuramoto–Sivashinsky Equation	220
12.2	Characterization of Space–Time Chaos	221
12.2.1	Liapunov Spectrum	222
12.2.2	Co-moving Liapunov Exponent	223
12.2.3	Chronotopic Liapunov Analysis	224
12.3	Nonlinear Nonequilibrium Space–Time Dynamics	225
12.3.1	Fully Developed Turbulence	225
12.3.2	Spatiotemporal Intermittency	227
12.3.3	Molecular Dynamics	227
	Outlook	231
	Appendix	233
A	Derivation of the Lorenz Model	233
B	Stability Analysis and the Onset of Convection and Turbulence in the Lorenz Model	235
C	The Schwarzian Derivative	236
D	Renormalization of the One-Dimensional Ising Model	238
E	Decimation and Path Integrals for External Noise	240
F	Shannon’s Measure of Information	243
F.1	Information Capacity of a Store	243
F.2	Information Gain	244
G	Period Doubling for the Conservative Hénon Map	245
H	Unstable Periodic Orbits	249
	Remarks and References	257
	Index	283

Preface

Since 1994 when the last edition of the present monograph was published, the field of Nonlinear Science has developed tremendously. It is nowadays no longer possible to give a comprehensible introduction into, and a balanced overview of the different branches within this field. Following the general practice of the previous editions it is the scope of this fourth augmented edition to introduce aspects of Nonlinear Dynamics at a level which is accessible to a wide audience. We have intensified and added three new topics:

- Control of chaos is one of the most popular branches of Nonlinear Science. As a particular new aspect we have included a comprehensive discussion of time-delayed feedback control which is widely used in applications.
- Topics in synchronization became recently quite popular from a fundamental as well as an applied point of view. We introduce basic concepts as well as novel notions like phase synchronization or strange nonchaotic, attractors, at an elementary level.
- Spatiotemporal chaos covers a wide range of topics, from classical fields in physics such as hydrodynamics to current research topics in theoretical biophysics, which are commonly related with the nonlinear dynamics of a large number of degrees of freedom. We introduce here basic features of relevant model systems as well as selected concepts for quantitative analysis. But our exposition is far from complete.

The fourth edition benefits from data and figures that have been provided by several colleagues, in particular by R. Klages, J. Kurths, A. Pikovski, H. Posch, and M. Rosenblum. It is a pleasure to thank E. Schöll for his kind hospitality during a stay at Berlin University of Technology, where parts of the new edition were written. We are indebted to the publisher, in particular to Dr. M. Bär and R. Schulz, for their continual help in preparing the manuscript. Despite the remarkable support from various people the present edition could still contain mistakes. We apologize in advance for such inconsistencies and we invite the reader to report to us any deficiencies.

Kiel/London, October 2004
H. G. Schuster, W. Just

Preface to the Third Edition

Since the last edition of this book in 1989 the field of deterministic chaos has continued to grow. Within the wealth of new results there are three major trends.

- Unstable periodic orbits have been rediscovered as building blocks of chaotic dynamics, especially through the work of Cvitanovich *et al.* (1990). They developed an expansion of physical averages in terms of primitive cycles (see also Appendix H).
- Exploiting the concept of unstable periodic orbits, Ott, Grebogi and Yorke demonstrated in 1990 that deterministic chaos can be controlled. They found that small time-dependent changes in the control parameter of the system can stabilize previously unstable periodic cycles in such a way that the system becomes nonchaotic (see Chapter 10).
- There are new theoretical and experimental results in the field of quantum chaos which are described excellently in the new books by Gutzwiller (1990), Haake (1991) and Reichl (1992).

During the preparation of the new edition, J. C. Gruel helped with the pictures of the new chapter, Mrs. H. Heimann typed the new text, M. Poulson and R. Wengenmayr from VCH Publishers took care of the editorial work. H. J. Stockmann and H. J. Stein contributed the fascinating pictures of simulations of quantum chaos in microwave resonators. I would like to thank all these people for their cooperation and patience.

Kiel, August 1994
H. G. Schuster

Preface to the Second Edition

This is a revised and updated version of the first edition, to which new sections on sensitive parameter dependence, fat fractals, characterization of attractors by scaling indices, the Farey tree, and the notion of global universality have been added. I thank P. C. T. de Boer, J. L. Grant, P. Grassberger, W. Greulich, F. Kaspar, K. Pawelzik, K. Schmidt, and S. Smid for helpful hints and remarks, and Mrs. Adlfinger and Mrs. Boffo for their patient help with the manuscript.

Kiel, August 1987
H. G. Schuster

Preface to the First Edition

Daily experience shows that, for many physical systems, small changes in the initial conditions lead to small changes in the outcome. If we drive a car and turn the steering wheel only a little, our course will differ only slightly from that which the car would have taken without this change. But there are cases for which the opposite of this rule is true: For a coin which is placed on its rim, a slight touch is sufficient to determine the side on which it will fall. Thus

the sequence of heads and tails which we obtain when tossing a coin exhibits an irregular or chaotic behavior in time, because extremely small changes in the initial conditions can lead to completely different outcomes. It has become clear in recent years, partly triggered by the studies of nonlinear systems using high-speed computers, that a sensitive dependence on the initial conditions, which results in a chaotic time behavior, is by no means exceptional but is a typical property of many systems. Such behavior has, for example, been found in periodically stimulated cardiac cells, in electronic circuits, at the onset of turbulence in fluids and gases, in chemical reactions, in lasers, etc. Mathematically, all nonlinear dynamical systems with more than two degrees of freedom, i. e., especially many biological, meteorological or economic models, can display chaos and, therefore, become unpredictable over longer time scales. "Deterministic chaos" is now a very active field of research with many exciting results. Methods have been developed to classify different types of chaos, and it has been discovered that many systems show, as a function of an external control parameter, similar transitions from order to chaos. This universal behavior is reminiscent of ordinary second-order phase transitions, and the introduction of renormalization and scaling methods from statistical mechanics has brought new perspectives into the study of deterministic chaos. It is the aim of this book to provide a self-contained introduction to this field from a physicist's point of view. The book grew out of a series of lectures, which I gave during the summer terms of 1982 and 1983 at the University of Frankfurt, and it requires no knowledge which a graduate student in physics would not have. A glance at the table of contents shows that new concepts such as the Kolmogorov entropy, strange attractors, etc., or new techniques such as the functional renormalization group, are introduced at an elementary level. On the other hand, I hope that there is enough material for research workers who want to know, for example, how deterministic chaos can be distinguished experimentally from white noise, or who want to learn how to apply their knowledge about equilibrium phase transitions to the study of (nonequilibrium) transitions from order to chaos. During the preparation of this book the manuscripts, preprints and discussion, the remarks of G. Eilenberger, K. Kehr, H. Leschke, W. Selke, and M. Schmutz were of great help. P. Berge, M. Dubois, W. Lauterborn, W. Martienssen, G. Pfister and their coworkers supplied several, partly unpublished, pictures of their experiments. H. O. Peitgen, P. H. Richter and their group gave permission to include some of their most fascinating computer pictures in this book (see cover and Section 6.4). All contributions are gratefully appreciated. Furthermore, I want to thank W. Greulich, D. Hackenbracht, M. Heise, L. L. Hirst, R. Liebmann, I. Neil, and especially I. Procaccia for carefully reading parts of the manuscript and for useful criticism and comments. I also acknowledge illuminating discussions with V. Emery, P. Grassberger, D. Grepel, S. Grossmann, S. Fishman, and H. Horner. It is a pleasure to thank R. Hornreich for the kind hospitality extended to me during a stay at the Weizmann Institute, where several chapters of this book were written, with the support of the Minerva foundation. Last but not least, I thank Mrs. Boffo and Mrs. Knolle for their excellent assistance in preparing the illustrations and the text.

Frankfurt, October 1984

H. G. Schuster

Legends to Plates I–XX

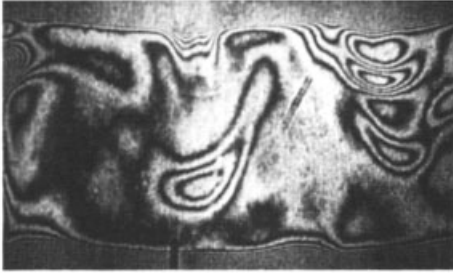
Many of these plates are part of Chapter 6. Accordingly, references mentioned in the legends are to be found on pages 89–125.

- I. *Biperiodic flow in a Bénard experiment.* Figs. 1–8 show interferometric pictures of a Bénard cell in the biperiodic regime; that is, there are two incommensurate frequencies in the power spectrum (see also pages 2.1.2–2.1.2). The time between successive pictures is 10 s. The first period lasts 40 s after which the “mouth” in the middle of the pictures repeats itself (see Figs. 1 and 5). But the details, e. g., in the upper right corners of Figs. 1 and 5 are not the same; that is, the motion is not simply periodic. (From a film taken by P. Berge and M. Dubois, CEN Saclay, Gif-sur-Yvette, France.) [page xv]
- II. *Nonlinear electronic oscillator* (see also Fig. 46 on page 66): The current-versus-voltage phase portraits (at the nonlinear diode) are shown on the oscilloscope screen. For increasing driving voltage one observes the period-doubling route. The nonlinearity of the diode that has been used in this experiment differs from eq. 4.119. (Picture taken by W. Meyer-Ilse, after Klinker *et al.*, 1984.) [page xvi]
- III. *Taylor instability.* a) Formation of rolls, b) the rolls start oscillating, c) a more complicated oscillatory motion, d) chaos. (After Pfister, 1984; see also pages 133–136.) [page xvii]
- IV. *Disturbed heartbeats.* The voltage difference (black) across the cell membrane of one cell of an aggregate of heart cells from embryonic chicken shows a) phase locking with the stimulating pulse and b) irregular dynamics, displaying escape or interpolation beats if the time between successive periodic stimuli (red) is changed from 240 ms in a) to 560 ms in b). (After Glass *et al.*, 1983; see also page 7.3.3.) [page xvii]
- V. *Chaotic electrical conduction in BSN crystals.* The birefringence pattern of a ferroelectric BSN crystal shows domain walls which mirror the charge transport near the onset of chaos (see also Fig. 116 on page 153). For clarity, the dark lines in the original pattern have been redrawn in red. (After Martin *et al.*, 1984.) [page xvii]
- VI. *Power spectra of cavitation noise:* The noise amplitude is depicted in colors, and the input pressure is increasing linearly with time. One observes (with increasing pressure) a subharmonic route $f_0 \rightarrow f_0/2 \rightarrow f_0/4 \rightarrow \text{chaos}$. This picture is the colored version of Fig. 47c on page 67. (Picture taken by E. Suchla, after Lauterborn and Cramer, 1981.) [page xviii]
- VII. *The Cassini division.* The ring of Saturn (a) shows a major gap (b), the so-called Cassini division, because the motion on this orbit is unstable (see also Fig. 142 on page 174).

(NASA pictures no. P-23068 and P-23207 with permission from Bildarchiv, Baader Planetarium.) [page xviii]

Plates VIII–XV show fractal boundaries in the complex plane:

- VIII. *Newton's algorithm* for $f(z) = z^3 - 1 = 0$. The basins of attraction for the three roots of $z^3 = 1$ are shown in red, green and blue (after Peitgen and Richter, 1984; see also pages 122–124). [page xix]
- IX. *Mandelbrot's set* (black) in the complex plane. (After Peitgen and Richter, 1984; see also page 125). [page xix]
- X–XII. Enlargements of regions A, D, E in Plate IX (after Peitgen and Richter, 1984). [pages xx–xxi]
- XIII. Enlargement of the “tail of the seahorse” in Plate IX (after Peitgen and Richter, 1984). [page xxi]
- XIV. “*Eye of the seahorse*” in Plate IX (after Peitgen and Richter, 1984). [page xxii]
- XV. Detail of the “tail” in Plate IX (after Peitgen and Richter, 1984). [page xxii]
- XVI. *Liapunov exponent* λ (depicted in colors) of the circle map ($\theta_{n+1} = \theta_n + \Omega - (K/2\pi) \times \sin(2\pi\theta_n)$) as a function of the parameters $K = 0 \dots 10$ (y-axis) and $\Omega = 0 \dots 1$ (x-axis). The arrow indicates the critical line at $K = l$. (After K. Schmidt, priv. comm.; see also Fig. 107 on page 138.) [page xxiii]
- XVII. *Liapunov exponent* λ (depicted in colors) of the driven pendulum with additional external torque ($\ddot{\theta} + 1.58\dot{\theta} + K \sin \theta = \Omega \cos(1.76t) + \Omega$) as a function of the parameters $K = 0 \dots 20$ (y-axis) and $\Omega = 0 \dots 20$ (x-axis). (After K. Schmidt, priv. comm.; see also pages 151–153.) [page xxiii]
- XVIII. *Experiments with microwaves* in irregularly shaped resonators make it possible to simulate quantum mechanical properties of classically chaotic systems in an easy fashion. The picture shows the color-coded distribution of amplitudes of standing electromagnetic waves which follow the wave equation 9.10 in a stadium-shaped resonator for different excitation frequencies. (After H. J. Stockmann (1993), the pictures were taken by J. Stein, Marburg.) [page xxiv]
- XIX. *Fractal diffusion coefficient* of a chaotic dynamical system (“chain of boxes”) generalizing a simple random walk. The dotted red line shows a trajectory performing deterministic diffusion. The diffusion coefficient as a function of the slope of the map yields a “wave-like” structure. Self-similarity is illustrated by the inset showing a blow up of a small region of the curve (after Klages, 2004). [page xxv]
- XX. *Lifetime of the fixed point* of the Hénon map in the plane of control parameters. Within the triangle the fixed point becomes stable and the lifetime becomes infinite (cf. Chapter 10 and Fig. 164 for further details). [page xxv]



1



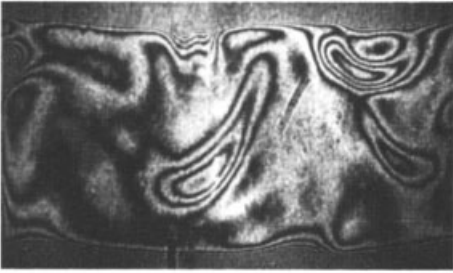
2



3



4



5



6



7



8

Plate I.

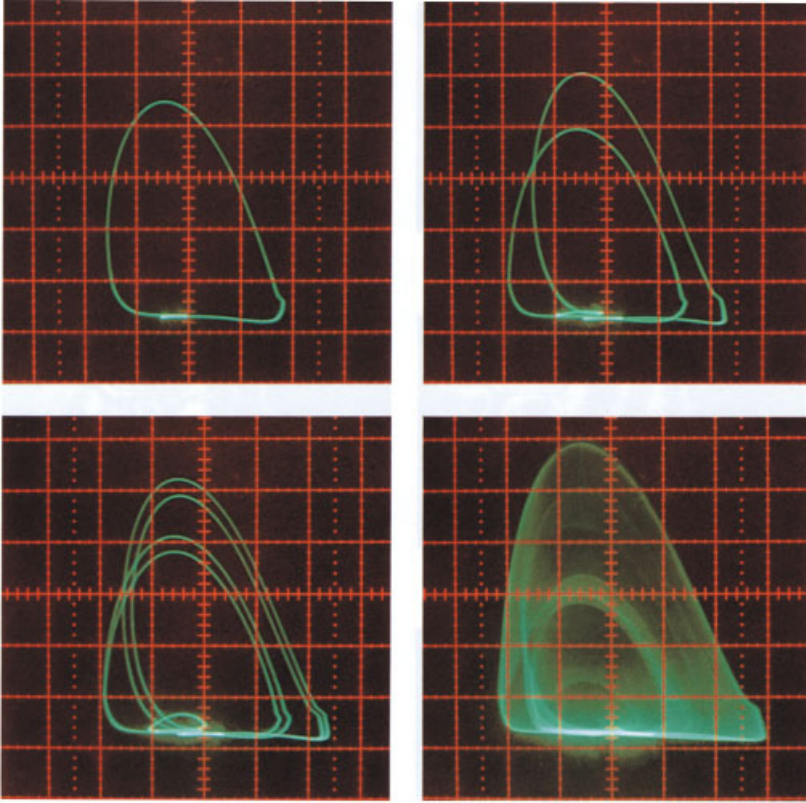


Plate II.



Plate III.

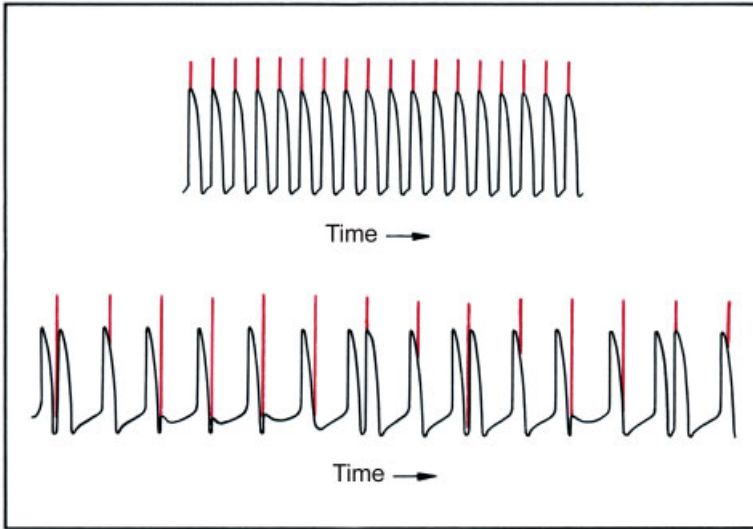


Plate IV.

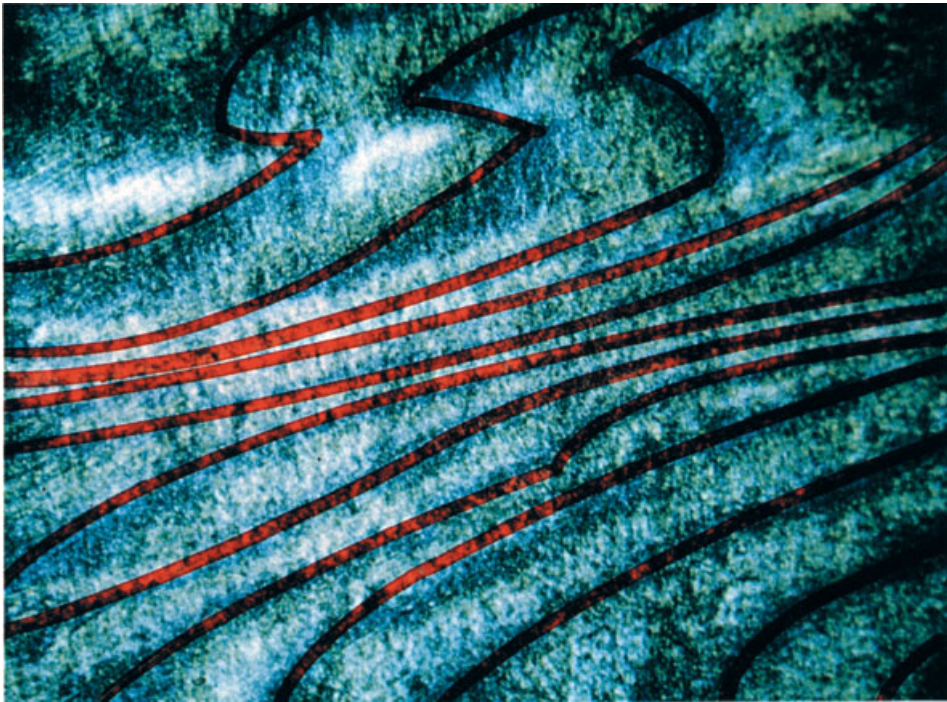


Plate V.

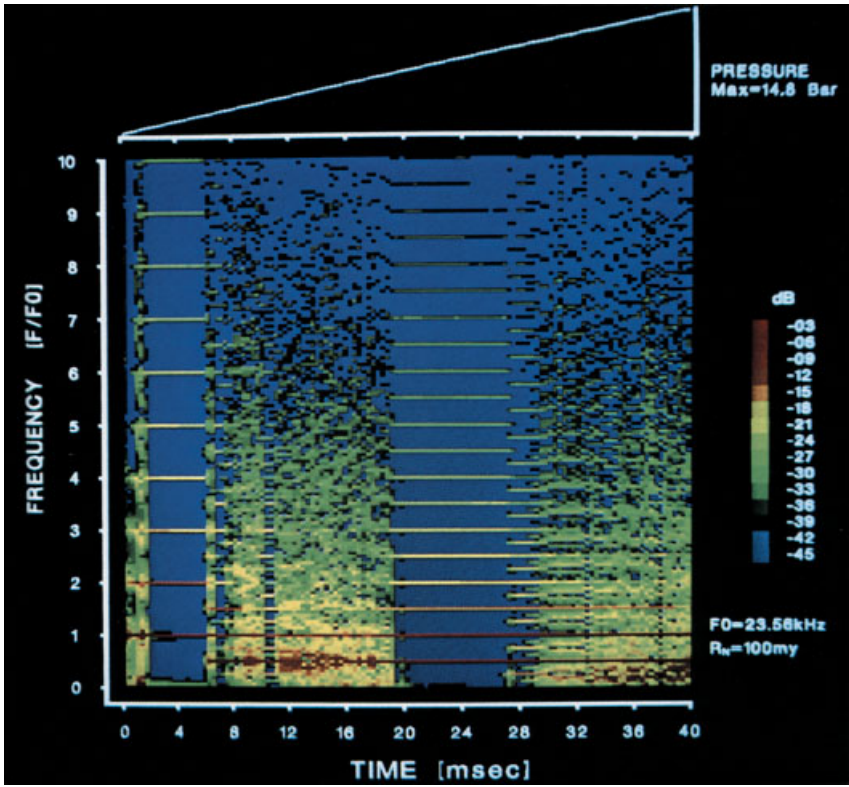


Plate VI.

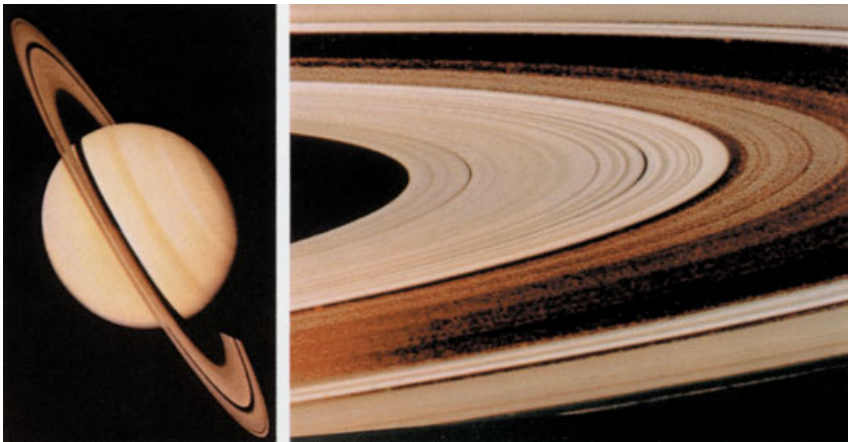


Plate VII.

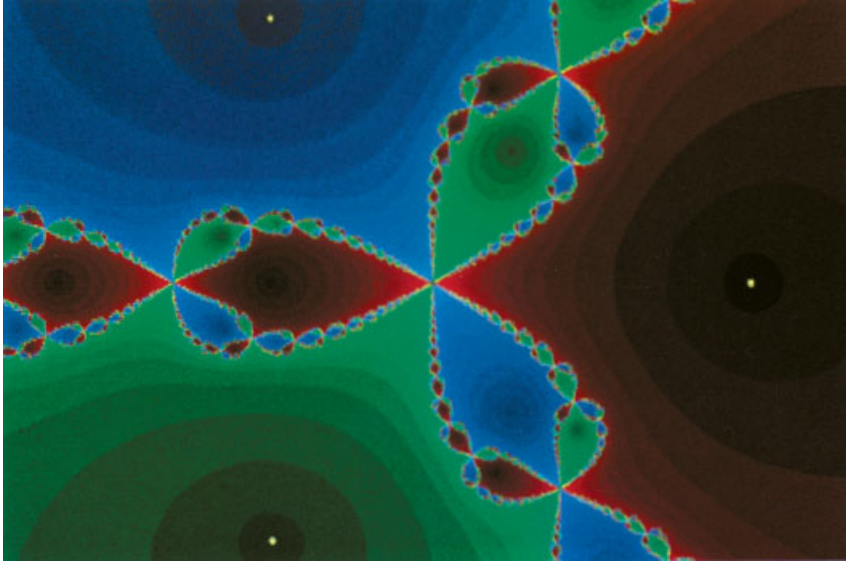


Plate VIII.

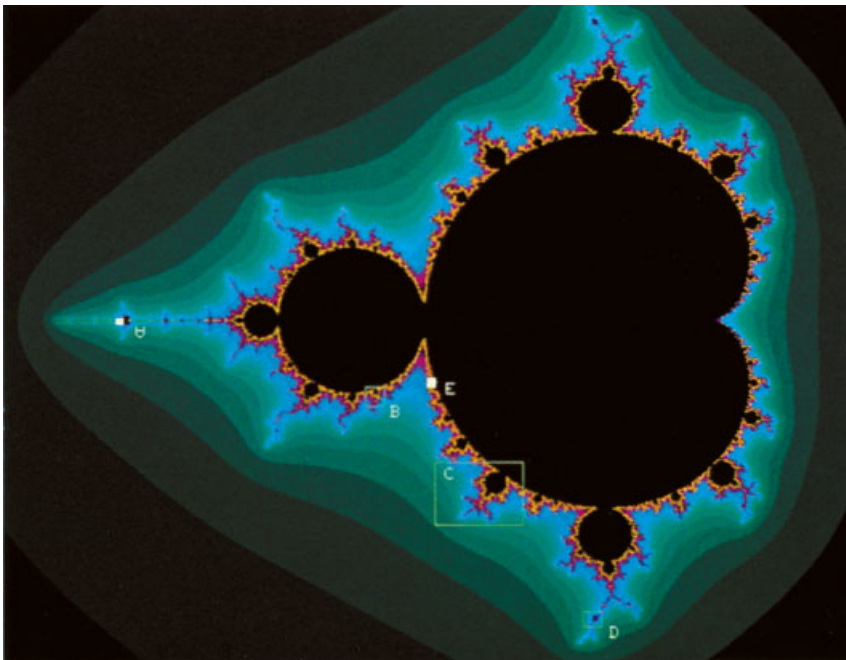


Plate IX.

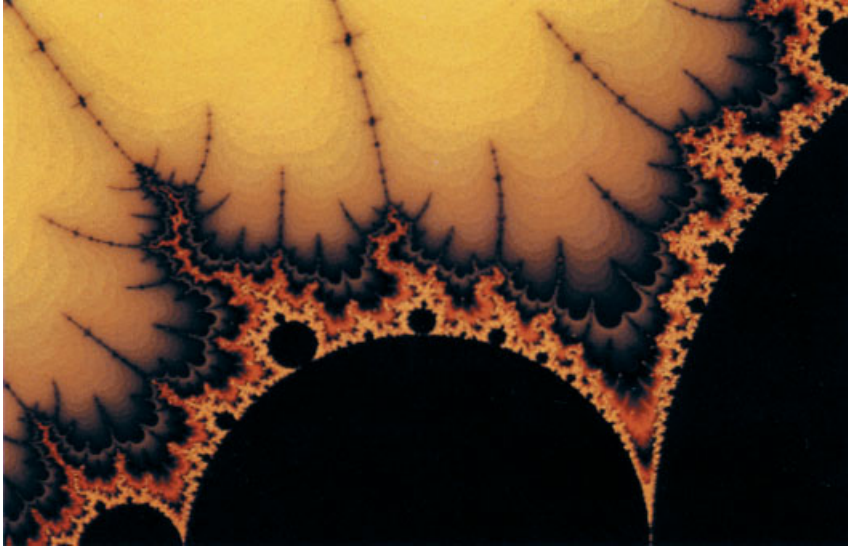


Plate X.

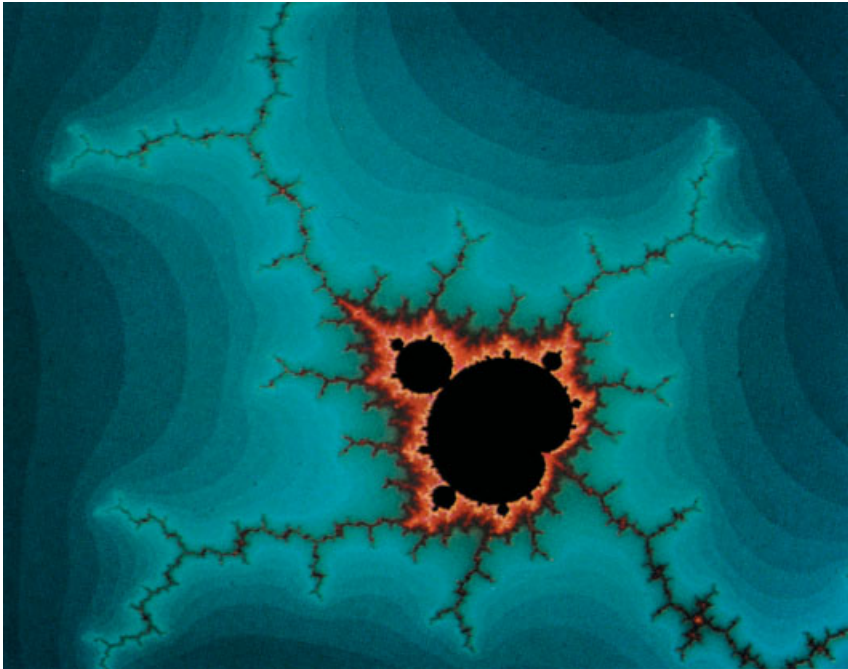


Plate XI.



Plate XII.

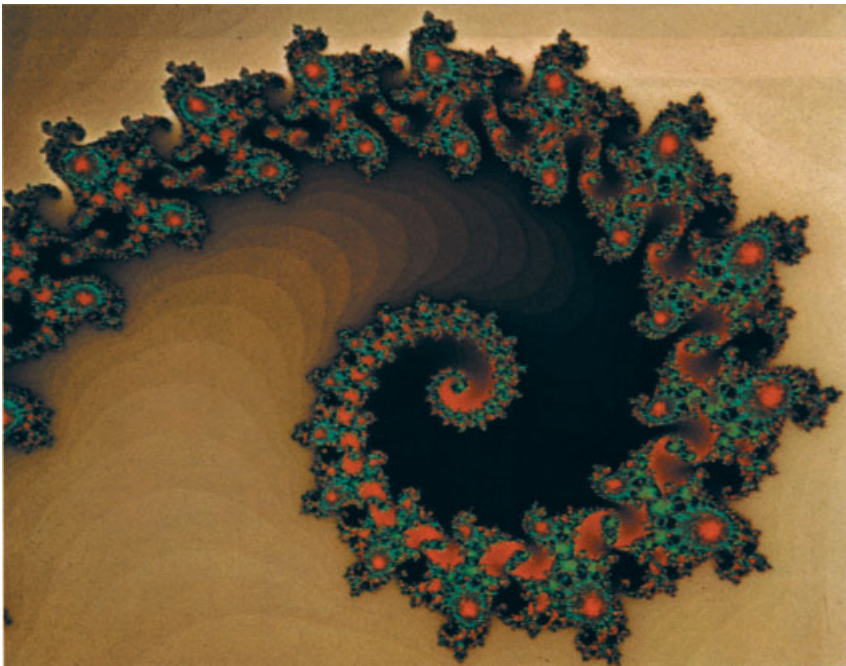


Plate XIII.

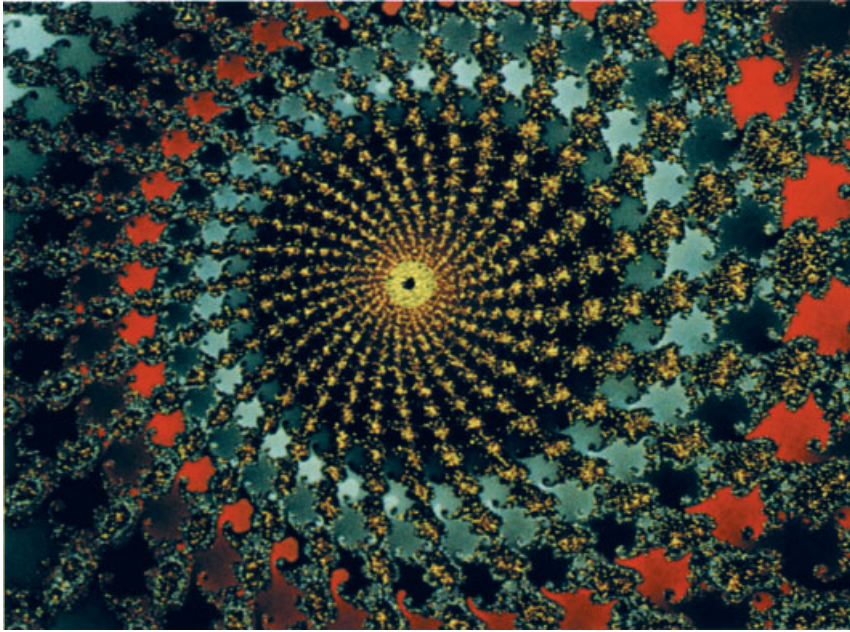


Plate XIV.



Plate XV.

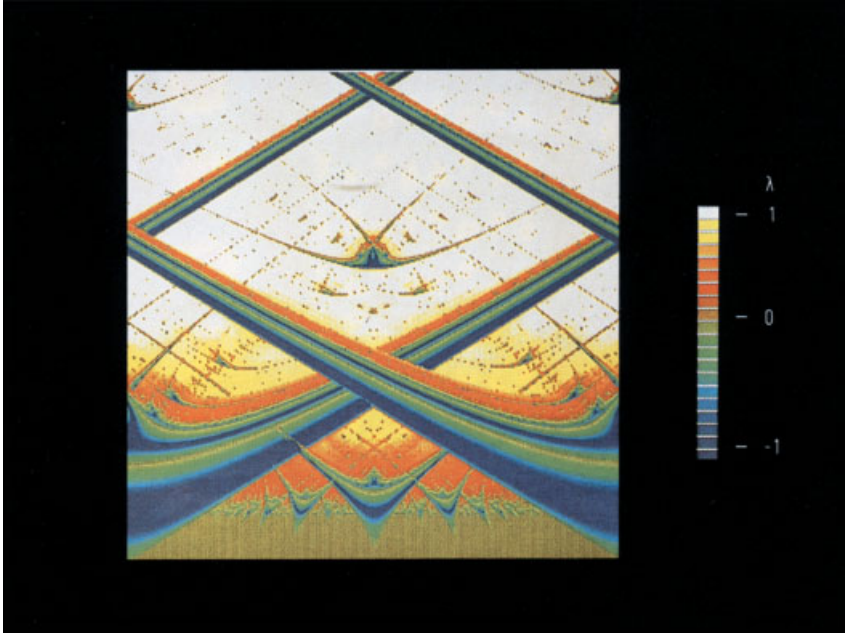


Plate XVI.

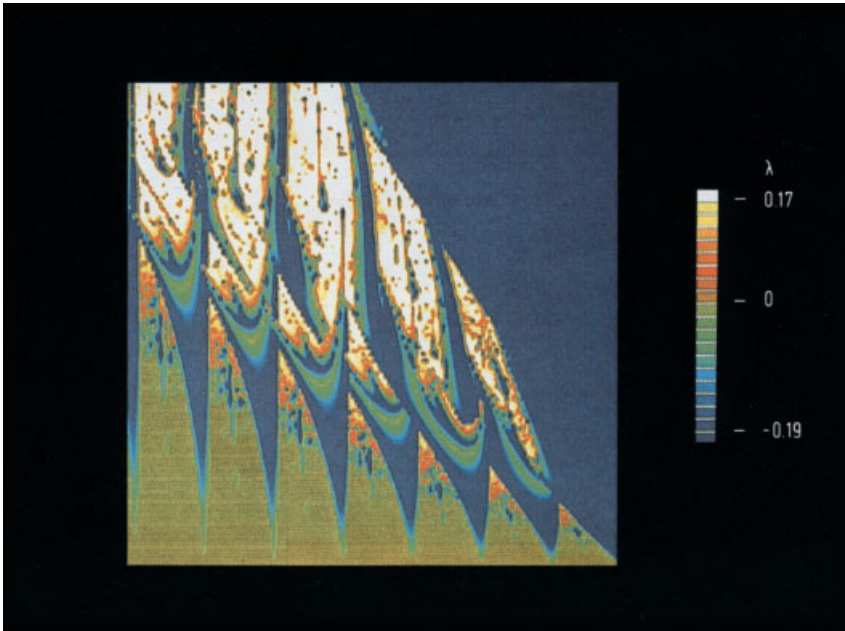


Plate XVII.

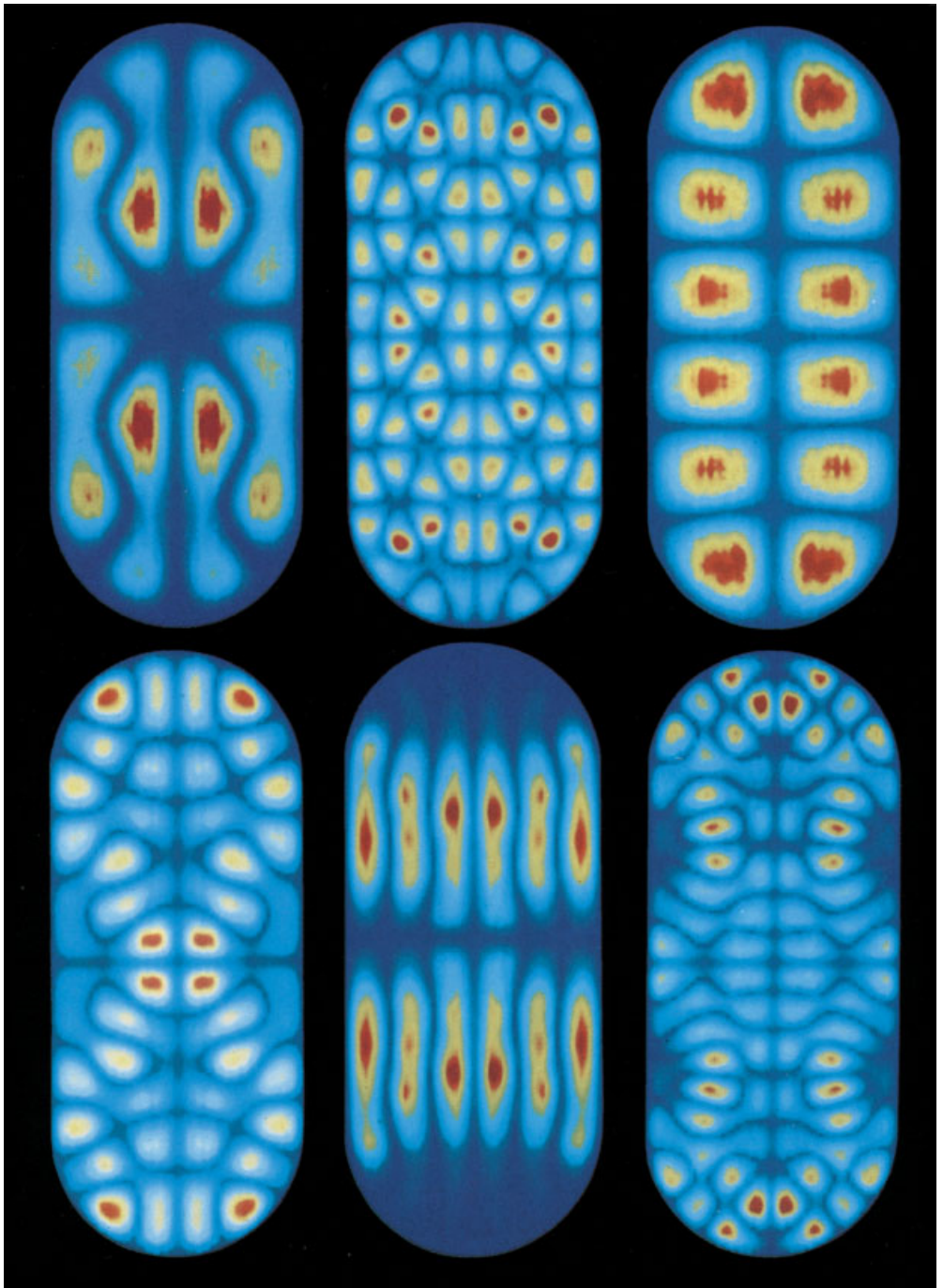


Plate XVIII.

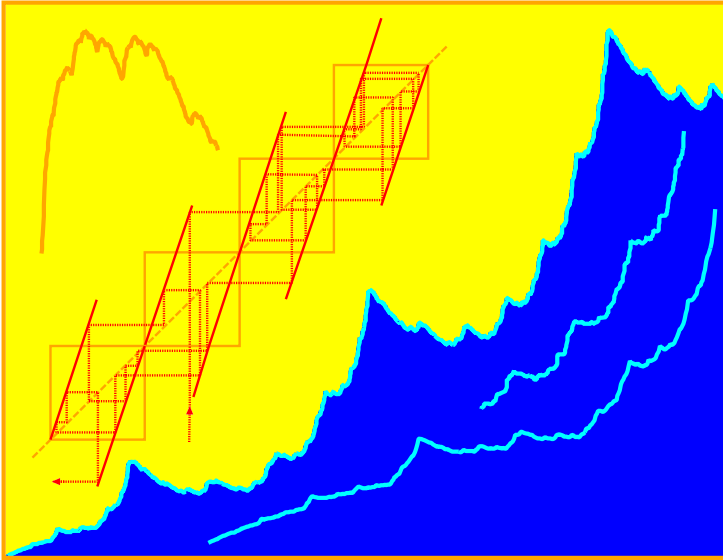


Plate XIX.

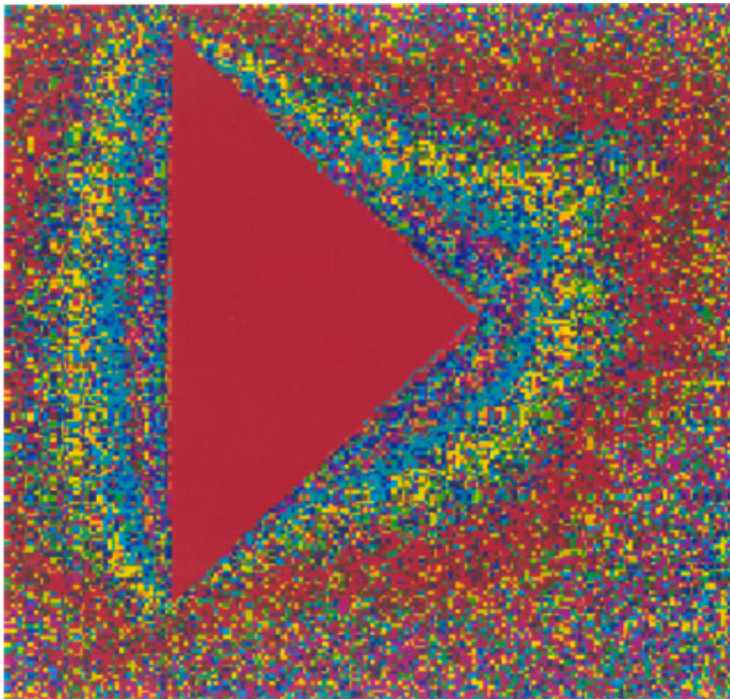


Plate XX.

1 Introduction

*Ante mare et terras et, quod tegit omnia,
caelum Unus erat toto naturae vultus in
orbe, Quem dixere Chaos, rudis
indigestaque moles Nec quicquam nisi
pondus iners congestaque eodem Non
bene iunctarum discordia semina rerum.*
Ovid

It seems appropriate to begin a book which is entitled “Deterministic Chaos” with an explanation of both terms. According to the Encyclopaedia Britannica the word “chaos” is derived from the Greek “ $\chi\alpha\omicron\sigma$ ” and originally meant the infinite empty space which existed before all things. The later Roman conception interpreted chaos as the original crude shapeless mass into which the Architect of the world introduces order and harmony. In modern usage which we will adopt here, chaos denotes a state of disorder and irregularity.

In the following, we shall consider physical systems whose time dependence is deterministic, i. e., there exists a prescription, either in terms of differential or difference equations, for calculating their future behavior from given initial conditions. One could assume naively that deterministic motion (which is, for example, generated by continuous differential equations) is rather regular and far from being chaotic because successive states evolve continuously from each other. But it was already discovered at the turn of the century by the mathematician H. Poincaré (1892) that certain mechanical systems, whose time evolution is governed by Hamilton’s equations, could display chaotic motion. Unfortunately, this was considered by many physicists as a mere curiosity, and it took another 70 years until, in 1963, the meteorologist E. N. Lorenz found that even a simple set of three coupled, first-order, nonlinear differential equations can lead to completely chaotic trajectories. Lorenz’s paper, the general importance of which is recognized today, was also not widely appreciated until many years after its publication. He discovered one of the first examples of deterministic chaos in dissipative systems.

In the following, deterministic chaos denotes the irregular or chaotic motion that is generated by nonlinear systems whose dynamical laws uniquely determine the time evolution of a state of the system from a knowledge of its previous history. In recent years – due to new theoretical results, the availability of high speed computers, and refined experimental techniques – it has become clear that this phenomenon is abundant in nature and has far-reaching consequences in many branches of science (see the long list in Table 1, which is far from complete).

Table 1: Some nonlinear systems which display deterministic chaos. (For numerals, see “References” on page 259.)

Forced pendulum [1]
Fluids near the onset of turbulence [2]
Lasers [3]
Nonlinear optical devices [4]
Josephson junctions [5]
Chemical reactions [6]
Classical many-body systems (three-body problem) [7]
Particle accelerators [8]
Plasmas with interacting nonlinear waves [9]
Biological models for population dynamics [10]
Stimulated heart cells (see Plate IV at the beginning of the book) [11]

We note that nonlinearity is a necessary, but not a sufficient condition for the generation of chaotic motion. (Linear differential or difference equations can be solved by Fourier transformation and do not lead to chaos.) The observed chaotic behavior in time is neither due to external sources of noise (there are none in the Lorenz equations) nor to an infinite number of degrees of freedom (in Lorenz’s system there are only three degrees of freedom) nor to the uncertainty associated with quantum mechanics (the systems considered are purely classical). The actual source of irregularity is the property of the nonlinear system of separating initially close trajectories exponentially fast in a bounded region of phase space (which is, e. g., three-dimensional for Lorenz’s system).

It becomes therefore practically impossible to predict the long-time behavior of these systems, because in practice one can only fix their initial conditions with finite accuracy, and errors increase exponentially fast. If one tries to solve such a nonlinear system on a computer, the result depends for longer and longer times on more and more digits in the (irrational) numbers which represent the initial conditions. Since the digits in irrational numbers (the rational numbers are of measure zero along the real axis) are irregularly distributed, the trajectory becomes chaotic.

Lorenz called this sensitive dependence on the initial conditions the butterfly effect, because the outcome of his equations (which describe also, in a crude sense, the flow of air in the earth’s atmosphere, i. e., the problem of weather forecasting) could be changed by a butterfly flapping wings. This also seems to be confirmed sometimes by daily experience.

The results described above immediately raise a number of fundamental questions:

- Can one predict (e. g., from the form of the corresponding differential equations) whether or not a given system will display deterministic chaos?
- Can one specify the notion of chaotic motion more mathematically and develop quantitative measures for it?
- What is the impact of these findings on different branches of physics?
- Does the existence of deterministic chaos imply the end of long-time predictability in physics for some nonlinear systems, or can one still learn something from a chaotic signal?

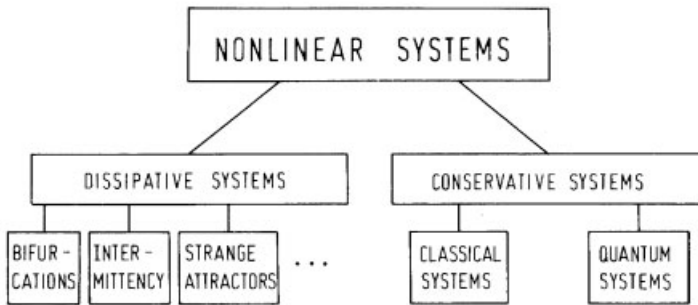


Figure 1: Classification of systems which display deterministic chaos. (We consider in the following only classical dissipative systems, i. e., no quantum systems with dissipation.)

The last question really goes to the fundamentals of physics, namely the problem of predictability. The shock which was associated with the discovery of deterministic chaos has therefore been compared with that which spread when it was found that quantum mechanics only allows statistical predictions.

Those questions mentioned above, to which some answers already exist, will be discussed in the remainder of this book. It should be clear, however, that there are still many more unsolved than solved problems in this relatively new field.

The rest of the introduction takes the form of a short survey which summarizes the contents of this book. Figure 1 shows that one has to distinguish between deterministic chaos in dissipative systems (e. g., a forced pendulum with friction) and conservative systems (e. g., planetary motion which is governed by Hamilton's equations).

The first six chapters are devoted to dissipative systems. We begin with a review of some representative experiments in which deterministic chaos has been observed by different methods. As a next step, we explain the mechanism which leads to deterministic chaos for a simple model system and develop quantitative measures to characterize a chaotic signal. This allows us to distinguish different types of chaos, and we then show that, up to now, there are at least three routes or transitions in which nonlinear systems can become chaotic if an external control parameter is varied. Interestingly enough, all these routes can be realized experimentally, and they show a fascinating universal behavior which is reminiscent of the universality found in second-order equilibrium phase transitions. (Note that the transitions to chaos in dissipative systems only occur when the system is driven externally, i. e., is open.) In this context, universality means that there are basic properties of the system (such as critical exponents near the transition to chaos) that depend only on some global features of the system (for example, the dimensionality).

The most recent route to chaos has been found by Grossmann and Thomaes (1977), Feigenbaum (1978), and Coulet and Tresser (1978). They considered a simple difference equation which, for example, has been used to describe the time dependence of populations in biology, and found that the population oscillated in time between stable values (fixed points) whose number doubles at distinct values of an external parameter. This continues until the number of fixed points becomes infinite at a finite parameter value, where the variation in time of the

population becomes irregular. Feigenbaum has shown, and this was a major achievement, that these results are not restricted to this special model but are in fact universal and hold for a large variety of physical, chemical, and biological systems. This discovery has triggered an explosion of theoretical and experimental activity in the field. We will study this route in Chapter 4 and show that its universal properties can be calculated using the functional renormalization group method.

A second approach to chaos, the so-called intermittency route, has been discovered by Manneville and Pomeau (1979). Intermittency means that a signal which behaves regularly (or laminarly) in time becomes interrupted by statistically distributed periods of irregular motion (intermittent bursts). The average number of these bursts increases with the variation of an external control parameter until the motion becomes completely chaotic. It will be shown in Chapter 5 that this route also has universal features and provides a universal mechanism for $1/f$ -noise in nonlinear systems.

Yet a third possibility was found by Ruelle and Takens (1971) and Newhouse (1978). In the seventies they suggested a transition to turbulent motion which was different from that proposed much earlier by Landau (1944, 1959). Landau considered turbulence in time as the limit of an infinite sequence of instabilities (Hopf bifurcations) each of which creates a new basic frequency. However, Ruelle, Takens, and Newhouse showed that after only two instabilities in the third step, the trajectory becomes attracted to a bounded region of phase space in which initially close trajectories separate exponentially, such that the motion becomes chaotic. These particular regions of phase space are called strange attractors. We will explain this concept in Chapter 6, where we will also discuss several methods of extracting information about the structure of the attractor from the measured chaotic time signal. The Ruelle–Takens–Newhouse route is (as are the previous two routes) well verified experimentally, and we will present some experimental data which show explicitly the appearance of strange attractors in Chapter 7.

To avoid the confusion which might arise by the use of the word turbulence, we note that what is meant here, is only turbulence in time. The results of Ruelle, Takens, and Newhouse also concern the onset of turbulence or chaotic motion in time. It is in fact one of the aims (but not yet the result) of the study of deterministic chaos in hydrodynamic systems, to understand the mechanisms for fully developed turbulence, which implies irregular behavior in time and space.

We now come to the second branch in Fig. 1, which denotes chaotic motion in conservative systems. Many textbooks give the incorrect impression that most systems in classical mechanics can be integrated. But as mentioned above, Poincaré (1892) was already aware that, e. g., the nonintegrable three-body problem of classical mechanics can lead to completely chaotic trajectories. About sixty years later, Kolmogorov (1954), Arnold (1963), and Moser (1967) proved, in what is now known as the KAM theorem, that the motion in the phase space of classical mechanics is neither completely regular nor completely irregular, but that the type of trajectory depends sensitively on the chosen initial conditions. Thus, stable regular classical motion is the exception, contrary to what is implied in many texts.

A study of the long-time behavior of conservative systems, which will be discussed in Chapter 8, is of some interest because it touches on such questions as: Is the solar system stable? How can one avoid irregular motion in particle accelerators? Is the self-generated deterministic chaos of some Hamiltonian systems strong enough to prove the ergodic hypoth-

esis? (The ergodic hypothesis lies at the foundation of classical statistical mechanics and implies that the trajectory uniformly covers the energetically allowed region of classical phase space such that time averages can be replaced by the average over the corresponding phase space.)

In Chapter 8 we consider the behavior of quantum systems whose classical limit displays chaos. Such investigations are important, for example, for the problem of photodissociation, where a molecule is kicked by laser photons, and one wants to know how the incoming energy spreads over the quantum levels. (The corresponding classical system could show chaos because the molecular forces are highly nonlinear.) For several examples we show that the finite value of Planck's constant leads, together with the boundary conditions, to an almost-periodic behavior of the quantum system even if the corresponding classical system displays chaos. Although the difference between integrable and nonintegrable (chaotic) classical systems is still mirrored in some properties of their quantum counterparts (for example in the energy spectra), many problems in this field remain unsolved.

As already mentioned in the preface, the field of deterministic chaos continued to grow after the last edition of this book in 1989. Especially the concept of unstable periodic orbits has been rediscovered and developed further by Cvitanovich *et al.* (1990). Unstable periodic orbits are the building blocks of chaotic dynamics, and their importance was already known by Poincaré (1892) and Ruelle (1978).

Exploiting this concept, Ott, Grebogi and Yorke showed in 1990 that deterministic chaos can be controlled. As we will show in Chapter 10, unstable periodic orbits, which are contained in all chaotic systems, can be stabilized by small time-dependent changes of the control parameter of the system in such a way that the dynamical behavior becomes non-chaotic. Control of chaos is, because of its possible technical applications, an extremely active field where one would hope to make interesting new progress, especially for spatially coupled chaotic systems.

Synchronization phenomena are related to control problems as, in very simple cases, a desired state can be reached by external periodic modulation. But synchronization includes much richer phenomena, especially when nonlinear and chaotic dynamical systems are considered. Chapter 11 presents a brief introduction into this field.

The study of spatiotemporal chaotic motion is still in its infancy. In Chapter 12 we present a selection of phenomena and approaches which may turn out to be among the cornerstones on which a consistent and systematic exposition of this topic may be based. However, an ultimate answer is currently not available.

2 Experiments and Simple Models

In the first part of this chapter, we review some experiments in which deterministic chaos has been detected by different methods. In the second part, we present some simple systems which exhibit chaos and which can be treated analytically.

2.1 Experimental Detection of Deterministic Chaos

In the following section, we will discuss the appearance of chaos in four representative systems.

2.1.1 Driven Pendulum

Let us first consider the surprisingly simple example of a periodically driven pendulum. Its equation of motion is

$$\ddot{\theta} + \gamma\dot{\theta} + \sin\theta = A\cos(\omega t) \quad (2.1)$$

where the dot denotes the derivative with respect to time t , γ is the damping constant, and the right hand side describes a driving torque with amplitude A and frequency ω . (The coefficients of $\ddot{\theta}$ and $\sin\theta$ have been normalized to unity by choosing appropriate units for t and A). This equation has been numerically integrated for different sets of parameters (A , ω , γ), and Fig. 2 shows that the variation of the angle θ with time simply “looks chaotic” if the amplitude A of the driving torque reaches a certain value A_c . This is a possible, but rather imprecise criterion for chaos.

Before we proceed to improvements, three comments are in order. First, we would like to recall the well-known fact that the linearized version of the pendulum equation can be integrated exactly and does not lead to chaos. The emergence of chaos in the solutions of eq. (2.1) is, therefore, due to the nonlinear term $\sin\theta$. Second, it follows from Fig. 2b and 2d that chaos sets in if the pendulum is driven over the summit where the system displays sensitive dependence on initial conditions (a tiny touch determines, at $\theta = \pi$, whether the pendulum makes a left or right turn). Third, we would like to point out that as a function of the parameters A and ω , the behavior of the pendulum switches rather wildly between regular and chaotic motion, as shown in Fig. 2e.

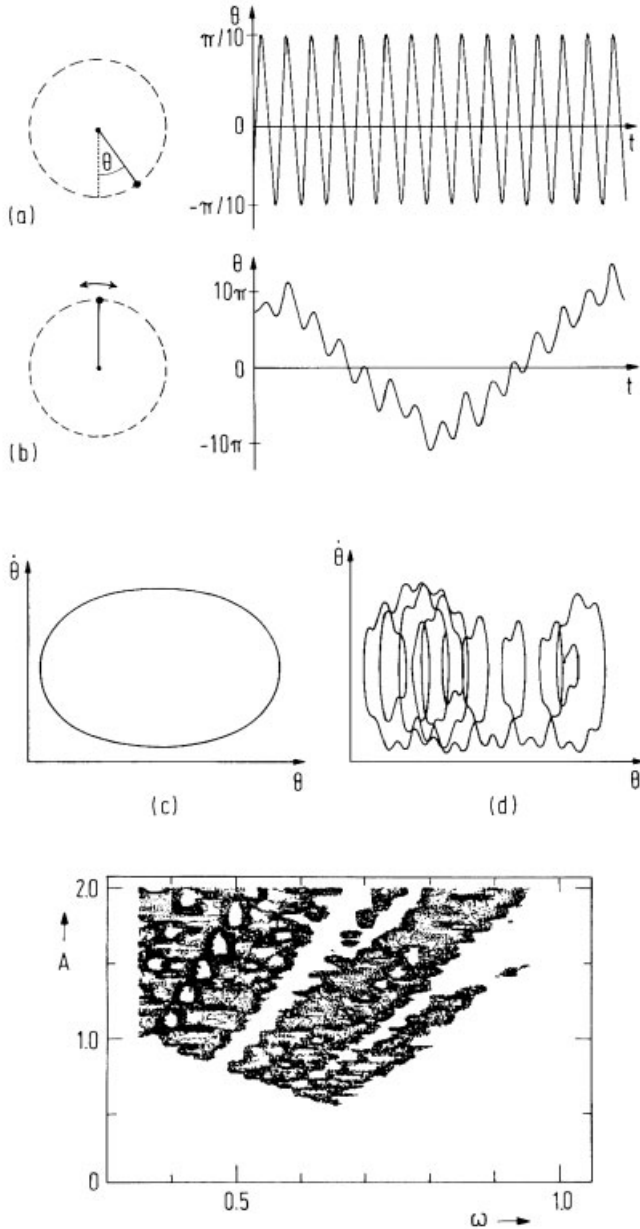


Figure 2: Transition to chaos in a driven pendulum. a) Regular motion at small values of the amplitude A of the driving torque. b) Chaotic motion at $A = A_c$ (note the different scales for θ). c) and d) Regular and irregular trajectories in phase space $(\dot{\theta}, \theta)$ which correspond to a) and b). e) Phase diagram of the driven pendulum ($\gamma = 0.2$, $\theta(0) = 0$, $\dot{\theta}(0) = 0$). Black points denote parameter values (A, ω) for which the motion is chaotic. (After Bauer, priv. comm.)

2.1.2 Rayleigh–Bénard System in a Box

Chaotic motion means that the signal displays an irregular and aperiodic behavior in time. To distinguish between multiply periodic behavior (which can also look rather complicated) and chaos, it is often convenient to Fourier-transform the signal $x(t)$:

$$x(\omega) = \lim_{T \rightarrow \infty} \int_0^T dt e^{i\omega t} x(t) . \quad (2.2)$$

For multiply periodic motion, the power spectrum

$$P(\omega) \equiv |x(\omega)|^2 \quad (2.3)$$

consists only of discrete lines of the corresponding frequencies, whereas chaotic motion (which is completely aperiodic) is indicated by broad noise in $P(\omega)$ that is mostly located at low frequencies. Such a transition from periodic motion to chaos is presented in the second line of Table 2 which shows the power spectrum of the velocity of the liquid in the x -direction for a Bénard experiment.

In the Bénard experiment, a fluid layer (with a positive coefficient of volume expansion) is heated from below in a gravitational field, as shown in Fig. 3. The heated fluid at the bottom “wants” to rise, and the cold liquid at the top “wants” to fall, but these motions are opposed by viscous forces. For small temperature differences ΔT , viscosity wins; the liquid remains at rest and heat is transported by uniform heat conduction. This state becomes unstable at a critical value R_a , of the Rayleigh number R (which is proportional to ΔT , see Appendix A), and a state of stationary convection rolls develops. If R increases, a transition to chaotic motion is observed beyond a second threshold R_c .

In order to avoid the appearance of complex spatial structures, actual experiments to detect chaos (in time) in a Rayleigh–Bénard system are usually performed in a small cell (see Fig. 3c). The boundary conditions limit the number of rolls, that is the number of degrees of freedom that are counted by the number of Fourier components needed to describe the spatial structure of the fluid pattern. Besides ΔT , the observed dynamical behavior depends sensitively on the liquid chosen and on the linear dimensions (a , b , c) of the box (see, for example, Libchaber and Maurer, 1982). Table 2 shows the power spectrum of the velocity in

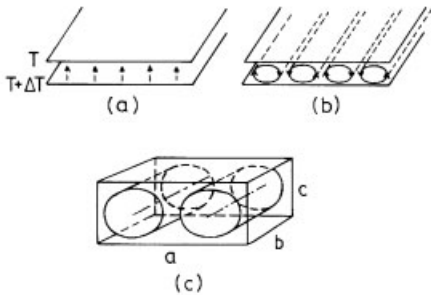
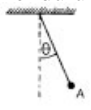
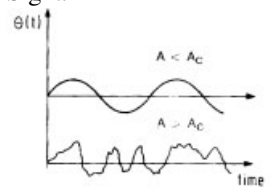
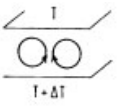
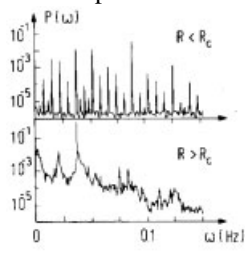
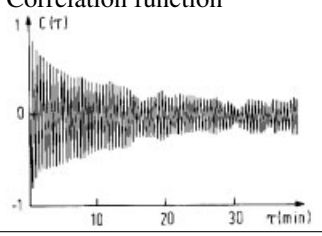
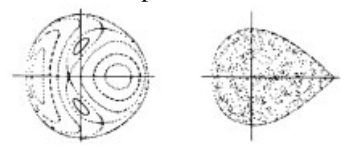


Figure 3: The Rayleigh–Bénard instability. a) and b) Transition from heat conduction to convection rolls in an infinitely extended two-dimensional fluid layer. c) Experiments to detect deterministic chaos in time are performed in a “match box”.

Table 2: Detection of chaos in simple systems.

System	Equation of Motion	Indication
Pendulum 	$\ddot{\theta} + \gamma\dot{\theta} + g \sin \theta = A \cos \omega t$ $x = \theta, y = \dot{\theta}, z = \omega t$ $\dot{x} = y$ $\dot{y} = -\gamma y - g \sin x + A \cos z$ $\dot{z} = \omega$	Signal 
Bénard experiment 	$\dot{x} = -\sigma x + \sigma y$ $\dot{y} = rx - y - xz$ $\dot{z} = xy - bz$	Power Spectrum 
Belousov–Zhabotinsky Reaction $\text{Ce}_2(\text{SO}_4)_3$ \vdots Ce^{4+}	$\dot{\vec{x}} = \vec{F}(\vec{x}, \lambda)$ $\vec{x} = [c_1, c_2, \dots, c_d]$	Correlation function 
Hénon–Heiles System	$H = \frac{1}{2} \sum_{i=1}^2 (p_i^2 + q_i^2) + q_1^2 q_2 - \frac{1}{3} q_2^3$ $\dot{\vec{p}} = -\frac{\partial H}{\partial \vec{q}}, \quad \dot{\vec{q}} = \frac{\partial H}{\partial \vec{p}}$	Poincaré Map 

the x -direction, measured via the Doppler effect in light scattering experiments (Swinney and Gollub, 1978; see also plate I [at the beginning of the book] for a set of interferometric pictures of a Bénard cell). To describe the Bénard experiment theoretically, Lorenz truncated the complicated differential equations which describe this system (see Appendix A) and obtained the equations of the so-called Lorenz model:

$$\dot{X} = -\sigma X + \sigma Y \quad (2.4a)$$

$$\dot{Y} = rX - Y - XZ \quad (2.4b)$$

$$\dot{Z} = XY - bZ \quad (2.4c)$$

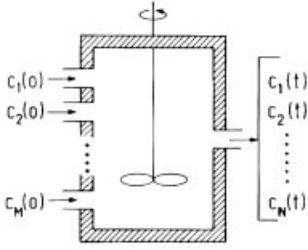
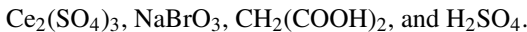


Figure 4: Flow of chemicals in a well stirred reactor. $c_1(0) \dots c_M(0)$ are the initial concentrations of the chemicals, and $c_1 \dots c_N(t)$ are the output concentrations.

where σ and b are dimensionless constants which characterize the system, and r is the control parameter which is proportional to ΔT . The variable X is proportional to the circulatory fluid flow velocity, Y characterizes the temperature difference between ascending and descending fluid elements, and Z is proportional to the deviations of the vertical temperature profile from its equilibrium value. A numerical analysis of this apparently simple set of nonlinear differential equations shows that its variables can exhibit chaotic motion above a threshold value r_c (see Appendix B). It should be noted, however, that the Lorenz equations describe the Bénard experiment only in the immediate vicinity of the transition from heat conduction to convection rolls because the spatial Fourier coefficients retained by Lorenz only describe simple rolls. The chaos found by Lorenz in eqs. (2.4a–c) is, therefore, different from the chaos seen in the experimental power spectrum in Table 2. To describe the experimentally observed chaos, many more spatial Fourier components have to be retained.

2.1.3 Stirred Chemical Reactions

Another system in which chaotic motion has been studied experimentally in great detail is the Belousov–Zhabotinsky reaction. In this chemical process, an organic molecule (e. g., malonic acid) is oxidized by bromate ions; the oxidation is catalyzed by a redox system ($\text{Ce}^{4+}/\text{Ce}^{3+}$). The reactants, which undergo 18 elementary reaction steps (see Epstein *et al.*, 1983), are:



It is not our aim to describe these reactions in detail but to demonstrate that stirred chemical reactions provide convenient model systems to study the onset of chaos. Figure 4 shows how a chemical reaction is maintained in a steady state away from equilibrium by continuously pumping the chemicals into a flow reactor where they are stirred to ensure spatial homogeneity. For example, the reaction



is described by the equations:

$$\dot{c}_A = -k_1 c_A c_B + k_2 c_C - r[c_A - c_A(0)] \quad (2.6a)$$

$$\dot{c}_B = -k_1 c_A c_B + k_2 c_C - r[c_B - c_B(0)] \quad (2.6b)$$

$$\dot{c}_C = k_1 c_A c_B - k_2 c_C - r \quad (2.6c)$$

where eq. 2.6a can be interpreted as follows. The concentration c_A decreases due to collisions between A and B (which generate C), increases due to decays of C (into A and B), and decreases if the flow rate r increases since for $k_1 = k_2 = 0$, eq. 2.6a can be integrated to $c_A(t) - c_A(0) \sim \exp(-rt)$.

Generalizing, the reactions of M chemicals of concentrations c_i can be described by a set of first-order nonlinear differential equations

$$\dot{c}_i = g_i\{c_j\} - r[c_i - c_i(0)] \equiv F_i\{c_j, \lambda\} \quad (2.7)$$

where the function $g_j\{c_j\}$ involves nonlinear terms of the form c_i^2 and $c_i c_j$ if three-body collisions are neglected. The reactions can be studied as a function of the set of control parameters $\lambda \equiv \{c_i(0), k_j, r\}$ that involves the initial concentrations $\{c_i(0)\}$, the temperature dependent reaction velocities $\{k_j\}$ and the flow rate r . Since r influences all individual reactions and can be easily manipulated by changing the pumping rate of the chemicals, it is usually used as the only control parameter.

Let us now come back to the Belousov–Zhabotinsky reaction. The variable which signals chaotic behavior in this system is the concentration c of the Ce^{4+} ions. It is measured by the selective light absorption of these ions. The mean residence time of the substances in the open reactor (i. e., r^{-1}) acts as an external control parameter corresponding to ΔT in the previous experiment.

Table 2 shows a transition to chaos in this system which is detected via the change in the autocorrelation function

$$C(\tau) = \lim_{T \rightarrow \infty} \frac{1}{T} \int_0^T dt \hat{c}(t) \hat{c}(t + \tau); \quad \hat{c}(t) = c(t) - \lim_{T \rightarrow \infty} \frac{1}{T} \int_0^T dt c(t) \quad (2.8)$$

This function measures the correlation between subsequent signals. It remains constant or oscillates for regular motion and decays rapidly (mostly with an exponential tail) if the signals become uncorrelated in the chaotic regime (Roux *et al.*, 1981).

It should be noted that the power spectrum $P(\omega)$ is proportional to the Fourier transformation of $C(\tau)$

$$P(\omega) = |\hat{c}(\omega)|^2 \propto \lim_{T \rightarrow \infty} \int_0^T d\tau e^{i\omega\tau} C(\tau) \quad (2.9)$$

that is, both quantities contain the same information. Equation (2.9) can be derived by the usual rules for Fourier transformations if one continues $\hat{c}(t)$ periodically in T so that $\hat{c}(t) = \hat{c}(t + nT)$ and n is an integer which leads to

$$\hat{c}(\omega) = \lim_{T \rightarrow \infty} \int_0^T dt e^{i\omega t} \hat{c}(t) = \lim_{T \rightarrow \infty} \int_{-T}^T dt \cos(\omega t) \hat{c}(t). \quad (2.10)$$

2.1.4 Hénon–Heiles System

Let us finally have a look at a simple nonintegrable example from classical mechanics that displays chaotic motion. In 1964 Hénon and Heiles numerically studied the canonical equations of motion of the Hamiltonian

$$H = \frac{1}{2}(p_1^2 + p_2^2) + \frac{1}{2}(q_1^2 + q_2^2) + q_1^2 q_2 - \frac{1}{3} q_2^3. \quad (2.11)$$

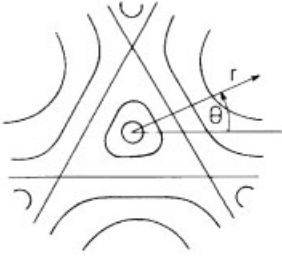


Figure 5: Equipotential lines $V(r, \theta) = \text{const.}$ of the Hénon–Heiles system [eq. (2.12)] in polar coordinates.

This equation describes, in Cartesian coordinates q_1 and q_2 , two nonlinearly coupled harmonic oscillators and, in polar coordinates (r, θ) , a single particle in a noncentrosymmetric potential

$$V(r, \theta) = \frac{r^2}{2} + \frac{r^3}{3} \sin(3\theta) \quad (2.12)$$

that is obtained from $1/2(q_1^2 + q_2^2) + q_1^2 q_2 - 1/3 q_2^3$ via $q_1 = r \cos \theta$ and $q_2 = r \sin \theta$ (see Fig. 5).

Their investigation was motivated by empirical evidence that a star moving in a weakly disturbed cylindrically symmetric potential should have, in addition to the energy E , another constant of the motion I . This would imply that, for bounded motion, the trajectory of the Hénon–Heiles system in phase space

$$\vec{x}(t) = [p_1(t), p_2(t), q_1(t), q_2(t)] \quad (2.13)$$

where p_1, p_2 are the momenta, is confined (via $E[\vec{x}(t)] = \text{const.}$ and $I[\vec{x}(t)] = \text{const.}$) to a two-dimensional closed surface. In order to check this proposal, Hénon and Heiles followed a method introduced by Poincaré (1893) and plotted the points in which the trajectory $\vec{x}(t)$ cuts the (p_2, q_2) plane. If the motion would be confined to a two-dimensional manifold, these points should form closed curves corresponding to the cut of the two-dimensional closed surface with the (p_2, q_2) plane. The last line in Table 2 shows that, at low energies, different initial conditions in the Hénon–Heiles system indeed lead to closed curves in the Poincaré map. However, for high enough energy (which acts as control parameter for this system) the lines decay, and the points in the Poincaré map of the Hénon–Heiles model become plane-filling. This indicates, according to Fig. 6, highly irregular chaotic motion in phase space and the absence of an additional constant of the motion I .

To summarize:

1. We have presented four possible criteria for chaotic motion:
 - The time dependence of the signal “looks chaotic”.
 - The power spectrum exhibits broadband noise.
 - The autocorrelation function decays rapidly.
 - The Poincaré map shows space-filling points.

In all four criteria, chaos is indicated by a qualitative change. Later, we will introduce some more quantitative measures to characterize deterministic chaos.

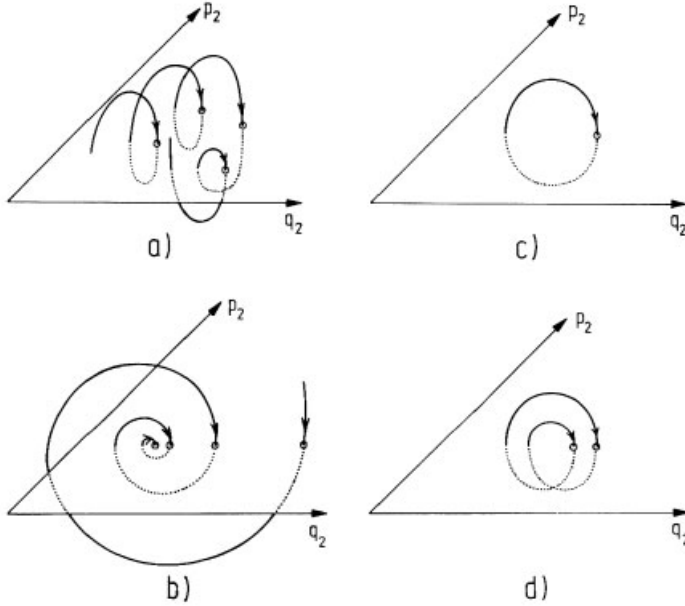


Figure 6: Qualitatively different trajectories can be distinguished by their Poincaré sections: a) chaotic motion; b) approach of a fixed point; c) cycle; d) cycle of period two.

2. A common feature of the systems listed in Table 2 is that they can be characterized by low-dimensional first-order differential equations

$$\dot{\vec{x}} = \vec{F}(\vec{x}, \lambda); \quad \vec{x} = (x_1 \dots x_d) \quad (2.14)$$

that are autonomous (i. e., \vec{F} does not contain the time explicitly) and nonlinear (\vec{F} is a nonlinear function of the $\{x_j\}$).

These equations lead to chaotic motion if an external control parameter λ (which can be the amplitude of the driving torque for the pendulum or the temperature difference ΔT in the Lorenz model, etc.) is varied. One distinguishes between *conservative systems*, for which a volume element in phase space $\{\vec{x}\}$ only changes its shape but retains its volume in the course of time (an example is the Hénon–Heiles Hamiltonian system for which the Liouville theorem holds) and *dissipative systems*, for which volume elements shrink as time increases (see also Chapter 7).

It is often convenient to study the flow described by the equations of motion (2.14) via the corresponding $(d - 1)$ -dimensional Poincaré map

$$\vec{x}(n+1) = \vec{G}[\vec{x}(n), \lambda]; \quad \vec{x}(n) = [x_1(n), \dots, x_{d-1}(n)] \quad (2.15)$$

that is generated by cutting the trajectory in d -dimensional phase space with a $(d - 1)$ -dimensional hyperplane (see Fig. 6) and by denoting the points which are generated with increasing time by $\vec{x}(1), \vec{x}(2) \dots$ etc. The classifications “conservative” and “dissipative” can then be generalized from flows to maps [see Chapter 6, eqs. (6.6a, b)].

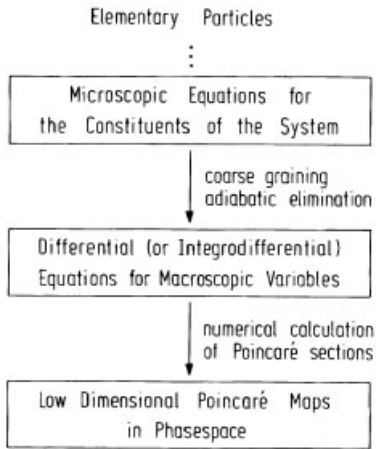


Figure 7: Hierarchy for the levels of description of dynamical systems

Let us finally comment on the way in which we shall proceed with our description of real physical systems. One can generally distinguish several levels of description as shown in Fig. 7.

A typical example of such a reduction process is given in Appendix A where the Navier–Stokes equations (which already represent a coarse grained description of molecular motion) are, for the boundary conditions of a Bénard experiment, reduced to the three differential equations of the Lorenz model which lead in turn to different Poincaré maps (see Figs. 49, 67) corresponding to different parameter values. Another example has been given by Haken (1975) who reduced the quantum mechanical equations for a single mode laser to a system of three rate equations (which is equivalent to the Lorenz system) by concentrating on macroscopic photon densities and using the adiabatic approximation (“Slaving principle”).

In the following, we shall not be concerned with the details of this reduction process since the step from microscopic equations to differential equations for macroscopic variables has already been covered in several excellent books (Haken 1982, 1984), and the reduction of differential equations to Poincaré maps can be done numerically. It should also be clear that this reduction of a many-constituent system to a map, which describes only a few degrees of freedom, is not always possible; a counterexample would be fully developed spatio-temporal turbulence. Nevertheless, since it has been found experimentally effective for many physical systems (see the following chapters), we shall in the remainder of this book concentrate mostly on the last level in Fig. 7 where the dynamics of a system has been reduced to a one- or two-dimensional Poincaré map. We shall use these maps as starting points for our description of chaotic systems in the same sense as one uses the (coarse grained) Ginzburg–Landau Hamiltonian to derive universal properties of second-order phase transitions (Wilson and Kogut, 1974). It will then be shown that only some general features of these maps (such as, for example, the existence of a simple maximum) determine how chaos emerges. The various “routes to chaos” differ in the way in which the signal behaves before becoming completely chaotic.

Although universal features of several routes to chaos have been discovered and verified experimentally it should be stated explicitly that it is presently practically impossible to theoretically predict, for example, from the Navier–Stokes equations with given boundary conditions, the route to chaos for a given experimental hydrodynamic system. This situation could be compared to ordinary second-order phase transitions where one knows a lot about universality classes and critical exponents (for example, of magnetic systems) but where it is still a formidable and often unsolved problem to predict the transition temperature of a given magnet (Ma 1976). However, this limitation should not disappoint us. The beauty of physics reveals itself only after asking the right questions, and it seems, from the results summarized in this book (see especially Table 12 on page 158) that it is equally so for dynamical systems where the question about universal features has led to the discovery of a beautiful unifying pattern behind different phenomena in this field.

2.2 The Periodically Kicked Rotator

One of the simplest dynamical systems which displays chaotic behavior in time is the periodically kicked damped rotator shown in Fig 8. Its equation of motion is

$$\ddot{\varphi} + \Gamma\dot{\varphi} = F \equiv Kf(\varphi) \sum_{n=0}^{\infty} \delta(t - nT), \quad n \text{ integer} \quad (2.16)$$

where the dot denotes the time derivatives; Γ is the damping constant, T is the period between two kicks, and we normalize the moment of inertia to unity. If we make the substitutions $x = \rho$, $y = \dot{\rho}$, $z = t$, eq. (2.16) can be rewritten as a system of first-order nonlinear autonomous differential equations

$$\dot{x} = y \quad (2.17a)$$

$$\dot{y} = -\Gamma y + Kf(x) \sum_{n=0}^{\infty} \delta(z - nT) \quad (2.17b)$$

$$\dot{z} = 1. \quad (2.17c)$$

These can be reduced to a two-dimensional map for the variables $(x_n, y_n) = \lim_{\varepsilon \rightarrow 0} [x(nT - \varepsilon), y(nT - \varepsilon)]$ by integration. The general solution of (2.17b) for $(n+1)T - \varepsilon > t > nT - \varepsilon$ is

$$y(t) = y_n e^{-\Gamma(t-nT)} + K \sum_{m=0}^{\infty} f(x_m) \int_{nT-\varepsilon}^t dt' e^{\Gamma(t'-t)} \delta(t' - mT). \quad (2.17)$$

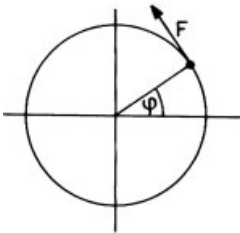


Figure 8: Rotator kicked by a force F .

This yields

$$y_{n+1} = e^{-\Gamma T} [y_n + Kf(x_n)] \quad (2.18a)$$

and by integrating (2.17a) using (2.18a) we obtain:

$$x_{n+1} = x_n + \frac{1 - e^{-\Gamma T}}{\Gamma} [y_n + Kf(x_n)] . \quad (2.18b)$$

Equations (2.18a) and (2.18b) are the main results of this section. They reduce the initial set of three-dimensional differential equations to a two-dimensional discrete map, which yields a stroboscopic picture of the variables. Below, we list several important limits of this two-dimensional map which will be discussed in some detail in the following sections.

2.2.1 Logistic Map

This is a one-dimensional quadratic map defined by

$$x_{n+1} = rx_n(1 - x_n) \quad (2.19)$$

where r is an external parameter, and the range of x_n is changed from a circle to the interval $[0, 1]$. It can be obtained from (2.18b) in the strong damping limit ($\Gamma \rightarrow \infty$) if $K \rightarrow \infty$, so that $\Gamma/K = 1$ and $f(x_n) = (r - 1)x_n - rx_n^2$.

2.2.2 Hénon Map

This can be considered as a two-dimensional extension of the logistic map (Hénon, 1976):

$$x_{n+1} = 1 - ax_n^2 + y_n \quad (2.20a)$$

$$y_{n+1} = bx_n \quad (2.20b)$$

where a and $|b| \leq 1$ are external parameters.

To obtain this map from (2.18a) and (2.18b), we rewrite these equations as

$$y_{n+1} = e^{-\Gamma T} [y_n + Kf(x_n)] \quad (2.21a)$$

$$x_{n+1} = x_n + \frac{e^{\Gamma T} - 1}{\Gamma} y_{n+1} \quad (2.21b)$$

and solve (2.21b) for y_{n+1} :

$$y_{n+1} = (x_{n+1} - x_n)\Gamma / (e^{\Gamma T} - 1) . \quad (2.22)$$

If we put y_{n+1} and y_n back into (2.21a), this becomes for $T = 1$:

$$x_{n+1} + e^{-\Gamma} x_{n-1} = (1 + e^{-\Gamma})x_n + \frac{1 - e^{-\Gamma}}{\Gamma} Kf(x_n) . \quad (2.23)$$

Choosing

$$\frac{1 - e^{-\Gamma}}{\Gamma} Kf(x_n) \equiv -(1 + e^{-\Gamma})x_n - 1 + ax_n^2; \quad b \equiv -e^{-\Gamma} , \quad (2.24)$$

eq. (2.23) yields

$$x_{n+1} = 1 - ax_n^2 + bx_{n-1} \quad (2.25)$$

which is equivalent to (2.20a–b). (Our derivation holds only for $b < 0$, but the map is mathematically defined for $-1 \leq b \leq 1$.)

2.2.3 Chirikov Map

This is simply the map of an undamped ($\Gamma \rightarrow 0$) rotator that is kicked by an external force $Kf(x_n) = -K \sin x_n$ (Chirikov, 1979). In this limit eq. (2.18a) and (2.18b) reduce to

$$p_{n+1} = p_n - K \sin \theta_n \quad (2.26a)$$

$$\theta_{n+1} = \theta_n + p_{n+1} \quad (2.26b)$$

where we have chosen $T = 1$ and introduced the conventional notation $x_n = \theta_n$ and $y_n = p_n$.

We shall see in the following chapters that, despite the apparent simplicity of all three maps, their iterates exhibit extremely rich and physically interesting structures.

3 Piecewise Linear Maps and Deterministic Chaos

The nonlinear Poincaré maps introduced in the previous chapter still lead to a rather complicated dynamical behavior (as we shall see in Chapter 4). In this section, we therefore study some simple one-dimensional piecewise linear maps. Although these maps are not directly connected to physical systems, they are extremely useful models which, in part one of this section, allow us to explain the mechanism which leads to deterministic chaos. In the second part, we will introduce three quantitative measures which characterize chaotic behavior and calculate these quantities explicitly for a triangular map. Finally, in Section 3.3 we show that the iterates of certain one-dimensional maps can display deterministic diffusion.

3.1 The Bernoulli Shift

Let us consider the one-dimensional map

$$x_{n+1} = \sigma(x_n) = 2x_n \bmod 1; \quad n = 0, 1, 2, \dots \tag{3.1}$$

which is shown in Fig 9. If we start with a value x_0 the map generates a sequence of iterates $x_0, x_1 = \sigma(x_0), x_2 = \sigma(x_1) = \sigma(\sigma(x_0)) \dots$. In order to investigate the properties of this sequence we write x_0 in binary representation:

$$x_0 = \sum_{v=1}^{\infty} a_v 2^{-v} \hat{=} (0, a_1 a_2 a_3 \dots) \tag{3.2}$$

where a_v has the values zero or unity. For $x_0 < 1/2$, we have $a_1 = 0$, and $x_0 > 1/2$ implies $a_1 = 1$. Therefore, the first iterate $\sigma(x_0)$ can be written as

$$\sigma(x_0) = \begin{cases} 2x_0 & \text{for } a_1 = 0 \rightarrow \\ 2x_0 - 1 & \text{for } a_1 = 1 \rightarrow \end{cases} = (0, a_2 a_3 a_4 \dots) \tag{3.3}$$

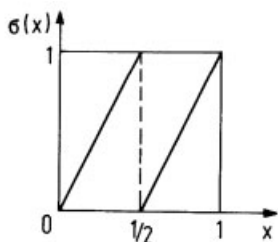


Figure 9: The transformation $\sigma(x) = 2x \bmod 1$.

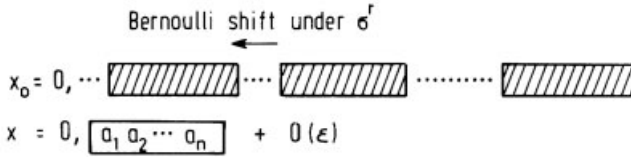


Figure 10: Emergence of ergodicity by a Bernoulli shift in irrational numbers.

i. e., the action of σ on the binary representation of x is to delete the first digit and shift the remaining sequence to the left. This is called the *Bernoulli shift*.

The Bernoulli property of $\sigma(x)$ demonstrates:

1. The sensitive dependence of the iterates of σ on the initial conditions. Even if two points x and x' differ only after their n th digit a_n , this difference becomes amplified under the action of σ , and their n th iterates $\sigma^n(x)$ and $\sigma^n(x')$ already differ in the first digit because $\sigma^n(x) = (0, a_n \dots)$ where $\sigma^2(x) = \sigma[\sigma(x)]$, etc.
2. The sequence of iterates $\sigma^n(x_0)$ has the same random properties as successive tosses of a coin. To see this, we attach to $\sigma^n(x_0)$ the symbol *R* or *L* depending on whether the iterate is contained in the right or left part of the unit interval. If we now prescribe an arbitrary sequence *RLLR...*, e. g., by tossing a coin, we can always find an x_0 for which the series of iterates $x_0, \sigma^1(x_0), \sigma^2(x_0) \dots$ generates this sequence. This follows because $\sigma^n(x_0) = (0, a_n a_{n+1} \dots)$ corresponds to *R* or *L* if and only if $a_n = 1$ or $a_n = 0$; i. e., the sequence *RLLR...* is isomorphous to the binary representation of x_0

$$\begin{array}{cccccc}
 x_0 & = & (0, & 1 & 0 & 0 & 1 & \dots) \\
 & & & \downarrow & \downarrow & \downarrow & \downarrow & \\
 & & & R & L & L & R &
 \end{array} \tag{3.4}$$

Thus, the prescription of a sequence by tossing a coin becomes equivalent to choosing a special value of x_0 .

3. The mechanism by which ergodicity emerges in a deterministic system. Let us first note that we can approximate each point x in the unit interval arbitrarily well by a finite sequence of binary digits $0, a_1, a_2 \dots a_n$ up to a difference $\epsilon = 2^{-n}$, say. It will now be shown that the images $\sigma^r(x_0)$ ($r = 1, 2, 3 \dots$) of an “arbitrary” irrational number $x_0 \in [0, 1]$ approach x to an order ϵ an infinite number of times; i. e., the system behaves ergodically.

This follows because a) almost all irrational numbers in $[0, 1]$ (with the exception of a set of measure zero) in their binary representation contain any finite sequence of digits infinitely often (see References on page 261) and b) the Bernoulli property of $\sigma(x)$ shifts these sequences to the initial position as depicted in Fig. 10. This argument goes right to the heart of the problem of chaotic motion in deterministic systems, and it shows how chaos arises from the amplification of the intrinsic “numerical noise” of irrational numbers.

This mechanism of generating deterministic chaos is also quite universal. Its two basic ingredients are the stretching and backfolding property of the map.

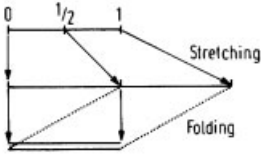


Figure 11: Stretching and folding of the unit interval under the action of $\sigma(x)$.

Initially, for $x_0 < 1/2$ say, x_0 becomes stretched after each iteration by a factor 2 (see Fig. 11). But for $n > n_0$ with $2^{n_0} \cdot x_0 \geq 1$, the second branch of $\sigma(x)$ becomes important, and x_n is folded back to the unit interval as shown in Fig. 11. For a general nonlinear map of the unit interval onto itself, the combination of stretching and backfolding (due to the restriction to $[0, 1]$) drives the iterates of an initial point repeatedly over the unit interval and leads to chaotic motion.

Let us briefly comment on the possible physical consequences of this stretching property of nonlinear maps. The initial conditions (i. e., the x_0) of a physical system can only be determined with finite precision. This “arbitrarily” small but finite error becomes exponentially amplified ($\sigma^n(x_0) = 2^n x_0 \bmod 1$) via the nonlinear evolution equation. Such an equation thus acts like a microscope which makes the limits of our precision in physical measurements visible. Can we, therefore, anticipate that the concept of the continuum with its distinction of rational and irrational numbers is non-physical and that all physical variables will be quantized? (The Heisenberg uncertainty relation, which limits the precision of our observations for conjugate variables, has also been found in a gedanken experiment in which one tries to measure the location and the momentum of an electron via a light microscope with arbitrary accuracy.) This and related questions, and speculations, are discussed in an interesting article by J. Ford in *Physics Today*, April 1983.

3.2 Characterization of Chaotic Motion

In this section, we introduce the Liapunov exponent as well as the invariant measure and the correlation function as quantitative measures to characterize the chaotic motion which is generated by one-dimensional Poincaré maps.

3.2.1 Liapunov Exponent

We have already seen in the previous section that adjacent points become separated under the action of a map

$$x_{n+1} = f(x_n) \quad (3.5)$$

which leads to chaotic motion. The Liapunov exponent $\lambda(x_0)$ measures this exponential separation as shown in Fig. 12. From Fig. 12 one obtains:

$$\varepsilon e^{N\lambda(x_0)} = |f^N(x_0 + \varepsilon) - f^N(x_0)| \quad (3.6)$$

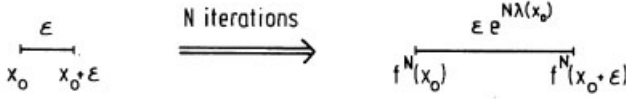


Figure 12: Definition of the Liapunov exponent.

which, in the limits $\epsilon \rightarrow 0$ and $N \rightarrow \infty$, leads to the correct formal expression for $\lambda(x_0)$:

$$\begin{aligned} \lambda(x_0) &= \lim_{N \rightarrow \infty} \lim_{\epsilon \rightarrow 0} \frac{1}{N} \log \frac{f^N(x_0 + \epsilon) - f^N(x_0)}{\epsilon} \\ &= \lim_{N \rightarrow \infty} \frac{1}{N} \log \frac{df^N(x_0)}{dx_0}. \end{aligned} \quad (3.7)$$

This means that $e^{\lambda(x_0)}$ is the average factor by which the distance between closely adjacent points becomes stretched after one iteration.

The Liapunov exponent also measures the average loss of information (about the position of a point in $[0, 1]$) after one iteration. In order to see this, we use in eq. (3.7) the chain rule

$$\begin{aligned} \left. \frac{d}{dx} f^2(x) \right|_{x_0} &= \left. \frac{d}{dx} f[f(x)] \right|_{x_0} = f'[f(x_0)]f'(x_0) \\ &= f'(x_1)f'(x_0); \quad x_1 \equiv f(x_0) \end{aligned} \quad (3.8)$$

to write the Liapunov exponent as

$$\begin{aligned} \lambda(x_0) &= \lim_{N \rightarrow \infty} \frac{1}{N} \log \left| \frac{d}{dx_0} f^N(x_0) \right| = \lim_{N \rightarrow \infty} \frac{1}{N} \log \left| \prod_{i=0}^{N-1} f'(x_i) \right| \\ &= \lim_{N \rightarrow \infty} \frac{1}{N} \sum_{i=0}^{N-1} \log |f'(x_i)|. \end{aligned} \quad (3.9)$$

As a next step, we discuss the loss of information after one iteration with a linear map. We separate $[0, 1]$ into n equal intervals and assume that a point x_0 can occur in each of them with equal probability $1/n$. By learning which interval contains x_0 , we gain the information

$$I_0 = - \sum_{i=1}^n \frac{1}{n} \text{ld} \frac{1}{n} = \text{ld} n \quad (3.10)$$

where ld is the logarithm to the base 2 (see Appendix F). If we decrease n , the information I_0 is reduced, and it becomes zero for $n = 1$. It is shown in Fig. 13 that a linear map $f(x)$ changes the length of an interval by a factor $a = |f'(0)|$. The corresponding decrease of resolution leads to a loss of information after the mapping:

$$\Delta I = - \sum_{i=1}^{a/n} \frac{a}{n} \text{ld} \frac{a}{n} + \sum_{i=1}^n \frac{1}{n} \text{ld} \frac{1}{n} = - \text{ld} a = - \text{ld} |f'(0)| \quad (3.11)$$

Generalizing this expression to a situation where $|f'(x)|$ varies from point to point and, averaging over many iterations, leads to the following expression for the mean loss of information:

$$\overline{\Delta I} = - \lim_{N \rightarrow \infty} \frac{1}{N} \sum_{i=0}^{N-1} \text{ld} |f'(x_i)| \quad (3.12)$$

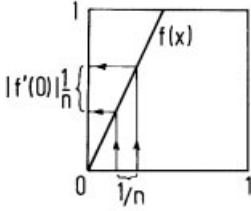


Figure 13: Increase of an interval $1/n$ by a linear map.

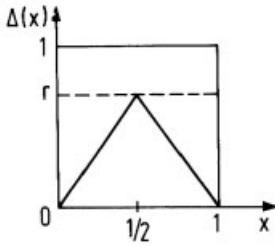


Figure 14: The triangular map $\Delta(x)$.

which is, via eq. (3.9), proportional to the Liapunov exponent:

$$\lambda(x_0) = (\log 2) \cdot |\overline{\Delta}|. \tag{3.13}$$

This relation between the Liapunov exponent and the loss of information is a first step towards characterization of chaos in a coordinate-invariant way, as will be explored on a deeper level in Chapter 6.

By way of an example, we now calculate the Liapunov exponent for the triangular map,

$$\Delta(x) = r \left(1 - 2 \left| \frac{1}{2} - x \right| \right) \tag{3.14}$$

shown in Fig. 14. The function $\Delta(x)$ serves as a useful model because, for $r > 1/2$, it generates chaotic sequences $x_0, \Delta(x_0), \Delta[\Delta(x_0)] \dots$, and due to its simple form, all quantities that characterize the chaotic state can be calculated explicitly.

In order to get acquainted with this map, we first consider its fixed points and their stability for different values of r .

Generally, a point x^* is called a fixed point of a map $f(x)$ if

$$x^* = f(x^*) \tag{3.15}$$

i. e., the fixed points are the intersections of $f(x)$ with the bisector.

A fixed point is locally stable if all points x_0 in the vicinity of x^* are attracted to it, i. e., if the sequence of iterates of x_0

$$x_0, x_1, x_2, \dots, x_n \equiv x_0, f(x_0), f[f(x_0)] \dots \underbrace{f[f \dots f(x_0) \dots]}_n, \dots \tag{3.16}$$

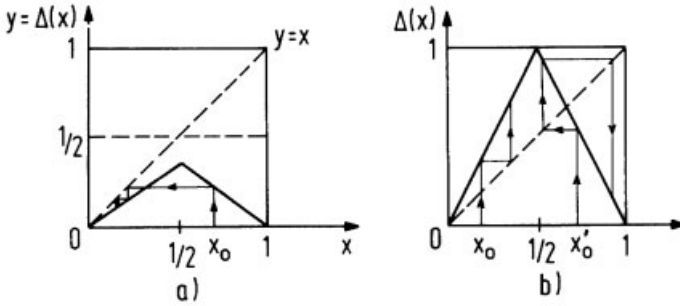


Figure 15: a) Stable fixed point at $x^* = 0$ for $r < 1/2$; b) two unstable fixed points for $r = 1$.

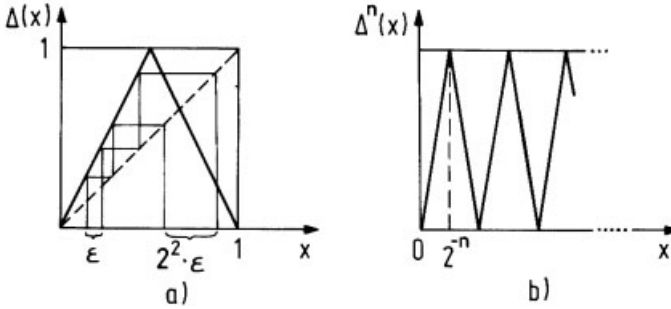


Figure 16: a) Separation of points by iteration with $\Delta(x)$ and b) the n th iterate $\Delta^n(x)$.

converges to x^* . The analytical criterion for local stability is

$$\left| \frac{d}{dx} f(x^*) \right| < 1 \tag{3.17}$$

because the distance δ_n to x^* shrinks as

$$\begin{aligned} \delta_{n+1} &= |x_{n+1} - x^*| = |f(x_n) - x^*| \\ &= |f(x^* + \delta_n)| \simeq \left| \frac{d}{dx} f(x^*) \right| \cdot \delta_n \end{aligned} \tag{3.18}$$

Figure 15 a shows that for $r < 1/2$ the origin $x = 0$ is the only stable fixed point to which all points $[0, 1]$ are attracted. For $r > 1/2$ two unstable fixed points emerge. Figure 15b shows how, for $r = 1$, the iterates of x_0 and x'_0 move away from the “fixed points” $x_1 = 0$ and $x_2 = 2/3$, respectively. In the following, we shall consider only the case $r = 1$, which is representative for $r > 1/2$.

What can we say about a sequence of iterates if there are no stable fixed points? First of all we notice that points which are close together, become more and more separated during the first iterations, as shown in Fig. 16. If we plot the n th iterate $\Delta^n(x)$, we see from Fig. 16 that again it is piecewise linear and has the slope $\left| \frac{d}{dx} \Delta^n(x) \right| = 2^n$, except for the countable set of points $j \cdot 2^{-n}$ where $j = 0, 1 \dots 2^n$. Therefore, the separation of “almost all” points

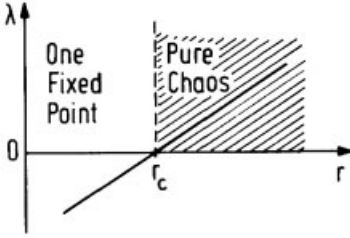


Figure 17: The Liapunov exponent for the triangular map as a function of r in the vicinity of r_c .

x_0 , $x_0 + \varepsilon$ grows exponentially with n after n iterations, and the Liapunov exponent becomes (independent of x_0):

$$\lambda = \log 2. \quad (3.19)$$

For the general triangular map, eq. (3.14), the Liapunov exponent simply becomes $\lambda = \log 2r$, and for $r > 1/2$ we have $\lambda > 0$; i. e., we lose information about the position of a point in $[0, 1]$ after an iteration, whereas $r < 1/2$ implies $\lambda < 0$, and we gain information because all points are attracted to $x^* = 0$.

The Liapunov exponent changes sign at $r = 1/2$ and, therefore, acts like an “order parameter”, which indicates the onset of chaos, as shown in Fig. 17. To make the analogy to critical phenomena even closer, we observe that $\lambda = \log 2r$ scales with a power law near the “critical point” $r_c = 1/2$.

$$\lambda \propto (r - r_c). \quad (3.20)$$

This shows that even the simple transition to chaos in the triangular map displays some features that are reminiscent of an equilibrium phase transition. As we have already mentioned before, we will investigate this aspect more generally in Chapter 4. It should also be noted here that the definition of the Liapunov exponent can be extended to higher dimensional maps. This will be treated in Chapter 6, where we will also discuss the relation between the Liapunov exponent and the Kolmogorov entropy and its possible connection to the Hausdorff dimension. But before we come to these problems, we will first investigate the question of how the iterates of a one-dimensional map are distributed over the unit interval.

3.2.2 Invariant Measure

The invariant measure $\rho(x)$ determines the density of the iterates of a unimodular map

$$x_{n+1} = f(x_n), \quad x_n \in [0, 1], \quad n = 0, 1, 2, \dots \quad (3.21)$$

over the unit interval and is defined via

$$\rho(x) \equiv \lim_{N \rightarrow \infty} \frac{1}{N} \sum_{i=0}^N \delta[x - f^i(x_0)]. \quad (3.22)$$

If $\rho(x)$ does not depend on x_0 , the system is called ergodic (see also Section 8.2.2). For this case, eq. (3.22) allows us to write “time averages” over a function $g(x)$ as averages over the invariant measure,

$$\lim_{N \rightarrow \infty} \frac{1}{N} \sum_{i=0}^N g(x_i) \equiv \lim_{N \rightarrow \infty} \frac{1}{N} \sum_{i=0}^N g[f^i(x_0)] = \int_0^1 dx \rho(x) g(x). \quad (3.23)$$

This is the one-dimensional analog of the thermodynamic average in classical statistical mechanics which allows us (if the motion in phase space is ergodic) to replace the time average by an ensemble average over a stationary distribution ρ :

$$\lim_{T \rightarrow \infty} \frac{1}{T} \int_0^T dt A[\vec{x}(t)] = \int d\vec{x} \tilde{\rho}(\vec{x}) A(\vec{x}). \quad (3.24)$$

Here A is a function of the time-dependent vector $\vec{x} = [\vec{p}(t), \vec{q}(t)]$ which is composed of the coordinates \vec{q} and momenta \vec{p} which follow Hamilton’s equations,

$$\dot{q}_i = \frac{\partial H}{\partial p_i}, \quad \dot{p}_i = -\frac{\partial H}{\partial q_i} \quad (3.25)$$

and $\tilde{\rho}$ is, for example, the microcanonical distribution $\tilde{\rho} = \delta[H(\vec{x}) - E]$ for an isolated system of energy E . Note, however, that our one-dimensional example corresponds to a dissipative system [see e. g., Chapter 2, eq. (2.15)] whereas Hamilton’s equations (3.25) describe a conservative model.

For Hamiltonian systems, the dynamical behavior of a general density distribution $\rho(\vec{x}, t)$ in phase space is described by Liouville’s equation:

$$\tilde{\rho}(\vec{x}, t) = -iL\rho(\vec{x}, t) \quad (3.26)$$

where

$$L = i \left[\frac{\partial H}{\partial \vec{p}} \frac{\partial}{\partial \vec{q}} - \frac{\partial H}{\partial \vec{q}} \frac{\partial}{\partial \vec{p}} \right] \quad (3.27)$$

is the Liouville operator.

The corresponding evolution equation for our one-dimensional model whose time evolution is given by the map (3.21) can be derived as follows. If we have a point x_0 , it evolves to $f(x_0)$ after one iteration. This means that a delta-function distribution $\delta(x - x_0)$ evolves after one time step to $\delta[x - f(x_0)]$ which can be written as

$$\delta[x - f(x_0)] = \int_0^1 dy \delta[x - f(y)] \delta(y - x_0). \quad (3.28)$$

Generalizing this to the evolution of an arbitrary density $\rho_n(x)$ at time n we obtain the so-called Frobenius–Perron equation

$$\rho_{n+1}(x) = \int dy \delta[x - f(y)] \rho_n(y) \quad (3.29)$$

which governs the time evolution of $\rho_n(x)$. The invariant measure $\rho(x)$ has to be stationary because eq. (3.23) makes sense only if $\rho(x)$ is independent of time n , that is, $\rho(x)$ is an eigenfunction of the Frobenius–Perron operator with eigenvalue 1:

$$\rho(x) = \int_0^1 dy \delta[x - f(y)] \rho(y). \quad (3.30)$$

Formally, this equation has many solutions (e. g., $\delta(x - x^*)$ where $x^* = f(x^*)$ is an unstable fixed point). But fortunately, only one of the solutions is physically relevant, namely that one which is, for example, obtained by solving eq. (3.30) on a computer. In the presence of weak random noise (which is caused by rounding errors in the computer or physical fluctuations in real systems), the probability to hit an unstable repelling fixed point x^* is zero, and therefore such spurious solutions are automatically eliminated (Eckmann and Ruelle, 1985). In the following, the invariant measure $\rho(x)$, always means the physically relevant invariant measure which is stable if a small random noise is added to the system.

Let us consider again, as an example, the triangular map at $r = 1$:

$$\Delta(x) = \begin{cases} 2x & \text{for } x \leq \frac{1}{2} \\ 2(1-x) & \text{for } x > \frac{1}{2} \end{cases} \quad (3.31)$$

In this case, eq. (3.30) becomes:

$$\rho(x) = \frac{1}{2} \left[\rho\left(\frac{x}{2}\right) + \rho\left(1 - \frac{x}{2}\right) \right] \quad (3.32)$$

which has the obvious normalized solution $\rho(x) = 1$.

We can also show that this solution is unique. Starting from an arbitrary normalized distribution $\rho_0(x)$, and operating on it n times with (3.29), yields

$$\rho_n(x) = \frac{1}{2^n} \sum_{j=1}^{2^n-1} \left[\rho_0\left(\frac{j-1}{2^{n-1}} + \frac{x}{2^n}\right) + \rho_0\left(\frac{j}{2^{n-1}} - \frac{x}{2^n}\right) \right] \quad (3.33)$$

which converges towards

$$\rho(x) = \lim_{n \rightarrow \infty} \rho_n(x) = -\frac{1}{2} \left[\int_0^1 dx \rho_0(x) + \int_0^1 dx \rho_0(x) \right] = 1. \quad (3.34)$$

This means that, for the triangular map at $r = 1$, the chaotic sequence of iterates $x_0, f(x_0), f(f(x_0)) \dots$ uniformly covers the interval $[0, 1]$, and the system is ergodic. As in the case of the Liapunov exponent, we will later study invariant density for more complicated maps and show that it is not always a constant.

3.2.3 Correlation Function

The correlation function $C(m)$ for a map (3.21) is defined by

$$C(m) = \lim_{N \rightarrow \infty} \frac{1}{N} \sum_{i=0}^{N-1} \hat{x}_{i+m} \hat{x}_i \quad (3.35)$$

where

$$\hat{x}_i = f^i(x_0) - \bar{x}; \quad \bar{x} = \lim_{N \rightarrow \infty} \frac{1}{N} \sum_{i=0}^{N-1} f^i(x_0). \quad (3.36)$$

From this definition follows that $C(m)$ yields another measure for the irregularity of the sequence of iterates $x_0, f(x_0), f^2(x_0) \dots$. It tells us how much the deviations of the iterates from their average value,

$$\hat{x}_i = x_i - \bar{x} \quad (3.37)$$

that are m steps apart (i. e., \hat{x}_{i+m} and \hat{x}_i) “know” about each other, on the average.

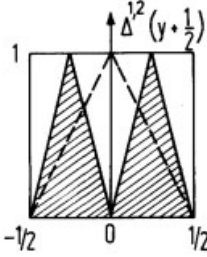


Figure 18: The first and second iterates $\Delta^{1,2}(y + 1/2)$ are symmetric about $y = 0$; the triangular areas are independent of $m = 1, 2$.

If the invariant measure $\rho(x)$ for a given map $f(x)$ is known, $C(m)$ can be written in the following form:

$$C(m) = \int_0^1 dx \rho(x) x f^m(x) - \left[\int_0^1 dx \rho(x) x \right]^2 \quad (3.38)$$

Here, we used the commutative property of the iterates,

$$x_{i+m} = f^{i+m}(x_0) = f^i f^m(x_0) = f^m f^i(x_0) . \quad (3.39)$$

We, therefore, find for the example of the triangular map:

$$C(m) = \int_0^1 dx x \Delta^m(x) - \left[\int_0^1 dx x \right]^2 \quad (3.40a)$$

$$\begin{aligned} &= \int_{-1/2}^{1/2} dy y \Delta^m \left(y + \frac{1}{2} \right) + \frac{1}{2} \int_{-1/2}^{1/2} dy \Delta^m \left(y + \frac{1}{2} \right) - \frac{1}{4} \\ &= \frac{1}{12} \delta_{m,0} \end{aligned} \quad (3.40b)$$

i. e., the sequence of iterates is delta-correlated.

This result follows because a) $\Delta^n(y + 1/2)$ is symmetric about $y = 0$; therefore, the first integral in (3.40b) vanishes for $m > 0$, and b) the second integral is independent of m , as shown in Fig. 18. To summarize:

We have found for a general one-dimensional map that a sequence $x_0, f(x_0) \dots f^n(x_0) \dots$ can be characterized a) by a Liapunov exponent, which tells us how adjacent points become separated under the action of f ; b) by the invariant density, which serves as a measure of how the iterates become distributed over the unit interval; and c) by the correlation function $C(m)$, which measures the correlation between iterates that are m steps apart.

For the triangular map, the Liapunov exponent is $\lambda = \log 2r$, which changes its sign at $r = 1/2$. It therefore serves as an order parameter for the onset of chaos. For $r = 1$, the chaotic state is characterized by a constant stationary density $\rho(x) = 1$ and delta-correlated iterates, i. e., $C(m) = (1/12) \delta_{m,0}$.

3.3 Deterministic Diffusion

In this section, we show that the iterates of certain one-dimensional periodic maps diffuse. This diffusion indicates that the reduced map generates chaotic motion.

One normally associates diffusion with the Brownian motion of a particle in a liquid. Its equation of motion, in the case of high friction where the acceleration term $\propto \ddot{x}$ can be neglected, is

$$\dot{x} \propto \xi(t). \quad (3.41)$$

The $\xi(t)$ are random forces, which are generated by the thermal agitation of the molecules. If one assumes, as usual, that the $\xi(t)$ are Gaussian-correlated,

$$\langle \xi(t) \rangle = 0; \quad \langle \xi(t)\xi(t') \rangle \propto \delta(t-t') \quad (3.42)$$

one obtains from eqs. (3.41) and (3.42):

$$\langle x(t) \rangle = 0 \quad \text{and} \quad \langle x^2(t) \rangle \propto t. \quad (3.43)$$

This means that the squared distance from the origin increases linearly with time if the particle is kicked by random forces (in contrast to $x^2 \propto t^2$ for a constant force $k \propto \dot{x}$). One can show, with a little more effort, that (3.43) also remains valid (for $t \rightarrow \infty$) if the acceleration term is retained [see, for example, Haken's book on Synergetics (1982)].

Let us now have a look at the piecewise linear periodic map

$$x_{\tau+1} = F(x_{\tau}) = x_{\tau} + f(x_{\tau}); \quad \tau = 0, 1, 2, \dots \quad (3.44)$$

where $f(x_{\tau})$ is periodic in x_{τ} ,

$$f(x_{\tau} + n) = f(x_{\tau}), \quad n = 0, \pm 1, \pm 2, \dots, \quad (3.45)$$

shown in Fig. 19.

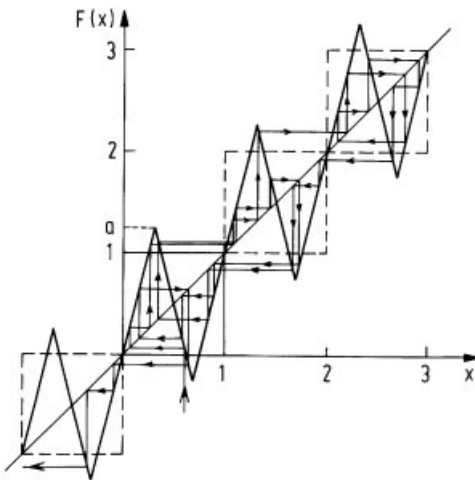


Figure 19: Piecewise linear periodic map with a diffusive trajectory (after Grossmann, 1982).

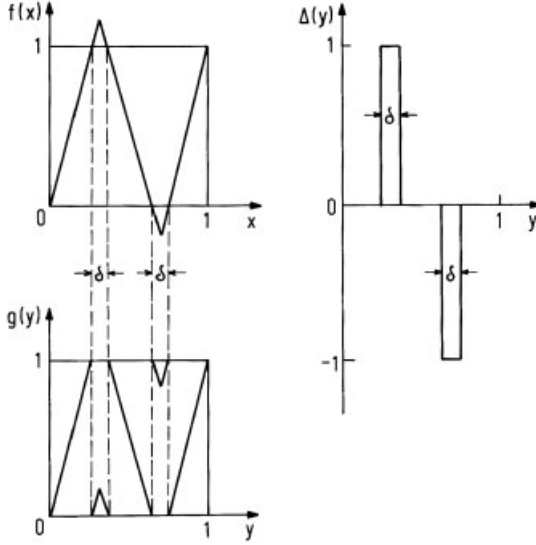


Figure 20: Decomposition of a piecewise linear map.

One sees that the trajectory moves slowly away from the origin. Now we will show that this motion is in fact diffusive. However, this diffusion is not generated by random forces (as in the case of Brownian motion discussed above), but rather because the trajectory loses its “memory” within one or several boxes due to chaotic motion. To substantiate this statement, we calculate $\langle x^2 \rangle$ explicitly for the map (3.44).

We decompose the coordinate of a trajectory into the box number N_τ and the position $y_\tau \in [0, 1]$ within a box (Grossmann, 1982):

$$x_\tau = N_\tau + y_\tau . \quad (3.46)$$

The map (3.44) then becomes

$$N_{\tau+1} + y_{\tau+1} = F(N_\tau + y_\tau) = N_\tau + y_\tau + f(y_\tau) \quad (3.47)$$

which is equivalent to the coupled dynamical laws:

$$N_{\tau+1} - N_\tau = [y_\tau + f(y_\tau)] \equiv \Delta(y_\tau) \quad (3.48a)$$

$$y_{\tau+1} = y_\tau + f(y_\tau) - [y_\tau + f(y_\tau)] \equiv g(y_\tau) \quad (3.48b)$$

where $[z]$ denotes the integer part of z . Figure 20 shows the function $\Delta(y_\tau)$, which is an integer number, describing the magnitude of the jump, and $g(x_\tau)$ gives the remaining part of the coordinate at $\tau + 1$.

Using (3.48a), the distances to the origin can be written as

$$N_t = \sum_{\tau=0}^{t-1} (N_{\tau+1} - N_\tau) = \sum_{\tau=0}^{t-1} \Delta(y_\tau), \quad \text{for } N_0 = 0 . \quad (3.49)$$

This yields for the mean squared distance:

$$\langle N_t^2 \rangle = \sum_{\tau, \lambda}^{t-1} \langle \Delta(y_\tau) \Delta(y_\lambda) \rangle \quad (3.50)$$

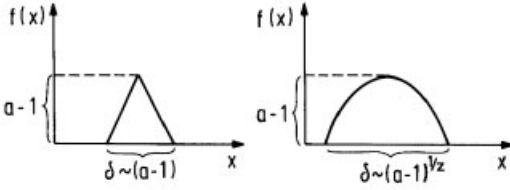


Figure 21: The variation of δ as $(a-1)^{1/z}$ if $f(x)$ has a maximum of order z (schematically).

where the average $\langle \dots \rangle$ is over all initial conditions y_0 , and we assumed for simplicity $\langle N_t \rangle = 0$. For the case when the motion generated by $g(y)$ is so chaotic that there are no correlations among the y_τ , i. e.,

$$\langle \Delta(y_\lambda) \Delta(y_\tau) \rangle \propto \delta_{\lambda, \tau} \quad (3.51)$$

one finds from (3.47):

$$\lim_{t \rightarrow \infty} \frac{\langle N_t^2 \rangle}{t} = \lim_{t \rightarrow \infty} \frac{1}{t} \sum_{\tau=0}^{t-1} \langle \Delta^2(y_\tau) \rangle \quad (3.52)$$

$$= \int dy \rho(y) \Delta^2(y). \quad (3.53)$$

The step from (3.52) to (3.53) is only possible if $g(y)$ has an invariant density that obeys

$$\rho(y) = \int dx \delta[g(x) - y] \rho(x). \quad (3.54)$$

Equation (3.53) means that $\langle N_t^2 \rangle$ increases linearly with t , i. e.,

$$\langle N_t^2 \rangle = 2Dt \quad \text{for } t \gg 1 \quad (3.55)$$

with a diffusion coefficient

$$D \equiv \frac{1}{2} \int dy \rho(y) \Delta^2(y). \quad (3.56)$$

It should be clear from the derivation that diffusion occurs as long as the y_τ 's are sufficiently uncorrelated such that the two sums in (3.50) contract to a single sum. (For completely correlated motion of the y_τ 's, $\langle N_t^2 \rangle$ becomes proportional to t^2 .) This means that the mere presence of diffusion for a periodic map indicates chaotic motion which destroys correlations within one box. We will generalize and use this characterization of chaos to some extent in Chapter 9, where we discuss area-preserving maps.

Let us finally derive a simple scaling law for the diffusion coefficient that has a purely geometric origin. If the intervals δ , through which the trajectories can move from cell to cell, are small enough (such that one can neglect the variation of ρ in this region, i. e., $\rho(x \in \delta) = \bar{\rho}$), then eq. (3.56) can be written as

$$D \approx \frac{1}{2} \bar{\rho} \delta \quad (3.57)$$

because Δ^2 has only the values zero or unity. Figure 21 shows that D scales like

$$D \propto (a-1)^{1/z} \quad (3.58)$$

if the map $f(x)$ has a maximum (and minimum) of order z .

4 Universal Behavior of Quadratic Maps

In this chapter, we study the logistic map

$$x_{n+1} = f_r(x_n) = rx_n(1 - x_n) \quad (4.1)$$

shown in Fig. 22. It has already been shown in Chapter 2 that eq. (4.1) describes the angles x_n of a strongly damped kicked rotator. But the logistic map, which is, arguably, the simplest nonlinear difference equation, appears in many contexts.

It has already been introduced in 1845 by P. F. Verhulst to simulate the growth of a population in a closed area. The number of species x_{n+1} in the year $n + 1$ is proportional to the number in the previous year x_n and to the remaining area, which is diminished, proportionally, to x_n , i. e., $x_{n+1} = rx_n(1 - x_n)$ where the parameter r depends on the fertility, the actual area of living, etc.

Another example is a savings account with a self-limiting rate of interest (Peitgen and Richter, 1984). Consider a deposit z_0 which grows with a rate of interest ε as $z_{n+1} = (1 + \varepsilon)z_n = \dots (1 + \varepsilon)^{n+1}z_0$. To prohibit unlimited wealth, some politician could suggest that the rate of interest should be reduced proportionally to z_{n+1} , i. e., $\varepsilon \rightarrow \varepsilon_0(1 - z_n/z_{\max})$. Then the account develops according to $z_{n+1} = [1 + \varepsilon_0(1 - z_n/z_{\max})]z_n$ which becomes equal to eq. (4.1) for $x_n = z_n\varepsilon_0/z_{\max}(1 + \varepsilon_0)$ and $r = 1 + \varepsilon_0$.

One could expect for both examples that due to the feedback mechanism the quantities of interest (population and bank account) develop towards mean values. But as found by Grossmann and Thomae (1977), by Feigenbaum (1978), and by Couillet and Tresser (1978), and many others (see May, 1976, for earlier references) the iterates x_1, x_2, \dots of eq. (4.1) display, as a function of the external parameter r , a rather complicated behavior that becomes chaotic for large r (see Fig. 23).

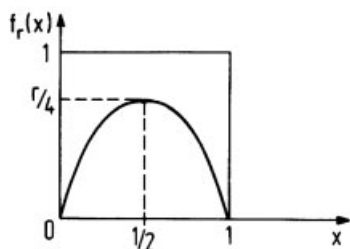


Figure 22: The quadratic map $f_r(x)$ on the unit interval.

Once can, therefore, understand the conclusion that May (1976) draws at the end of his article in *Nature*: “Perhaps we would all be better off, not only in research and teaching, but also in everyday political and economical life, if more people would take into consideration that simple dynamical systems do not necessarily lead to simple dynamical behavior.”

However, chaotic behavior is not tied to the special form of the logistic map. Feigenbaum has shown that the route to chaos that is found in the logistic map, the “Feigenbaum route”, occurs (with certain restrictions which will be discussed below) in all first-order difference equations $x_{n+1} = f(x_n)$ in which $f(x_n)$ has (after a proper rescaling of x_n) only a single maximum in the unit interval $0 \leq x_n \leq 1$. It was found by Feigenbaum that the scaling behavior at the transition to chaos is governed by universal constants, the Feigenbaum constants α and δ , whose value depends only on the order of the maximum (e. g., quadratic, i. e., $f'(x_{\max}) = 0$, $f''(x_{\max}) < 0$, etc.). Because the conditions for the appearance of the Feigenbaum route are rather weak (it is practically sufficient that the Poincaré map of a system is approximately one-dimensional and has a single maximum), this route has been observed experimentally in many nonlinear systems.

The following sections of this chapter contain a rather detailed derivation of the universal properties of this route. We begin with a summary, which is intended to be a guide through the more mathematical parts.

Section 4.1 gives an overview of the numerical results for the iterates of the logistic map. It shows that the number of fixed points of $f_r(x)$ (towards which the iterates converge) doubles at distinct, increasing values of the parameter r_n . At $r = r_n$ the number of fixed points becomes infinite; and beyond this (finite) r -value, the behavior of the iterates is chaotic for most values of r .

In Section 4.2, we investigate the pitchfork bifurcation, which provides the mechanism for the successive doubling of fixed points. It is shown that the doubling can be understood by examining the image of even iterates ($f[f(x)]$, $f[f[f(x)]]$, ...) of the original map $f(x)$. This relates the generation of new fixed points to a law of functional composition. We, therefore, introduce the doubling transformation T that describes functional composition together with simultaneous rescaling along the x - and y -axis ($Tf(x) = -\alpha f[f(-x/\alpha)]$) and show that the Feigenbaum constant α (which is related to the scaling of the distance between iterates) can be calculated from the (functional) fixed point f^* of T ($Tf^* = f^*$). This establishes the universal character of α . The other Feigenbaum constant δ (which measures the scaling behavior of the r_n -values) then appears as an eigenvalue of the linearized doubling transformation.

After having provided a method of calculating universal properties of the iterates, we consider several applications in Section 4.3. As a first step, we determine the relative separations of the iterates and show that the iterates form (at the accumulation point r_∞) a self-similar point set with a fractal dimensionality. We then Fourier-transform the distribution of iterates to obtain the experimentally measurable, and therefore important, power spectrum.

In any real dissipative nonlinear system, there are, due to the coupling to other degrees of freedom, also fluctuating forces, which when they are incorporated explicitly into the difference equations, tend to wash out the fine structure of the distribution of iterates. We determine the influence of this effect on the power spectrum and show that the rate at which higher subharmonics become suppressed, scales via a power law with the noise level.

Up to this point, we have only considered the behavior of the iterates near the transition to chaos. It will be shown next that in the chaotic region ($r_\infty \leq r \leq 4$) periodic and chaotic

r values are densely interwoven and one finds a sensitive dependence on parameter values. We also discuss the concept of structural universality and calculate the invariant density of the logistic map at $r = 4$.

Finally, in Section 4.5 we present a summary that explains the parallels between the Feigenbaum route to chaos and ordinary equilibrium second-order phase transitions. This chapter ends with a discussion of the measurable properties of the Feigenbaum route and a review of some experiments in which this route has been observed.

4.1 Parameter Dependence of the Iterates

To provide an overview in this section, we present several results for the logistic map obtained by computer iteration of eq. (4.1) for different values of the parameter r . Figure 23 shows the accumulation points of the iterates $\{f_r^n(x_0)\}$ for $n > 300$ as a function of r together with the Liapunov exponent λ obtained via eq. (3.9).

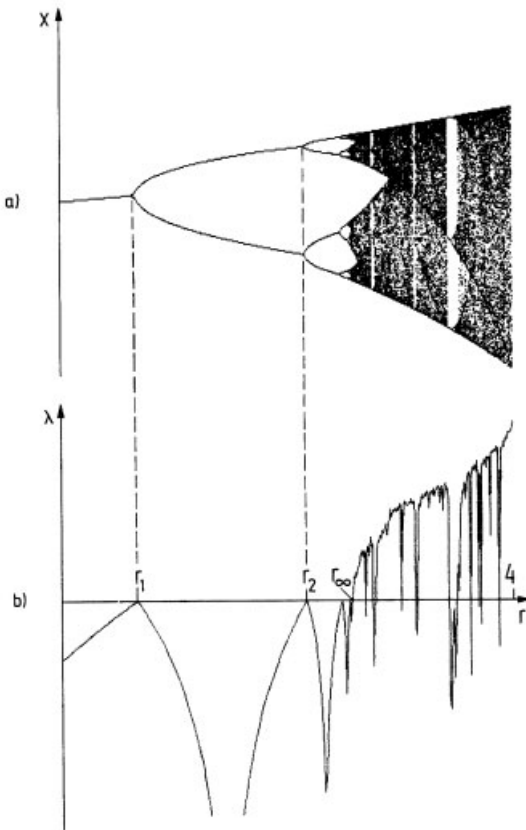


Figure 23: a) Iterates of the logistic map, b) Liapunov exponent λ (after W. Desnizza, priv. comm.).

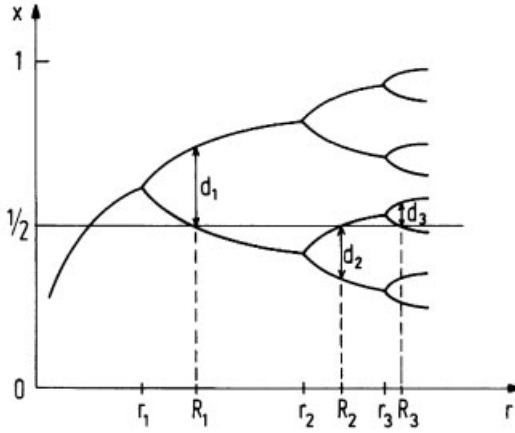


Figure 24: Distances d_n of the fixed points closest to $x = 1/2$ for superstable 2^n -cycles (schematically).

We distinguish between a “bifurcation regime” for $1 < r < r_\infty$ where the Liapunov exponent is always negative (it becomes only zero at the bifurcation points r_n) and a “chaotic region” for $r_\infty < r \leq 4$, where λ is mostly positive, indicating chaotic behavior. The “chaotic regime” is interrupted by r -windows with $\lambda < 0$ where the sequence $\{f_r^n(x_0)\}$ is again periodic.

The numerical results can be summarized as follows:

1. Periodic regime

- (a) The values r_n where the number of fixed points changes from 2^{n-1} to 2^n , scale like

$$r_n = r_\infty - \text{const.} \delta^{-n} \quad \text{for } n \gg 1. \quad (4.2)$$

- (b) The distances d_n of the point in a 2^n -cycle that are closest to $x = 1/2$ (see Fig. 24) have constant ratios:

$$\frac{d_n}{d_{n+1}} = -\alpha \quad \text{for } n \gg 1. \quad (4.3)$$

- (c) The Feigenbaum constants δ and α have the values

$$\delta = 4.6692016091\dots \quad (4.4a)$$

$$\alpha = 2.5029078750\dots \quad (4.4b)$$

Let us also note for later use that the R_n of Fig. 24 scale similar to r_n :

$$R_n - r_\infty = \text{const.}' \delta^{-n}, \quad (4.5)$$

furthermore

$$R_\infty = r_\infty = 3.5699456\dots$$

2. Chaotic regime

- (a) The chaotic intervals move together by inverse bifurcations until the iterates become distributed over the whole interval $[0, 1]$ at $r = 4$.
- (b) The r -windows are characterized by periodic p -cycles ($p = 3, 5, 6 \dots$) with successive bifurcations $p, p \cdot 2^1, p \cdot 2^2$ etc. The corresponding r -values scale like eq. (4.2) with the same δ but different constants.
- (c) Also, period triplings $p \cdot 3^n$ and quadruplings $p \cdot 4^n$, etc. occur at $\bar{r} = \bar{r}_\infty - \overline{\text{const.}} \delta^{-n}$ with different Feigenbaum constants $\bar{\delta}$, which are again universal (e. g., $\bar{\delta} = 55.247 \dots$ for $p \cdot 3^n$).

4.2 Pitchfork Bifurcation and the Doubling Transformation

In this section, we show that the “Feigenbaum route” in Fig. 23 is generated by pitchfork bifurcations that relate the emergence of new branches to a universal law of functional composition. By introducing the doubling transformation T (which describes this law), we show that the Feigenbaum constants α and δ are indeed universal. They appear as the (negative inverse) value of the eigenfunction of T at $x = 1$ and as the only relevant eigenvalue of the linearized doubling operator, respectively.

4.2.1 Pitchfork Bifurcations

As a first step, we investigate the stability of the fixed points of $f_r(x)$ and $f_r^2(x) = f_r[f_r(x)]$ as a function of r . Figure 25 shows that $f_r(x)$ has, for $r < 1$, only one stable fixed point at zero, which becomes unstable for $1 < r < 3$ in favor of $x^* = 1 - 1/r$.

For $r > 3 = r_1$ we have $|f'_r(x^*)| = |2 - r| > 1$; i. e., x^* also becomes unstable according to criterion (3.17). What happens then?

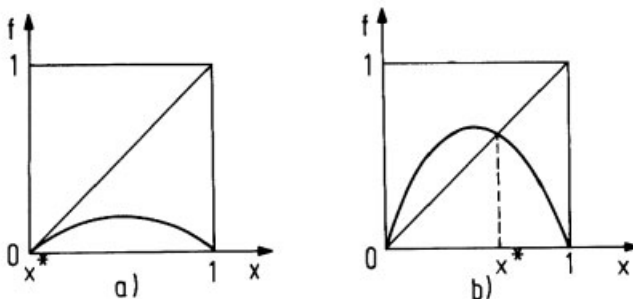


Figure 25: The fixed points of f , for a) $r < 1$ and b) $1 < r < 3$.

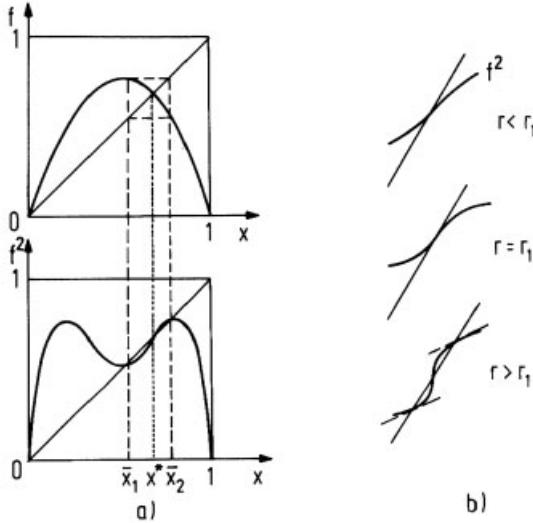


Figure 26: a) $f(x)$ and $f^2(x) = f[f(x)]$ for $r > r_1$. b) Generation of two new stable fixed points in f^2 via a pitchfork bifurcation. (The bifurcation diagram looks like a pitchfork, see p. 159)

Figure 26 shows $f_r(x)$ together with its second iterate $f_r^2(x)$ for $r > r_1$. We note four properties of f^2 (the index r is dropped for convenience):

1. It has three extrema with $f^{2'} = f'[f(x)]f'(x) = 0$ at $x_0 = 1/2$, because $f'(1/2) = 0$, and at $x_{1,2} = f^{-1}(1/2)$, because $f'[f[f^{-1}(1/2)]] = f'(1/2) = 0$.
2. A fixed point x^* of $f(x)$ is also a fixed point of $f^2(x)$ (and all higher iterates).
3. If a fixed point x^* becomes unstable with respect to $f(x)$, it becomes also unstable with respect to f^2 (and all higher iterates) because $|f'(x^*)| > 1$ implies $|f^{2'}(x^*)| = |f'[f(x^*)]f'(x^*)| = |f'(x^*)|^2 > 1$.
4. For $r > 3$, the old fixed point x^* in f^2 becomes unstable, and two new stable fixed points \bar{x}_1, \bar{x}_2 are created by a pitchfork bifurcation (see Fig. 26b).

The pair \bar{x}_1, \bar{x}_2 of stable fixed points of f^2 is called an attractor of $f(x)$ of period two because any sequence of iterates which starts in $[0, 1]$ becomes attracted by \bar{x}_1, \bar{x}_2 in an oscillating fashion as shown in Fig. 27.

It is easy to see that $f(x)$ maps these new fixed points of f^2 onto each other, i. e.,

$$f(\bar{x}_1) = \bar{x}_2 \text{ and } f(\bar{x}_2) = \bar{x}_1 \quad (4.6)$$

because $f^2(\bar{x}_1) = \bar{x}_1$ implies

$$ff[f(x)] = f[f(x)] = f(x), \quad (4.7)$$

i. e., $f(\bar{x}_1)$ is also a fixed point of f^2 , and \bar{x}_2 is the only possible choice. ($f(\bar{x}_1) = 0$ or x^* are at variance with $ff(\bar{x}_1) = \bar{x}_1$.)

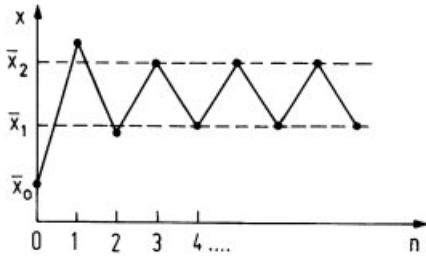


Figure 27: Iterates of \bar{x}_0 if $f(x)$ has an attractor of period two (schematically).

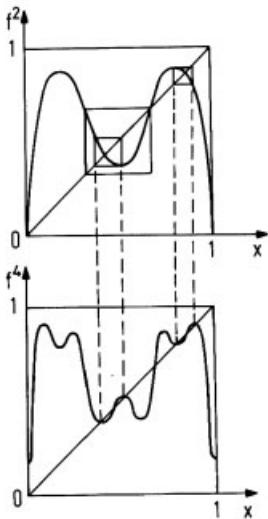


Figure 28: Two pitchfork bifurcations in f^4 lead to an attractor of period 4.

If we now increase r beyond a value r_2 the fixed points of f^2 also become unstable. Because the derivative is the same at \bar{x}_1 and \bar{x}_2

$$f^{2'}(\bar{x}_1) = f'[f(\bar{x}_1)]f'(\bar{x}_1) = f'(\bar{x}_2)f'(\bar{x}_1) = f^{2'}(\bar{x}_2) \tag{4.8}$$

they even become unstable simultaneously.

Figure 28 shows that after this instability the fourth iterate $f^4 = f^2 \cdot f^2$ displays two more pitchfork bifurcations which lead to an attractor of period four; i.e., one observes *period doubling*. These two examples can be generalized as follows:

1. For $r_{n-1} < r < r_n$ there exists a stable 2^{n-1} -cycle with elements $x_0^*, x_1^*, \dots, x_{2^{n-1}-1}^*$, that is characterized by

$$f_r(x_i^*) = x_{i+1}^*, \quad f_r^{2^{n-1}}(x_i^*), \quad \left| \frac{d}{dx_0^*} f_r^{2^{n-1}}(x_0^*) \right| = \left| \prod_i f_r'(x_i^*) \right| < 1 \tag{4.9}$$

2. At r_n , all points of the 2^{n-1} -cycle become unstable simultaneously via pitchfork bifurcations in

$$f_r^{2^n} = f_r^{2^{n-1}} \cdot f_r^{2^{n-1}} \quad (4.10)$$

that, for $r_n < r < r_{n+1}$, lead to a new stable 2^n -cycle.

Our last conclusion represents a first step towards universality because it connects the mechanism of subsequent bifurcations to a general law of functional composition.

Let us add as a caveat that not all quadratic maps of the unit interval onto itself display an infinite sequence of pitchfork bifurcations, but only those which have a negative Schwarzian derivative (see Appendix C).

4.2.2 Supercycles

To progress further, we now consider the so-called supercycles. A 2^n -supercycle is simply a superstable 2^n -cycle defined by

$$\frac{d}{dx_0} f_{R_n}^{2^n}(x_0^*) = \prod_i f'_{R_n}(x_i^*) = 0 \quad (4.11)$$

which implies that it always contains $x_0^* = 1/2$ as a cycle element because this is the only point where $f'_r = 0$. Referring to Fig. 24, we can see that the distances d_n are just the distances between the cycle elements $x^* = 1/2$ and $x_1 = f_{R_n}^{2^{n-1}}(1/2)$, i. e.,

$$d_n = f_{R_n}^{2^{n-1}}\left(\frac{1}{2}\right) - \frac{1}{2}. \quad (4.12)$$

In the following it is convenient to perform a coordinate transformation that displaces $x = 1/2$ to $x = 0$ such that (4.12) becomes

$$d_n = f_{R_n}^{2^{n-1}}(0). \quad (4.13)$$

From the previous section, we see that eq. (4.3) implies

$$\lim_{n \rightarrow \infty} (-\alpha)^n d_{n+1} = d_1 \quad (4.14)$$

i. e., the sequence of scaled iterates $f_{R_{n+1}}^{2^n}(0)$ converges:

$$\lim_{n \rightarrow \infty} (-\alpha)^n f_{R_{n+1}}^{2^n}(0) = d_1. \quad (4.15)$$

Figure 29 suggests that (4.15) can be generalized to the whole interval, and the rescaled functions $(-\alpha)^n f_{R_{n+1}}^{2^n}(0)[x/(-\alpha)^n]$ converge to a limiting function $g_1(x)$:

$$\lim_{n \rightarrow \infty} (-\alpha)^n f_{R_{n+1}}^{2^n} \left[\frac{x}{(-\alpha)^n} \right] = g_1(x) \quad (4.16)$$

Equation (4.16) shows that $g_1(x)$ is determined only by the behavior of $f_{R_{n+1}}^{2^n}$ around $x = 0$ (see also Fig. 28) and should, therefore, be universal for all functions f with a quadratic maximum.

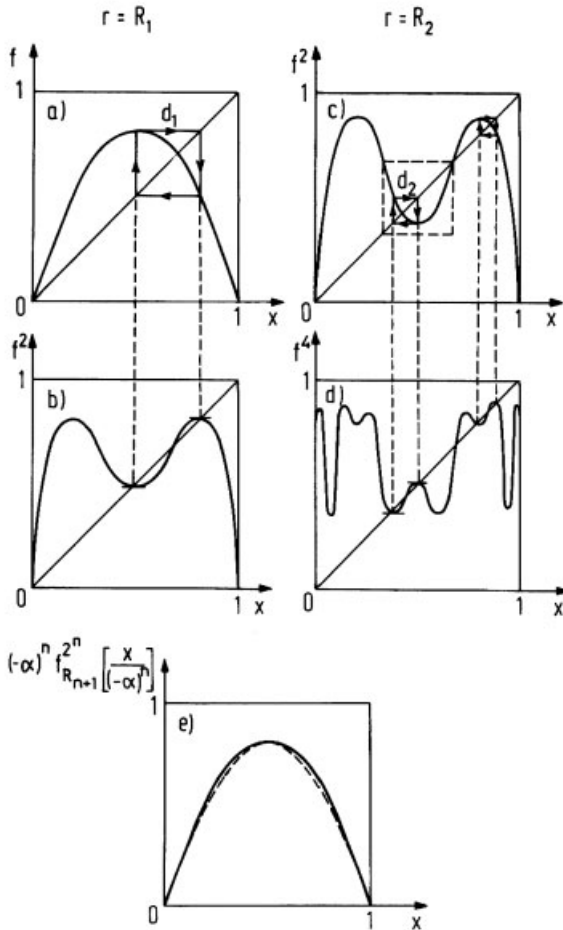


Figure 29: The rescaled iterates $f_{R_{n+1}}^{2^n}(x)$ converge towards a universal function. a)–d) Superstable cycles at R_1 and R_2 . Note the horizontal tangents in b) and d). e) The content of the dashed square of c) is rescaled (dashed line) and compared to the whole of a) (full line).

4.2.3 Doubling Transformation and α

As the next step, we introduce, by analogy with eq. (4.16), a whole family of functions

$$g_i(x) = \lim_{n \rightarrow \infty} (-\alpha)^n f_{R_{n+i}}^{2^n} \left[\frac{x}{(-\alpha)^n} \right]; \quad i = 0, 1, \dots \quad (4.17)$$

We notice that all these functions are related by the *doubling transformation* T:

$$g_{i-1}(x) = (-\alpha)g_i \left[g_i \left(-\frac{x}{\alpha} \right) \right] \equiv Tg_i(x) \quad (4.18)$$

because

$$\begin{aligned}
 g_{i-1}(x) &= \lim_{n \rightarrow \infty} (-\alpha)^n f_{R_{n+i-1}}^{2^n} \left[\frac{x}{(-\alpha)^n} \right] \\
 &= \lim_{n \rightarrow \infty} (-\alpha)(-\alpha)^{n-1} f_{R_{n-1+i}}^{2^{n-1+1}} \left[-\frac{1}{\alpha} \frac{x}{(-\alpha)^{n-1}} \right] \\
 &= \lim_{m \rightarrow \infty} (-\alpha)(-\alpha)^m f_{R_{m+i}}^{2^m} \left\{ \frac{1}{(-\alpha)^m} (-\alpha)^m f_{R_{m+i}}^{2^m} \left[-\frac{1}{\alpha} \frac{x}{(-\alpha)^m} \right] \right\} \\
 &= -\alpha g_i \left[g_i \left(-\frac{x}{\alpha} \right) \right].
 \end{aligned} \tag{4.19}$$

By taking the limit $i \rightarrow \infty$ in (4.18), the function

$$g(x) \equiv \lim_{i \rightarrow \infty} g_i(x) \tag{4.20}$$

becomes a fixed point of the doubling operator T:

$$g(x) = \mathbf{T}g(x) = -\alpha g \left[g \left(-\frac{x}{\alpha} \right) \right]. \tag{4.21}$$

This equation determines α universally by

$$g(0) = -\alpha g[g(0)]. \tag{4.22}$$

It can easily be shown that $\mu g(x/\mu)$ is also a solution of the fixed-point equation (4.21) with the same α . Thus, the theory has nothing to say about absolute scales, and we fix μ by setting

$$g(0) = 1. \tag{4.23}$$

Although a general theory for the solution of the functional equation (4.21) is still lacking, we can obtain a unique solution if we specify the nature of the maximum of $g(x)$ at $x = 0$ (for example quadratic) and require that $g(x)$ is a smooth function. If we use for $g(x)$ in the quadratic case the extremely short power law expansion

$$g(x) = 1 + bx^2 \tag{4.24}$$

the fixed point equation (4.21) becomes

$$1 + bx^2 = -\alpha(1 + b) - \left(\frac{2b^2}{\alpha} \right) + O(x^4) \tag{4.25}$$

which yields

$$b = (-2 - \sqrt{12})/4 \simeq -1.366; \quad \alpha = |2b| \simeq 2.73. \tag{4.26}$$

These values only differ by 10% from Feigenbaum's numerical results

$$\begin{aligned}
 g(x) &= 1 - 1.52763x^2 + 0.104815x^4 + 0.0267057x^6 - \dots \\
 \alpha &= 2.502807876\dots
 \end{aligned} \tag{4.27}$$

This establishes the universality of α .

4.2.4 Linearized Doubling Transformation and δ

What can we say about the scaling along the r -axis? The values $r = R_n$ for which a 2^n -cycle becomes superstable, are determined by the condition that $x = 1/2$ is an element of the supercycle (see eq. (4.11), i. e., $x = 1/2$ is a fixed point of $f_{R_n}^{2^n}(x)$):

$$f_{R_n}^{2^n}\left(\frac{1}{2}\right) = \frac{1}{2} \quad (4.28)$$

which after translation by $1/2$ becomes [see eqs. (4.12–4.13)]:

$$f_{R_n}^{2^n}(0) = 0. \quad (4.29)$$

This equation has a large number of solutions because it also yields the 2^n -supercycles that occur in the windows of the chaotic regime. In order to single out the R_n -values in the bifurcation region with

$$r_1 < R_1 < r_2 < R_2 < r_3 \dots, \quad (4.30)$$

Equation (4.29) is solved starting from $n = 0$, and the R_n are ordered as in eq. (4.30).

The R_n tell us how R_∞ is approached. In order to prove the scaling relation (4.5),

$$R_n - R_\infty \propto \delta^{-n}, \quad (4.31)$$

we expand $f_R(x)$ around $f_{R_\infty}(x)$:

$$f_R(x) = f_{R_\infty}(x) + (R - R_\infty)\delta f(x) + \dots$$

where

$$\delta f(x) \equiv \left. \frac{\partial f_R(x)}{\partial R} \right|_{R_\infty}. \quad (4.32)$$

Let us now apply the doubling operator T to this equation. A straightforward linearization in δf yields

$$Tf_R = Tf_{R_\infty} + (R - R_\infty)L_{f_{R_\infty}}\delta f + O[(\delta f)^2] \quad (4.33)$$

where L_f is the linear operator

$$L_f\delta f = -\alpha \left\{ f' \left[f \left(-\frac{x}{\alpha} \right) \right] \delta f \left(-\frac{x}{\alpha} \right) + \delta f \left[f \left(-\frac{x}{\alpha} \right) \right] \right\}. \quad (4.34)$$

Note that L_f is only defined with respect to a function f .

Repeated application of T yields

$$T^n f_R = T^n f_{R_\infty} + (R - R_\infty)L_{T^{n-1}f_{R_\infty}} \dots L_{f_{R_\infty}}\delta f + O[(\delta f)^2]. \quad (4.35)$$

We observe that, according to eqs. (4.17–4.20), $T^n f_{R_\infty}$ converges to the fixed point,

$$T^n f_{R_\infty}(x) = (-\alpha)^n f_{R_\infty}^{2^n} \left[\frac{x}{(-\alpha)^n} \right] \cong g(x) \quad \text{for } n \gg 1, \quad (4.36)$$

and (4.35) becomes approximately:

$$T^n f_R(x) \cong g(x) + (R - R_\infty)L_g^n \delta f(x) \quad \text{for } n \gg 1. \quad (4.37)$$



Figure 30: Parametrization of r by n and μ (schematically), i. e., $r_n = R_{n,1} \hat{=} (n, 1)$ and $R_n = R_{n,0} \hat{=} (n, 0)$.

This equation can be further simplified if we expand $\delta f(x)$ with respect to the eigenfunctions φ_v of L_g ,

$$L_g \varphi_v = \lambda_v \varphi_v; \quad \delta f = \sum_v c_v \varphi_v; \quad v = 1, 2, \dots \quad (4.38)$$

$$\rightarrow L_g^n \delta f = \sum_v c_v \lambda_v^n \varphi_v \quad (4.39)$$

and assume that only one of the eigenvalues λ_v is larger than unity, i. e.,

$$\lambda_1 > 1; \quad |\lambda_v| < 1 \quad \text{for } v \neq 1. \quad (4.40)$$

We then obtain only the contribution from λ_1 in (4.39),

$$L_g^n \delta f \cong c_1 \lambda_1^n \varphi_1 \quad \text{for } n \gg 1, \quad (4.41)$$

and (4.37) reduces to

$$T^n f_{R_n}(x) \cong g(x) + (R - R_\infty) \cdot \delta^n \cdot a \cdot h(x) \quad \text{for } n \gg 1 \quad (4.42)$$

where we introduced $c_1 \equiv \alpha$, $\varphi_1 \equiv h$, $\lambda_1 \equiv \delta$.

The eigenvalue $\lambda_1 \equiv \delta$ is identical with Feigenbaum's constant because for $R = R_n$ and $x = 0$, (4.42) yields

$$T^n f_{R_n}(0) = g(0) + (R_n - R_\infty) \cdot \delta^n \cdot a \cdot h(0) \quad (4.43)$$

and from (4.29) we have the condition

$$T^n f_{R_n}(0) = (-\alpha)^n f_{R_n}^{2^n}(0) = 0. \quad (4.44)$$

This leads to the desired result (note $g(0) = 1$)

$$\lim_{n \rightarrow \infty} (R_n - R_\infty) \cdot \delta^n = \frac{-1}{a \cdot h(0)} = \text{const}. \quad (4.45)$$

The last equation can be generalized if we introduce the slopes

$$\mu \equiv \frac{d}{dx_0} f_r^{2^n}(x_0^*) = \prod_i f_r'(x_i^*) \quad (4.46)$$

as a parameter and characterize r by the pair (n, μ) , as shown in Fig. 30. Then we obtain from (4.43):

$$\lim_{n \rightarrow \infty} (R_{n,\mu} - R_\infty) \cdot \delta^n = \frac{g_{0,\mu}(0) - g(0)}{\alpha \cdot h(0)} \quad (4.47a)$$

where

$$g_{0,\mu}(x) = \lim_{n \rightarrow \infty} (-\alpha)^n f_{R_n,\mu}^{2^n} \left[\frac{x}{(-\alpha)^n} \right] \quad (4.47b)$$

is again a universal function of μ .

At the bifurcation points, r_n , the slopes always have the same value $\mu = 1$ (see Fig. 30). Therefore, the r_n scale according to (4.47) with the same δ as the R_n of the superstable cycles (with $\mu = 0$):

$$r_n - r_\infty \propto \delta^{-n} \quad \text{for } n \gg 1. \quad (4.48a)$$

Note that the accumulation point is the same for all μ :

$$\lim_{n \rightarrow \infty} R_{n,\mu} = R_\infty = r_\infty \quad (4.48b)$$

because $r_n \leq R_{n,\mu} \leq r_{n+1}$ and $r_{n+1} - r_n \rightarrow 0$ for $n \rightarrow \infty$.

The numerical value for δ can be obtained [by combining (4.34–4.42)] from the universal eigenvalue equation

$$L_g h(x) = -\alpha \left\{ g' \left[g \left(-\frac{x}{\alpha} \right) \right] h \left(-\frac{x}{\alpha} \right) + h \left[g \left(-\frac{x}{\alpha} \right) \right] \right\} = \delta \cdot h(x). \quad (4.49)$$

To make things simple we retain in the power law expansion for $h(x)$ only the first term $h(0)$, such that (4.49) becomes an algebraic equation for δ :

$$-\alpha \{ g' [g(0)] + 1 \} = \delta. \quad (4.50a)$$

The value $g' [g(0)] = g'(1)$ follows for functions with a quadratic maximum (i. e., $g''(0) \neq 0$) by differentiating the fixed-point equation (4.21) twice:

$$\begin{aligned} g''(x) &= - \left\{ g'' \left[g \left(-\frac{x}{\alpha} \right) \right] \left[g' \left(-\frac{x}{\alpha} \right) \right]^2 + g' \left[g \left(-\frac{x}{\alpha} \right) \right] g'' \left(-\frac{x}{\alpha} \right) \right\} / \alpha \\ &\rightarrow g''(1) = -\alpha. \end{aligned} \quad (4.50b)$$

Thus (4.50a) becomes

$$\delta = \alpha^2 - \alpha. \quad (4.50c)$$

(For functions with a maximum of order $2z$ one finds $\delta = \alpha^{1+z} - \alpha$.)

Using our previously determined value $\alpha = 2.73$, we obtain $\delta = 4.72$ from (4.50), i. e., an accuracy of about 1% with respect to Feigenbaum's numerical result $\delta = 4.6692016\dots$ This is not so bad if one considers the crudeness of our approximation.

It is of course much more laborious to show that δ is indeed the only eigenvalue of L_g which is larger than unity. Extensive computer calculations by Feigenbaum and the analytical results of Collet, Eckmann, and Lanford (1980) have proven this assumption.

Summarizing, the two main results of this section are,

1. the fixed-point equation for the doubling operator (4.21)

$$Tg(x) = -\alpha g \left[g \left(-\frac{x}{\alpha} \right) \right] = g(x) \quad (4.51)$$

which establishes the universality of α ;

2. the linearized doubling transformation (4.42)

$$T^n f_R(x) = g(x) + (R - R_\infty) \cdot \delta^n \cdot a \cdot h(x) \quad \text{for } n \gg 1 \quad (4.52)$$

which shows that δ is universal and determines the way in which a function is repelled from the fixed-point function $g(x)$.

Universality emerges here because the linearized doubling operator L_g has only one *relevant* eigenvalue $\lambda_1 > 1$ such that all functions $f(x)$ – with the exception of $\phi_1(x)$ – renormalize, after several applications of T , to the fixed-point function $g(x)$ because the eigenvalues belonging to $f - g = \sum_{v \neq 1} c_v \phi_v$ are smaller than unity, i. e., are *irrelevant*.

4.3 Self-Similarity, Universal Power Spectrum, and the Influence of External Noise

In this section, we calculate the distances between the elements of a 2^n -cycle and determine its power spectrum. It is then shown that external noise changes the power spectrum drastically and destroys higher subharmonics. Finally, we discuss the bifurcation diagram for $r > r_\infty$ and show that the chaotic behavior of the iterates (of the logistic map) at $r = 4$ is related to the chaos of a triangular map.

The power spectrum is an important tool for characterizing irregular motion. In order to calculate this quantity for a system that exhibits the Feigenbaum route to chaos, we identify the time variable with n and determine as a first step the relative positions of the cycle elements.

4.3.1 Self-Similarity in the Positions of the Cycle Elements

All we know up to now about the positions of the cycle elements is that according to eqs. (4.3) and (4.13) the distances $d_n(0)$ of the supercycle elements closest to $x = 0$ scale with α , i. e.,

$$\frac{d_{n+1}(0)}{d_n(0)} = -\frac{1}{\alpha} \quad \text{for } d_n(0) = f_{R_n}^{2^{n-1}}(0), \quad n \gg 1. \quad (4.53)$$

It is now our aim to generalize these equations. We will calculate for all m the distance $d_n(m)$ of the m th element x_m of a 2^n -supercycle to its nearest neighbor $f_{R_n}^{2^{n-1}}(x_m)$,

$$d_n(m) \equiv x_m - f_{R_n}^{2^{n-1}}(x_m) \quad (4.54)$$

and the change of $d_n(m)$ if one increases n ,

$$\sigma_n(m) \equiv \frac{d_{n+1}(m)}{d_n(m)}. \quad (4.55)$$

The function $\sigma(m)$ changes sign after 2^n cycle steps,

$$\sigma_n(m + 2^n) = -\sigma_n(m) \quad (4.56)$$

because

$$\begin{aligned} d_{n+1}(m + 2^n) &= f_{R_{n+1}}^{2^n}(x_m) - f_{R_{n+1}}^{2^n}[f_{R_{n+1}}^{2^n}(x_m)] \\ &= f_{R_{n+1}}^{2^n}(x_m) - x_m = -d_{n+1}(m) \end{aligned} \quad (4.57)$$

and $d_n(m)$ is left invariant ($f_{R_n}^{2^n}(x_m) = x_m$).

Let us now consider the values $m = 2^{n-1}$, $i = 0 \dots n$, and evaluate $\sigma(m)$ in the limit $n \gg 1$. The definitions (4.54), (4.55) yield

$$\begin{aligned} \sigma_n[2^{n-i}] &= \frac{f_{R_{n+1}}^{2^{n-i}}(0) - f_{R_{n+1}}^{2^n}[f_{R_{n+1}}^{2^{n-i}}(0)]}{f_{R_n}^{2^{n-i}}(0) - f_{R_n}^{2^{n-1}}[f_{R_n}^{2^{n-i}}(0)]} \\ &= \frac{f_{R_{(n-i)+1}}^{2^{n-i}}(0) - f_{R_{(n-i)+1}}^{2^{n-1}}[f_{R_{n+1}}^{2^n}(0)]}{f_{R_{(n-i)+1}}^{2^{n-i}}(0) - f_{R_{(n-i)+1}}^{2^{n-1}}[f_{R_{(n-1)+1}}^{2^{n-1}}(0)]} \end{aligned} \quad (4.58)$$

and because

$$f_{R_{l+j}}^{2^l}(x) \cong (-\alpha)^{-l} g_j[(-\alpha)^l x] \quad \text{for } l = n - i \rightarrow \infty \quad (4.59)$$

this becomes

$$\sigma_n[2^{n-i}] = \frac{g_{i+1}(0) - g_{i+1}[(-\alpha)^{-i} g_1(0)]}{g_i(0) - g_i[(-\alpha)^{-i+1} g_1(0)]} \quad \text{for } n \gg 1. \quad (4.60)$$

We note that the functions $g_i(x)$ can be obtained from (4.17) and (4.43) for $i \gg 1$:

$$g_i(x) = \lim_{n \rightarrow \infty} \mathbf{T}^n f_{R_{n+1}}(x) = g(x) - \delta^{-i} \cdot h(x). \quad (4.61)$$

For smaller i one uses the recursion eq. (4.18),

$$g_{i-1}(x) = \mathbf{T}g_i(x). \quad (4.62)$$

If we introduce, for convenience, the new variable $x = \frac{m}{2^{n+1}}$ and drop the index n , the symmetry relation (4.56) reads

$$\sigma\left(x + \frac{1}{2}\right) = -\sigma(x). \quad (4.63)$$

This generates from our familiar scaling relation (4.53) the value of σ at $x = 1/2$:

$$\sigma(0) = \frac{-1}{\alpha} \rightarrow \sigma\left(\frac{1}{2}\right) = -\sigma(0) = \frac{1}{\alpha}. \quad (4.64)$$

But starting instead from (4.60) we obtain

$$\begin{aligned} \sigma(0^+) &= \lim_{i \rightarrow \infty} \sigma(x = 2^{-1-i}) \\ &= \lim_{i \rightarrow \infty} \frac{g(0) - g[(-\alpha)^{-i} g_1(0)]}{g(0) - g[(-\alpha)^{-i+1} g_1(0)]} = \frac{1}{\alpha^2} \end{aligned} \quad (4.65)$$

because

$$g[(-\alpha)^{-i} g_1(0)] \approx g(0) + \frac{1}{2} g''(0) (-\alpha)^{-2i} g_1^2(0) \quad (4.66)$$

and from there and (4.63):

$$\left(\frac{1}{2} + 0^+\right) = -\sigma(0^+) = -\frac{1}{\alpha^2}. \quad (4.67)$$

This means that $\sigma(x)$ is discontinuous at $x = 0$ and $x = 1/2$.

More elaborate calculations show that $\sigma(x)$ jumps at all rationals as depicted in Fig. 31. Fortunately, the discontinuities decrease rapidly as the number of terms in the binary expansion of the rational increases, and it is therefore often sufficient to consider only the jumps at $x = 0, 1/4, 1/2$.

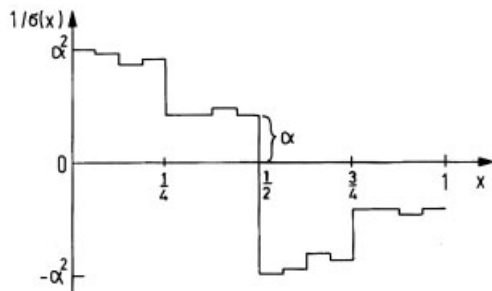


Figure 31: The function $\sigma(x) = \sigma_m (m = 2^n \cdot x)$, $n \gg 1$ [see eq. (4.55)] indicates how distances between adjacent points change if one passes, for $n \gg 1$, from a 2^n - to a 2^{n+1} -superstable cycle (after Feigenbaum, 1980).

4.3.2 Hausdorff Dimension

According to Fig. 31, the distances between nearby points in a supercycle change with universal ratios after each bifurcation. The self-similarity of this pattern can be characterized by the Hausdorff dimension of the attractor.

If, for a set of points in d dimensions, the number $N(l)$ of d -spheres of diameter l needed to cover the set increases like

$$N(l) \propto l^{-D} \quad \text{for } l \rightarrow 0 \quad (4.68)$$

then D is called the *Hausdorff* dimension of the set. [The quantity defined in eq. (4.68) is actually the capacity dimension which agrees for our purposes with the Hausdorff dimension whose rigorous definition is, e. g., elaborated in Falconer's book on the *Geometry of Fractal Sets* (1985)]. For the self-similar sets shown in Fig. 32, D can be calculated from

$$D = -\frac{\log[N(l)/N(l')]}{\log(l/l')} \quad (4.69)$$

We note that the length L of the Cantor set shown in Fig. 32 is indeed zero:

$$L = 1 - \frac{1}{3} - \frac{2}{9} - \frac{4}{27} \dots = 1 - \frac{1}{3} \sum_{v=0}^{\infty} \left(\frac{2}{3}\right)^v = 0. \quad (4.70)$$

The Hausdorff dimension D^* of a 2^n -cycle can be calculated in the limit $n \rightarrow \infty$ as follows. If for a 2^n -supercycle we need $N(l) = 2^n$ segments of length l to cover all its points, then from Fig. 31 it is found that the mean minimum length l' to cover all $N(l') = 2^{n+1}$ cycles is given approximately by

$$l' \approx \frac{1}{2^{n+1}} \left[2^n \frac{l}{\alpha} + 2^n \frac{l}{\alpha^2} \right] \quad (4.71)$$

which yields

$$D^* = -\log 2 / \log \left[\frac{1}{2} \left(\frac{1}{\alpha} + \frac{1}{\alpha^2} \right) \right] \cong 0.543. \quad (4.72)$$

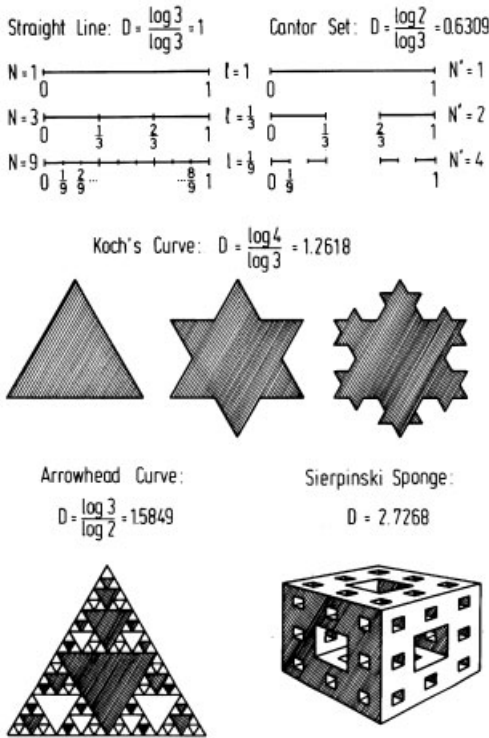


Figure 32: Hausdorff dimension of a straight line and of some typical self-similar point sets, so-called fractals (drawn after Mandelbrot, 1982). It is understood that the ramifications continue ad infinitum. Koch's curve is a line of infinite length that encloses a finite area.

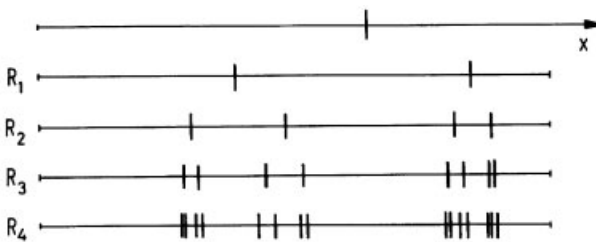


Figure 33: Positions of the cycle elements for $f_{R_n}(x) = R_n x(1 - x)$.

This value differs only by 5% from Grassberger's (1981) analytical and numerical result $D^* = 0.5388\dots$ (The numerical result was obtained by covering the attractor with successively smaller segments l and counting $N(l)$).

Figure 33 demonstrates the typical Cantor-set structure of the attractor. We will now show that this leads to a remarkably simple change in the measurable power spectrum after each bifurcation step.

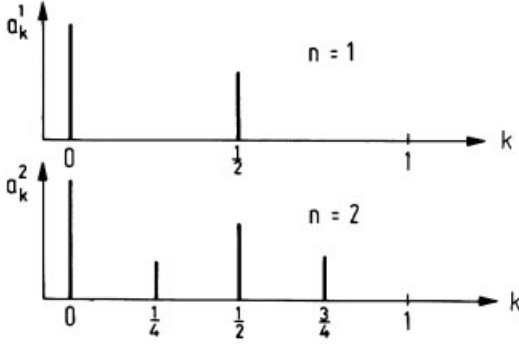


Figure 34: Change of the Fourier components after one bifurcation (schematically).

4.3.3 Power Spectrum

The power spectrum $P(k)$ can be obtained by resolving the element $x^n(t) \equiv f_{R_n}^t(0)$ of a 2^n -cycle ($t = 1, 2, \dots, 2^n \equiv T_n$) into its Fourier components a_k^n

$$x^n(t) = \sum_k a_k^n e^{\frac{2\pi i k}{T_n} t}. \quad (4.73)$$

The periodicity of the cycle implies

$$x^n(t) = x^n(t + 2^n) \rightarrow e^{2\pi i k} = 1 \rightarrow k = 0, 1, \dots, 2^n - 1 \quad (4.74)$$

i. e., after each bifurcation step from $n \rightarrow n + 1$, 2^n new subharmonics with frequencies $k/2^{n+1}$ ($k = 1, 3, 5, \dots$) are obtained, as shown in Fig. 34. The corresponding change in the a_k^n 's can be calculated from $\sigma(m)$.

As a first step, we invert (4.73):

$$a_k^n = \frac{1}{2^n} \sum_{t=1}^{2^n} e^{\frac{2\pi i k t}{2^n}} x^n(t) \approx \frac{1}{T_n} \int_0^{T_n} dt e^{\frac{2\pi i k t}{T_n}} x^n(t) \quad (4.75)$$

and by splitting the interval $[0, T_{n+1}]$ into two halves with $T_n = 1/2 T_{n+1}$ we obtain:

$$a_k^{n+1} = \int_0^{T_n} \frac{dt}{2T_n} [x^{n+1}(t) + (-1)^k x^{n+1}(t + T_n)] e^{-\frac{\pi i k t}{T_n}}. \quad (4.76)$$

The new even harmonics a_{2k}^{n+1} are essentially represented by the old spectrum at n (see Fig. 34), because

$$\begin{aligned} a_{2k}^{n+1} &= \int_0^{T_n} \frac{dt}{2T_n} [x^{n+1}(t) + x^{n+1}(t + T_n)] e^{-\frac{2\pi i k t}{T_n}} \\ &\approx \int_0^{T_n} \frac{dt}{T_n} x^{n+1}(t) e^{-\frac{2\pi i k t}{T_n}} \approx \int_0^{T_n} \frac{dt}{T_n} x^n(t) e^{-\frac{2\pi i k t}{T_n}} = a_k^n. \end{aligned} \quad (4.77)$$

The calculation of the odd components is somewhat more delicate, and we require our previously calculated function $\sigma(x)$.

From (4.76) we have

$$a_{2k+1}^{n+1} = \int_0^{T_n} \frac{dt}{2T_n} [x^{n+1}(t) - x^{n+1}(t+T_n)] e^{-\frac{(2k+1)\pi it}{T_n}} \quad (4.78)$$

and

$$\begin{aligned} x^{n+1}(t) - x^{n+1}(t+T_n) &= x^{n+1}(t) - f_{R_{n+1}}^{2^n} [x^{n+1}(t)] = d^{n+1}(t) \\ &= \sigma\left(\frac{1}{2T_n}\right) d^n(t) \end{aligned} \quad (4.79)$$

with

$$\begin{aligned} d^n(t) &= x^n(t) - x^n(t+T_{n-1}) = \sum_k a_k^n [1 - (-1)^k] e^{\frac{2\pi i k t}{T_n}} \\ &= 2 \sum_k a_{2k+1}^n e^{\frac{2\pi i (2k+1)t}{T_n}}. \end{aligned} \quad (4.80)$$

Thus, we obtain:

$$\begin{aligned} a_{2k+1}^{n+1} &= \sum_k a_{2k'+1}^n \int_0^{T_n} \frac{dt}{T_n} \sigma\left(\frac{t}{2T_n}\right) e^{\frac{2\pi i t}{T_n} [2k'+1 - \frac{1}{2}(2k+1)]} \\ &\approx \sum_{k'} a_{2k'+1}^n \left[\frac{1}{\alpha^2} + \frac{1}{\alpha} + i(-1)^k \left(\frac{1}{\alpha} - \frac{1}{\alpha^2} \right) \right] \frac{1}{2\pi i} \frac{1}{2k'+1 - \frac{1}{2}(2k+1)} \end{aligned} \quad (4.81)$$

because

$$\begin{aligned} \int_0^1 d\xi \sigma\left(\frac{\xi}{2}\right) e^{2\pi i \xi y} &\approx \frac{1}{\alpha^2} \int_0^{1/2} d\xi e^{2\pi i \xi} + \frac{1}{\alpha} \int_{1/2}^1 d\xi e^{2\pi i \xi y} \\ &= \frac{1}{2\pi i} \frac{1}{y} [(e^{\pi i y} - 1)/\alpha^2 + (e^{2\pi i y} - e^{\pi i y})/\alpha] \end{aligned} \quad (4.82)$$

where $\sigma(x)$ is approximated by a simple piecewise constant function.

Replacing the sum over k' in (4.81) by an integral and using

$$\frac{1}{2\pi i} \int dk' x_{2k'+1}^n \frac{1}{2k'+1 - \frac{1}{2} + (2k+1)} \approx \frac{1}{4} x_{(1/2)(2k+1)}^n \quad (4.83)$$

we eventually obtain:

$$|a_{2k+1}^{n+1}| \approx \mu^{-1} |a_{(1/2)(2k+1)}^n|, \quad \mu^{-1} = \frac{1}{4\alpha} \sqrt{2 \left(1 + \frac{1}{\alpha^2}\right)} \quad (4.84)$$

$$\mu^{-1} = 0.1525, \quad \text{i. e., } 10 \log_{10} \mu = 8.17 \text{ dB}.$$

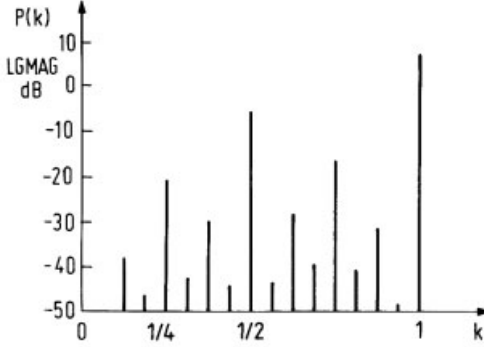


Figure 35: Numerically determined power spectrum for a quadratic map. Subsequent odd subharmonics differ by a factor μ^{-1} (after Collet and Eckmann, 1980).

Therefore, the amplitudes of the odd subharmonics, which appear after each bifurcation step, are “in the mean” just the averaged amplitudes of the old odd components reduced by a constant factor μ^{-1} . (The many approximations which have been made in deriving (4.84) require this cautious restriction to averages.) The universal pattern

$$|a_{2k}^{n+1}| \approx |a_k^n|, \quad |a_{2k+1}^{n+1}| \approx 0.152 |a_{(1/2)(2k+1)}^n| \quad (4.85)$$

is shown schematically in Fig. 34 and is reasonably consistent, e. g., with the numerical result found for the quadratic map $f(x) = 1 - 1.401155x^2$ depicted in Fig. 35.

4.3.4 Influence of External Noise

The full details of this power spectrum cannot be observed experimentally because there will always be some external noise due to the coupling to other degrees of freedom (see Fig. 36). In order to discuss this perturbation quantitatively, we add a noise term ξ_n to the logistic equation:

$$x_{n+1} = f_r(x_n) + \xi_n \quad (4.86)$$

and calculate its influence on the cascade of bifurcations.

Here, ξ_n are Gaussian-distributed variables with averages

$$\langle \xi_n \xi_{n'} \rangle = \sigma^2 \delta_{n,n'} \quad (4.87)$$

(similarly their Fourier components ξ_k are Gaussian-distributed), and σ measures the intensity of the white noise. We recall that the new Fourier components $|a_k^{n+1}|$ of a 2^{n+1} -cycle are a factor of μ^{-1} smaller than the old components $|a_k^n|$. This means that any finite external noise eventually suppresses all subharmonics above a certain n , as shown in Fig. 36c.

In fact the values R_n (above which all subharmonics become unobservable because they have merged into the chaos provided by the external noise) and the corresponding amplitude σ_n are related by a power law

$$(R_\infty - R_n) \propto \sigma_n^\gamma \quad (4.88)$$

where $\gamma = \log \delta / \log \mu$.

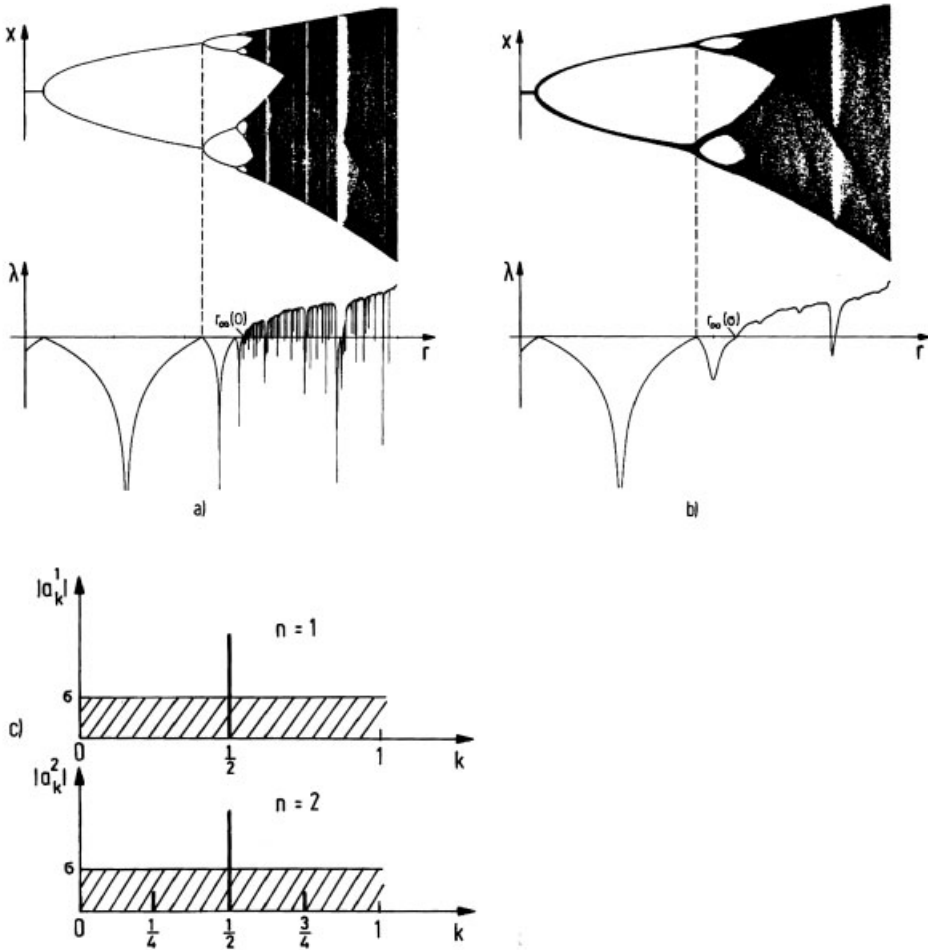


Figure 36: a) Iterates of the logistic map $n = 1$ and its Liapunov exponent λ , compared to b) the corresponding quantities in the presence of external noise with amplitude $\sigma = 10^{-3}$ (after Crutchfield, Farmer and Huberman, 1982). Although the noise washes out the fine structure in the iterates and in λ , there is still a sharp transition to chaos which is indicated by the change of sign of λ in b). c) Suppression of subharmonics in the presence of white noise σ . Note that the subharmonic amplitudes are reduced by a factor μ^{-1} for $n \rightarrow n + 1$ (schematically).

This can be derived as follows: If at R_1 a noise level σ_1 is just sufficient to suppress the first subharmonic $|a_k^1|$ then all $|a_k^n| = \mu^{-n}|a_k^1|$ will disappear at R_n for $\sigma_n = \mu^{-n}$. If the common n is eliminated, the corresponding scaling relations

$$(R_\infty - R_n) \propto \delta^{-n} \tag{4.89a}$$

$$\sigma_n \propto \mu^{-n} \tag{4.89b}$$

yield (4.88).

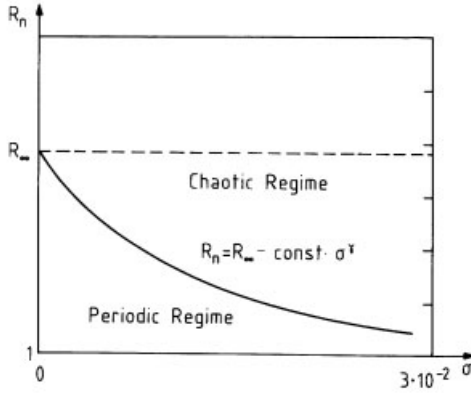


Figure 37: Suppression of the periodic regime by the presence of external noise for the logistic map (after Crutchfield, Farmer and Huberman, 1982).

The decrease of R_n with increasing noise amplitude as in (4.88) has been verified numerically as shown in Fig. 37.

The external noise, which produces chaos for $R_n < R_\infty$ plays a similar role as a magnetic field which causes a finite magnetization above the critical point of a magnet. This analogy has been worked out by Shraiman, Wayne, and Martin (1981) who have shown, for example, that the Liapunov exponent scales in the presence of external noise like

$$\lambda = r^\beta \lambda_0 [r^{-1/\gamma} \sigma]; \quad \beta = \log 2 / \log \delta; \quad r = R_\infty - R \quad (4.90a)$$

or equivalently

$$\lambda = \sigma^\theta \lambda_1 [r \sigma^{-\gamma}]; \quad \theta = \log 2 / \log \mu \quad (4.90b)$$

where $\lambda_{0,1}$ are universal functions (see Fig. 38). These results have also been obtained by

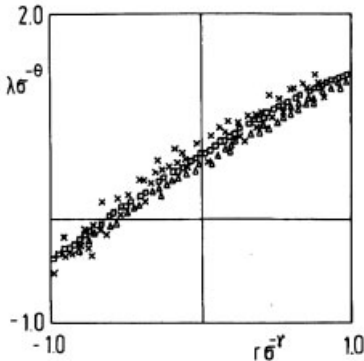


Figure 38: Numerical determination of the scaling function $\lambda_1(\gamma)$ in eq. (4.90b). The quantity $\lambda \sigma^{-\theta}$ is plotted against 100 values of $\gamma = r \sigma^{-\gamma}$ at each of three noise levels: $\sigma = 10^{-6}$ (\square), 10^{-8} (\triangle) and 10^{-10} (\times) (after Crutchfield *et al.*, 1981).

Feigenbaum and Hasslacher (1982) using a decimation of path integrals. Their method, which has a wide range of potential applications, is explained in Appendix E. Equation (4.90a) is reminiscent of the scaling behavior of the magnetization M at a second-order phase transition:

$$M = r^\beta f(r^{1/\gamma}h) \quad (4.91)$$

where $r = |T - T_c|$ is the temperature distance to the critical point, and h is the magnetic field. For the onset of chaos, where λ changes sign, eq. (4.90a) yields

$$0 = \lambda_0[r^{-1/\gamma}\sigma] \rightarrow r^{-1/\gamma} \cdot \sigma = \text{const.} \quad (4.92)$$

i. e., our equation (4.88).

4.4 Behavior of the Logistic Map for $r_\infty \leq r$

Let us now discuss the behavior of the logistic map for $r \geq r_\infty$. We have already seen above that at r_∞ the sequence of bifurcations ends in a set of infinitely many points, the so-called Feigenbaum attractor, which has a Hausdorff dimension $D = 0.548\dots$. Figure 23 shows that the Liapunov exponent λ of the logistic map at r_∞ is still zero, i. e., the Feigenbaum attractor is no strange attractor (see Chapter 6 for the definition of this object). But according to Fig. 23, λ becomes mostly positive for $r > r_\infty$, and it is therefore reasonable to say that chaos starts at the end of the bifurcation region. Although the detailed behavior of the iterates (of the logistic map) appears rather complicated in this region, it shows regularities which are again dictated by the doubling operator and therefore universal. It will be shown in the first part of this section that for $r_\infty < r$, periodic and chaotic regions are densely interwoven, and one finds a sensitive dependence on the parameter values. Next we discuss the structural universality discovered by Metropolis, Stein and Stein (1973) which preceded the work of Feigenbaum (1978). Finally we calculate the invariant density at $r = 4$ and explain the scaling of the reverse band-splitting bifurcations.

4.4.1 Sensitive Dependence on Parameters

Figure 32 shows that for $r_\infty < r \leq 4$ “chaotic parameter values” r with $\lambda > 0$ and non-chaotic r with $\lambda < 0$ are densely interwoven. Close to every parameter value where there is chaos, one can find another r value which corresponds to a stable periodic orbit, that is, the logistic map displays a sensitive dependence on the parameter r . The practical implications of this behavior are worse than those of sensitive dependence on initial conditions. When chaos occurs, the only alternative is to resort to statistical predictions. But for sensitive dependence on parameters, statistical averages become unstable under variations in parameters because the average behavior of the system may be completely different in the periodic and in the chaotic case.

Although there is a rigorous proof (Jacobson, 1981) that the total length of chaotic parameter intervals in $r_\infty \leq r \leq 4$ is finite, there remain the following questions:

- Which fraction of parameter values is chaotic?
- What is the probability that a change in the parameter values will lead to a change in qualitative behavior. Since it is no longer possible to distinguish experimentally (i. e.,

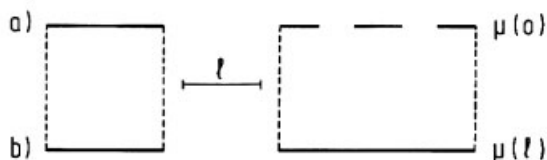


Figure 39: a) Piece of a fat fractal with measure $\mu(0)$, b) its coarse grained measure $\mu(l)$ is larger than $\mu(0)$ because only those holes that are bigger than the resolution l are deleted.

when one has finite precision) between chaotic and nonchaotic parameter values, one can only make statistical predictions for the parameter dependence of the system.

An answer to these questions has been given by D. Farmer (1985) who calculated numerically the coarse grained measure (i. e., total length) $\mu(l)$ of all chaotic parameter intervals for $f(x) = rx(1-x)$ and $g(x) = r\sin(\pi x)$. Coarse grained means that all nonchaotic holes on the r axis, with a size larger than l , were deleted (see Fig. 39).

Figure 40 shows that $\mu(l)$ scales like

$$\mu(l) = \mu(0) + Al^\beta \quad (4.93)$$

where $\beta = 0.45 \pm 0.05$ is numerically the same for both maps, whereas $\mu(0) = 0.8979$ (0.8929) for $f(x)$ and $g(x)$ respectively.

The set of chaotic parameter values with a scaling behavior described by eq. (4.93) is an example of a “fat” fractal. Fat fractals have, in contrast to the “thin” fractals considered on page 49, a finite measure (i. e., volume). A typical example of a fat Cantor set is shown in Fig. 41 which is obtained by deleting from the unit interval the central 1/3, 1/9, 1/27... of each piece.

The remaining lengths scale like $l_n = 1/2[1 - (1/3)^n]l_{n-1}$. Using $N_n = 2^n$, the Hausdorff dimension D of this fat Cantor set becomes $D = 1$ via eq. (4.69). However, its volume scales

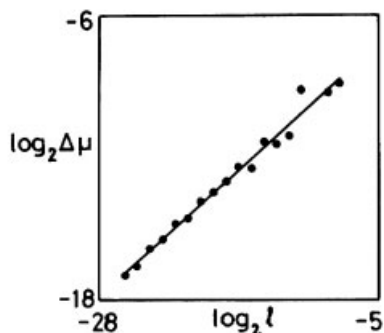


Figure 40: The logarithm of the change $\Delta\mu(l) = \mu(l) - \mu(0)$ in the coarse grained measure of chaotic parameter intervals plotted against the logarithm of the resolution l (after Farmer, 1985).

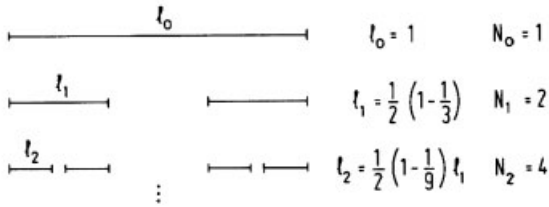


Figure 41: Fat fractal which is constructed by deleting the central $1/3$ then $1/9 \dots$ of each remaining subinterval (compare this to the thin fractal in Fig. 32).

according to:

$$\begin{aligned}
 \mu(l_n) - \mu(0) &= N_n l_n - N_\infty l_\infty = \prod_{j=1}^n \left[1 - \left(\frac{1}{3}\right)^j \right] - \prod_{j=1}^{\infty} \left[1 - \left(\frac{1}{3}\right)^j \right] \propto \\
 &\propto 1 - \prod_{j=n+1}^{\infty} \left[1 - \left(\frac{1}{3}\right)^j \right] \propto 1 - \left(\frac{1}{3}\right)^n \quad \text{for } n \rightarrow \infty.
 \end{aligned} \tag{4.94}$$

Via $l_n \propto (1/2)^n$ for $n \rightarrow \infty$ then follows:

$$\mu(l) - \mu(0) \propto l^\beta \quad \text{with } \beta = \log 3 / \log 2. \tag{4.95}$$

Let us now come back to the physical meaning of eq. (4.93). It answers both questions raised above. The measure $\mu(0)$ gives the fraction of chaotic parameter values in $r_\infty < r < 4$. The exponent β determines the probability p that a variation in r will change the qualitative behavior of the iterates. If one is sitting on a chaotic parameter value, p is proportional to the probability of finding a nonchaotic hole of size l , that is, $p \propto \mu(l) - \mu(0) \propto l^\beta$.

This situation means, for numerical computations of the logistic map (which are usually done with a precision $l \sim 10^{-14}$) that the odds of a mistake (i. e., that a trajectory believed to be chaotic is actually periodic) are, for $\beta \cong 0.45$, of the order 10^{-6} , which is acceptable.

According to Farmer (1985), one speaks only then of sensitive dependence on parameters, if $\beta < 1$ (i. e., if the odds of a mistake are larger than in the trivial case where one has $p \sim l^{-1}$).

It has been found (Farmer, 1986) that the set of parameter values where quasiperiodic behavior occurs in the subcritical circle map is also a fat fractal (see Chapter 7). This implies sensitive dependence on parameters which distinguish between quasi-periodic and mode-locked behavior (i. e., sensitive parameter dependence is not necessarily tied to chaos). Let us finally note that the fact that the exponent β is numerically the same for the logistic map $f(x)$ and the sine map $g(x)$ indicates a sort of *global universality* which is different from that originally found by Feigenbaum since it *applies to a set of positive measure* (volume) rather than just special points as period-doubling transitions.

4.4.2 Structural Universality

Structural universality in unimodal maps was discovered by Metropolis, Stein and Stein (1973). They considered the iterates of the logistic map $f(x)$ in the periodic windows. Starting from $x_0 = 1/2$, i. e., from the x value which corresponds to the maximum of $f(x)$, the

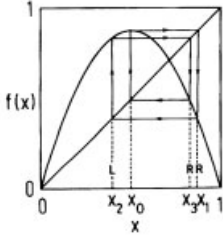


Figure 42: The map $x_{n+1} = rx_n(1 - x_n)$ with $r = 3.49856$ displays a 4-cycle of the type RLR .

sequence of iterates $f^n(x_0)$ on a periodic attractor can be characterized by a string $RL\dots$ where R or L indicates whether $f^{n+1}(x_0)$ is to the right or left of x_0 (see e. g., Fig. 42). Table 3, which has been computed by Metropolis *et al.* (1973), shows that the sequence of strings is (up to cycles of length 7) the same for $f(x) = rx(1 - x)$ and $g(x) = q \sin \pi x$. This numerical result (which has actually been calculated for cycles up to length 11 and for other unimodal

Table 3: Universal sequences for two unimodal maps.

Period	U-sequence	Parameter value r in $x_{n+1} = rx_n(1 - x_n)$	Parameter value q in $x_{n+1} = q \sin(\pi x_n)$
2	R	3.2360680	.7777338
4	RLR	3.4985617	.8463822
6	RLR^3	3.6275575	.8811406
7	RLR^4	3.7017692	.9004906
5	RLR^2	3.7389149	.9109230
7	RLR^2LR	3.7742142	.9213346
3	RL	3.8318741	.9390431
6	RL^2RL	3.8445688	.9435875
7	RL^2RLR	3.8860459	.9568445
5	RL^2R	3.9057065	.9633656
7	RL^2R^3	3.9221934	.9687826
6	RL^2R^2	3.9375364	.9735656
7	RL^2R^2L	3.9510322	.9782512
4	RL^2	3.9602701	.9820353
7	RL^3RL	3.9689769	.9857811
6	RL^3R	3.9777664	.9892022
7	RL^3R^2	3.9847476	.9919145
5	RL^3	3.9902670	.9944717
7	RL^4R	3.9945378	.9966609
6	RL^4	3.9975831	.9982647
7	RL^5	3.9993971	.9994507

maps) suggests that the ordering of the sequence of $RL\dots$ strings is universal for all maps on the $[0, 1]$ interval which have a differentiable maximum and fall off monotonically on both sides. This so-called *structural universality* has been put on a rigorous footing by Guckenheimer (1980). It does not depend on the order of the maximum as the *metric universality* of Feigenbaum (1978) (a “metric” is needed there to measure the distances which scale). But it should be noted that structural universality seems to be restricted to one-dimensional maps because in higher dimensions, up to now, no ordering has been found, and one can have coexisting cycles of different length with different basins of attraction (see also Section 6.4).

From the mathematical point of view, the sequence of cycles in an unimodal map $f(x)$ is completely described by Sarkovskii’s theorem (1964). It states that if $f(x)$ has a point x which leads to a cycle of period p then it must also have a point x' which leads to a q -cycle for every $q \leftarrow p$ where q and p are elements in the following sequence:

$$\begin{aligned}
 &1 \leftarrow 2 \leftarrow 4 \leftarrow 8 \leftarrow 16 \dots 2^m \dots \leftarrow \\
 &\dots 2^m \cdot 9 \leftarrow 2^m \cdot 7 \leftarrow 2^m \cdot 5 \leftarrow 2^m \cdot 3 \dots \leftarrow \\
 &\dots 2^2 \cdot 9 \leftarrow 2^2 \cdot 7 \leftarrow 2^2 \cdot 5 \leftarrow 2^2 \cdot 3 \dots \leftarrow \\
 &\dots 2 \cdot 9 \leftarrow 2 \cdot 7 \leftarrow 2 \cdot 5 \leftarrow 2 \cdot 3 \dots \leftarrow \\
 &\dots 9 \leftarrow 7 \leftarrow 5 \leftarrow 3 \dots \leftarrow
 \end{aligned}
 \tag{4.96}$$

where the symbol \leftarrow means “precede” (for a proof, see references of this chapter). It should be emphasized that Sarkovskii’s theorem is only a statement concerning different x values at a fixed parameter value. It says nothing about the stability of the periods nor about the range of parameter values for which it could be observed. It follows, from the sequence in eq. (4.96), that if $f(x)$ has period three, then this implies that it must also have all periods n where n is an arbitrary integer. This is the famous theorem of Li and Yorke (1975) “Period three implies chaos”. But it should be noted that “chaos” in this theorem means only aperiodic behavior and does not imply automatically a positive Liapunov exponent.

4.4.3 Chaotic Bands and Scaling

The logistic map at $r = 4$,

$$x_{n+1} = 4x_n(1 - x_n) \equiv f_4(x_n), \tag{4.97}$$

can actually be solved by the simple change of variables:

$$x_n = \frac{1}{2}[1 - \cos(2\pi y_n)] \equiv h(y_n). \tag{4.98}$$

Then eq. (4.97) can be converted into

$$\begin{aligned}
 \frac{1}{2}[1 - \cos(2\pi y_{n+1})] &= [1 - \cos(2\pi y_n)][1 + \cos(2\pi y_n)] = \\
 &\frac{1}{2}[1 - \cos(4\pi y_n)]
 \end{aligned}
 \tag{4.99}$$

which has one solution:

$$y_{n+1} = 2y_n \bmod 1 \equiv g(y_n) \quad \text{or} \quad y_n = 2^n y_0 \bmod 1. \tag{4.100}$$

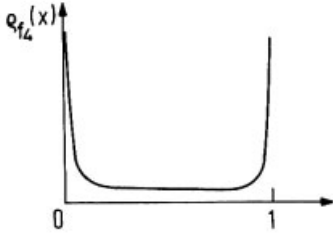


Figure 43: The invariant density for $f_4 = 4x(1-x)$ (schematically).

This implies the following solution to eq. (4.98):

$$x_n = \frac{1}{2} [1 - \cos(2\pi 2^n y_0)] \quad (4.101)$$

$$\text{where } y_0 = \frac{1}{2\pi} \arccos(1 - 2x_0). \quad (4.102)$$

Using eqs. (4.97–4.100), the invariant density $\rho_4(x)$ of $f_4(x)$ can be calculated from its definition:

$$\rho_4(x) = \lim_{N \rightarrow \infty} \frac{1}{N} \sum_{n=0}^{N-1} \delta(x - x_n) = \lim_{N \rightarrow \infty} \frac{1}{N} \sum_{n=0}^{N-1} \delta[x - h(y_n)].$$

Using $\rho(y) = 1$ [which holds in analogy to the triangular map on page 27 also for the map in eq. (4.100)] eq. (4.101) becomes:

$$\rho_4(x) = \int_0^1 dy \rho(y) \delta[x - h(y)] = \frac{2}{|h'[y(x)]|} \quad (4.103)$$

i. e.,

$$\rho_4(x) = \frac{1}{\pi} \frac{1}{\sqrt{x(1-x)}} \quad (4.104)$$

as depicted in Fig. 43.

These results show that the map $f_r(x)$ becomes ergodic for $r = 4$ and that the invariant density of a chaotic map need not always be a constant.

For the Liapunov exponent eq. (4.104) yields at $r = 4$:

$$\lambda = \int_0^1 dx \rho_4(x) |f'(x)| = \log 2 \quad (4.105)$$

i. e., the same value as for the map in eq. (4.100) which demonstrates that the Liapunov exponent is indeed invariant under a change of the coordinates.

Figure 44 makes it plausible that the r -values for the inverse cascade (in which the chaotic regime at $r = 4$, which extends from $0 \leq x \leq 1$, is decomposed into finer and finer subintervals I_n that merge into the Feigenbaum attractor) are again determined by the law of functional composition.

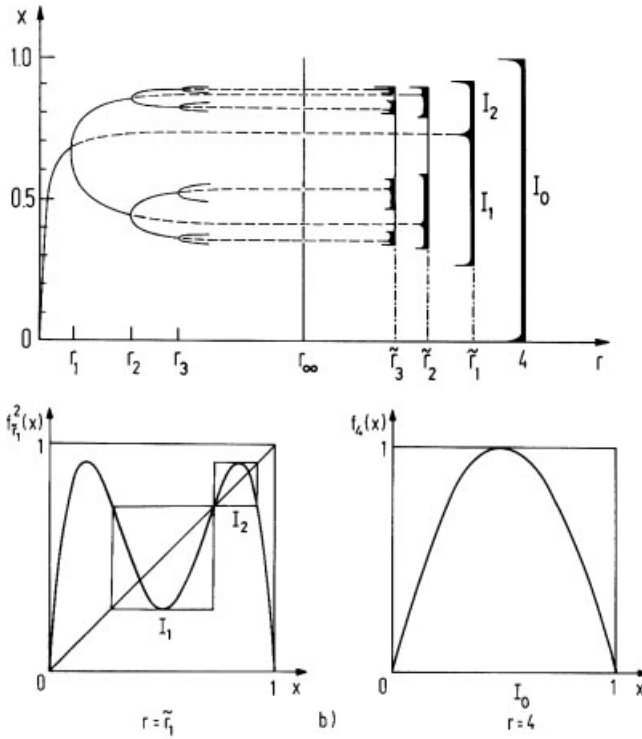


Figure 44: a) Bifurcations for $r < r_\infty$ and the corresponding merging of chaotic regions for $r > r_\infty$; the dark areas indicate the corresponding invariant densities (see Fig. 43). Note the nonlinear scale on the abscissa. (After Grossmann and Thomae, 1977.) b) The lengths I_n of the chaotic intervals are again related to functional composition and the \tilde{r}_n therefore scale like $\tilde{r}_n - r_\infty \sim \delta^{-n}$.

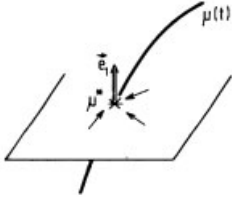
4.5 Parallels between Period Doubling and Phase Transitions

In the first part of this section we present a dictionary of the corresponding terms used in the bifurcation route to chaos and in the renormalization-group theory for second-order phase transitions. In the second part we summarize the measurable properties that characterize the Feigenbaum route and discuss some representative experiments.

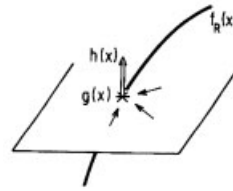
We have already seen in Chapter 3 that the Liapunov exponent corresponds to the order parameter near a second-order phase transition. Table 4 shows that for the bifurcation route to chaos the analogy to a magnetic phase transition can be worked out in more detail. Both phenomena show a certain self-similarity (in the bifurcation pattern and in the pattern of spin-up/spin-down clusters near a critical point) which forms the basis for a renormalization-group treatment. Universality emerges then because there are only a few relevant eigenvalues (see also Appendices E and D).

Table 4: Parallels between phase transitions and period doubling.

Phase transitions	Period doubling
Ginzburg–Landau functional $H = \int d^d x [c(\nabla\sigma)^2 + t\sigma^2 + u\sigma^4]$ with parameter vector $\mu = (c, t, u)$	One-dimensional map $f_R(x)$
Distance to the critical point $t = T - T_c$	Distance from R_∞ $R - R_\infty$
Order parameter $\langle \sigma(x) \rangle$ (Magnetization)	Liapunov exponent λ_R (changes sign at R_∞)
Formation of block spins \rightarrow renormalization-group transformation R with fixed point H^* ($\hat{=} \mu^*$) $R[\mu^{**}] = \mu^*$	Functional composition \rightarrow doubling operator T with fixed point g $T[g] = g$
Linearized renormalization-group transformation $R_{2^n}[\mu^*] = \mu^* + (T - T_c)2^{ny_1} \vec{e}_1$	Linearized doubling transformation $T^n f_R(x) = g(x) + (R - R_\infty) \cdot \delta^n \cdot a \cdot h(x)$
Parameter space: critical surface	Space of functions: stable manifold



$\vec{e}_1 =$ unstable direction



$a \cdot h(x) =$ one-dimensional unstable manifold

We can also derive scaling laws for the Liapunov exponent λ and the correlation function $C(m)$ which are similar to those for the magnetization and the spin-spin correlation near a magnetic phase transition.

According to (3.9), the Liapunov exponent of a map f is (for $x_0 = 0$) is given by

$$\lambda(f) = \lim_{n \rightarrow \infty} \frac{1}{n} \sum_{i=0}^n \log |f'[f^i(0)]|. \quad (4.106)$$

Using

$$Tf \cdot Tf \cdots Tf = (Tf)^i = -\alpha f^{2^i} \left(-\frac{x}{\alpha} \right) \quad (4.107)$$

and

$$\frac{d}{dx} Tf = f' \left[f \left(-\frac{x}{\alpha} \right) \right] f' \left(\frac{x}{\alpha} \right) \quad (4.108)$$

we find

$$\lambda[\mathbb{T}f] = 2 \lim_{n \rightarrow \infty} \frac{1}{2n} \sum_{i=0}^{2n+1} \log |f'[f^i(0)]| = 2\lambda[f] \quad (4.109)$$

which can be iterated to

$$\lambda[f] = 2^{-n} \lambda[\mathbb{T}^n f]. \quad (4.110)$$

By choosing $f = f_R$, we can use

$$\mathbb{T}^n f_R(x) = g(x) + (R - R_\infty) \cdot \delta^n \cdot a \cdot h(x) \quad (4.111)$$

in (4.110) which yields, by setting $(R - R_\infty)\delta^n = 1$, the scaling relation

$$\lambda_{f_R} = (R - R_\infty)^\beta \lambda[g(x) + a \cdot h(x)] \quad (4.112)$$

with $\beta = \log 2 / \log \delta$ as a critical exponent.

This equation describes the approach of the Liapunov exponent to zero if a sequence of R s with the same μ (see Fig. 30) approaches R_∞ ; i. e., the power law $\lambda \propto (R - R_\infty)^\beta$ holds for the envelope of λ .

In a similar way, for the correlation function (3.35)

$$C[m, f] = \lim_{n \rightarrow \infty} \frac{1}{n} \sum_{i=0}^n f^i(0) f^{i+m}(0) \quad (4.113)$$

one finds the scaling relation

$$\begin{aligned} C[m, \mathbb{T}f] &= \alpha^2 \lim_{n \rightarrow \infty} \frac{1}{n} \sum_{i=0}^n f^{2i}(0) f^{2i+2m}(0) \\ &= \alpha^2 \lim_{n \rightarrow \infty} \left\{ 2 \frac{1}{2n} \sum_{i=0}^{2n} f^i(0) f^{i+2m}(0) - \right. \\ &\quad \left. - \frac{1}{n} \sum_{i=0}^{n-1} [f(0)] f^{2i+2m}[f(0)] \right\} \end{aligned} \quad (4.114)$$

i. e.,

$$C[m, \mathbb{T}f] = \alpha^2 C[2m, f] \quad (4.115)$$

and by using again (4.107):

$$C[m, f_R] = \alpha^{-2n} C[2^{-n}m, g(x) + (R - R_\infty) \cdot \delta^n \cdot a \cdot h(x)]. \quad (4.116)$$

Equation (4.116) leads to a variety of scaling laws, depending on which combination of variables we set equal to unity. We mention that at R_∞ the correlation function decays with a power law in m :

$$C[m, f_{R_\infty}] = \alpha^{-2n} C[2^{-n}m, g(x)] = m^{-\eta} C[1, g(x)] \quad (4.117)$$

with $\eta = \log \alpha^2 / \log 2$.

These power laws have the following counterparts in magnetic phase transitions:

$$\lambda \propto |R - R_\infty|^\beta \hat{=} M \propto |T - T_c|^\beta \quad (4.118a)$$

$$C(m) \propto m^{-\eta} \text{ at } R_\infty \hat{=} C(|x|) \propto |x|^{-\eta} \text{ at } T_c \quad (4.118b)$$

where M is the magnetization and $C(|x|)$ is the spin-spin correlation function.

4.6 Experimental Support for the Bifurcation Route

After a preponderance of theory, let us now present some experimental support for the Feigenbaum route. First, we summarize its measurable fingerprints:

- There exists an infinite cascade of period doublings which leads to subharmonics in the power spectrum at frequencies $2^{-n} \cdot f_0$ where f_0 is the basic frequency.
- Each subharmonic lies below the preceding level by a factor $\mu^{-1} = 0.1525$ ($10 \log_{10} \mu = 8.17$ dB).
- The control parameter r scales for subsequent subharmonics n like $r_n - r_\infty \propto \delta^{-n}$.
- External noise destroys the fine structure of the power spectrum, and the noise level must decrease by a factor μ^{-1} to make one more subharmonic observable.
- The Poincaré map of the system is one-dimensional and shows a single quadratic maximum.

Following Feigenbaum's work, the bifurcation route to chaos has been found in many experimental systems, from the kicked pendulum and chemical reactions... to optically bistable devices. Below we discuss three representative examples in more detail.

Figures 45 and 46 show the power spectra for a Bénard experiment and for a nonlinear driven electrical *RCL*-oscillator.

The experimental set up for the Bénard experiment has already been described in Chapter 2. (We note that depending on the parameters of the liquid, the size of the cell, etc., the Bénard system exhibits different routes to chaos.) Libchaber and Maurer (1980) found the following properties of the Feigenbaum route in a Bénard experiment with liquid helium:

1. With increasing temperature difference (which is proportional to the control parameter r) there appear subharmonics of frequencies $f/2$, $f/4$, $f/8$ and $f/16$ where f is the basic frequency.
2. Subsequent subharmonics differ by about 10 dB in qualitative agreement with theory ($\mu \hat{=} 8.2$ dB).

Higher subharmonics are probably suppressed by external noise.

Although these results leave little doubt that the Feigenbaum route is involved, the explicit reduction of the hydrodynamic equations, which describe the system to a one-dimensional Poincaré map with a single quadratic maximum, has still not been demonstrated.

The situation is somewhat better for the nonlinear *RCL*-oscillator shown in Fig. 46. The nonlinear element in this circuit is, according to Linsay (1981), the capacitor-diode, which leads to the following nonlinear relation between charge q and voltage V :

$$V(q) = \left[1 + \frac{V(q)}{0.6} \right]^{0.43} \frac{q}{C_0}. \quad (4.119)$$

The differential equation for the time dependence of q is

$$L\ddot{q} + R\dot{q} + V(q) = V_0 \sin(2\pi f_1 t) \quad (4.120)$$

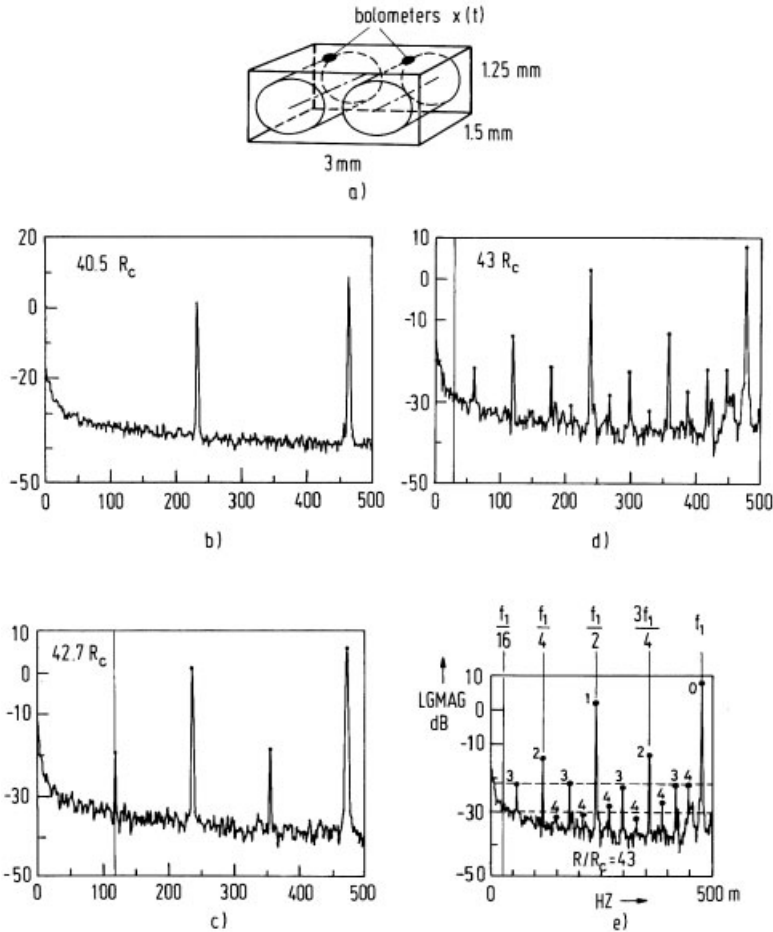


Figure 45: a) Bénard cell with only two-roll convection pattern of liquid helium, basic frequency $f = 0.5 \text{ s}^{-1}$. b)–d) Power spectrum of the temperature $x(t)$ with increasing Rayleigh number which is proportional to r . e) The heights of the n th subharmonics are compared with Feigenbaum's theory (horizontal lines). (After Libchaber and Maurer, 1980.)

and the circuit acts like an analog computer for a driven nonlinear oscillator. Figure 46 shows that for special values of V , (which is proportional to the control parameter r) the sequence of current signals $I_n = I(t_0 + nT)$, where the time $T = 1/f_1$, can indeed be generated from a one-dimensional map with a quadratic maximum. (The current is related to the charge via $I = \dot{q}$, and I_n corresponds to x_n). The corresponding power spectrum exhibits, as expected, all the features of the bifurcation route and yields an estimate for δ which deviates by 10% from Feigenbaum's asymptotic value. See also the phase portraits ($I(t)$ versus $V(t)$) for the nonlinear RCL -oscillator of Lauterborn *et al.* (1984) in Plate I at the beginning of the book. We note also that there exists theoretical (Rollins and Hunt, 1982) and experimental (S. Mar-

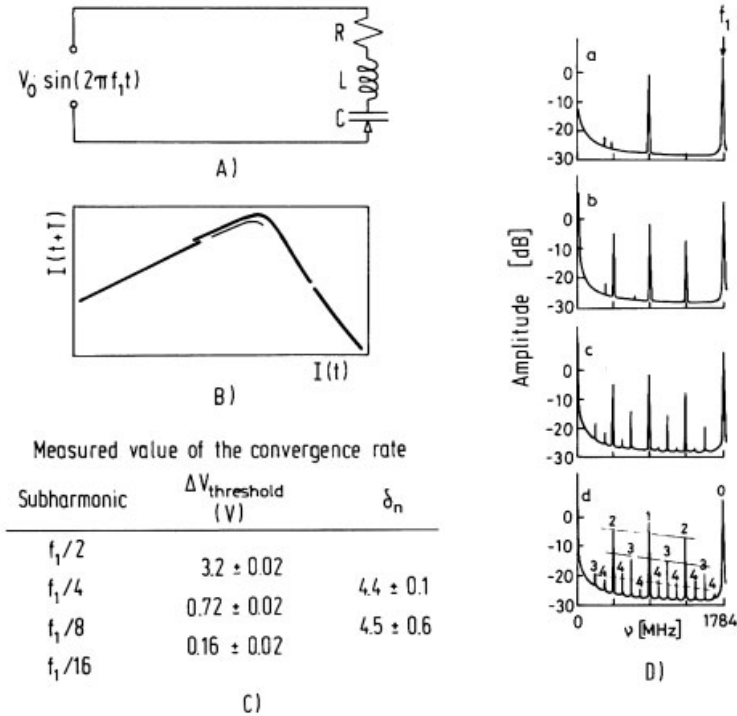


Figure 46: A) Circuit for the driven nonlinear RCL -oscillator. B) The observed current $I(t+T)$ vs. $T(t)$ yields a one-dimensional map with a single maximum. C) Determination of δ from the values of the control parameter V_0 . D) a–c: Subharmonics in the power spectrum for increasing V_0 ; d: comparison with Feigenbaum's theory (horizontal lines). (After Linsay, 1981.)

tin, priv. comm.) evidence that the chaotic behavior of RCL -oscillators with Varactor diodes (which were used in the experiments above) is not caused by the nonlinearity of the diode but by its large recovery time. But, this situation can again be described by a one-dimensional noninvertible map.

To demonstrate that the Feigenbaum route indeed occurs in quite different systems, we finally describe an experiment by Lauterborn and Cramer (1981) in which this route has been observed in acoustics (Fig. 47a). They irradiated water with sound of high intensity and measured the sound output of the liquid. The nonlinear elements in this system are cavitations, i. e., bubbles filled with water vapor which are created by the pressure gradients of the initial sound wave and whose wall oscillations are highly nonlinear.

Figure 47 shows a sequence of power spectra that is obtained experimentally (b) and from a numerical calculation (c) (in which only a single spherical bubble was considered). With increasing input pressure (which is the external control parameter), one observes a subharmonic route to chaos that, besides the sequence $f_0 \rightarrow f_0/2 \rightarrow f_0/4 \dots \rightarrow \text{chaos}$, also contains $f_0/3$. Moreover, the system shows signs of reverse bifurcations where it returns from chaotic behavior to a line spectrum.

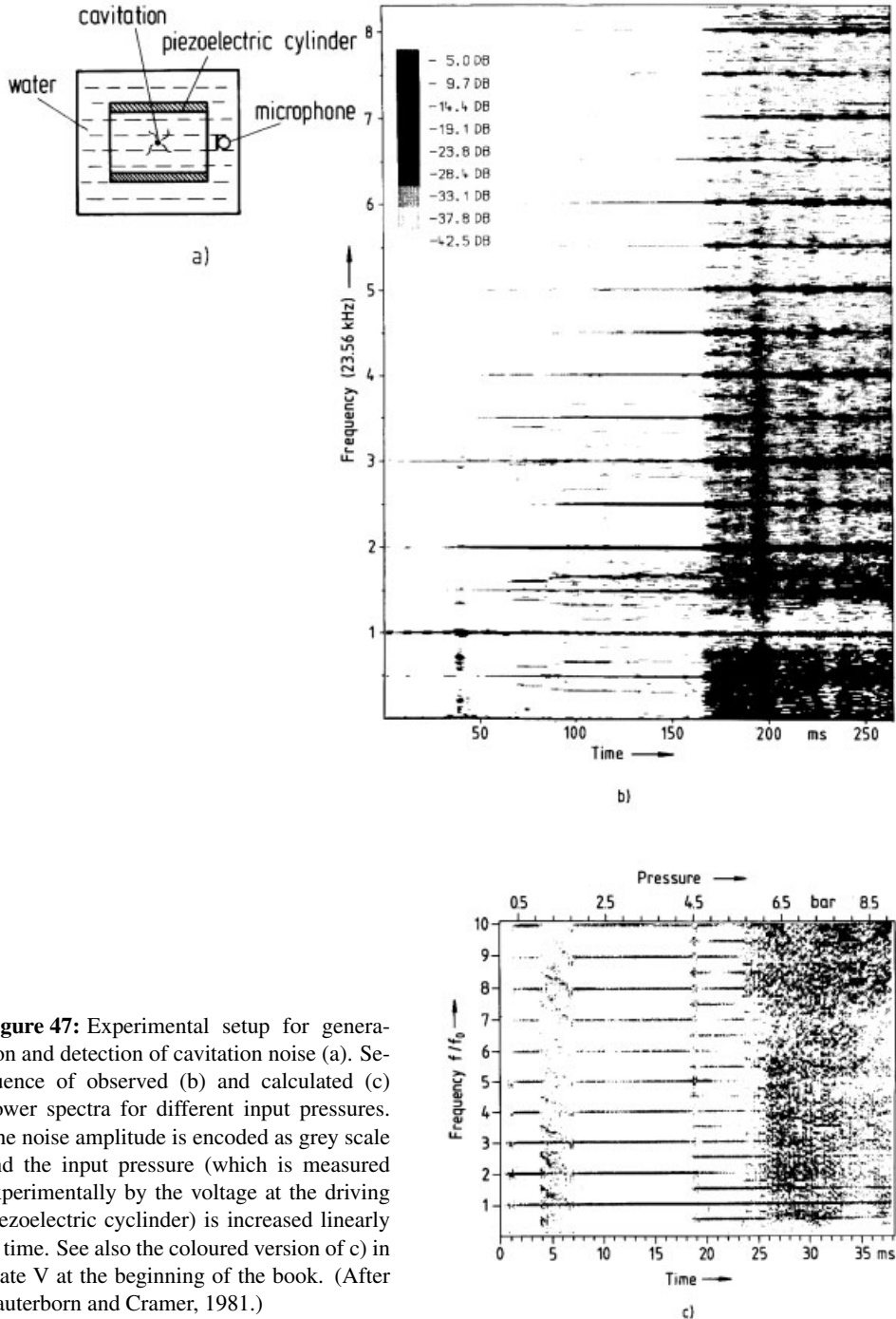


Figure 47: Experimental setup for generation and detection of cavitation noise (a). Sequence of observed (b) and calculated (c) power spectra for different input pressures. The noise amplitude is encoded as grey scale and the input pressure (which is measured experimentally by the voltage at the driving piezoelectric cylinder) is increased linearly in time. See also the coloured version of c) in Plate V at the beginning of the book. (After Lauterborn and Cramer, 1981.)

5 The Intermittency Route to Chaos

By intermittency we mean the occurrence of a signal that alternates randomly between long regular (laminar) phases (so-called intermissions) and relatively short irregular bursts. Such signals have been detected in a large number of experiments. It has also been observed that the number of chaotic bursts increases with an external parameter, which means that intermittency offers a continuous route from regular to chaotic motion. In the first section of this chapter, we present mechanisms for this phenomenon proposed by Pomeau and Manneville (1979) and discuss type-I intermittency which is generated by an inverse tangent bifurcation. It is shown in the second section that the transition to chaos via intermittency has in fact universal properties and represents one of the rare examples where the (linearized) renormalization-group equations can be solved exactly. These results will be used in Section 5.3 to demonstrate that intermittency provides a universal mechanism for $1/f$ -noise in nonlinear systems. In the final section, we summarize typical properties of the intermittency route and discuss some experiments.

5.1 Mechanisms for Intermittency

The intermittency route to chaos has been investigated in a pioneering study by Pomeau and Manneville (1979). They solved numerically the differential equations of the Lorenz model,

$$\dot{X} = \sigma(X - Z) \tag{5.1a}$$

$$\dot{Y} = -XZ + rX - Y \tag{5.1b}$$

$$\dot{Z} = XY - bZ \tag{5.1c}$$

and for the Y -component they found the behavior shown in Fig. 48.

For $r < r_c$, $Y(t)$ executes a stable periodic motion. Above the threshold r_c the oscillations are interrupted by chaotic bursts, which become more frequent as r is increased until the motion becomes truly chaotic.

Pomeau and Manneville gave the following interpretation for this behavior: The stable oscillations for $r < r_c$ correspond to a stable fixed point in the Poincaré map (see also Fig. 6). Above r_c this fixed point becomes unstable. Because there are essentially three ways in which a fixed point can lose its stability (in all of them the modulus of the eigenvalues of the linearized Poincaré map becomes larger than unity), Pomeau and Manneville distinguished the three types of intermittency shown in Table 5. (See also Table 7, p. 85, for the form of the signal.)

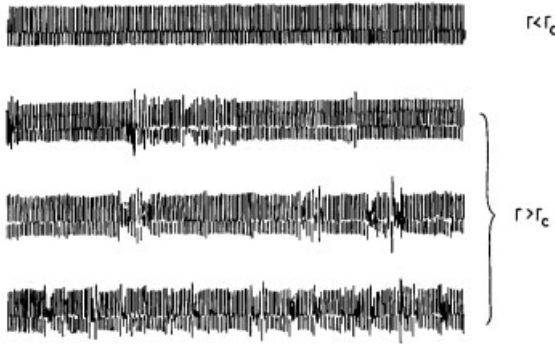


Figure 48: Time plot of one coordinate in the Lorenz model (after Pomeau and Manneville 1980).

Table 5: Three types of intermittency.

Type	Characteristic behavior and maps	Typical map ($\epsilon < 0 \rightarrow \epsilon > 0$)	Eigenvalues
I	A real eigenvalue crosses the unit circle at +1. $x_{n+1} = \epsilon + x_n + ux_n^2$		
II	Two conjugate complex eigenvalues cross the unit circle simultaneously. $r_{n+1} = (1 + \epsilon)r_n + ur_n^3$ $\theta_{n+1} = \theta_n + \Omega$		
III	A real eigenvalue crosses the unit circle at -1. $x_{n+1} = -(1 + \epsilon)r_n - ur_n^3$		

5.1.1 Type-I Intermittency

Figure 49 shows a Poincaré map for the Lorenz model, after Pomeau and Manneville who plotted the values y_n where $y(t)$ crossed the plane $x = 0$. If this figure is compared with Table 5, it is seen that the Lorenz model displays intermittency of type I.

This transition to chaos is characterized by an *inverse tangent bifurcation* in which two fixed points (a stable and an unstable one) merge as depicted in Fig. 50.

For $r > r_c$ the map has no stable fixed points. However, a sort of “memory” of a fixed point is displayed since the motion of the trajectory slows down in the vicinity of x_c and numerous iterations are required to move through the narrow channel between the map and the bisector. This leads to the long laminar regions for values of r just above r_c in Fig. 48.

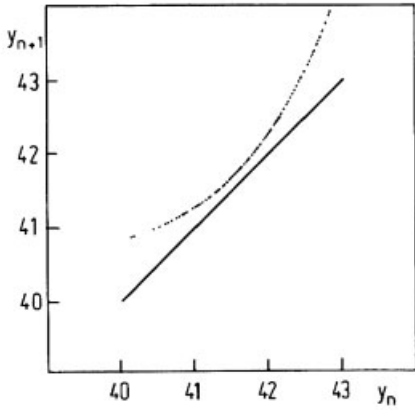


Figure 49: Poincaré map of the Lorenz model for r slightly above $r_c = 166$ (after Pomeau and Manneville, 1980).

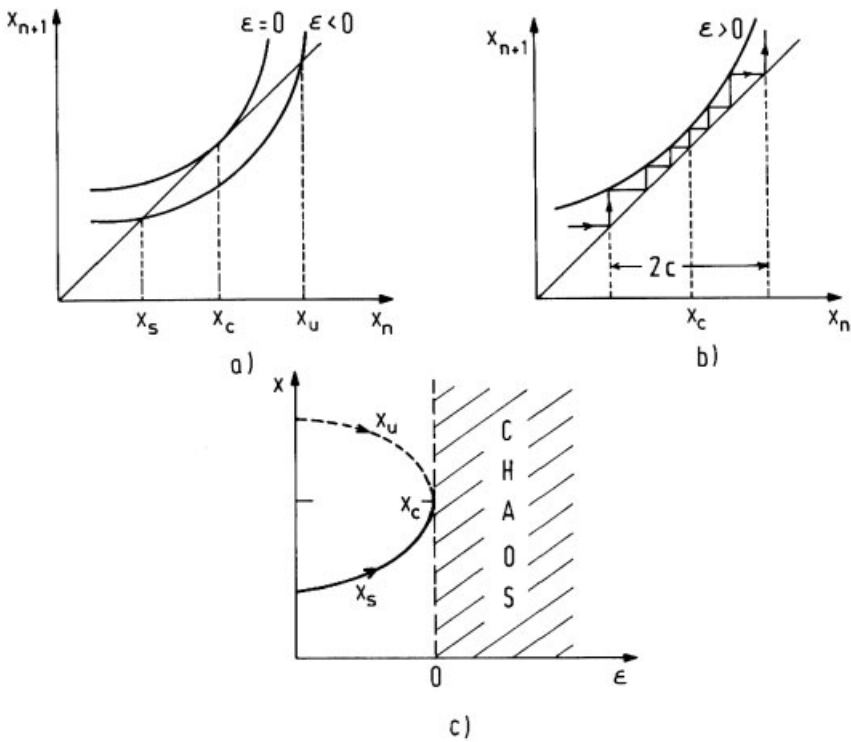


Figure 50: Mechanism for type-I intermittency. a) Poincaré map for $\epsilon = r - r_c \leq 0$, b) Poincaré map for $\epsilon > 0$ and motion of the trajectory, (note that the “ghost of the fixed point” x_c attracts trajectories on the left hand side and repels them on the right hand side), c) inverse tangent bifurcation.

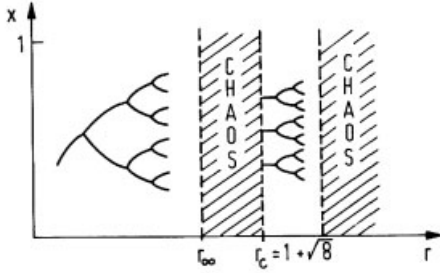


Figure 51: Window with period three in the chaotic regime.

After the trajectory has left the channel, the motion becomes chaotic until reinjection into the vicinity of x_c starts a new regular phase. The theory of Pomeau and Manneville explains only the laminar motion but gives no information about the mechanism which generates chaos. Another example for type-I intermittency appears in the logistic map

$$x_{n+1} = f(x_n) = rx_n(1 - x_n). \quad (5.2)$$

Numerically, it is found that for $r_c = 1 + \sqrt{8}$ this map exhibits a cycle of period three with subsequent bifurcations, i. e., there is a window in the chaotic regime as shown schematically in Fig. 51. The iterates for r -values larger and smaller than r_c are shown in Fig. 52. There is a regular cycle of period three slightly above r_c ; but below r_c laminar regions occur interrupted by chaos.

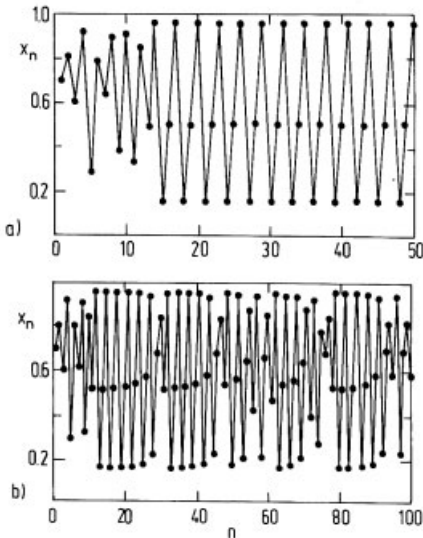


Figure 52: Iterates of the logistic map starting from $x = 0.7$; a) in the stable three-cycle region $r_c - r = -0.02$; b) in the intermittent region $r_c - r = 0.002$. (After Hirsch *et al.* 1981.)

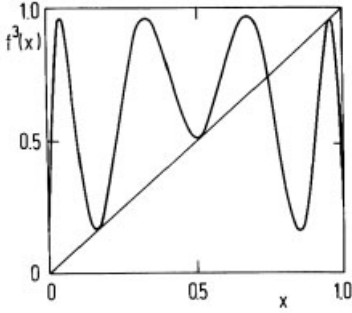


Figure 53: The threefold iterated map $f_r^3(x)$ for $r = r_c$

An explanation of this peculiar behavior follows from Fig. 53, which shows the third iterate of $f_r(x)$ at $r = r_c$. There are three fixed points that become unstable for $r < r_c$ and lead to intermittency of type I. It should be noted that inverse tangent bifurcations provide (in contrast to pitchfork bifurcations in which the number of fixed points is doubled) the only mechanism by which an uneven number of fixed points can be generated in the logistic map.

5.1.2 Length of the Laminar Region

As the next step, we calculate the average length $\langle l \rangle$ of a laminar region (as a function of the distance $\varepsilon = r - r_c$ from the critical point) for the logistic map. It will become clear from our derivation that the result for $\langle l \rangle(\varepsilon)$ is not confined to this special map but holds for any Poincaré map that leads to type-I intermittency.

Expanding $f_r^3(x)$ around the points x_c and r_c that are determined by

$$\frac{d}{dx} f_{r_c}^3(x_c) = 1, \quad f_{r_c}^3(x_c) = x_c \quad (5.3)$$

we obtain

$$f_r^3(x) = f_r^3[x_c + (x - x_c)] = x_c + (x - x_c) + a_c(x - x_c)^2 + b_c(r - r_c) \quad (5.4)$$

where

$$2a_c \equiv \left. \frac{d^2 f_r^3}{dx^2} \right|_{x_c, r_c} \quad b_c \equiv \left. \frac{df_r^3}{dr} \right|_{x_c, r_c} \quad (5.5)$$

(A similar equation holds for all three fixed points of $f_r^3(x)$, but we choose the middle point for convenience as the result is independent of the constants).

With $y \equiv (x - x_c)/b_c$ and $a_c \equiv a_c \cdot b_c > 0$ the recursion for the map

$$x_{n+1} = f_r^3(x_n) \quad (5.6)$$

transforms via (5.4) in the vicinity of x_c into

$$y_{n+1} = y_n + ay_n^2 + \varepsilon; \quad \varepsilon = r - r_c. \quad (5.7)$$

(A similar map is obtained if the Poincaré map in Fig. 49 is expanded around the point of tangency). The laminar regions are now defined by the requirement that subsequent iterates change only very little; i. e., their distance to x_c should be smaller than a threshold value c :

$$|y_n| < c \ll 1. \quad (5.8)$$

In this region we can therefore safely replace the difference equation (5.7) by the differential equation,

$$\frac{dy}{dl} = ay^2 + \varepsilon \quad (5.9)$$

(l counts the iterations in the laminar region) which after integration yields

$$l(y_{\text{out}}, y_{\text{in}}) = \frac{1}{\sqrt{a\varepsilon}} \left[\arctan \left[\frac{y_{\text{out}}}{\sqrt{\varepsilon/a}} \right] - \arctan \left[\frac{y_{\text{in}}}{\sqrt{\varepsilon/a}} \right] \right] \quad (5.10)$$

To find the average length $\langle l \rangle$ of a laminar region, we assume that after having left the laminar region at $y_{\text{out}} = c$, the point becomes, after some irregular bursts, reinjected to $|y| < c$ at y_{in} , with a probability function $P(y_{\text{in}})$, which is symmetric about x_c , i. e., $P(y_{\text{in}}) = P(-y_{\text{in}})$.

This yields

$$\langle l \rangle = \int_{-c}^c dy_{\text{in}} P(y_{\text{in}}) l(c, y_{\text{in}}) = \frac{1}{\sqrt{a\varepsilon}} \arctan \left[\frac{c}{\sqrt{\varepsilon/a}} \right]. \quad (5.11)$$

For $c/\sqrt{\varepsilon/a} \gg 1$, the average length $\langle l \rangle$ varies as

$$\langle l \rangle \propto \varepsilon^{-1/2}. \quad (5.12)$$

This characteristic variation was first derived by Pomeau and Manneville (1980) and is valid numerically for the logistic map as shown in Fig. 54.

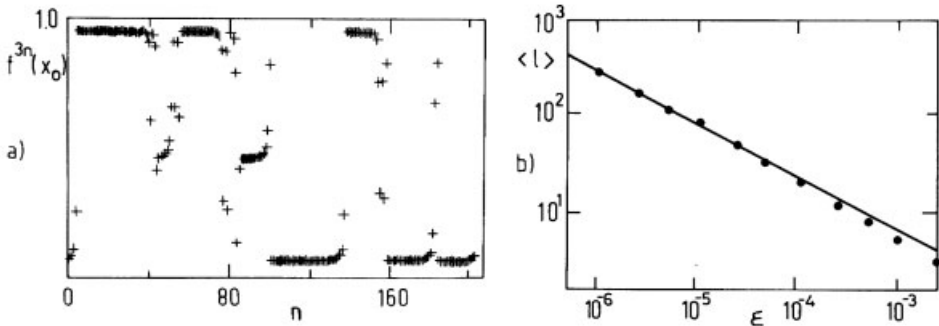


Figure 54: a) Sequence of third iterates $f_r^{3n}(x_0)$ for $r_c - r = 0.0001$ showing regions of laminar behavior interrupted by intermittent irregularities; b) the points show $\langle l \rangle$ versus ε for $c = 10^{-2}$, and the line is the asymptotic limit $\langle l \rangle = (\pi/2)(\varepsilon a)^{-1/2}$. (After Hirsch *et al.*, 1981.)

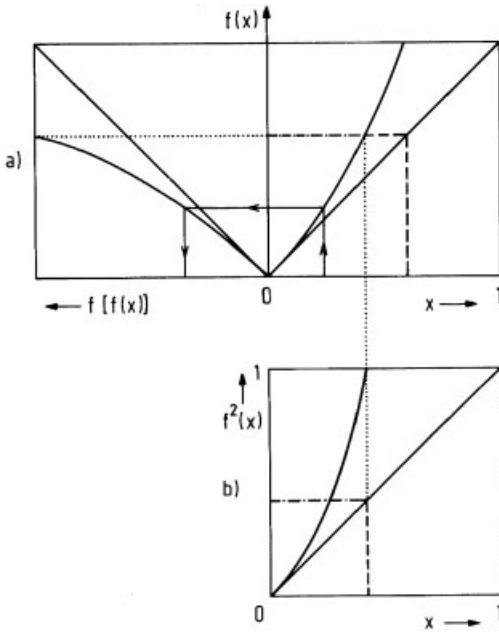


Figure 55: $f(x)$ and $f^2(x)$ vs. x for $x \geq 0$. a) The second iterate is constructed by plotting, in addition to b) the square which contains $f(x)$, the same square rotated through 90° . The arrows indicate how $f[f(x)]$ is obtained. b) The second iterate $f^2(x)$ looks similar to the original $f(x)$ in the dotted square.

5.2 Renormalization-Group Treatment of Intermittency

The intermittency phenomenon has also been investigated by the renormalization-group method using the doubling operator which we encountered previously for the Feigenbaum route. The idea is as follows: One considers a generalization $f(x)$ of the map (5.7) for $\varepsilon = 0$ to arbitrary exponents $z > 1$ which for $x \rightarrow 0$ has the form

$$f(x \rightarrow 0) = x + u|x| . \tag{5.13}$$

Its second iterate $f^2(x)$ shows (because of the linear term in x), after proper rescaling, the same asymptotic behavior (see Fig. 55). This is reminiscent of Fig. 29 for the logistic map. It could, therefore, be asked whether repeated application of the doubling operator T to a function of type (5.13) could also lead to a fixed point $f^*(x)$ of T :

$$Tf^*(x) = \alpha f^* \left[f^* \left(\frac{x}{\alpha} \right) \right] = f^*(x) \tag{5.14}$$

but with the boundary conditions (5.13), i. e., $f^*(0) = 0$ and $f^{*l}(0) = 1$ instead of $f^*(0) = 1$ and $f^{*l}(0) = 0$ for the Feigenbaum bifurcations.

It has been shown by Hu and Rudnick (1982) that together with the new boundary condition (5.13) the fixed-point equation (5.14), which is characteristic for intermittency, can be solved exactly.

Here, the trick is to write the recursion relation

$$x' = f(x) \quad (5.15)$$

in implicit form

$$G(x') = G(x) - a \quad (5.16)$$

i. e.,

$$x'(x) = G^{-1}[G(x) - a] = f(x) \quad (5.17)$$

where a is a free parameter. The fixed-point equation

$$\alpha f^*[f^*(x)] = f^*(\alpha x) \quad (5.18)$$

then becomes

$$\alpha x''(x) = x'(\alpha x) \quad (5.19)$$

or by operating on this with G :

$$G(\alpha x'') = G[x'(\alpha x)] = G(\alpha x) - a. \quad (5.20)$$

Next, eq. (5.16) is used to obtain

$$G(x'') = G(x') - a = G(x) - 2a \quad (5.21)$$

i. e.,

$$\frac{1}{2}G(x'') = \frac{1}{2}G(x) - a. \quad (5.22)$$

Comparison of (5.20) and (5.22) indicates that to solve the fixed-point equation, G must have the property

$$\frac{1}{2}G^*(x) = G^*(\alpha x). \quad (5.23)$$

The simple choice $G^*(x) = |x|^{-(z-1)}$ with $\alpha = 2^{\frac{1}{z-1}}$ yields the desired result.

The fixed-point function therefore becomes

$$f^*(x) = G^{*-1}[G^*(x) - a] = [|x|^{-(z-1)} - a]^{-1/(z-1)} \quad (5.24)$$

which for $a = (z-1)u$ fulfils boundary condition (5.13). This derivation shows that the fixed-point map for intermittency is mathematically related to a translation $G(x') = G(x) - a$; however, a simple physical explanation for this connection is not clear.

It is of course enough to find the fixed-point function $f^*(x)$ but one wants to classify the perturbations to f^* according to their relevance (see, e. g., Table 4). We investigate, therefore, how the doubling transformation T acts (to linear order in ε) on a function

$$f_\varepsilon(x) = f^*(x) + \varepsilon h_\lambda(x) \quad \text{for } \varepsilon \ll 1. \quad (5.25)$$

Using the definition (5.14) for T we find:

$$\begin{aligned} T f_\varepsilon &= \alpha f_\varepsilon \left[f_\varepsilon \left(\frac{x}{\alpha} \right) \right] \\ &= \alpha f^* \left[f^* \left(\frac{x}{\alpha} \right) + \varepsilon h_\lambda \left(\frac{x}{\alpha} \right) \right] + \varepsilon \alpha h_\lambda \left[f^* \left(\frac{x}{\alpha} \right) + \varepsilon h_\lambda \left(\frac{x}{\alpha} \right) \right] \\ &= \alpha f^* \left[f^* \left(\frac{x}{\alpha} \right) \right] + \varepsilon \alpha \left\{ f^{*'} \left[f^* \left(\frac{x}{\alpha} \right) \right] h_\lambda \left(\frac{x}{\alpha} \right) + h_\lambda \left[f^* \left(\frac{x}{\alpha} \right) \right] \right\} + O(\varepsilon^2) \\ &= f^*(x) + \lambda \varepsilon h_\lambda(x) + O(\varepsilon^2). \end{aligned} \quad (5.26)$$

The last equation holds only if $h_\lambda(x)$ is an eigenfunction, with the eigenvalue λ , of the linearized doubling operator L_{f^*} :

$$L_{f^*}[h_\lambda(x)] \equiv \alpha\{f^{*'}[f^*(x)]h_\lambda(x) + h_\lambda[f^*(x)]\} = \lambda h_\lambda(\alpha x) \quad (5.27)$$

by analog to eq. (4.49) for the Feigenbaum route.

We now show that the method used above (to find the fixed-point function f^*) allows us also to find the spectrum of eigenvalues λ and the corresponding eigenfunctions h_λ . First we write $f_\varepsilon(x)$ in implicit form using eq. (5.17):

$$f_\varepsilon(x) = f^*(x) + \varepsilon h_\lambda(x) = x' = G_\varepsilon^{-1}[G_\varepsilon(x) - a]. \quad (5.28)$$

If we expand

$$G_\varepsilon(x) = G^*(x) + \varepsilon H_\lambda(x) \quad (5.29)$$

then $h_\lambda(x)$ can be expressed in terms of $H_\lambda(x)$ (and vice versa) by comparing the factors linear in ε on both sides of (5.28).

Next we consider the second iterate,

$$x''(x) = f_\varepsilon[f_\varepsilon(x)] \quad (5.30)$$

and apply G_ε to this. This yields

$$G_\varepsilon(x'') = G_\varepsilon(x') - a = G_\varepsilon(x) - 2a \quad (5.31)$$

or more explicitly:

$$G^*(x'') + \varepsilon H_\lambda(x'') = G^*(x) + \varepsilon H_\lambda(x) - 2a. \quad (5.32)$$

Because $G^*(x)$ has the form of a simple power of x we try a similar ansatz for $H_\lambda(x)$:

$$H_\lambda(x) = |x|^{-p}. \quad (5.33)$$

Using the property (5.23) of $G^*(x)$, (5.32) then becomes

$$G^*(\alpha x'') + \lambda \varepsilon H_\lambda(\alpha x'') = G^*(\alpha x) + \lambda \varepsilon H_\lambda(\alpha x) - a \quad (5.34)$$

or

$$G_{\lambda\varepsilon}(\alpha x'') = G_{\lambda\varepsilon}(\alpha x) - a \quad (5.35)$$

$$\rightarrow \alpha x'' = G_{\lambda\varepsilon}^{-1}[G_{\lambda\varepsilon}(\alpha x) - a] \quad (5.36)$$

where

$$\lambda = 2^{\frac{p+1-z}{z-1}}. \quad (5.37)$$

With (5.28) this translates into

$$\alpha f_\varepsilon[f_\varepsilon(x)] = f_{\lambda\varepsilon}(\alpha x) = f^*(\alpha x) + \lambda \varepsilon h_\lambda(\alpha x). \quad (5.38)$$

By comparing this result with eq. (5.26) we see that λ is indeed the eigenvalue of h_λ , which is determined by

$$f^*(\alpha x) + \lambda \varepsilon h_\lambda(\alpha x) = G_{\lambda\varepsilon}^{-1}[G_{\lambda\varepsilon}(\alpha x) - a]. \quad (5.39)$$

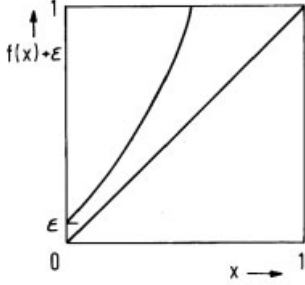


Figure 56: Shift ε from tangency.

Solving (5.39) to order ε one obtains

$$h_\lambda(x) = \frac{1}{up} \left[|x|^{-(z-1)} - u(z-1) \right]^{-\frac{z}{z-1}} \cdot \left\{ |x|^{-p} - \left[|x|^{-(z-1)} - u(z-1) \right]^{-\frac{p}{z-1}} \right\} \quad (5.40)$$

eqs. (5.37) and (5.40) represent the main results of this section. They provide the information as to how T acts (to linear order in the deviation $f - f^*$) on a function f that obeys the boundary condition (5.13), because we obtain by expanding $f(x) - f^*(x)$ into $h_\lambda(x)$:

$$\begin{aligned} T^n f(x) &= T^n(f^*(x) + f(x) - f^*(x)) \\ &= T^n(f^*(x) + \sum_\lambda c_\lambda h_\lambda(x)) = f^*(x) + \sum_\lambda \lambda^n c_\lambda h_\lambda(x) \end{aligned} \quad (5.41)$$

The intermittency route therefore represents – in contrast to the Feigenbaum route – one of the rare examples where the linearized renormalization-group equations can be solved exactly.

As an application, we now calculate the dependence of the duration $\langle l \rangle$ of a laminar region on the shift ε of the map from tangency shown in Fig. 56.

The eigenfunction h_λ in eq. (5.40) has been normalized, so that its lowest order term in x is $|x|^{2z-1-p}$. We therefore see that a constant shift ε from tangency corresponds to a relevant perturbation with $p = 2z - 1$. The eigenvalue λ_ε , that corresponds to this is

$$\lambda_\varepsilon = 2^{\frac{z}{z-1}} \quad (5.42)$$

With this information we can determine $\langle l \rangle(\varepsilon)$ by a simple scaling procedure.

Because $\langle l \rangle$ is related to the number of iterates of x_0 , and $f^2(x) = f[f(x)]$ only requires half as many steps as $f(x)$, we arrive at the scaling relation

$$\langle l \rangle [Tf(x_0)] = \frac{1}{2} \langle l \rangle [f(x_0)] . \quad (5.43)$$

Using (5.26) this becomes after many iterations

$$\langle l \rangle [f(x_0)] = 2^n \langle l \rangle [T^n f(x_0)] = f^*(x_0) + \varepsilon \lambda_\varepsilon^n h_\lambda(x_0)$$

from which for $\varepsilon \lambda_\varepsilon^n = 1$ we obtain with (5.42):

$$\langle l \rangle \propto \varepsilon^{-v} \quad \text{with} \quad v = \frac{z-1}{z} . \quad (5.44)$$

For $z = 2$ this agrees with our previous result (5.12). One can show with the same method that a perturbation which is linear in x , i. e.,

$$f(x) = f^*(x) + \varepsilon x \quad (5.45)$$

leads to

$$\langle l \rangle \propto \varepsilon^{-1} \quad (5.46)$$

and perturbations εx^m with $m > z$ are irrelevant.

Finally, we mention that the effect of external noise with amplitude σ on intermittency has been treated by Hirsch, Nauenberg, and Scalapino (1982) with the net result that $\langle l \rangle$ scales like

$$\langle l \rangle = \varepsilon^{-\nu} g(\sigma^\mu \varepsilon) \quad \text{with} \quad \mu = \frac{z-1}{z+1} \quad (5.47)$$

where g is a universal function.

5.3 Intermittency and 1/f-Noise

It has been observed experimentally that the power spectra S_f of a large variety of physical systems (see Table 6) diverge at low frequencies with a power law $1/f^\delta$ ($0.8 < \delta < 1.4$). This phenomenon is called 1/f-noise. Despite considerable theoretical efforts, a general theory encompassing $1/f^\delta$ -divergencies in several experiments is still lacking.

In the following, we show that a class of maps which generates intermittent signals also displays $1/f^\delta$ -noise, and we link the exponent δ to the universal properties of the map using the renormalization-group approach. Although the intermittency mechanism for 1/f-noise is – as we shall demonstrate below – well verified numerically for maps, it still remains unresolved, whether it also provides an explanation for the experiments shown in Table 6. (We do not think that the intermittency mechanism which is very sensitive to external perturbations could explain the robust 1/f-noise found in resistors, cf. Fig. 57. But there is a good chance to find this mechanism in chemical reactions and in the Bénard convection; see Manneville (1980), and Dubois *et al.* (1983).)

Table 6: Systems showing 1/f-noise.

System	Signal	System	Signal
Carbon film	Current	Zener diode	Current
Metal film	Current	Bipolar transistor	Current
Semiconductor	Current	Field effect transistor	Current
Metal contact	Current	Thermocell	Thermovoltage
Semiconductor contact	Current	Electrolytic concentration cell	Voltage
Ionic solution contact	Current	Quartz oscillator	Frequency
Superconductor	Flux	Earth (5 days mean of rotation)	Frequency
Flow vacuum tube	Current	Sound and speech sources	Loudness
Junction diode	Current	Nerve membrane	Potential
Schottky diode	Current	Highway traffic	Current

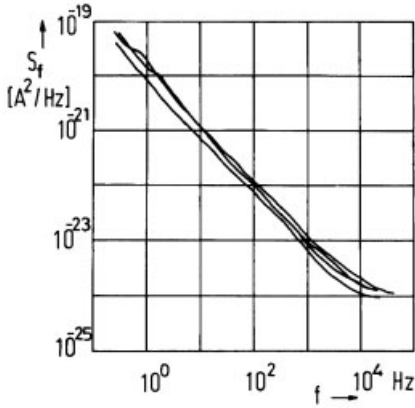


Figure 57: Example for $1/f$ -noise in the current of a bipolar transistor (after D. Wolf, 1978).

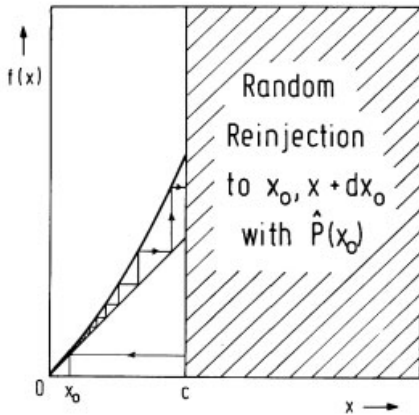


Figure 58: The map $f(x)$ has the limiting behavior $f(x \rightarrow 0) = x + ux^2$ and is arbitrary beyond $x = c$ with the only requirement that this part of the map produces random reinjection into the region $0 \leq x_0 \leq c$ with a probability $\hat{P}(x_0)$.

We want to calculate the power spectrum S_f for the map

$$X_{n+1} = f(x_n) \quad (5.48)$$

in Fig. 58 where $x_n \geq 0$. In other words, we only use that part of the map where the “ghost of the fixed point” is repulsive (compare Figs. 50 and 65). Therefore our mechanism for $1/f$ -noise only works for type-III (and type-II) intermittency (Ben-Mizrachi *et al.*, 1985). It is useful to express S_f via the correlation function $C(m)$:

$$S_f \propto \lim_{N \rightarrow \infty} \frac{1}{N} \sum_{m=0}^N \cos(2\pi mf) C(m) \quad (5.49)$$

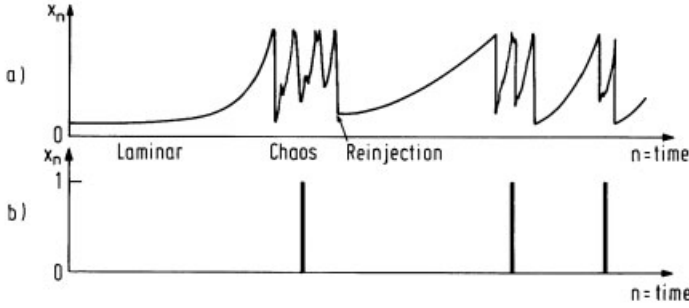


Figure 59: a) The iterates $x_n = f^n(x_0)$ as a function of time, showing laminar and chaotic behavior according to whether the trajectory is in $[0, c]$ or in the chaotic region; b) the idealized signal.

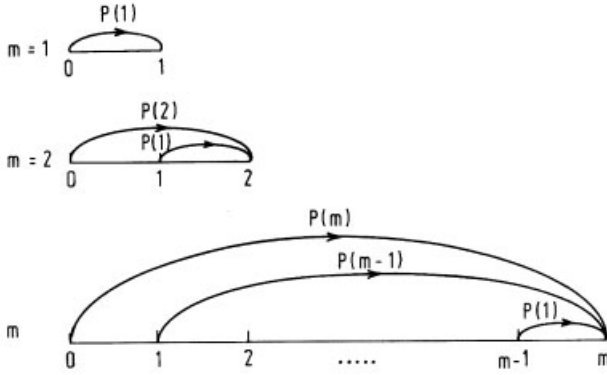


Figure 60: The probability of finding a signal at m , assuming there was a signal at zero, can be expressed by $P(l)$.

where

$$C(m) = \lim_{N \rightarrow \infty} \frac{1}{N} \sum_{n=0}^N x_{n+m} x_n . \tag{5.50}$$

(This result follows by Fourier transformation from the definitions in eqs. (5.49) and (5.50).) To evaluate $C(m)$, we idealize the signal as shown in Fig. 59b, i.e., we assume that x_n is practically zero in the laminar regions and replace the short burst regions by lines of height one. $C(m)$ then becomes proportional to the conditional probability of finding a signal at time m , given that there occurred a signal at time zero.

Next, we express $C(m)$ in terms of the probability $P(l)$ of finding an intermission of length l , which we shall calculate below in a universal way. Figure 60 shows that

$$\begin{aligned} C(1) &= P(1) \\ C(2) &= P(2) + P(1)^2 = P(2) + C(1)P(1) \\ C(m) &= P(m) + C(1)P(m-1) + \dots + C(m-1)P(1) \end{aligned} \tag{5.51}$$

which can be written as

$$C(m) = \sum_{k=0}^m C(m-k)P(k) + \delta_{m,0} \quad (5.52)$$

if we define $P(0) = 0, C(0) = 1$.

We now use eq. (5.24) to calculate the probability $P(l)$ of finding a laminar region of length l for (5.48).

$P(l)$ is related to the probability $\hat{P}(x_0)$ via

$$\hat{P}(x_0) dx_0 = \hat{P}[x_0(l)] \left| \frac{dx_0}{dl} \right| dl \equiv P(l) dl \quad (5.53)$$

$$\rightarrow P(l) = \hat{P}[x_0(l)] \left| \frac{dx_0}{dl} \right| \quad (5.54)$$

and since it follows from Fig. 58 that

$$f^l(x_0) = c \rightarrow x_0 = x_0(l) \quad (5.55)$$

$x_0(l)$ can be calculated by using the doubling operator. In the absence of relevant perturbations (which will be discussed later), we have

$$T^n f(x_0) = \alpha^n f^{2^n}(x_0/\alpha^n) \approx f^*(x_0), \quad \text{for } n \gg 1 \quad (5.56)$$

i. e., the function is driven to the fixed point. This yields

$$f^{2^n}(x_0) = \alpha^{-n} f^*(\alpha^n x_0). \quad (5.57)$$

Here both $\alpha = 2^{\frac{1}{z-1}}$ and $f^*(x) = |x|[1 - (z-1)u|x|^{z-1}]^{-\frac{1}{z-1}}$ depend only on z which determines the universality class. If we use (5.57) in (5.55), we obtain for $l = 2^n$:

$$x_0(l) \propto l^{\frac{1}{z-1}} \quad (5.58)$$

and with (5.54) this yields the desired universal result for $P(l)$,

$$P(l) \propto \hat{P}(0) l^{-\frac{z}{z-1}}. \quad (5.59)$$

Here we assumed that $\hat{P}(x_0)$ varies only slowly with x_0 , i. e., $\hat{P}(x_0) \propto l^{-\frac{1}{z-1}} \rightarrow 0 \approx \hat{P}(0)$, for $l \gg 1$.

We pass on to continuous time variables since we are only interested in the long-time limit, and solve (5.52) by Laplace transformation using the convolution theorem. This yields

$$C_s = \frac{1}{1-P_s} \quad \text{with} \quad g_s \equiv \int_0^\infty dt e^{-st} g(t) \quad (5.60)$$

from which we obtain S_f as

$$S_f = \int_0^\infty dt \cos(2\pi ft) C(t) = \frac{1}{2} [C_{s \rightarrow 2\pi i f} - C_{s \rightarrow -2\pi i f}]. \quad (5.61)$$

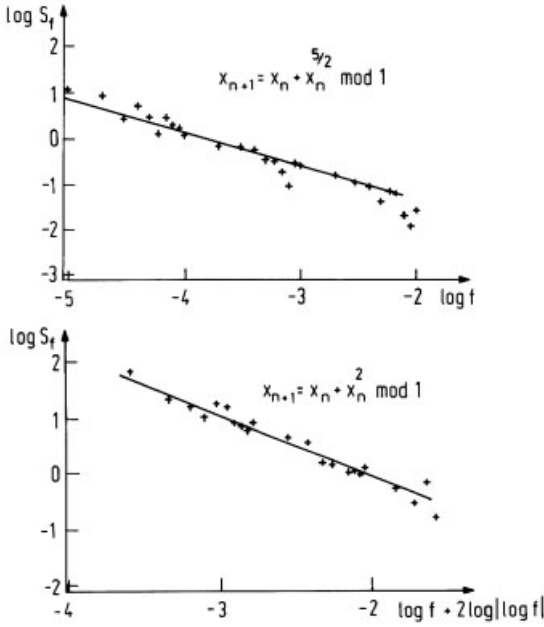


Figure 61: Numerically determined power spectra for $z = 5/2$ and $z = 2$ compared to eq. (5.62) (after Procaccia and Schuster, 1983).

Substitution of $P(l)$ from (5.59) into (5.60) and (5.61) yields

$$\lim_{f \rightarrow 0} S_f \propto \begin{cases} f^{-\frac{2z-5}{z-1}} & z > 3 \\ \frac{|\log f|^2}{f^{1/2}} & z = 3 \\ f^{-\frac{1}{z-1}} & 2 < z < 3 \\ \frac{1}{f|\log f|^2} & z = 2 \\ f^{-\frac{2z-3}{z-1}} & \frac{3}{2} < z < 2 \\ |\log f| & z = \frac{3}{2} \\ \text{const.} & z < \frac{3}{2} \end{cases} \quad (5.62)$$

(The results for $z \geq 3$ are from Ben-Mizrachi *et al.*, 1985.)

Figure 61 shows that this result agrees reasonably well with the numerically determined power spectra of the map

$$x_{n+1} = x_n + x_n^z \text{ mod } 1 \quad (5.63)$$

for

$$z = \frac{5}{2} \quad \text{and} \quad z = 2. \quad (5.64)$$

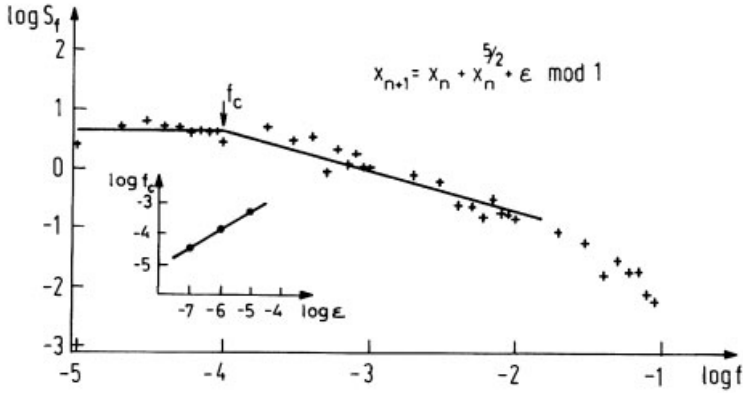


Figure 62: Power spectrum of the map $x_{n+1} = \epsilon + x_n + x_n^{5/2} \pmod 1$. The inset shows the scaling of f_c with ϵ as predicted in eq. (5.62) (after Procaccia and Schuster, 1983).

Let us now briefly discuss the effect of perturbations. The low frequency divergence of the power spectrum arises because arbitrarily long laminar regions [$P(l) \propto l^{-z/(z-1)}$] occur with finite probability in the (unperturbed) map in Fig. 58. But we also showed in Section 5.2 that in the presence of relevant perturbations (as, e. g., a shift ϵ from tangency) the average duration of an intermission becomes finite:

$$\langle l \rangle \sim \epsilon^{-\nu}. \quad (5.65)$$

This yields a cutoff

$$f_c \sim \langle l \rangle^{-1} \sim \epsilon^{\nu} \quad (5.66)$$

in the $1/f^\delta$ -behavior of S_f as shown in Fig. 62.

5.4 Experimental Observation of the Intermittency Route


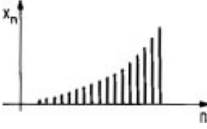
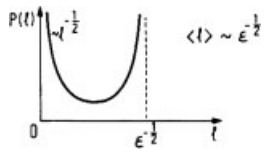

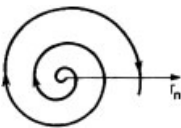
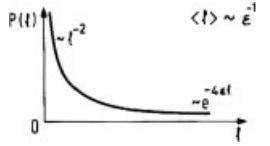

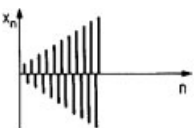
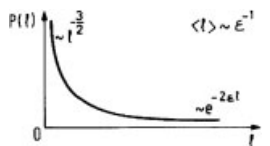
Table 7 summarizes some measurable characteristic properties of the intermittency route to chaos. The different types of intermittency can be distinguished by the form of the signal and by the distribution $P(l)$ of the laminar lengths. Below we present a derivation of $P(l)$ and describe two representative experiments in which type-I intermittency has been detected. Type-II intermittency has (to the best of our knowledge) not yet been found in a real experiment. This section closes with brief report on the first experimental observation of type-III intermittency.

5.4.1 Distribution of Laminar Lengths

We assume that the signal is randomly reinjected (with a probability $\hat{P}(x_0)$) into the laminar régime in such a way that we can use eq. (5.54):

$$P(l) = \hat{P}(x_0) \left| \frac{dx_0}{dl} \right|. \quad (5.67)$$

Table 7: Characteristic properties of different types of intermittency.

Type	Poincaré map	Laminar Signal	Distribution $P(l)$
I	 $x_{n+1} = x_n + x_n^2 + \epsilon$	 <p>increases monotonously</p>	 $\langle l \rangle \sim \epsilon^{-1/2}$
II	 $r_{n+1} = (1 + \epsilon)r_n + ur_n^3$ $\theta_{n+1} = \theta_n + \Omega$	 <p>spirals</p>	 $\langle l \rangle \sim \epsilon^{-1}$
III	 $r_{n+1} = -(1 + \epsilon)x_n - ux_n^3$	 <p>alternates</p>	 $\langle l \rangle \sim \epsilon^{-1}$

In order to obtain $x_0(l)$, we approximate, as in (5.9), the Poincaré map for type-I intermittency (see Table 4)

$$x_{n+1} = \epsilon + x_n + ux_n^2 \tag{5.68}$$

in the laminar region by the differential equation

$$\frac{dx}{dl} = \epsilon + ux^2 \tag{5.69}$$

This yields, by integration,

$$l = \frac{1}{\sqrt{\epsilon u}} \left[\arctan \left[\frac{c}{\sqrt{\epsilon u}} \right] - \arctan \left[\frac{x_0}{\sqrt{\epsilon u}} \right] \right] \tag{5.70}$$

where c is the maximum value of $x(l)$ in the laminar régime (see Fig. 58). $P(l)$ follows from eqs. (5.67) and (5.70):

$$P(l) = \frac{\epsilon}{2c} \left\{ 1 + \tan^2 \left[\arctan \left[\frac{c}{\sqrt{\epsilon u}} \right] \right] - l\sqrt{\epsilon u} \right\} \tag{5.71}$$

and

$$\langle l \rangle = \int_0^\infty dl P(l) l \sim \epsilon^{-1/2} \text{ for } \epsilon \rightarrow 0. \tag{5.72}$$

The distributions $P(l)$ for the two other types of intermittency are obtained in a similar way, with the net results

$$P(l) \sim \frac{\epsilon^2 e^{4\epsilon l}}{(e^{4\epsilon l} - 1)^2} \text{ for type II} \tag{5.73}$$

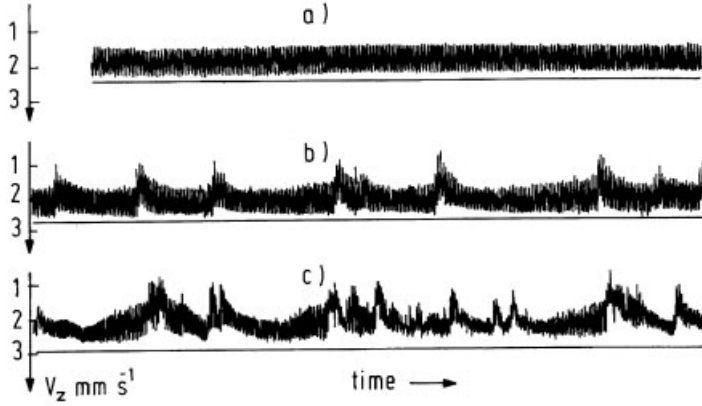


Figure 63: Intermittency for a Bénard experiment: The vertical velocity component measured in the middle of a Bénard cell changes with increasing Rayleigh number from periodic motion (a) via intermittent motion (b) to chaos (c) (after Berge *et al.*, 1980).

and

$$P(l) \sim \frac{\varepsilon^{3/2} e^{4\varepsilon l}}{(e^{4\varepsilon l} - 1)^{3/2}} \quad \text{for type III.} \quad (5.74)$$

For type-II intermittency eq. (5.67) has to be replaced by $P(l) = \hat{P}(r_0) |dr_0/dl|$ because the Poincaré map is two-dimensional.

5.4.2 Type-I Intermittency

Figure 63 shows the vertical velocity as a function of time for a Bénard experiment. The signal shows a behavior which is typical for type-I intermittency.

The nonlinear *RCL*-oscillator described on page 66 also displays the intermittency route. Type-I intermittency is indicated in Fig. 64 by the Poincaré map, the scaling behavior of the lengths of the laminar regions, and the maximum in $P(l)$ for $l > 0$.

5.4.3 Type-III Intermittency

Type-III intermittency has first been observed by M. Dubois, M. A. Rubio and P. Berge (1983) in Bénard convection in a small rectangular cell. They measured the local horizontal temperature gradient via the modulation of a light beam that was sent through the cell.

Figure 65 (on p. 88) shows the time dependence of the light intensity that is characteristic for type-III intermittency. The intermittency appears simultaneously with a period-doubling bifurcation. One observes the growth of a subharmonic amplitude together with a decrease in the fundamental amplitude. When the subharmonic amplitude reaches a high value, the signal loses its regularity, and turbulent bursts appear.

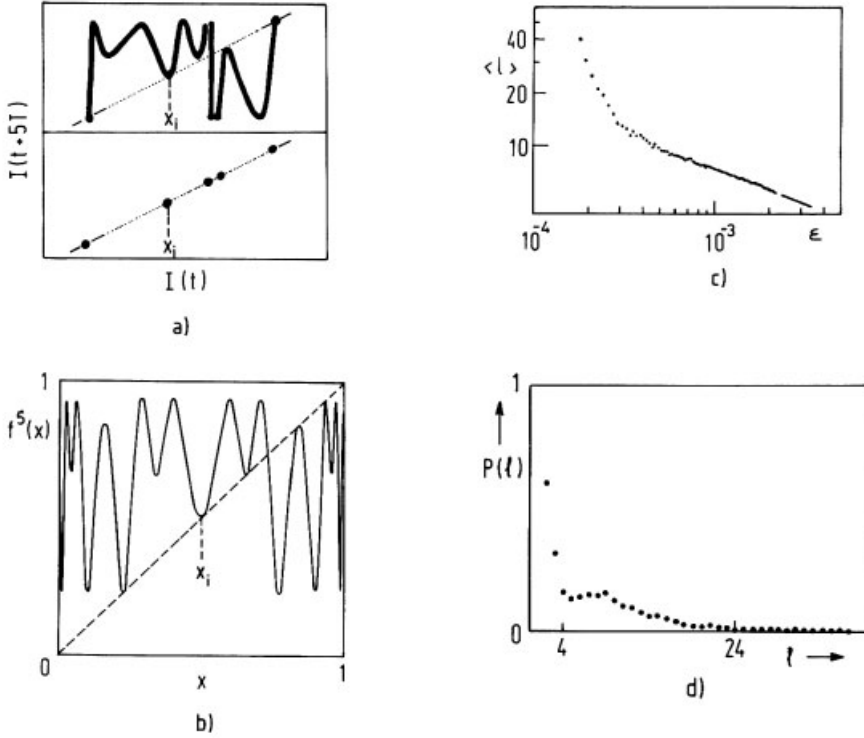


Figure 64: Intermittency in the nonlinear *RCL*-oscillator: a) $I(t+5T)$ versus $I(t)$ which corresponds to the fifth iterate of the logistic map at tangency which is shown in b). c) The measured averaged length for which the laminar regions scales like $\langle l \rangle \propto \epsilon^{-0.43}$ (where $\epsilon \sim V_0 - V_c$) is in reasonable agreement with the prediction of Manneville and Pomeau $\langle l \rangle \propto \epsilon^{-0.5}$. d) $P(l)$ vs. laminar lengths l (in units of $5T$) for $\epsilon = 2.5 \times 10^{-4}$. (After Jeffries and Perez, 1982.)

By plotting subsequent maxima I_n of both the subharmonic mode (even n , crosses) and the fundamental mode (odd n , squares), the Poincaré map shown in Fig. 65b is obtained. Its form can be described by

$$I_{n+2} = (1 + 2\epsilon)I_n + bI_n^3 \quad (5.75)$$

where b is a constant and $\epsilon \propto (R - R_c)$ measures the distance to the critical Rayleigh number R_c (which corresponds to the threshold of the intermittent behavior). Equation (5.75) can be derived from the map

$$I_{n+1} = f(I_n) = -(1 + \epsilon)I_n - uI_n^3 \quad (5.76)$$

with $b = u(2 + 4\epsilon)$. Its eigenvalue

$$\lambda = f'(0) = -(1 + \epsilon) \quad (5.77)$$

crosses the unit circle at -1 , which again signals type-III intermittency according to Table 5.

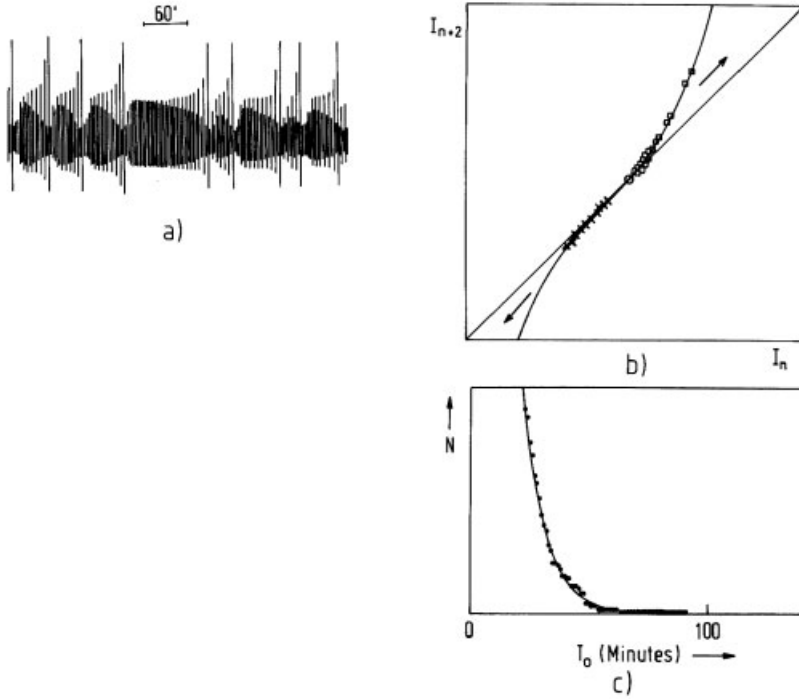


Figure 65: a) Time dependence of the light intensity which is roughly proportional to the local horizontal temperature gradient. b) Poincaré map I_{n+2} versus I_n constructed from the data in a) for $\varepsilon = 0.098$. The amplitudes of the light modulation in the turbulent bursts have not been drawn. Note that the “ghost of the fixed point” \circ is purely repulsive. c) Number N of laminar lengths with $l > T_0$, i. e., $N = \int_{T_0}^{\infty} P(l) dl$ versus T_0 . The experimental points agree with the line obtained (5.74) for $\varepsilon = 0.098$. (After Dubois *et al.*, 1983.)

6 Strange Attractors in Dissipative Dynamical Systems

In the first part of this chapter we show that nonlinear dissipative dynamical systems lead naturally to the concept of a strange attractor. In Section 6.2, the Kolmogorov entropy is introduced as the fundamental measure for chaotic motion. Section 6.3 deals with the problem of how much information about a strange attractor can be obtained from a measured random signal. We discuss the reconstruction of the trajectory in phase space from the measured time series of a single variable and introduce generalized dimensions and entropies. It is demonstrated how these quantities can be obtained from a measurement and how one can extract from them the distribution of singularities in the invariant measure that characterizes the static structure of a strange attractor and the fluctuation spectrum of the Kolmogorov entropy, which describes the dynamical evolution of the trajectory on the attractor. Finally we present, in the last section, a collection of pictures of strange attractors and fractal boundaries.

6.1 Introduction and Definition of Strange Attractors

In this section, we consider dissipative systems that can be described either by flows or maps. Let us begin with dissipative flows. These are described by a set of autonomous first-order differential equations,

$$\dot{\vec{x}} = \vec{F}(\vec{x}), \quad \vec{x} = (x_1, x_2, \dots, x_d) \quad (6.1)$$

and the term dissipative means that an arbitrary volume element V enclosed by some surface S in phase space $\{\vec{x}\}$ contracts. The surface S evolves by having each point on it follow an orbit generated by (6.1). This yields, by the divergence theorem,

$$\frac{dV}{dt} = \int_V d^d x \left(\sum_{i=1}^d \frac{\partial F_i}{\partial x_i} \right) \quad (6.2)$$

and dissipative systems are defined by $dV/dt < 0$.

An example of this kind of flow is given by the Lorenz model

$$\begin{aligned} \dot{X} &= -\sigma X + \sigma Y \\ \dot{Y} &= -XZ + rX - Y \\ \dot{Z} &= XY - bZ \end{aligned} \quad (6.3)$$

for which one finds via (6.2)

$$\frac{dV}{dt} = -(\sigma + 1 + b)V < 0; \quad (\sigma > 0, b > 0) \quad (6.4)$$

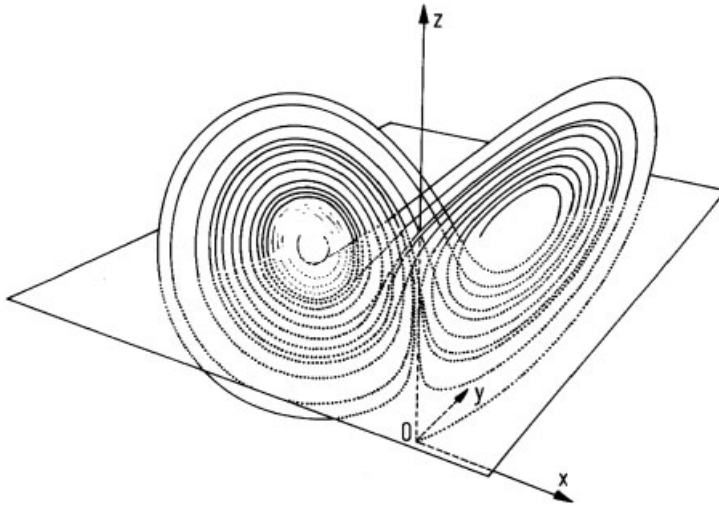


Figure 66: The Lorenz attractor, after a computer calculation by Lanford (1977).

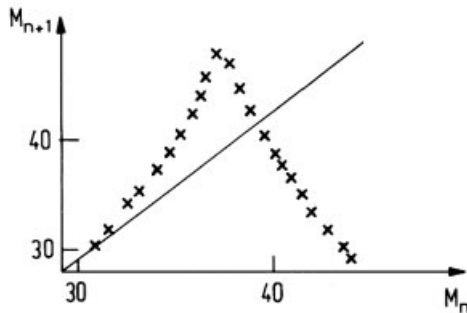


Figure 67: Successive maxima of Z of the Lorenz attractor (after E. N. Lorenz, 1963).

i. e., the volume element contracts exponentially in time:

$$V(t) = V(0) e^{-(\sigma+1+b)t} \quad (6.5)$$

If, on the other hand, the trajectory generated by the equations of the Lorenz model for $r = 28$, $\sigma = 10$, $b = 8/3$ is considered (see Fig. 66), one finds that it is: a) attracted to a bounded region in phase space; b) the motion is erratic, i. e., the trajectory makes one loop to the right, then a few loops to the left, then to the right, etc.; and c) there is a sensitive dependence of the trajectory on the initial conditions, i. e., if instead of $(0, 0.01, 0)$ an adjacent initial condition is taken, the new solution soon deviates from the old, and the number of loops is different. Figure 67 shows a plot of the n th maximum M_n of Z versus M_{n+1} . The resulting map is approximately triangular, which corresponds, according to the material discussed in Chapter 3, to a chaotic sequence of M_n s.

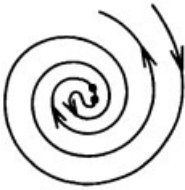


Figure 68: Self-trapping of a flow line in a bounded region of the plane. Exponential separation of points is at variance with continuity (note the opposing arrows).

Summarizing: The trajectory depends sensitively on the initial conditions; it is chaotic; it is attracted to a bounded region in phase space; and [according to eq. (6.4)] the volume of this region contracts to zero. This means that the flow of the three-dimensional Lorenz system generates a set of points whose dimension is less than three; i. e., its volume in three-dimensional space is zero. At first sight, one might think of the next lower integer dimension, two. However, this is forbidden by the *Poincaré—Bendixson* theorem which states that there is no chaotic flow in a bounded region in two-dimensional space. We refer, e. g., to the monograph by Hirsch and Smale (1965) for a rigorous proof of this theorem. However, Fig. 68 makes it plausible that both the continuity of the flow lines and the fact that a line divides a plane into two parts restrict the trajectories in two dimensions so strongly that the only possible attractors for a bounded region are limit cycles or fixed points. The solution to this problem is that the set of points to which the trajectory in the Lorenz system is attracted, the so-called Lorenz attractor, has a Hausdorff dimension which is noninteger and lies between two and three (the precise value is $D = 2.06$). This leads, in a natural way, to the concept of a strange attractor which appears in a large variety of physical, nonlinear systems.

A *strange attractor* has the following properties (a more formal definition can be found in the review articles by Eckmann and Ruelle, 1985):

- a) It is an attractor, i. e., a bounded region of phase space $\{\vec{x}\}$ to which all sufficiently close trajectories from the so-called basin of attraction are attracted asymptotically for long enough times. We note that the basin of attraction can have a very complicated structure (see the pictures in Section 6.4). Furthermore, the attractor itself should be indecomposable, i. e., the trajectory should visit every point on the attractor in the course of time. A collection of isolated fixed points is no single attractor.
- b) The property which makes the attractor strange is the sensitive dependence on the initial conditions, i. e., despite the contraction in volume, lengths need not shrink in all directions, and *points, which are arbitrarily close initially, become exponentially separated at the attractor for sufficiently long times*. This leads to a positive Kolmogorov entropy, as we shall see in the next section.

All strange attractors that have been found up to now in dissipative systems have fractal Hausdorff dimensions. Since there exists no generally accepted formal definition of a strange attractor (Ruelle, 1980; Mandelbrot, 1982), it is not yet clear whether a fractal Hausdorff dimension follows already from a)–b) or should be additionally required for a strange attractor. A strange attractor arises typically when the flow contracts the volume element in some directions, but stretches it along the others. To remain confined to a bounded domain, the volume

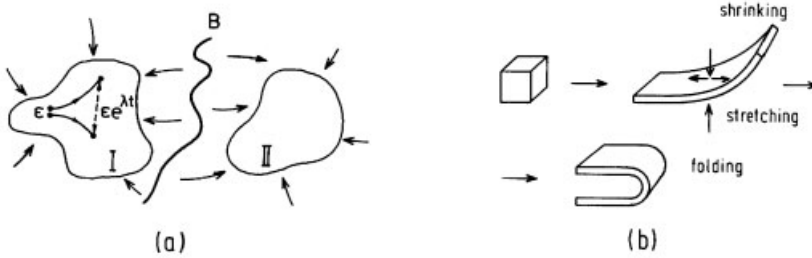


Figure 69: a) Two strange attractors I and II with different basins of attraction separated by a boundary B . b) Deformation of a volume element on a strange attractor with increasing time. This leads to the foliated fractal structure shown in Fig. 91c.

element is folded at the same time. By analogy to the broken linear maps in Chapter 3, this stretching and backfolding process produces a chaotic motion of the trajectory at the strange attractor (see also Fig. 69).

Because the definition given above describes the properties of a set of points, the concept of a strange attractor is not confined to flows, and dissipative maps can also generate strange attractors. A map

$$\vec{x}(n+1) = \vec{G}[\vec{x}(n)]; \quad \vec{x}_1(n) = [x_1(n), \dots, x_d(n)] \quad (6.6a)$$

is called dissipative if it leads to a contraction of volume in phase space, i. e., if the absolute value of its Jacobian J , by which a volume element is multiplied after each iteration, is smaller than unity:

$$|J| = \left| \det \left(\frac{\partial G_i}{\partial x_j} \right) \right| < 1. \quad (6.6b)$$

The Poincaré—Bendixson theorem that restricts the dimension of strange attractors generated by flows to values larger than two does not hold for maps. This is because maps generate discrete points and the restrictions imposed by the continuity of the flow are lifted. Dissipative maps can therefore lead to strange attractors that also have dimensions smaller than two. Let us consider two illustrative examples which, because of their lower dimensionality, are easier to visualize than the Lorenz attractor.

6.1.1 Baker's Transformation

Figure 70 shows the usual baker's transformation, which is an area-preserving map (reminiscent of a baker kneading dough), and the non-area preserving, dissipative baker's transformation. The mathematical expression for the latter is

$$x_{n+1} = 2x_n \bmod 1 \quad (6.7a)$$

$$y_{n+1} = \begin{cases} ay_n & \text{for } 0 \leq x_n < \frac{1}{2} \\ \frac{1}{2} + ay_n & \text{for } \frac{1}{2} \leq x_n \leq 1 \end{cases} \quad (6.7b)$$

where $a < 1/2$.

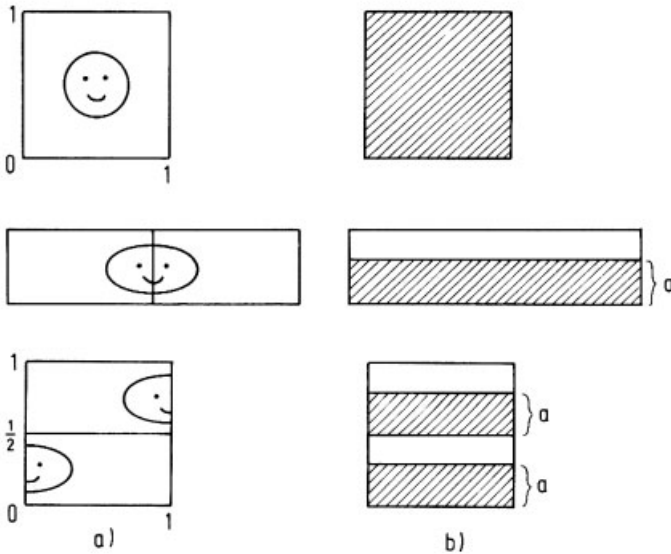


Figure 70: a) Baker's transformation; b) dissipative baker's transformation.

The first equation (6.7a) is our old friend from Chapter 3: the transformation σ which leads to the Bernoulli shift. It has a Liapunov exponent (in the x -direction), $\lambda_x = \log 2 > 0$, which leads to the sensitive dependence on the initial conditions, and makes the object resulting from repeated applications of this map to the unit square, a strange attractor. The attractor is an infinite sequence of horizontal lines, and its basin of attraction consists of all points within the unit square. The Liapunov exponent in the y -direction is $\lambda_y = \log a < 0$, and lengths are contracted in this direction such that the net result (of stretching in the x - and shrinking in the y -direction) is a volume contraction, as required for a dissipative map.

The Hausdorff dimension D_B of this strange attractor can be calculated as follows: In the x -direction the attractor is simply one-dimensional (as the map $\sigma(x)$ of Chapter 3). The Hausdorff dimension in the y -direction follows from its definition

$$\lim_{l \rightarrow 0} N(l) \propto l^{-D_y} \quad (6.8)$$

and from the self-similarity of the attractor in the vertical direction, shown in Fig. 70b. This yields

$$\frac{N(a)}{N(a^2)} = \frac{1}{2} = a^{-D_y} \rightarrow D_y = \log \left(\frac{1}{2} \right) / \log a \quad (6.9)$$

and finally

$$D_B = 1 + D_y = 1 + \frac{\log 2}{|\log a|} . \quad (6.10)$$

6.1.2 Dissipative Hénon Map

This is the two-dimensional analogue of the logistic map introduced by Hénon (1976), and we recall its recursion relation from Chapter 2

$$x_{n+1} = 1 - ax_n^2 + y_n \quad (6.11a)$$

$$y_{n+1} = bx_n. \quad (6.11b)$$

This map is area contracting, i. e., is dissipative for $|b| < 1$ because its Jacobian is just

$$\left| \det \begin{pmatrix} -2ax_n & 1 \\ b & 0 \end{pmatrix} \right| = |b|. \quad (6.12)$$

The action of the map is shown in Fig. 71.

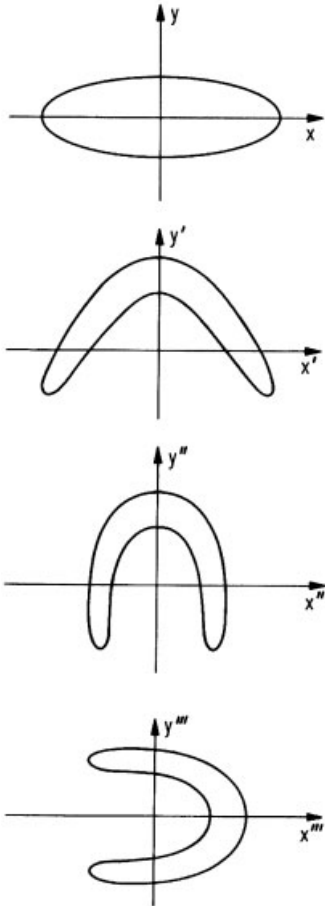


Figure 71: Decomposition of the action of the Hénon map $T = T_3 \cdot T_2 \cdot T_1$ on an ellipse.

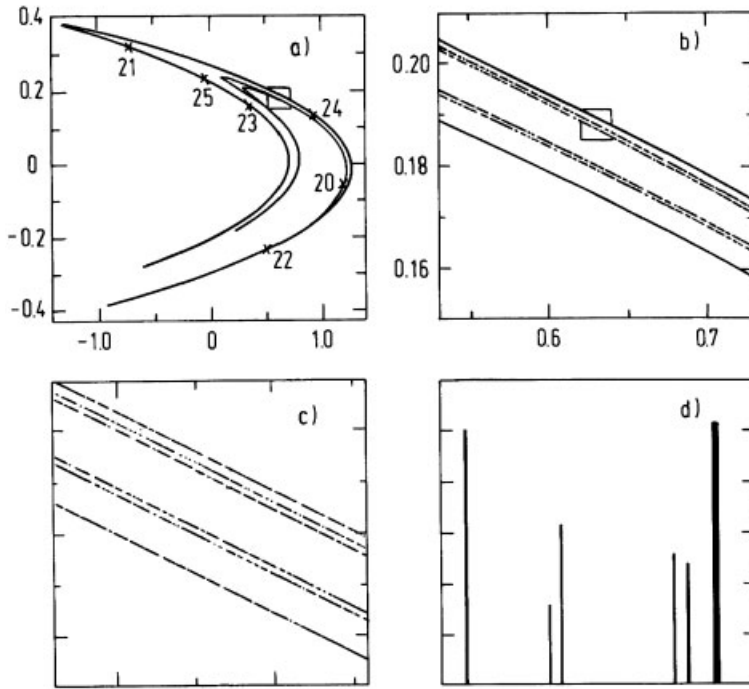


Figure 72: a) The Hénon attractor for 10^4 iterations. Some successive iterates have been numbered to illustrate their erratic movement on the attractor. b), c) Enlargements of the squares in the preceding figure. d) The height of each bar is the relative probability to find a point in one of the six leaves in c). (After Farmer, 1982a, b.)

Let us now examine its iterates for, e. g., $b = 0.3$, $a = 1.4$. Figure 72 a shows the result of an iteration with 10^4 steps, and we have indicated the dynamics by enumerating some successive points on the attractor that looks like a very tangled curve. Figures 72b–c show details of the regions inside the box of the previous figure and reveal the self-similar structure of the attractor. The Hausdorff dimension of the Hénon attractor is: $D(a = 1.4, b = 0.3) = 1.26$. This result was obtained by placing a square net of width l over the diagram, counting the number $N(l)$ of squares occupied by points, and forming $D = -\lim_{l \rightarrow 0} \log N(l) / \log l$. If Fig. 72c is resolved into six “leaves”, then the relative probability of each leaf can be estimated by simply counting its number of points. The height of each bar in Fig. 72d is the relative probability, and the width is the thickness of the corresponding leaf.

The different heights of the bars in Fig. 72d show that the Hénon attractor is inhomogeneous. This inhomogeneity cannot be described by the Hausdorff dimension alone and in the following we shall therefore introduce an infinite set of dimensions which characterize the static structure (i. e., the distribution of points) of the attractor. However, before this step, it is useful to discuss the Kolmogorov entropy that describes the dynamical behavior at the strange attractor.

6.2 The Kolmogorov Entropy

The Kolmogorov entropy (Kolmogorov, 1959) is the most important measure by which chaotic motion in (an arbitrary-dimensional) phase space can be characterized.

Before we introduce this quantity, it is useful to recall that the thermodynamic entropy S measures the disorder in a given system. A simple example, for a system where S increases, is that of gas molecules that are initially confined to one half of a box, but are then suddenly allowed to fill the whole container. The disorder in this system increases because the molecules are no longer separated from the other half of the box. This increase in disorder is coupled with an increase in our ignorance about the state of the system (before the confinement was lifted, we knew more about the positions of the molecules).

More precisely, the entropy S , which can be expressed as

$$S \propto \sum_i P_i \log P_i \quad (6.13)$$

where $\{P_i\}$ are the probabilities of finding the system in states $\{i\}$, measures, according to Shannon *et al.* (1949) (see Appendix F), the information needed to locate the system in a certain state i^* , i. e., S is a measure of our ignorance about the system.

This example from statistical mechanics shows that disorder is essentially a concept from information theory. It is therefore not too surprising that the Kolmogorov entropy K which measures “how chaotic a dynamical system is”, can also be defined by Shannon’s formula in such a way that K becomes proportional to the rate at which information about the state of the dynamical system is lost in the course of time.

6.2.1 Definition of K

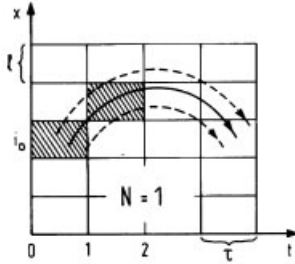
K can be calculated as follows (Farmer, 1982a, b): Consider the trajectory $\vec{x}(t) = [x_1(t), \dots, x_d(t)]$ of a dynamical system on a strange attractor and suppose that the d -dimensional phase space is partitioned into boxes of size l^d . The state of the system is now measured at intervals of time τ . Let $P_{i_0 \dots i_n}$ be the joint probability that $\vec{x}(t=0)$ is in box i_0 , $\vec{x}(r=\tau)$ that it is in box i_1 , \dots , and $\vec{x}(t+n\tau)$ that it is in box i_n . According to Shannon, the quantity

$$K_n = - \sum_{i_0 \dots i_n} P_{i_0 \dots i_n} \log P_{i_0 \dots i_n} \quad (6.14)$$

is proportional to the information needed to locate the system on a special trajectory i_0^*, \dots, i_n^* with precision l (if one knows a priori only the probabilities $P_{i_0 \dots i_n}$). Therefore, $K_{n+1} - K_n$ is the additional information needed to predict in which cell i_{n+1}^* the system will be if we know that it was previously in $i_0^* \dots i_n^*$. This means, that $K_{n+1} - K_n$; measures our loss of information about the system from time n to time $n+1$.

The K -entropy is defined as the average rate of loss of information:

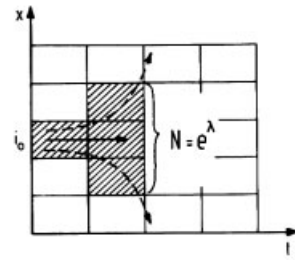
$$\begin{aligned} K &= \lim_{\tau \rightarrow 0} \lim_{l \rightarrow 0} \lim_{N \rightarrow \infty} \frac{1}{N\tau} \sum_{n=0}^{N-1} (K_{n+1} - K_n) = \\ &= - \lim_{\tau \rightarrow 0} \lim_{l \rightarrow 0} \lim_{N \rightarrow \infty} \frac{1}{N\tau} \sum_{i_0 \dots i_{N-1}} P_{i_0 \dots i_{N-1}} \log P_{i_0 \dots i_{N-1}} \end{aligned} \quad (6.15)$$

Table 8: K-entropies for (one-dimensional) regular, chaotic and random motion.*Regular motion*

Initially adjacent points stay adjacent

$$P_{i_0} = l, P_{i_0 i_1} = l \cdot 1$$

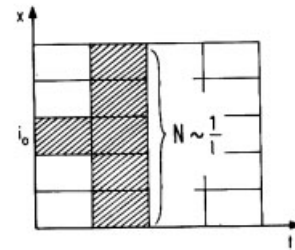
$$K = 0$$

Chaotic motion

Initially adjacent points become exponentially separated

$$P_{i_0} = l, P_{i_0 i_1} = l e^{-\lambda}$$

$$K = \lambda > 0$$

Random motion

Initially adjacent points are distributed with equal probability over all newly allowed intervals

$$P_{i_0} = l, P_{i_0 i_1} \propto l^2$$

$$K \propto -\log l \rightarrow \infty$$

Here we assumed for simplicity that a) $P_{i_0 i_1}$ factorizes into $P_{i_0} \cdot (1/N)$ where N is the number of possible new intervals which evolve from i_0 and b) $K_{n+1} - K_n = K_1 - K_0$ for all n .

The limit $l \rightarrow 0$ (which has to be taken *after* $N \rightarrow \infty$) makes K independent of the particular partition. For maps with discrete time steps $\tau = 1$, the limit $\tau \rightarrow 0$ is omitted. Table 8 shows that K is indeed a useful measure of chaos. K becomes zero for regular motion, it is infinite in random systems, but it is a constant larger than zero if the system displays deterministic chaos.

6.2.2 Connection of K to the Liapunov Exponents

For one-dimensional maps, K is just the positive Liapunov exponent [see Table 8 and eq. (3.11)]. In higher dimensional systems, we loose information about the system because the cell in which it was previously located spreads over new cells in phase space at a rate which is

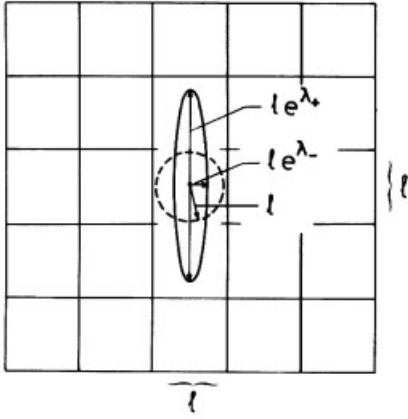


Figure 73: A two-dimensional map transforms a small circle into an ellipse with minor and major radii distorted according to the Liapunov exponents λ_x , and λ_y . Note that e^{λ_y} does not enter K because, due to this exponent, *no* new cells are covered after one time step.

determined by the positive Liapunov exponents (see Fig. 73). It is therefore plausible that the rate K at which information about the system is lost is equal to the (averaged) sum of positive Liapunov exponents (Pesin, 1977):

$$K = \int d^d x \rho(\vec{x}) \sum_i \lambda_i^+(\vec{x}). \quad (6.16)$$

Here $\rho(\vec{x})$ is the invariant density of the attractor. In most cases, the λ s are independent of \vec{x} ; the integral then becomes unity, and K reduces to a simple sum.

The definition of the Liapunov exponent λ for a one-dimensional map $G(x)$ [see eq. (3.9)],

$$e^\lambda = \lim_{N \rightarrow \infty} \left(\prod_{n=0}^{N-1} \left| \frac{dG}{dn_x} \right| \right)^{1/N} \quad (6.17)$$

can be easily generalized to d dimensions, where we have d exponents for the different spatial directions,

$$(e^{\lambda_1}, e^{\lambda_2}, \dots, e^{\lambda_d}) = \lim_{N \rightarrow \infty} (\text{magnitude of the eigenvalues of } \prod_{n=0}^{N-1} J(\vec{x}_n))^{1/N} \quad (6.18)$$

and

$$J(\vec{x}) = \left(\frac{\partial G}{\partial x_j} \right) \quad (6.19)$$

is the Jacobian matrix of the map $\vec{x}_{n+1} = \vec{G}(\vec{x}_n)$.

Note that the eigenvalues $\{\lambda_i\}$ of the Jacobian matrix are invariant under coordinate transformations in phase space, i. e., from (6.16), K is also invariant, as one would expect for such an important physical quantity.

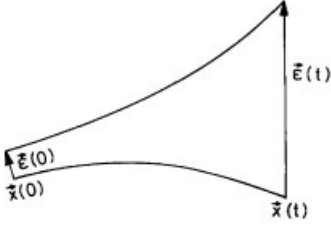


Figure 74: Exponential separation of nearby trajectories in phase space (schematically).

Let us briefly comment on the computation of Liapunov exponents for flows. First, there is a difference in the calculation of Liapunov exponents for maps λ_M and flows (λ_F) which can be explained by the following trivial example.

The Liapunov exponent λ_M of the map

$$x_{n+1} = ax_n \rightarrow x_n = e^{n \log a} x_0 \quad (6.20)$$

is obviously $\lambda_M = \log a$. Whereas one obtains for the flow

$$\dot{x} = ax \rightarrow x(t) = e^{at} x(0), \quad (6.21)$$

the result that nearby trajectories separate with rate a , i. e., the Liapunov exponent λ_F is simply $\lambda_F = a$. (Both examples show no chaos, of course, because backfolding is missing).

For general flows described by an autonomous differential equation

$$\dot{\vec{x}} = \vec{f}(\vec{x}), \quad (6.22)$$

the difference $\vec{E}(t)$ of infinitesimal neighbored trajectories (see Fig. 74) develops according to

$$\dot{\vec{E}} = M(t)\vec{E} \quad (6.23)$$

where

$$M_{ij}(t) = \frac{\partial f_i}{\partial x_j} \{\vec{x}[t, \vec{x}(0)]\} \quad (6.24)$$

is the Jacobian matrix taken at the point $\vec{x}(t)$. Therefore, in order to integrate eq. (6.23) one has to integrate eq. (6.22) first to know $\vec{x}[t, \vec{x}(0)]$. However, eq. (6.23) can be integrated formally yielding

$$\vec{E}(t) = \left\{ \hat{T} \exp \left[\int_0^t dt' M(t') \right] \right\} \vec{E}(0) \equiv L(t)\vec{E}(0) \quad (6.25)$$

where the time ordering operator \hat{T} has to be introduced because the matrices $M(t)$ and $M(t')$ usually do not commute at different times t and t' . The Liapunov exponents $\lambda_1 \dots \lambda_d$ of the flow are, in analogy to eq. (6.18), defined as

$$(e^{\lambda_1}, e^{\lambda_2}, \dots, e^{\lambda_d}) = \lim_{t \rightarrow \infty} (\text{magnitude of the eigenvalues of } L(t))^{1/t}. \quad (6.26)$$

The Liapunov exponents in eq. (6.26) generally depend on the choice of the initial point $\vec{x}(0)$. Even if $\vec{x}(t)$ moves on a strange attractor, a change in $\vec{x}(0)$ could place the system into the basin of attraction of another attractor with a different set of λ_i 's (see, e. g., Fig. 69).

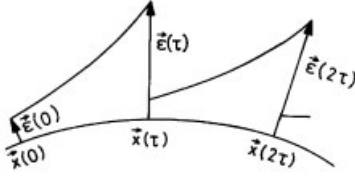


Figure 75: Numerical calculation of the largest Liapunov exponent λ_m . To avoid overflow, one calculates the divergence of nearby trajectories for finite timesteps τ , renormalizes $\vec{\varepsilon}(i\tau)$ to unity after each step and takes the average:

$$\begin{aligned}\varepsilon(\tau) &= \vec{\varepsilon}(0) \exp(\lambda_1 \tau); \quad \vec{\varepsilon}(2\tau) = \frac{|\vec{\varepsilon}(\tau)|}{|\vec{\varepsilon}(\tau)|} e^{\lambda_2 \tau} \dots \\ \lambda_m &= \lim_{n \rightarrow \infty} \frac{1}{n} \sum_{i=1}^n \lambda_i = \lim_{n \rightarrow \infty} \frac{1}{n\tau} \sum_{i=1}^n \log |\vec{\varepsilon}(i\tau)|.\end{aligned}$$

We will not discuss all numerical methods which have been developed in order to extract the Liapunov exponents from eqs. (6.22–6.24) (see the References of this section for some examples), but only explain the simplest method which yields the largest Liapunov exponent λ_m .

Expanding in eq. (6.25), $\vec{\varepsilon}(0)$ with respect to the eigenvectors \vec{e}_j of $L(t)$, i. e.,

$$\vec{\varepsilon}(0) = \sum_{j=1}^d a_j \vec{e}_j; \quad a_j = \vec{e}_j \cdot \varepsilon(0) \quad (6.27)$$

we obtain by using

$$L(t)\vec{e}_j \propto e^{\lambda_j t} \vec{e}_j \quad \text{for } t \rightarrow \infty. \quad (6.28)$$

via eq. (6.25):

$$|\vec{\varepsilon}(t)| = \left| \sum_{j=1}^d a_j \vec{e}_j e^{\lambda_j t} e^{i\psi_j t} \right| \propto e^{\lambda_m t} \quad \text{for } t \rightarrow \infty. \quad (6.29)$$

Here, ψ_j denotes the phase angle of the j th eigenvalue of $L(t)$, which can be complex, and $e^{\lambda_m t}$ dominates the sum in eq. (6.29) because the remaining terms decay as $\exp[-|\lambda_m - \lambda_j|t]$. In order to obtain λ_m , one could therefore start with any randomly chosen value for $\vec{\varepsilon}(0)$, calculate $\vec{\varepsilon}(t)$ by numerical integration of eqs. (6.22–6.24), and extract λ_m via eq. (6.29). To avoid overflow in the computer, this is usually done in steps as shown in Fig. 75.

Plate XVII, at the beginning of this book, and Fig. 76 display the parameter dependence of λ_m for the driven pendulum with an additional torque and for the Lorenz model, respectively. In both cases, one observes a sensitive dependence of order $\lambda_m < 0$ and chaos $\lambda_m > 0$ on the parameter values.

6.2.3 Average Time over which the State of a Chaotic System can be Predicted

The K -entropy also determines the average time over which the state of a system, displaying deterministic chaos, can be predicted. Consider, e. g., the simple one-dimensional triangular map in Fig. 15b, which is confined to the unit square. After n time steps, an interval l increases

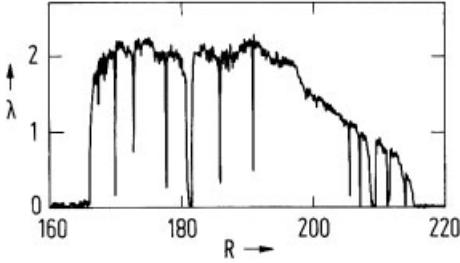


Figure 76: The largest Liapunov exponent of the Lorenz model (eqs. (2.4) for $\sigma = 10$, $b = 8/3$) as a function of the parameter $r = R$ (after K. Schmidt priv. comm.).

to $L = l e^{\lambda n}$. If L becomes larger than 1, we can no longer locate the trajectory in $[0, 1]$, and all we can say is that the system has a probability

$$\rho_0(x) dx \quad (6.30)$$

of being in an interval $[x, x + dx] \in [0, 1]$, where $\rho_0(x)$ is the invariant density of the system. In other words, precise predictions about the state of this system are only possible for times n that are smaller than T_m :

$$l e^{\lambda T_m} = 1 \rightarrow T_m = \frac{1}{\lambda} \log \left(\frac{1}{l} \right). \quad (6.31)$$

Above T_m one can only make statistical predictions. Equation (6.31) can be generalized to higher dimensional dynamical systems by replacing λ by the K -entropy (Farmer, 1982a):

$$T_m \propto \frac{1}{K} \log \left(\frac{1}{l} \right). \quad (6.32)$$

Note that the precision l , with which the initial state is located, only influences T_m logarithmically. Let us summarize our results about the K -entropy:

- It measures the average rate at which information about the state of a dynamical system is lost with time.
- For one-dimensional maps, it is equal to the Liapunov exponent. In higher dimensional systems, K measures the average deformation of a cell in phase space and becomes equal to the integral over phase space of the sum of the positive Liapunov exponents.
- It is inversely proportional to the time interval over which the state of a chaotic system can be predicted.

Furthermore, in the next section, we shall show that K can be directly obtained by measuring the time dependence of one component of a chaotic system. These results show that the K -entropy is the fundamental quantity by which chaotic motion can be characterized, and we define a strange attractor as an attractor with a positive K -entropy.

6.3 Characterization of the Attractor by a Measured Signal

Having experimentally observed a seemingly chaotic signal, one wants to know what information it contains about the strange attractor. To provide an answer, we proceed in several steps.

First, we will explain the result of Takens (1981) who has shown that, after the transients have died out, one can reconstruct the trajectory on the attractor (the whole time dependent vector $\vec{x}(t) = [x_1(t), x_2(t) \dots]$ in phase space) from the measurement of a single component, say $x_1(t)$. A knowledge of the time series of one variable is therefore sufficient to reconstruct the statistical and dynamical properties of the strange attractor.

Since the whole trajectory contains too much information, we then follow a series of papers by Grassberger, Hentschel and Procaccia (1983), Halsey *et al.* (1986), Eckmann and Procaccia (1986) and introduce a set of averaged coordinate invariant numbers (generalized dimensions, entropies, and scaling indices) by which different strange attractors can be distinguished. For this purpose, we divide the attractor into boxes of linear dimension l , and denote by p_i the probability that the trajectory on the strange attractor visits box i . By averaging powers of the p_i 's over all boxes, we obtain the generalized dimensions D_q , defined by

$$D_q = -\lim_{l \rightarrow 0} \frac{1}{q-1} \left| \frac{1}{\log l} \right| \log \left(\sum_i p_i^q \right) \quad (6.33)$$

that are formally similar to the free energy F_β of ordinary equilibrium thermodynamics:

$$F_\beta = -\lim \frac{1}{\beta} \frac{1}{N} \log \left[\sum_i (e^{-E_i})^\beta \right] \quad (6.34)$$

where E_i are the energy levels of the system, N is its particle number, and β is the inverse temperature. Since $\sum_i p_i^q$, which appears in eq. (6.33), is for $q > 1$ the total probability that q points of the attractor are within one box, it is obvious that the D_q measure correlations between different points on the attractor and are therefore useful in characterizing its inhomogeneous static structure.

But, it will be shown below that the (negative) Legendre transform $f(\alpha)$ of the D_q (more precisely of $(q-1)D_q$):

$$f(\alpha) = -(q-1)D_q + q\alpha \quad (6.35a)$$

$$\alpha = \frac{\partial}{\partial q} [(q-1)D_q] \quad (6.35b)$$

is more appropriate to describe universal properties of strange point sets.

Let us briefly explain the meaning of $f(\alpha)$ (its connection to the D_q 's will be shown below). Assuming ergodicity, the probabilities p_i are, by construction, related to the invariant density $\rho(\vec{x})$ of the attractor:

$$p_i = \int_{|\vec{x}_i - \vec{x}| \leq l} d^d x \rho(\vec{x}) \quad (6.36)$$

where \vec{x}_i denotes the center of box i . If $p_i(l)$ diverges for $l \rightarrow 0$ as

$$p_i(l \rightarrow 0) \propto l^{\alpha_i} \quad (6.37)$$

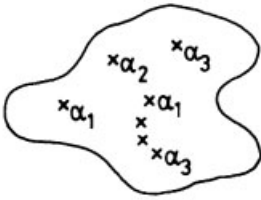


Figure 77: The invariant measure has different power law singularities on a strange attractor. $f(\alpha)$ measures the Hausdorff dimension of the set of points with the same power α .

the invariant density has, according to eq. (6.36), at \vec{x}_i a singularity whose strength is characterized by α_i . Since different points \vec{x}_i on the attractor can have different strengths α_i , it is useful to introduce a function $f(\alpha)$ which measures the Hausdorff dimension of the set of points $\{\vec{x}_i\}$ on the attractor which have the same strength of singularity α . $f(\alpha)$ characterizes the static distribution of points on the attractor and can therefore also be used for point sets which are not generated dynamically (see Fig. 77).

In order to describe the dynamical behavior of the trajectory on the attractor, we use the quantities $P_{i_0 \dots i_n}$ which we have introduced already to define the K -entropy via eq. (6.14). The $P_{i_0 \dots i_n}$ measure the probability that the trajectory visits a certain sequence $i_0 \dots i_n$ of boxes of size l in time n . By playing with these variables the same game as with the P_i , we introduce generalized entropies K , via:

$$K_q = - \lim_{l \rightarrow 0} \lim_{n \rightarrow \infty} \frac{1}{q-1} \frac{1}{n} \log \sum_{i_0 \dots i_n} P_{i_0 \dots i_n}^q \quad (6.38)$$

and show that their Legendre transform $g(\lambda)$ is connected to the fluctuations of the K -entropy around its mean value K , given by eq. (6.15).

It will also be demonstrated that both quantities, the D_q s and the K_q s (and therefore $f(\alpha)$ and $g(\lambda)$) can be extracted from a time series of a single variable. Two further important quantities, which can be obtained in this way, are the embedding dimension of the attractor, that is, the dimension of the space with the lowest integer dimension, which contains the attractor, and the amplitude of white noise on the signal. Thus irregularities originating from deterministic motion on the attractor can be separated from disturbing white noise.

6.3.1 Reconstruction of the Attractor from a Time Series

It is not always possible to measure all components of the vector $\vec{x}(n)$ simultaneously. This clearly holds for an infinite-dimensional system. If we define the dimension of a system by the number of initial conditions, then the so-called Mackey–Glass equation (Mackey and Glass, 1977)

$$\dot{x} = \frac{ax(t-\tau)}{1 + \{x(t-\tau)\}^{10}} - bx(t) \quad (6.39)$$

(which describes the regeneration of blood cells) obviously provides a simple example of an infinite-dimensional system, because all the $x(t)$ -values in the interval $t, t - \tau$ have to be known

(as initial conditions) to solve it. How do we proceed in this, or the less difficult case, where we have an attractor embedded in d -dimensional space, but measure only one component of the signal?

It has been shown by Takens (1981) that one can reconstruct certain properties of the attractor in phase space from the time series of a single component. Instead of the rather cumbersome proof, we present the following simplified argument. As an example, consider a two-dimensional flow generated by

$$\frac{d}{dt}\vec{x} = \vec{F}(\vec{x}) \quad \vec{x} = \{x, y\} \quad (6.40)$$

Every point $\{x(t + \tau), y(t + \tau)\}$ then originates uniquely from a point $\{x(t), y(t)\}$, and the relation between both points is one-to-one because the trajectories do not cross (otherwise the trajectory would not be determined uniquely by the initial conditions). Next, we construct a sequence of vectors

$$\vec{\xi}(t) = \{x(t), x(t + \tau)\} \quad (6.41)$$

$$\vec{\xi}(t + \tau) = \{x(t + \tau), x(t + 2\tau)\}.$$

Since the components of $\vec{\xi}$ are related to $\{x(t), y(t)\}$ via the one-to-one relationships

$$\xi_1(t) = x(t) \quad (6.42a)$$

$$\begin{aligned} \xi_2(t) &= x(t + \tau) = \int_t^{t+\tau} dt' F_1\{x(t'), y(t')\} + x(t) \\ &\cong \tau F_1\{x(t), y(t)\} + x(t) \end{aligned} \quad (6.42b)$$

with a Jacobian $|\tau(\partial F_1/\partial y)| \neq 0$, it is plausible that the information contained in the time sequences $\vec{x}(t_i)$ and $\vec{\xi}(t_i)$ ($t_i = i\tau$) is the same, and both sequences should lead to the same characteristic dimensions. A simple example for which $\vec{x}(t_i)$ and $\vec{\xi}(t_i)$ are indeed completely equivalent is a circle:

$$\begin{aligned} \vec{x}(t_i) &= \{x(t_i), y(t_i)\} = \{\sin(2\pi t_i), \cos(2\pi t_i)\} = \\ &= \left\{ \sin(2\pi t_i), \sin \left[2\pi \left(t_i + \frac{1}{4} \right) \right] \right\} = \left\{ x(t_i), x(t_i + \frac{1}{4}) \right\} = \vec{\xi}(t_i). \end{aligned} \quad (6.43)$$

But we should be aware that arguments are only heuristic and can only be applied “cum grano salis” to situations where strange attractors appear. What Takens (1981) actually proved is the following: “If $\vec{x} = \vec{F}(\vec{x})$ generates a d -dimensional flow, then eq. (6.44),

$$\vec{\xi}(t) = \{x_j(t), x_j(t + \tau), \dots, x_j[t + (D - 1)\tau]\} \quad (6.44)$$

where $x_j(t)$ is an arbitrary component of \vec{x} , provides a smooth embedding for this flow, if $D = 2d + 1$. The metric properties in both spaces (the d -dimensional $\{\vec{x}(t)\}$ and the $(2d + 1)$ -dimensional $\{\vec{\xi}(t)\}$) are the same in the sense that distances in $\{\vec{x}(t)\}$ and $\{\vec{\xi}(t)\}$ have a ratio which is uniformly bounded and bounded away from zero”.

The relation between the dimension of the original flow, d , and the embedding dimension D may be understood in terms of a simple topological argument. Consider, e. g., a closed orbit

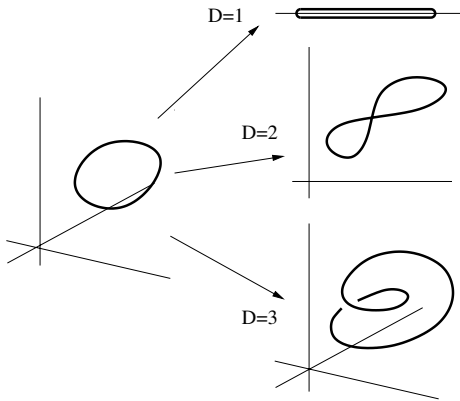


Figure 78: Diagrammatic view of the delay embedding of a limit cycle (left) with D -dimensional delay coordinates for $D = 1, 2$ and 3 (right).

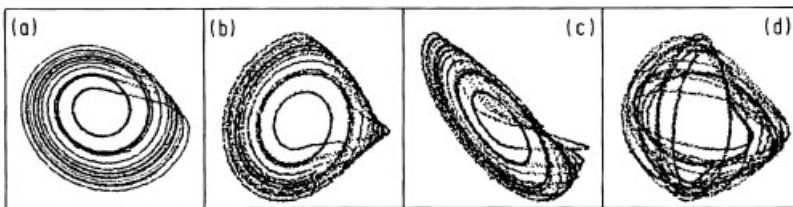


Figure 79: Reconstruction of the Rössler attractor for $a = 0.15$, $b = 0.20$, $c = 10.0$; $\vec{x}_0 = (10.0, 0, 0)$ from a time series: a) x, y coordinates of the “true” attractor obtained by numerical integration of eq. (6.45a–c); b) and c) reconstructions for $\tau = 0.23, 0.39, 3.26$, measured in units of the average orbital time, respectively. (After Fraser and Swinney, 1986.)

in the original phase space, i. e., a limit cycle in the \vec{x} -space (cf. Fig. 78). Clearly, its dimension is $d = 1$. Equation (6.44) yields a transformation to new coordinates. If one considers one-dimensional embeddings, $D = 1$, then the new coordinate is a scalar and the limit cycle is mapped onto a line. Of course this mapping is not invertible since self intersections occur in the $\vec{\xi}$ -space. If we choose $D = 2$ then still self intersections may appear and these intersection points are structurally stable, i. e., one cannot remove the intersection by a small perturbation. If we take a three-dimensional embedding, $D = 3 = 2d + 1$, then the image curve in $\vec{\xi}$ -space is typically free of any self intersection, so that eq. (6.44) yields the desired invertible transformation. A similar argument may be applied to objects of higher dimension, e. g., invariant manifolds and even to fractal attractors.

Figure 79 shows a reconstruction of (a projection of) the Rössler attractor (Rössler, 1976), which is generated by the system,

$$\dot{x} = -z - y \quad (6.45a)$$

$$\dot{y} = x + ay \quad (6.45b)$$

$$\dot{z} = b + z(x - c) \quad (6.45c)$$

from about 6×10^5 points for different choices of the delay time τ . Although for an infinite amount of noise-free data, τ could be chosen almost arbitrary (Takens, 1981), it can be seen from Fig. 79 that for a finite time series the quality of the reconstruction depends on τ . If τ is too small, $x(t)$ and $x(t + \tau)$ become practically indistinguishable and one obtains a linear dependence that is not present for the coordinates of the real trajectory. It is, therefore, reasonable to choose the decay time of the autocorrelation function $C(t)$ of the signal x_n for τ ,

$$C(t) = \lim_{N \rightarrow \infty} \frac{1}{N} \sum_{n=1}^{N-1} x_n x_{n+t} \equiv \langle x_0 x_t \rangle \quad (6.46a)$$

$$C(\tau) \approx \frac{1}{2} C(0) \quad (6.46b)$$

which ensures that $x(t)$ and $x(t + \tau)$ become linearly independent, but other choices for τ have also been proposed (Fraser and Swinney, 1986; Liebert, Kaspar and Schuster, 1987).

6.3.2 Generalized Dimensions and Distribution of Singularities in the Invariant Density

In this section, we discuss the meaning of the generalized dimensions D_q for special values of q and demonstrate explicitly the connection of D_q to the distribution $f(\alpha)$ of singularities in the invariant density of a strange attractor. Proceeding in a similar way as in Section 6.2, we chop the trajectory $\vec{x}(t) = [x_1(t) \dots x_d(t)]$ of a dynamical system on a strange attractor into a sequence of points $\vec{x}(t = 0)$, $\vec{x}(t = \tau) \dots x(t = N\tau)$ and partition the d -dimensional phase space into cells l^d . The probability p_i of finding a point of the attractor in cell number i ($i = 1, 2, \dots M(l)$) is then given by

$$p_i = \lim_{N \rightarrow \infty} \frac{N_i}{N} \quad (6.47)$$

where N_i is the number of points $\{\vec{x}(t = j\tau)\}$ in this cell.

The generalized dimensions D_q which are related to the q th powers of p_i via

$$D_q = \lim_{l \rightarrow 0} \frac{1}{q-1} \frac{\log \left(\sum_{i=0}^{M(l)} p_i^q \right)}{\log l}; \quad q = 0, 1, 2 \dots \quad (6.48)$$

For $q \rightarrow 0$ we obtain from (6.48)

$$D_0 = \lim_{l \rightarrow 0} \left(\log \sum_{i=0}^{M(l)} 1 \right) / \log l = - \lim_{l \rightarrow 0} \frac{\log M(l)}{\log l} \quad (6.49)$$

which is just the usual definition (4.68) of the Hausdorff dimension of the attractor (i. e., $D = D_0$).

As $q \rightarrow 1$, eq. (6.48) becomes

$$D_1 = -\lim_{l \rightarrow 0} \frac{S(l)}{\log l} \quad (6.50)$$

where

$$S(l) = -\sum_{i=0}^{M(l)} p_i \log p_i . \quad (6.51)$$

Since $S(l)$ is the information gained, if we know $\{p_i\}$ and learn that the trajectory is in a specific cell i , D_1 is called the information dimension. It tells us how this information gain increases as $l \rightarrow 0$.

For a homogeneous attractor where all p_i are the same, i. e., $p_i = 1/M(l)$, we have

$$S(l) = -\sum_{i=0}^{M(l)} \frac{1}{M(l)} \log \frac{1}{M(l)} = \log M(l) . \quad (6.52)$$

Furthermore, the information dimension is always less or equal to the Hausdorff dimension, that is,

$$D_1 \leq D_0 . \quad (6.53)$$

This can be proven by maximizing $S(l)$ under the constraint $\sum_i p_i = 1$:

$$\frac{\partial}{\partial p_j} \left[-\sum_{i=1}^{M(l)} p_i \log p_i + \lambda \sum_i p_i \right] = 0 \quad (6.54a)$$

$$\rightarrow p_j = e^{-1+\lambda} . \quad (6.54b)$$

After eliminating the Lagrange multiplier λ via the constraint, eq. (6.54b) yields

$$p_j = \frac{1}{M(l)} \quad (6.55)$$

$$S(l) \leq \max[S(l)] = \log M(l) \quad (6.56)$$

from which eq. (6.53) follows after division by $\log l$.

The inequality (6.53) has been generalized to (Hentschel and Procaccia, 1983):

$$D_{q'} \leq D_q \quad \text{for } q' > q \quad (6.57)$$

where the equality sign holds if the attractor is uniform.

In order to explain the connection between the D_q s and the singularities in the invariant density of an attractor, we calculate D_q for a one-dimensional system which has a power law singularity in its invariant density $\rho(x)$ at $x = 0$, i. e.,

$$\rho(x) = \frac{1}{2}x^{-1/2} \quad \text{for } x \in [0, 1] . \quad (6.58)$$

This is just the behavior of $\rho(x)$ near $x = 0$ for the logistic map at $r = 4$ [see eq. (4.104)] where we ignored the singularity at $x = 1$ to simplify our argument. (The D_q s will be the same for both systems).

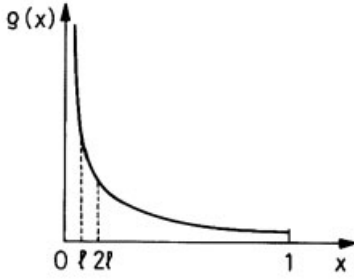


Figure 80: The invariant density $\rho(x) = 1/2(x)^{-1/2}$ for $0 \leq x \leq 1$, $x_1 = 0$, $x_2 = l, \dots$ (schematically).

Figure 80 shows that

$$p_i = \int_{x_i}^{x_{i+1}} \rho(x) dx \propto \begin{cases} l^{1/2} & \text{for } i = 1 \\ l^1 & \text{for } i \neq 1 \end{cases} \quad (6.59)$$

Thus,

$$\sum_i p_i^q = \left[\int_0^l \rho(x) dx \right]^q + \sum_{i \neq 1} [\rho(x_i)l]^q \quad (6.60a)$$

$$\cong \left[\int_0^l \rho(x) dx \right]^q + l^{q-1} \int_l^1 dx \rho(x)^q \quad (6.60b)$$

$$= (1-a)l^{q/2} + al^{q-1} \quad (6.60c)$$

where $a = \left(\frac{1}{2}\right)^q \left(1 - \frac{q}{2}\right)^{-1}$. Equation (6.60c) can be written as

$$\sum_i p_i^q \cong \int d\alpha \rho(\alpha) l^{-f(\alpha)} l^{\alpha q} \quad (6.61)$$

where

$$\rho(\alpha) = (1-\alpha)\delta\left(\alpha - \frac{1}{2}\right) + a\delta(\alpha - 1) \quad (6.62)$$

and

$$f(\alpha) = \begin{cases} 0 & \text{for } \alpha = \frac{1}{2} \\ 1 & \text{for } \alpha = 1 \end{cases} \quad (6.63)$$

The interpretation of eqs. (6.59–6.63) is as follows. Associated with different singularities for the density of states $\rho(x)$ (e. g., $\rho(x \rightarrow 0) \sim x^{-1/2}$, $\rho(x) \sim \text{const.}$ otherwise) which gives rise to different singularities for $p_i(l) \sim l^{\alpha_i}$ in eq. (6.59), are different exponents $f(\alpha)$ which measure the fractal dimension of the density of these singularities on the attractor. The singularity with exponent $\alpha = 1/2$ occurs just at one point, that is, $f(\alpha = 1/2) = 0$, whereas $\alpha = 1$ occurs in a whole one-dimensional interval, that is $f(\alpha = 1) = 1$. This concept of a distribution $f(\alpha)$ of

fractal dimensions which are associated with a whole set of singularities of strength α can be generalized to strange attractors, and it turns out that the functions $f(\alpha)$ are again universal, for example, for the Feigenbaum attractor or the attractor, which is associated with the transition from quasiperiodicity to chaos. This type of universality, which is again associated with a whole set of singularities and not just a single exponent, is also called global universality. (It should be noted that the term global universality is also used if a whole range of parameter values has universal properties as will be explained in Chapter 7).

By way of generalizing our example, we now make the scaling hypothesis that

$$p_i(l) \sim l^{\alpha_i} \quad (6.64)$$

(where i denotes the box i of linear dimension l) occurs in $\sum_i p_i^q$ with a density

$$\rho(\alpha) l^{-f(\alpha)} d\alpha \quad (6.65)$$

such that the sum can be estimated as:

$$Z_q \equiv \sum_i p_i^q \cong \int d\alpha \rho(\alpha) l^{-f(\alpha)} l^{\alpha q} = \int d\alpha \rho(\alpha) e^{[-f(\alpha) + \alpha q] \log l} \quad (6.66)$$

i. e., we wrote Z_q as an integral over the singularities α . In the limit $l \rightarrow 0$, the integral can be evaluated using the saddle point approximation [see Appendix E, eq. (E.7)] and becomes:

$$Z_q \propto e^{-[f(\alpha) - \alpha q] \log l} \quad (6.67)$$

where the dominating value of α is determined by:

$$\frac{\partial}{\partial \alpha} [q\alpha - f(\alpha)] = 0 \rightarrow f'(\alpha) = q \quad (6.68a)$$

$$\frac{\partial^2}{\partial \alpha^2} [q\alpha - f(\alpha)] > 0 \rightarrow f''(\alpha) < 0. \quad (6.68b)$$

This yields via eqs. (6.33) and (6.66–6.67) for D_q :

$$D_q = \{[q\alpha(q) - f(\alpha(q))]\}/(q-1) \quad (6.69)$$

and after differentiation

$$\alpha(q) = \frac{\partial}{\partial q} [(q-1)D_q]. \quad (6.70)$$

By eliminating, via eq. (6.70), the variable q in favor of α and using eq. (6.69), one obtains $f(\alpha)$ as (negative) Legendre transformation of $(q-1)D_q$:

$$f(\alpha) = q(\alpha) - [q(\alpha) - 1]D_{q(\alpha)}. \quad (6.71)$$

For our example with $\rho(x) = x^{-1/2}$, we find from eqs. (6.69–6.71):

	D_q	$\alpha(q)$	$f(\alpha)$
$q \geq 2$	$\frac{1}{2} \frac{q}{q-1}$	$\frac{1}{2}$	0
$q \leq 2$	1	1	1

i. e., the α -spectrum consists of two points, as calculated above [see eq. (6.63)].

Numerical determination of the dimensions D_q , by covering the phase space with a set of boxes of volume l^d and counting the number of iterates which lie in a certain cell, is rather cumbersome and in fact impossible for attractors of higher dimensions. However, we can replace the sum over the uniformly distributed boxes in $\sum_i p_i^q$ by a sum over nonuniformly distributed boxes around the points x_j of a time series which results, e. g., from a map $x_{n+1} = f(x_j)$.

$$\begin{aligned}
 \sum_i p_i^q &= \sum_i \left[\int_{\text{Box } i} \rho(x) \, dx \right]^q \\
 &\cong \sum_i [\rho(x_i)l]^q = \sum_i \rho(x_i)l [\rho(x_i)l]^{q-1} \\
 &\cong \int \rho(x) \, dx \tilde{p}(x)^{q-1} \cong \frac{1}{N} \sum_j \{ \tilde{p}[f^j(x_0)] \}^{q-1} \\
 &= \frac{1}{N} \sum_j \tilde{p}_j^{q-1}. \tag{6.72}
 \end{aligned}$$

Here x_i is an element of box i and $\tilde{p}[f^j(x_0)] \equiv \tilde{p}_j$, is the probability of the trajectory to be in a box of size l around the iterate $x_j = f^j(x_0)$. Equation (6.72) should make it plausible, mathematical rigor is not attempted, that the change from p_i^q to \tilde{p}_j^{q-1} is due to the fact that the points x_j of the time series (and the boxes around them) are nonuniformly distributed. We next generalize eq. (6.72) to higher dimensional systems and write the probability \tilde{p}_j , that an element of the time series falls into an interval l around the element \vec{x}_j as:

$$\tilde{p}_j = \frac{1}{N} \sum_i \Theta(l - |\vec{x}_i - \vec{x}_j|) \tag{6.73}$$

where $\Theta(x)$ is the Heaviside step function.

Using eqs. (6.72–6.73), $\sum_i p_i^q$ becomes

$$\sum_i p_i^q = \frac{1}{N} \sum_j \left[\frac{1}{N} \sum_i \Theta(l - |\vec{x}_i - \vec{x}_j|) \right]^{q-1} = C^q(l). \tag{6.74}$$

For $q=2$, this reduces to the correlation integral $C(l)$ introduced by Grassberger and Procaccia (1983a) which measures the probability of finding two points of an attractor in a cell of size l :

$$\begin{aligned}
 \sum_{i=0}^{M(l)} p_i^2 &= \text{the probability that two points of the attractor lie within a cell } r=0 \\
 &\cong \text{the probability that two points at the attractor are separated} \\
 &\quad \text{by a distance smaller than } l \\
 &= \lim_{N \rightarrow \infty} \frac{1}{N^2} \{ \text{number of pairs } ij \text{ whose distance } |\vec{x}_i - \vec{x}_j| \text{ is less than } l \} \\
 &= \lim_{N \rightarrow \infty} \frac{1}{N^2} \sum_{ij} \Theta(l - |\vec{x}_i - \vec{x}_j|) \\
 &= C(l) = \text{correlation integral}. \tag{6.75}
 \end{aligned}$$

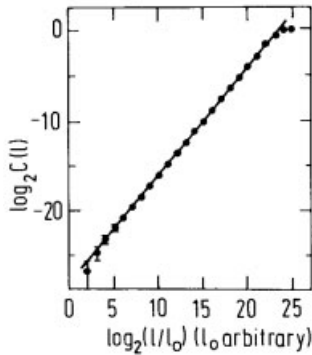


Figure 81: $\log_2 C(l)$ versus $\log_2 l$ for the Hénon map. The slope yields $D_2 = 1.21$ (after Grassberger and Procaccia, 1983a).

The correlation integral $C(l)$ can be used to determine the following properties from a measured time series:

- The correlation dimension D_2 :

$$D_2 = \lim_{l \rightarrow 0} \frac{1}{\log l} \log \sum_i p_i^2 \quad (6.76)$$

which yields a lower bound to the Hausdorff dimension D_0 , i. e., $D_2 < D_0$. Figure 81 shows how D_2 is determined from $C(l)$ for the Hénon map.

Figure 82 demonstrates how Takens' reconstruction of the trajectory from the measurement of a single variable (Takens, 1983) works for the computation of $C(l)$ for the Lorenz attractor.

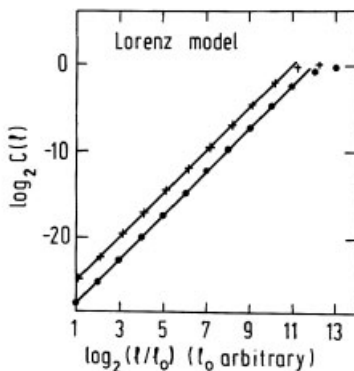


Figure 82: $\log C(l)$ versus $\log l$ for the Lorenz model. The lower line is obtained directly from the three-dimensional time series $\{x(t_i), y(t_i), z(t_i)\}$ whereas the upper line originates from the reconstructed series $\tilde{\xi}(t_i) = \{x(t_i), x(t_i + \tau), x(t_i + 2\tau)\}$. The slopes of both curves are the same, i. e., the correlation dimension $D_2 = 2.05$ obtained by both methods is the same, as stated above (Grassberger and Procaccia, 1983a).

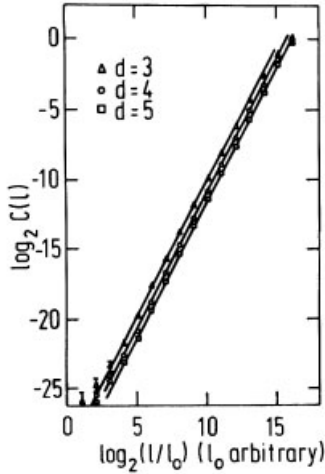


Figure 83: $D_2 = 1.95 \pm 0.03$ determined from a single-variable time series for the Mackey–Glass equation with parameter values $\tau = 17$, $a = 0.2$, $b = 0.1$ for different embedding dimensions d (Hentschel and Procaccia, 1983).

– *The embedding dimension d :*

Figure 83 shows the l dependence of the correlation integral for the Mackey–Glass system. Although this system has an infinite dimension, its correlation dimension is finite and smaller than 3. It is therefore sufficient to use a simple time series with a three-dimensional vector $\vec{\xi}(t_i) = \{x(t_i), x(t_i + \tau), x(t_i + 2\tau)\}$ to determine D_2 . The dimension d in $\vec{\xi}(t) = \{x(t_i) \dots x(t_i + (d-1)\tau)\}$, above which D_2 no longer changes, is the (minimal) *embedding dimension* of the attractor.

– *Separation of deterministic chaos and external white noise:*

The correlation integral can also be used as a tool to *distinguish between deterministic irregularities*, which arise from intrinsic properties of the strange attractor, and *external white noise*. Suppose we have a strange attractor embedded in d -dimensional space and we add an external white noise. Each point on the attractor then becomes surrounded by a uniform d -dimensional cloud of points. The radius of this cloud is given by the noise amplitude l_0 . For $l \gg l_0$, eq. (6.74) counts these clouds as points, and the slope of a plot of $\log C(l)$ versus $\log l$ yields the correlation exponent of the attractor. For $l \ll l_0$, most of the points counted lie within the uniformly filled d -dimensional cells, and the slope crosses over to d , as shown in Fig. 84 for the noisy Hénon attractor.

Finally, let us briefly comment on the intuitive meaning of the variable q and then present two examples of D_q and $f(\alpha)$ curves.

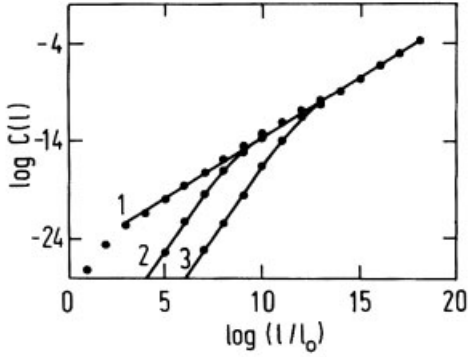


Figure 84: $\log C(l)$ as a function of $\log l$ for the Hénon map embedded in three dimensions. Curve 1 is for the map without noise and yields $D_2 = 1.25$. Curve 2 is for the map with random noise with amplitude $5 \cdot 10^{-3}$. Curve 3 is for the map with noise amplitude 5×10^{-2} . Curve 2 and 3 break at length scales that are determined by the noise level below which the slope is approximately 3 (Ben-Mizrachi *et al.*, 1983.)

If one replaces, in the definition of D_q via eq. (6.33), the p_i by the probabilities \tilde{p}_j , for a trajectory to fall in a box around an iterate (see eq. 6.72) then the resulting expression

$$D_q = -\lim_{l \rightarrow 0} \frac{1}{q-1} \left| \frac{1}{\log l} \right| \sum_j \tilde{p}_j(l)^{q-1} \quad (6.77)$$

resembles closely the expression F_β of the free energy of an N -particle equilibrium system at a temperature $T = \beta^{-1}$:

$$F_\beta = -\lim_{N \rightarrow \infty} \frac{1}{\beta} \cdot \frac{1}{N} \sum_i (e^{-E_i})^\beta. \quad (6.78)$$

The variable $|\log l|$ corresponds to the number of particles and $q-1$ corresponds to the inverse temperature β . It follows already from eq. (6.77) that, for $q \rightarrow +\infty$, the most concentrated parts of the measure (large \tilde{p}_i 's) are being stressed; whereas for $q \rightarrow -\infty$, the most rarified parts (small \tilde{p}_i 's) become dominant. In this sense, q indeed serves as the (inverse) temperature in statistical mechanics where at every temperature a different set of energy levels E_i (i. e., probabilities $\exp(-\beta E_i)$) becomes dominant in the free energy.

Fig. 85 shows the D_q and $f(\alpha)$ curves for the Feigenbaum attractor that is generated by the iterates of the logistic map $x_{n+1} = rx_n(1-x_n)$ at $r = r_\infty = 3.5699 \dots$ (see Section 4.4). The function $f(\alpha)$ must be concave because eq. (6.68b) requires $f''(\alpha) < 0$, and the maximum of $f(\alpha)$ at $\alpha = \alpha_m$ is equal to the Hausdorff dimension D_0 because at the maximum $f'(\alpha_m) = 0$ which yields via eqs. (6.68a–6.68b)

$$f'(\alpha_m) = q_m = 0 \quad (6.79)$$

and

$$D_0 = f(\alpha_m). \quad (6.80)$$

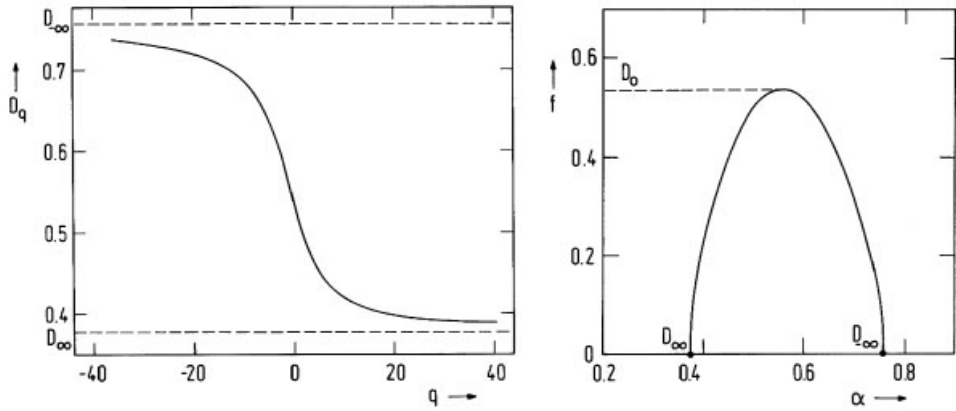


Figure 85: The functions D_q and $f(\alpha)$, computed from eqs. (6.33), (6.71), and (6.74), for the Feigenbaum attractor (after K. Pawelzik, priv. comm.).

Furthermore, we see from eq. (6.69) that, as long as $f(\alpha)$ remains bounded, the limiting dimension $D_{+\infty}$ becomes equal to the corresponding α values, i. e., $D_{+\infty} = \alpha(+\infty)$ which implies via eq. (6.59) $f[\alpha(+\infty)] = 0$. Thus, the zeros of $f(\alpha)$ are equal to $D_{\pm\infty}$, and the slope of $f(\alpha)$ is infinite at these points because of eq. (6.68a).

The dimension $D_{-\infty}$ which is associated with the most rarified regions of the Feigenbaum attractor can be calculated as follows. The size l_n , of the most rarified region on the 2^n attractor, which approaches the Feigenbaum attractor for $n \rightarrow \infty$, decreases as α^{-n} where α is the Feigenbaum constant. This is due to the fact that the function $\sigma(x)$ from Section 4.3 which measures the ratio of the distances between the elements of subsequent supercycles, has its maximum at α^{-1} (see Fig. 31); i. e., the largest distance decreases like α^{-n} . The probability p_n of a point on the 2^n cycle to lie within the interval l_n , is just $p_n = 2^{-n}$ because only one point of the cycle is contained in l_n . Putting everything together, $D_{-\infty}$ becomes:

$$D_{-\infty} = \lim_{q \rightarrow -\infty} \lim_{n \rightarrow \infty} \frac{1}{q-1} \frac{1}{\log l_n} \log p_n^{q-1} = \frac{\log 2}{\log \alpha} \cong 0.75551 \dots \quad (6.81)$$

which is in excellent agreement with the numerical result in Fig. 85 obtained from the time series of the logistic map. Figure 85 shows that D_q converges very slowly against its limits $D_{+\infty}$, but $\alpha(q = +\infty) = D_{+\infty}$ can be easily extrapolated from the corresponding $f(\alpha)$ curves. Thus, the transformation to $f(\alpha)$ leads to better estimates of $D_{+\infty}$ than the direct calculation of the D_q s. Another advantage of the $f(\alpha)$ spectrum is the fact that it represents (e. g., for the Feigenbaum attractor) a smooth universal curve which yields the global density of scaling indices. The universal function $\sigma(x)$ of Feigenbaum, which everywhere describes the local scaling (see Section 4.3), contains in principle the same (and even more) information as $f(\alpha)$, but it is nowhere differentiable and is, therefore, a function that is difficult to use. A further example where the merits of the $f(\alpha)$ representation of experimental data become obvious is given in Chapter 7 where we investigate the question whether an experimental orbit obtained from a forced Rayleigh–Bénard experiment is in the same universality class as the orbit generated from a circle map.

6.3.3 Generalized Entropies and Fluctuations around the K -Entropy

We generalize in this section the expression

$$K = \lim_{l \rightarrow 0} \lim_{n \rightarrow \infty} \frac{1}{n} \sum_{i_0 \dots i_{n-1}} P_{i_0 \dots i_{n-1}} \log P_{i_0 \dots i_{n-1}} \quad (6.82)$$

for the Kolmogorov entropy of a map [see eq. (6.15)] by introducing in analogy to the D_q s a whole set of entropies K_q :

$$K_q = - \lim_{l \rightarrow 0} \lim_{n \rightarrow \infty} \frac{1}{n} \frac{1}{q-1} \log \sum_{i_0 \dots i_{n-1}} P_{i_0 \dots i_{n-1}}^q \quad (6.83)$$

and we show, by way of an example, that their Legendre transformation is related to the spectrum of fluctuations $g(\lambda)$ around the K -entropy.

If we introduce a variable $T = e^{-n}$, eq. (6.83) can be rewritten as

$$K_q = \lim_{l \rightarrow 0} \lim_{T \rightarrow 0} \frac{1}{\log T} \frac{1}{q-1} \log \sum_{i_0 \dots i_{n-1}} P_{i_0 \dots i_{n-1}}^q \quad (6.84)$$

which looks – apart from the fact that we have a whole series of indices, instead of just one – similar to eq. (6.23) for the D_q s with l replaced by T . It is, therefore, reasonable to try, in analogy to eq. (6.64) the scaling ansatz

$$P_{i_0 \dots i_{n-1}} \propto T^{\lambda(i_0 \dots i_{n-1})} \quad (6.85)$$

where the number of $\lambda(i_0, \dots, i_n)$ in the interval λ , $\lambda + d\lambda$ is [in analogy to eq. (6.65)] proportional to

$$\rho(\lambda) T^{-g(\lambda)} d\lambda . \quad (6.86)$$

Using the same arguments as in eq. (6.86), we arrive at the limit $T \rightarrow 0$ at

$$K_q = \frac{1}{q-1} [\lambda q - g(\lambda)] \quad (6.87)$$

where λ is determined by the saddle point conditions:

$$g'(\lambda) = q \quad (6.88a)$$

and

$$g''(\lambda) < 0 . \quad (6.88b)$$

In order to see the physical meaning of the numbers λ and of the distribution $g(\lambda)$, we consider as a simple example the piecewise expanding map

$$f(x) = \begin{cases} \frac{x}{p} & \text{for } 0 \leq x \leq p \\ \frac{1-x}{1-p} & \text{for } p \leq x \leq 1 \end{cases} \quad (6.89)$$

shown in Fig. 86 and compute K_q and $g(\lambda)$ explicitly for the dynamical system defined by

$$x_{n+1} = f(x_n) . \quad (6.90)$$

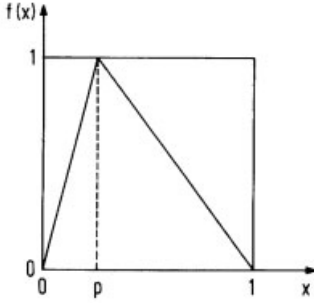


Figure 86: Tent map defined via eq. (6.89).

The probabilities $P_{i_0 \dots i_{n-1}}$ and the sums $\sum_{i_0 \dots i_{n-1}} P_{i_0 \dots i_{n-1}}^q \equiv S_q^n$ appearing in eq. (6.84) then become:

$$P_{i_0} = \begin{cases} p & \text{if } x_1 \in [0, p] \\ 1-p & \text{if } x_1 \in [p, 1] \end{cases} \rightarrow S_q^1 = p^q + (1-p)^q \quad (6.91)$$

$$P_{i_0 i_1} = \begin{cases} p^2 & \text{if } x_1, x_2 \in [0, p] \\ p(1-p) & \text{etc.} \\ (1-p)^2 & \end{cases} \rightarrow S_q^2 = [p^q + (1-p)^q]^2$$

i. e., $S_q^n = [p^q + (1-p)^q]^n$ which yields for K_q :

$$K_q = \frac{-1}{q-1} \log[p^q + (1-p)^q]. \quad (6.92)$$

For the limit $q \rightarrow 1$, we obtain from eq. (6.92) the Kolmogorov entropy

$$K_1 = p \log \left(\frac{1}{p} \right) + (1-p) \log \left(\frac{1}{1-p} \right). \quad (6.93)$$

K_1 is, as expected, equal to the positive Liapunov exponent λ_m of the system, which can also be obtained directly from

$$\lambda_m = \int dx \rho(x) \log |f'(x)| = p \log \left(\frac{1}{p} \right) + (1-p) \log \left(\frac{1}{1-p} \right) \quad (6.94)$$

where we used the fact that the invariant density $\rho(x) = 1$ for $f(x)$. (This can be checked by using eq. (6.89) in the Frobenius–Perron equation (3.29).

Next, we compute $\lambda(q)$ and $g(\lambda)$ via eqs. (6.87, 6.92):

$$\begin{aligned} \lambda(q) &= \frac{\partial}{\partial q} (q-1)K_q = \\ &= -[p^q \log p + (1-p)^q \log(1-p)] / [p^q + (1-p)^q] \end{aligned} \quad (6.95)$$

which becomes, for

$$x = p^q / [p^q + (1-p)^q], \quad (6.96)$$

equal to

$$\lambda = \lambda(x) = -[x \log p + (1-x) \log(1-p)] . \quad (6.97)$$

Similarly, we obtain from (6.87) and (6.96):

$$\begin{aligned} g[\lambda(q)] &= (q-1)K_q - q\lambda(q) = \\ &= -\log[p^q + (1-p)^q] + \\ &\quad + [p^q \log p^q + (1-p)^q \log(1-p)^q] / [p^q + (1-p)^q] \\ &= x \log x + (1-x) \log(1-x) . \end{aligned} \quad (6.98)$$

Equation (6.98) yields $g(\lambda)$ as shown in Fig. 89 if we eliminate x in favor of λ via eq. (6.97). The quantity $\lambda(x)$, which appears in eq. (6.97), has a very simple interpretation. It is just the “Liapunov exponent” of a *finite* series of iterates of length n which visits r times the interval $[0, p]$ in Fig. 86:

$$e^{n\lambda(y)} = \prod_j |f'(x_j)| = \left(\frac{1}{p}\right)^r \left(\frac{1}{1-p}\right)^{n-r} \quad (6.99)$$

$$\rightarrow \lambda(y) = -[y \log p + (1-y) \log(1-p)] \quad (6.100)$$

where $y = r/n$. The probability \hat{P} of finding it $\lambda(y)$ is equal to the probability of finding in a series of iterates, r times a point which is in $[0, p]$ and $(n-r)$ times a point which is located in $[p, 1]$, that is,

$$\hat{P} = \binom{n}{r} p^r (1-p)^{n-r} . \quad (6.101)$$

Using Stirlings’ formula $n! \cong n^n$, this becomes:

$$\begin{aligned} \log \hat{P} &\cong n \left[y \log \left(\frac{y}{p} \right) + (1-y) \log \left(\frac{1-y}{1-p} \right) \right] = \\ &= n[y \log y + (1-y) \log(1-y) - \lambda(y)] \end{aligned} \quad (6.102)$$

where we can again replace y by λ via eq. (6.90) to obtain $\hat{P}(\lambda)$.

By comparing eqs. (6.97–6.98) and (6.100, 6.102), we see that $e^{ng(\lambda)}$ is (apart from a factor e^{λ}) equal to the probability $\hat{P}(\lambda)$ of seeing in a finite series of iterates the “Liapunov exponent” λ . The Legendre transformation from the variable q in K_q to the variable λ yields, therefore, the distribution $g(\lambda)$ which describes the fluctuations of the Liapunov exponent for a time series of length n . Note that we used for our interpretation a map which is piecewise expanding (i. e., $|f'(x)| \geq 1$ for all $x \in [0, 1]$) and which yields, therefore, only positive expansion rates λ . For general systems (which can also be higher dimensional), our results generalize to the statement that $e^{ng(\lambda)}$ describes the fluctuation spectrum of the (sum of the) positive Liapunov exponents, i. e., of the Kolmogorov entropy for finite time series (see Fig. 87).

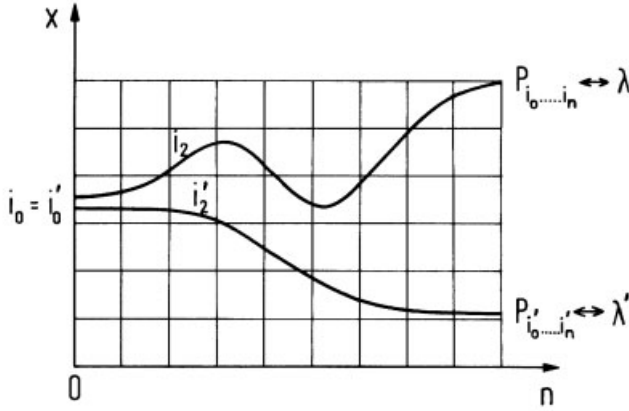


Figure 87: Different trajectories of length n occur with probabilities $P_{i_0...i_{n-1}}$. The distribution of the finite time “ K -entropies” $\lambda = -\lim_{l \rightarrow 0} (1/n) \sum_{i_0...i_{n-1}} P_{i_0...i_{n-1}} \log P_{i_0...i_{n-1}}$ is given by $e^{ng(\lambda)}$ where $g(\lambda)$ is the negative Legendre transformation of K_q .

The numerical computation of K_q from a measured time series proceeds in a fashion which is closely analogous to the D_q s. By generalizing eq. (6.74),

$$\sum_i p_i^q = \frac{1}{N} \sum_i \left\{ \frac{1}{n} \sum_j \Theta[l - |\bar{x}_i - \bar{x}_j|] \right\}^{q-1} = C_q(l), \tag{6.103}$$

to a whole trajectory of length n we obtain:

$$\begin{aligned} \sum_{i_0...i_{n-1}} P_{i_0...i_{n-1}}^q &= \frac{1}{N} \sum_i \left\{ \frac{1}{N} \sum_j \Theta \left[l - \sqrt{\sum_{m=0}^n (\bar{x}_{i+m} - \bar{x}_{j+m})^2} \right] \right\}^{q-1} \\ &\equiv C_n^q(l). \end{aligned} \tag{6.104}$$

This is again a generalization of a correlation integral $C_n(l)$ which has been introduced by Grassberger and Procaccia (1983b):

$$\begin{aligned} C_n(l) &= \lim_{N \rightarrow \infty} \frac{1}{N^2} \left\{ \text{number of pairs } ij \text{ with } \sqrt{\sum_{m=0}^{n-1} (\bar{x}_{i+m} - \bar{x}_{j+m})^2} < l \right\} \cong \\ &\cong \sum_{i_0...i_{n-1}} P_{i_0...i_n}^2 \end{aligned} \tag{6.105}$$

and which yields the correlation entropy:

$$K_2 = -\lim_{l \rightarrow 0} \lim_{n \rightarrow \infty} \frac{1}{n} \log \sum_{i_0...i_{n-1}} P_{i_0...i_{n-1}}^2. \tag{6.106}$$

K_2 represents, in analogy to eq. (6.57), a lower bound to the K -entropy $K = K_1 \geq K_2$, and $K_2 > 0$ provides a sufficient condition for chaos. Figure 88 shows the results for $C_n(l)$ and K_2 for the Hénon map with $a = 1.4$, $b = 0.3$.

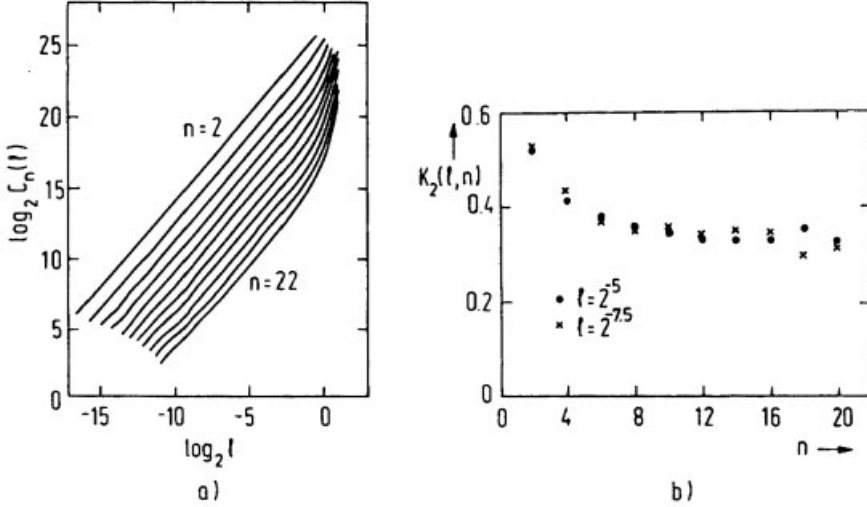


Figure 88: a) $\log C_n(l)$ versus $\log l$ for different values of n calculated from a series of $N = 15000$ points for the Hénon map. b) As $n \rightarrow \infty$ and $l \rightarrow 0$, $K_2(n, l)$ calculated from eq. (6.47) approaches the common value $K_2 = 0.325 \pm 0.2$ (Grassberger and Procaccia, 1983b).

However, eqs. (6.83, 6.104) yield, for $q \rightarrow 1$, an explicit expression for the K -entropy itself:

$$K = K_1 = \lim_{l \rightarrow 0} \lim_{n \rightarrow \infty} \frac{1}{n} \frac{1}{N} \sum_i \log \left\{ \frac{1}{N} \sum_j \Theta \left[l - \sqrt{\sum_{m=0}^{n-1} (\vec{x}_{i+m} - \vec{x}_{j+m})^2} \right] \right\} \quad (6.107)$$

which can be calculated from a measured signal. The condition $K > 0$ provides, of course, a sharper condition for chaos than $K_2 > 0$ (see also Cohen and Procaccia, 1985).

Let us finally summarize our results by a single formula which demonstrates that all generalized dimensions D_q and entropies K_q can be extracted from experimental data. Equations (6.83) and (6.104) yield for $n \rightarrow \infty$ and $l \rightarrow 0$:

$$\log C_n^q(l) \propto n(q-1)K_q. \quad (6.108)$$

If we watch the sequence of limits (first $n \rightarrow \infty$ then $l \rightarrow 0$), we can combine eqs. (6.33, 6.54, 6.74, 6.83, 6.104) and obtain the compact expression

$$\lim_{l \rightarrow 0} \lim_{n \rightarrow \infty} \log C_n^q(l) = (q-1)D_q \log l + n(q-1)K_q. \quad (6.109)$$

Therefore, a plot of $\log C_n^q(l)$ – which can be determined from an observed time series via eq. (6.104) – versus $\log l$ yields, for fixed q and different values of n , straight lines, with slopes $(q-1)D_q$ whose separations along the y -axis converge for $n \rightarrow \infty$ to $(q-1)K_q$ (see, e. g., Fig. 88 for $q = 2$). The spectra $f(\alpha)$ and $g(\lambda)$ can be obtained by Legendre transformation from these quantities. Figure 89 shows examples of K_q and $g(\lambda)$ curves that have been obtained by this method from a numerically generated time series of the tent map (6.89).

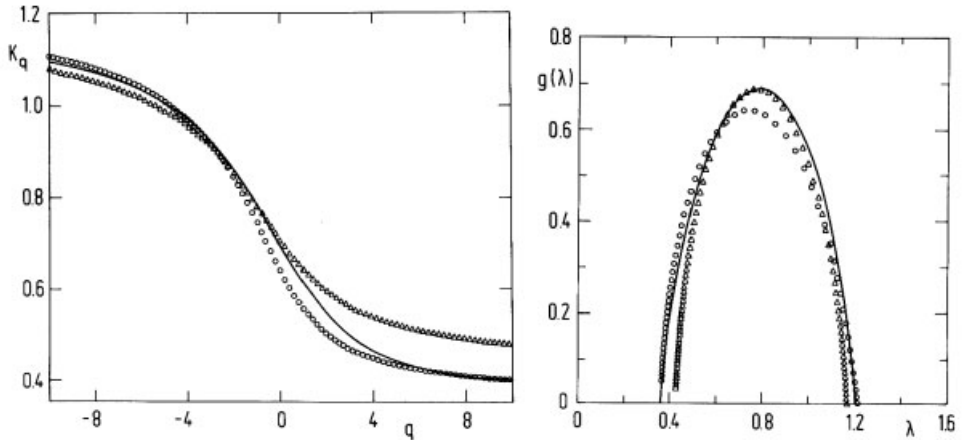


Figure 89: a) K_q - and b) $g(\lambda)$ -spectrum of the tent map [eq. (6.89)]. Full lines: Theoretical curves obtained from eqs. (6.87, 6.92). Dots: Numerical results obtained via eqs. (6.87, 6.109) for 2000 iterates. (After Pawelzik and Schuster, 1987.)

Let us finally add a word of caution. It is by no means completely straightforward to obtain, from an experimentally measured time series, the D_q and K_q curves, because the signal is noisy, the length of the series is finite, and the delay time which is needed to reconstruct the attractor [see eq. (6.44)] is generally unknown. All this adds a good deal of ambiguity to the application of the procedures described by eq. (6.109). We would like to call attention to the Proceedings of a conference on “Dimensions and Entropies in Chaotic Systems” (edited by Mayer-Kress, 1986) where merits and limits of different numerical procedures to extract dimensions, entropies, and Liapunov exponents from a time series are discussed.

6.3.4 Kaplan–Yorke Conjecture

Although we above made a distinction between dynamic properties of a strange attractor, such as the Liapunov exponents, and static properties measured by the D_q s, both quantities are in fact connected. For example, if we have a flow in three-dimensional phase space with two negative Liapunov exponents, we know that the attractor contracts to a line with $D_q = 1$ for all q (see Fig. 90).

Another example is the attractor which belongs to the non-area preserving baker’s transformation (6.7). Its Hausdorff dimension D_B [see eq. (6.10)] can be expressed in terms of the Liapunov exponents $\lambda_1 = \log 2$, $\lambda_2 = \log a$:

$$D_B = 1 + \frac{\lambda_1}{|\lambda_2|}. \quad (6.110)$$

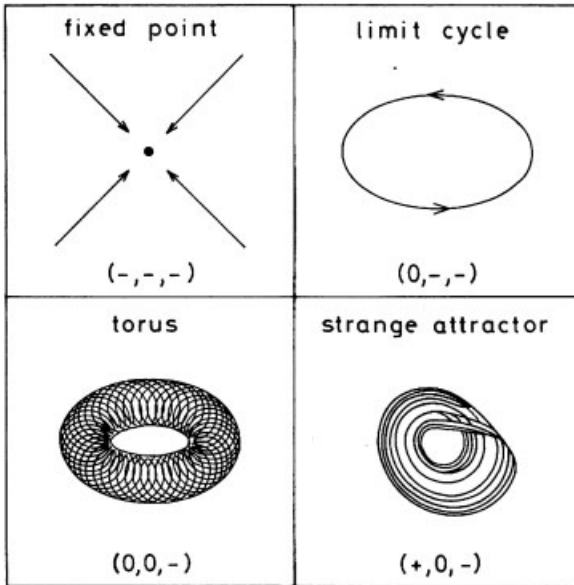


Figure 90: Connection between the dimensions of simple attractors embedded in three-dimensional phase space and the signs of their three Liapunov exponents given in the brackets. (Zero means that the Liapunov exponent has this value.) (After Shaw, 1981.)

Kaplan and Yorke (1979) conjectured the following more general formula for arbitrary strange attractors:

$$D_{KY} = j + \frac{\sum_{i=1}^j \lambda_i}{|\lambda_{j+1}|}. \quad (6.111)$$

Here D_{KY} is the Hausdorff dimension according to Kaplan and Yorke, and the Liapunov exponents are ordered $\lambda_1 > \lambda_2 > \dots > \lambda_d$, such that j is the largest integer for which $\sum_{i=1}^j \lambda_i > 0$. Although this formula has been checked numerically and shown to hold for some cases by Russel *et al.* (1980) (see Table 9), it seems to be rigorously valid only for homogenous attractors, and its range of applicability is still an active field of research.

Table 9: Test of the Kaplan–Yorke Conjecture.

System	D (numerically)	D_{KY}
Hénon map		
$a = 1.2, b = 0.3$	1.202 ± 0.003	1.200 ± 0.001
$a = 1.4, b = 0.3$	1.261 ± 0.003	1.264 ± 0.002
Zaslavsky map eq. (2.21a,b) for		
$f(x) = \cos x$	1.380 ± 0.007	1.387 ± 0.001

6.4 Pictures of Strange Attractors and Fractal Boundaries

D. Ruelle writes at the end of his article on strange attractors in *The Mathematical Intelligencer* (1980): “I have not (yet) spoken of the aesthetic appeal of strange attractors. These systems of curves, these clouds of points suggest sometimes fireworks or galaxies, sometimes strange and disquieting vegetal proliferations. A realm lies here to explore and harmonies to discover”. Figure 91 shows several examples of strange attractors that support this statement.

But we will see in the following that *already the boundaries of attraction* of simple rational maps of the complex plane onto itself *can have very complicated structures*. If these objects are plotted in color they show striking parallels to some of the self-similar pictures of M. C. Escher.

Let us begin with a study of the basins of attraction for the fixed points $z^* = (1, e^{2\pi i/3}, e^{4\pi i/3})$ of the map

$$z_{n+1} = z_n - (z_n^3 - 1)/(3z_n^2) \quad (6.112)$$

in the complex plane. (Equation (6.112) is just Newton’s algorithm for the solution of $f(z) = z^3 - 1 = 0$ ($0 = f(z) \approx f(z_0) + f'(z_0)(z - z_0) \rightarrow z_1 = z_0 - f(z_0)/f'(z_0)$, etc..))

One could think that the different basins of attraction for the roots z^* on the unit circle would be separated by straight lines. But, if one runs eq. (6.112) on a computer and colors starting points, which move to $1, e^{2\pi i/3}, e^{4\pi i/3}$, in red, green and blue, respectively (and black if the starting point does not converge), one sees from the results in Plate VIII (the color Plates I–XX are shown at the beginning of the book) that the boundary of the different basins forms highly interlaced self-similar structures (see also Fig. 92). This fractal boundary solves the nontrivial problem of how to paint a plane with three colors in such a way that each boundary point of a colored region (e. g., red) is also a boundary point of the other regions (green, blue).

The boundary of a basin of attraction of a rational map is nowadays called the *Julia set* (Julia, 1918) (for a more precise definition see, e. g., Brolin, 1965). “Usually” Julia sets are fractals (for $f(z) = z^2$ the Julia set is the unit circle), and the motion of iterates on these sets is chaotic.

Next we consider the map

$$z_{n+1} = f_c(z_n) = z_n^2 + c \quad (6.113)$$

in the complex plane for complex parameter values c . Equation (6.113) is the logistic map $x_{n+1} = rx_n(1 - x_n)$ in new variables $x = 1/2 - z/r$; $c = (2r - r^4)/4$.

The boundary of the basin of attraction of $z^* = \infty$ forms a Julia set J_c of $f_c(z)$, which depends on c :

$$J_c = \text{boundary of } \{z \mid \lim_{n \rightarrow \infty} f_c^n(z) \rightarrow \infty\} . \quad (6.114)$$

Figure 93 shows several examples of these sets. An important theorem by Julia (1981) and Fatou (1919) states that J_c is connected, if and only if, $\lim_{n \rightarrow \infty} f_c^n(0) \nrightarrow \infty$. Since this limit depends only on c , one is led to consider the set M of *parameter values* c in the complex plane for which J_c is connected, i. e.,

$$M = \{c \mid J_c \text{ is connected} = [c \mid \lim_{n \rightarrow \infty} f_c^n(0) \nrightarrow \infty] . \quad (6.115)$$

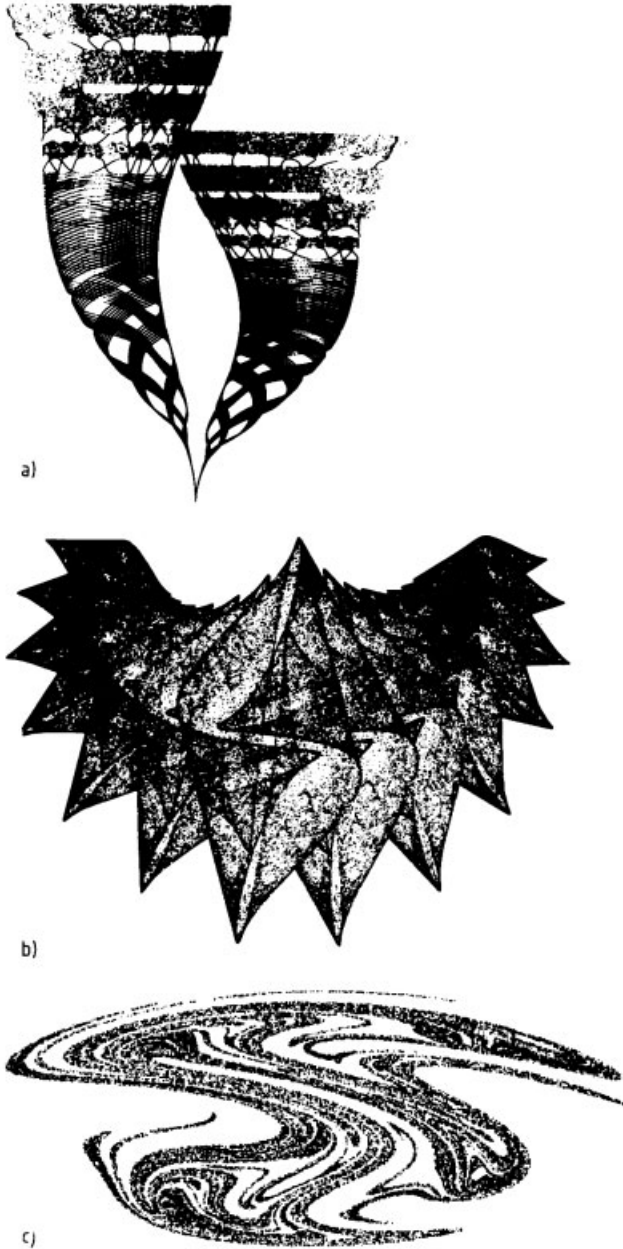


Figure 91: a), b), Both pictures are composed of different parts of strange attractors which arise if one iterates discretized versions of $\dot{y} = y(1 - y)$ and the pendulum equation, respectively (after Prüfer, 1984; Peitgen and Richter, 1984). c) Poincaré plot ($\bar{x}_n = \bar{x}(t = nT)$) of trajectories of the driven Duffing oscillator ($\ddot{x} + \gamma\dot{x} + ax + bx^3 = A + B \cos(2\pi t/T)$) in the chaotic regime (after Kawakami, 1984).

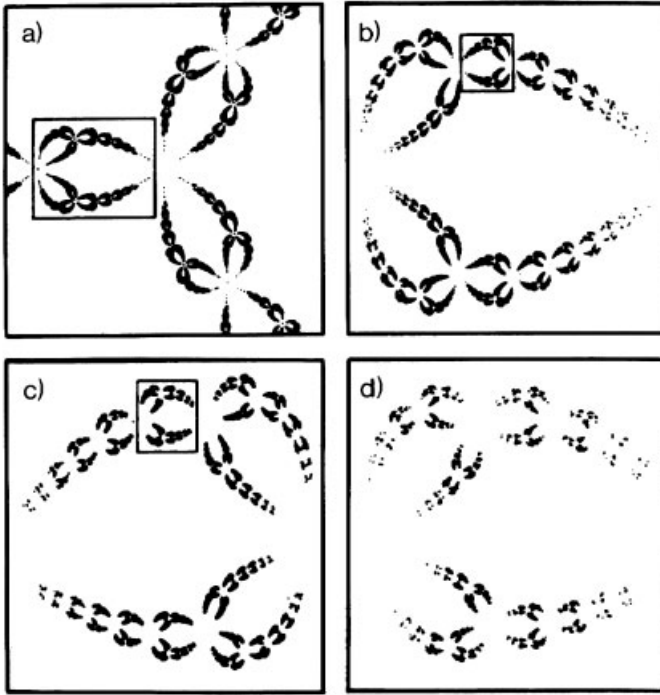


Figure 92: Self-similarity of the Julia set for eq. (6.112) (see also Plate VIII) (after Peitgen and Richter, 1984).

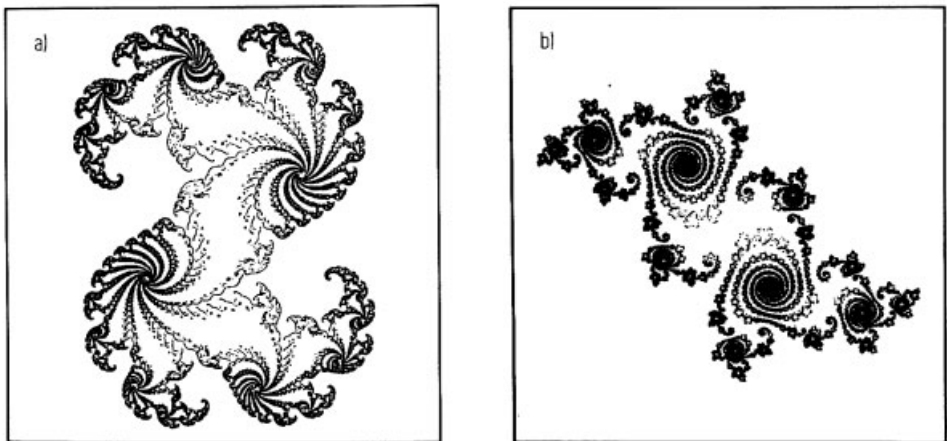


Figure 93: Two typical Julia sets of $f_c(z)$ in eq. (6.90). a) $c = 0.32 + 0.043i$, b) $c = -0.194 + 0.6557i$. (After Peitgen and Richter, 1984.)

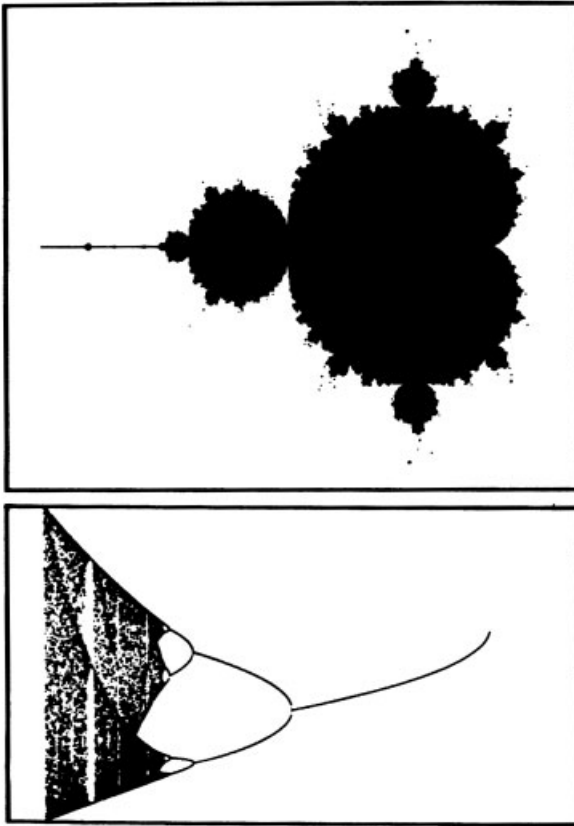


Figure 94: Correspondence between the structure of “Mandelbrot’s set” M in the c -plane and the structure of bifurcations of the (transformed) logistic map $x_{n+1} = x_n^2 + c$ along the real c -axis (after Peitgen and Richter, 1984).

The set M is called “Mandelbrot’s set” after B. B. Mandelbrot who first published (1980) a picture of M (see Fig. 94). It shows that M has also a fractal structure (but it is no Julia set). This study was extended by Peitgen and Richter (1984). If c does not belong to M , then $\lim_{n \rightarrow \infty} f_c^n(0) \rightarrow \infty$. Therefore, they define “level curves” in the following way: color a starting point according to the number of iterations it needs to leave a disk with a given radius R . As shown by Douady and Hubbard (1982), lines of equal color can be interpreted as equipotential lines if the set M is considered to be a charged conductor. Plates VIII–XV show the fascinating results of this procedure which brings us back to Ruelles’ remark at the beginning of this section.

7 The Transition from Quasiperiodicity to Chaos

In the first section of this chapter, we shall discuss the emergence of a strange attractor in the Ruelle–Takens–Newhouse route to turbulence (in time) and present some experimental support for this route. The subsequent section contains a study of the universal properties of the transition from quasiperiodicity to chaos via circle maps and we introduce two renormalization schemes, which are appropriate to describe local and global universality. In Section 7.3, we present experimental evidence that circle maps indeed provide a useful description of the transition from quasiperiodicity to chaos in real systems. The chapter ends with a critical review of different transition scenarios that lead to a chaotic behavior.

7.1 Strange Attractors and the Onset of Turbulence

We come now to one of the most fascinating and difficult questions; namely, how the onset of fluid turbulence in time (we will not consider the distribution of spatial inhomogeneities) is related to the emergence of a strange attractor.

To understand what has been undertaken in this area, we first introduce the Hopf bifurcation (Hopf, 1942).

7.1.1 Hopf Bifurcation

A simple Hopf bifurcation generates a limit cycle starting from a fixed point. For example, consider the following differential equations in polar coordinates:

$$\frac{dr}{dt} = -(\Gamma r + r^3); \quad \Gamma = a - a_c \quad (7.1a)$$

$$\frac{d\theta}{dt} = \omega. \quad (7.1b)$$

Their solutions are

$$r^2(t) = \frac{\Gamma r_0^2 e^{-2\Gamma t}}{r_0^2(1 - e^{-2\Gamma t}) + \Gamma} \quad \text{with} \quad r_0 = r(t=0) \quad (7.2a)$$

$$\theta(t) = \omega t \quad \text{with} \quad \theta(t=0) = 0. \quad (7.2b)$$

For $\Gamma \geq 0$ the trajectory approaches the origin (fixed point), whereas for $\Gamma < 0$ it spirals towards a limit cycle with radius $r_\infty = |(a - a_c)|^{1/2}$, as shown in Fig. 95.

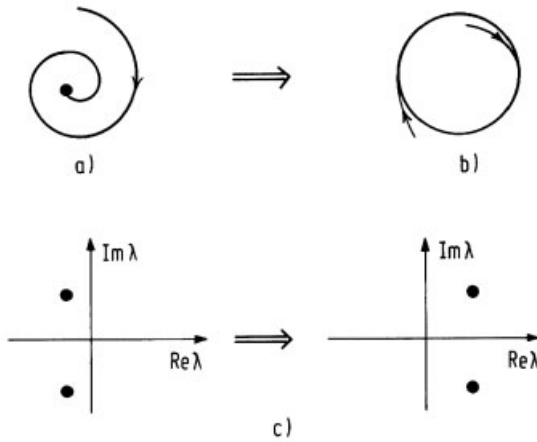


Figure 95: Hopf bifurcation from a fixed point (a) to a limit cycle (b), and behavior of the eigenvalues λ (c).

If (7.1a,b) is transformed into rectangular coordinates

$$\frac{dx}{dt} = -\{\Gamma + (x^2 + y^2)\}x - y\omega \quad (7.3a)$$

$$\frac{dy}{dt} = -\{\Gamma + (x^2 + y^2)\}y - x\omega \quad (7.3b)$$

and linearized about the origin, we obtain

$$\frac{d\vec{f}}{dt} = A\vec{f} \quad (7.4)$$

where $\vec{f} = (\Delta x, \Delta y)$, and A is the matrix

$$A = \begin{pmatrix} -\Gamma & -\omega \\ \omega & -\Gamma \end{pmatrix} \quad (7.5)$$

with eigenvalues $\lambda_{\pm} = -\Gamma \pm i\omega$. This means that at a Hopf bifurcation a pair of conjugate eigenvalues crosses the imaginary axis, as indicated in Fig. 95c.

7.1.2 Landau's Route to Turbulence

A Hopf bifurcation introduces a new fundamental frequency ω into the system. As early as 1944 Landau therefore suggested a route to turbulence (in time) in which the chaotic state is approached by an infinite sequence of Hopf instabilities, as shown in Fig. 96.

Although this route leads to a time dependence which becomes more and more complicated as more and more frequencies appear, the power spectrum always remains discrete and approaches the continuum limit only after an infinite sequence of Hopf bifurcations.

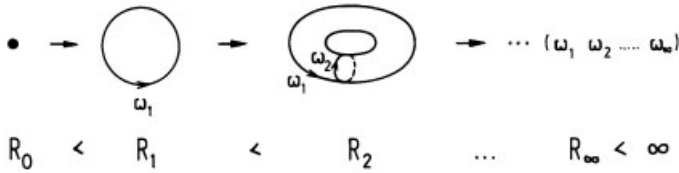


Figure 96: Landau's route to chaos. As the parameter R increases, more and more fundamental (i. e., incommensurate) frequencies are generated by Hopf bifurcations.

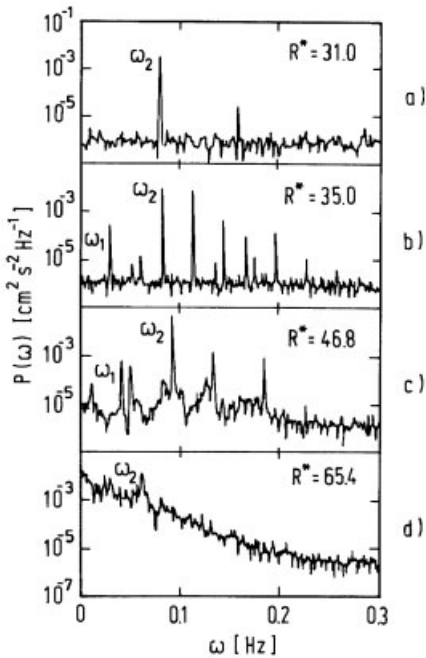


Figure 97: Power spectrum of the convection current for a Bénard experiment (after Swinney and Golub, 1978). With increasing (relative) Rayleigh number $R^* = R/R_c$ the following states are observed: a) periodic movement with one frequency and its harmonics, b) quasiperiodic motion with two incommensurate frequencies and their linear combinations, c) nonperiodic chaotic motion with some sharp lines, d) chaos.

7.1.3 Ruelle–Takens–Newhouse Route to Chaos

Figure 97 shows that this is not the case for the Bénard experiment. After the appearance of two fundamental frequencies, the power spectrum becomes continuous.

This experiment was in fact performed, after the theoretical work of Ruelle, Takens, and Newhouse (1978) who had suggested a route to chaos which is much shorter than that proposed by Landau (1944). They showed that, after three Hopf bifurcations, regular motion becomes highly unstable in favor of motion on a strange attractor (see Fig. 98).

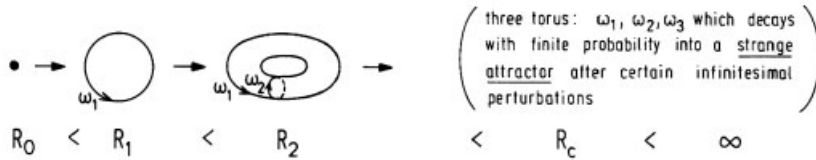


Figure 98: The Ruelle–Takens–Newhouse route to chaos.

To be precise, we quote their theorem verbatim (Ruelle, Takens, Newhouse) (1978): “Let v be a constant vector field on the n -torus $T^n = R^n/Z^n$. If $n > 3$, every C^2 neighborhood of v contains a vector field v' with a strange Axiom A attractor. If $n > 4$, we may take C^∞ instead of C^2 .” (Here C^2 means that the neighborhood of the vector field is twice continuously differentiable, an Axiom A attractor (see Smale, 1967) is essentially our strange attractor, and we finally mention that the original work of Ruelle and Takens (1971) described the decay of a four-torus instead of a three-torus as in the theorem above.)

This means practically that if a system undergoes three Hopf bifurcations, starting from a stationary solution as a parameter is varied, then it is “likely” that the system possesses a strange attractor after the third bifurcation. The power spectrum of such a system will exhibit one, then two, and then possibly three independent frequencies. When the third frequency is about to appear, some broad band noise will simultaneously appear if there is a strange attractor. Practically, the three torus can decay (into a strange attractor) immediately after the critical parameter value for its existence has been reached, such that one observes in the power spectrum only two independent frequencies, that is, two Hopf bifurcations and then chaos as shown in Fig. 97.

It is understandable that chaotic motion only becomes possible after two Hopf bifurcations, when the trajectory can explore additional dimensions, because doubly periodic motion corresponds to a trajectory on a torus (i. e., on a two-dimensional manifold), on which chaos is forbidden by the Poincaré–Bendixson theorem. However, Ruelle and Takens (1978) showed that a strange attractor is not only possible, but that there exist certain perturbations which definitely convert quasi-periodic motion on a three torus into chaotic motion on a strange attractor. The subtle point is that these perturbations can be infinitesimal; however, not all infinitesimal perturbations will lead to a destruction of the three torus such that the probability for the appearance of a strange attractor nevertheless can be small. The resulting attractor is, in contrast to the three-torus, robust with respect to small changes in the parameters of the system.

The proof of this theorem is mathematically too involved to be presented here. Instead, we will proceed as follows. First we will present the results of a numerical experiment by Grebogi, Ott and Yorke (1983) who investigated the strength of the perturbation which is needed to destroy a three-torus in favor of a strange attractor. Basically, they confirmed numerically the theorem of Ruelle, Takens and Newhouse (1978), which had been obtained analytically, but their calculations suggest that smooth perturbations must have a finite strength in order to generate a strange attractor from a three-torus. Next, we describe two experimental examples where three independent frequencies have been observed together with broadband noise in the

power spectrum, and two experiments in which the destruction of a two-torus into a strange attractor has been observed by reconstruction of the Poincaré map. Since, in the last two experiments, the third frequency has not been observed, one could ask whether there exists a direct transition from a two-torus to a strange attractor that is independent of the Ruelle–Takens–Newhouse (1978) mechanism. We leave this question open, because such a transition could be interpreted as an example of the Ruelle–Takens–Newhouse scenario in which the three-torus becomes destroyed by an infinitesimal perturbation at the very moment as it is about to appear, so that one practically observes the decay of a two-torus into a strange attractor (see, however, Curry and Yorke, 1978, for another interpretation). Finally, we discuss, in the next section, universal features of the transition from (two-frequency) quasiperiodicity to chaos in terms of simple circle maps, and describe some relevant experiments.

7.1.4 Possibility of Three-Frequency Quasiperiodic Orbits

Newhouse, Ruelle and Takens (1978) showed that, in a system with a phase-space flow consisting of three incommensurate frequencies, arbitrarily small changes to the system convert the flow from a quasiperiodic three-frequency flow to chaotic flow.

One might naively conclude that three-frequency flow is improbable since it can be destroyed by small perturbations. However, it has been shown numerically by Grebogi, Ott and Yorke (1983) that the addition of smooth nonlinear perturbations does not typically destroy three-frequency quasiperiodicity. (In the proof by Newhouse *et al.*, the small perturbations required to create chaotic attractors have small first and second derivatives, but do not necessarily have small third- and higher-order derivatives, as expected for physical applications.)

The calculation by Grebogi *et al.* (1983) can be summarized as follows: According to Section 7.2, the Poincaré map associated with a flow having two incommensurate frequencies (perturbed by $\varepsilon f(\theta)$) can be described by the map (7.13):

$$\theta_{n+1} = \theta_n + \Omega + \varepsilon f(\theta_n) \quad (7.6)$$

where $f(\theta)$ is periodic in θ , and θ_n is taken modulo 1. By analogy, a flow with three incommensurate frequencies corresponds to a map:

$$\theta_{n+1} = \theta_n + \omega_1 + \varepsilon P_1(\theta_n, \varphi_n) \quad (7.7a)$$

$$\varphi_{n+1} = \varphi_n + \omega_2 + \varepsilon P_2(\theta_n, \varphi_n) \quad (7.7b)$$

where θ_n and φ_n are again taken modulo 1, and $P_{1,2}$ are periodic in θ_n and φ_n . The parameters ω_1 , and ω_2 are incommensurate with each other and with unity; that is, integers p, r, q do not exist for which $p\omega_1 + q\omega_2 + r = 0$. By expressing $P_{1,2}$ as a Fourier sum of terms

$$A_{r,s} \sin[2\pi(r\theta + s\varphi + B_{r,s})] \quad (7.8)$$

and retaining (somewhat arbitrarily) only the terms $(r, s) = (0, 1), (1, 0), (1, 1), (1, -1)$, Grebogi *et al.* calculated the Liapunov exponents λ_1, λ_2 for the map (7.7) for random values of $\omega_1, \omega_2, A_{r,s}$ and $B_{r,s}$. Their results are summarized in Table 10, which shows that for a fixed typical choice of $P_{1,2}$ the measure of (ω_1, ω_2) yielding chaos approaches zero as $\varepsilon \rightarrow 0$. Three-frequency quasiperiodicity is possible only when $\varepsilon < \varepsilon_c$, where the map is invertible.

The data in this table were computed using 256 random values of (ω_1, ω_2) . The Liapunov exponents have been determined to the order 10^{-4} (Grebogi *et al.*, 1983a).

Table 10: Observed frequencies for different types of attractors.

Type of attractor	Liapunov exponents	$\frac{\varepsilon}{\varepsilon_c} = \frac{3}{8}$	$\frac{\varepsilon}{\varepsilon_c} = \frac{3}{4}$	$\frac{\varepsilon}{\varepsilon_c} = \frac{9}{8}$
Three-frequency quasiperiodic	$\lambda_1 = \lambda_2 = 0$	82 %	44 %	0 %
Two-frequency quasiperiodic	$\lambda_1 = 0 \lambda_2 < 0$	16 %	38 %	33 %
Periodic	$\lambda_1 < 0 \lambda_2 < 0$	2 %	11 %	31 %
Chaotic	$\lambda_1 > 0$	0 %	7 %	36 %

A transition from quasiperiodicity to chaos which still exhibits three-frequency quasiperiodicity (i. e., the decay of this state to a strange attractor is not complete) has been observed by Libchaber, Fauve, and Laroche (1983) in a Bénard experiment with mercury in a magnetic field (see Fig. 99) and by Martin, Leber and Martienssen (1984) in the voltage spectrum of a ferroelectric Barium-Sodium-Niobate (BSN) crystal (see Fig. 100).

In the first case, the horizontal field serves as a second control parameter and additionally increases the viscosity of the electrically conducting fluid. In the second, the $\text{Ba}_2\text{NaNb}_5\text{O}_{15}$

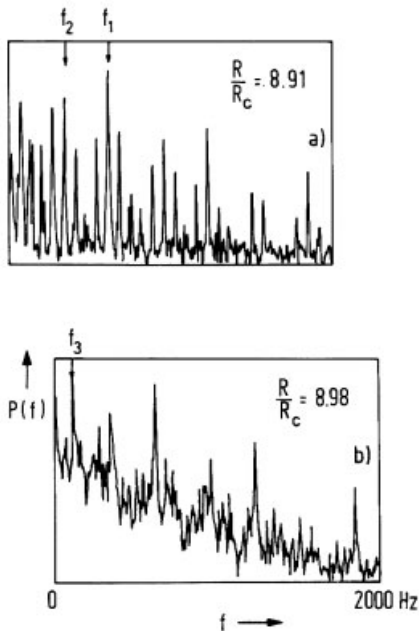


Figure 99: Log-linear plot of the power spectrum (of the local temperature) in a Bénard experiment with mercury in a magnetic field. a) Quasiperiodic region with two incommensurate frequencies f_1 and f_2 ; b) three-frequency periodicity, i. e., f_1 , f_2 and f_3 are present together with self-generated noise which decays exponentially. (Libchaber *et al.*, 1983.)

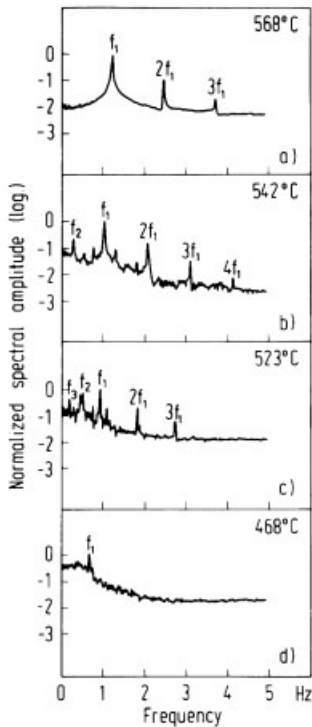


Figure 100: Power spectrum of the voltage across a BSN crystal through which a constant dc-current is maintained. With decreasing temperature, one observes a transition from one→two→three fundamental frequencies to chaos (after Martin, Leber and Martienssen, 1984).

crystal, which displays a nonlinear current–voltage characteristic, is placed into a heating oven through which a constant flow of humidified oxygen is maintained (part of the conduction mechanism is due to oxygen vacancies). A stabilized dc current is applied along the c -axis of the sample and one measures the voltage across the crystal together with the birefringence pattern. With increasing voltage, “domains” emerge from the cathode and disperse gradually through the crystal (see Plate IV at the beginning of the book). Since there are *three* control parameters (temperature, current density and oxygen flow), BSN provides an interesting system for experimental studies of chaos.

7.1.5 Break-up of a Two-Torus

It has been mentioned above that the conversion of quasiperiodic motion into chaotic motion on a strange attractor could occur apparently from a two-torus if the three-torus is so unstable that the third incommensurate frequency cannot be observed. Such transitions belong in principle also to the Ruelle–Takens–Newhouse scenario (see, however, Curry and Yorke, 1978) and have been seen in two hydrodynamic experiments.

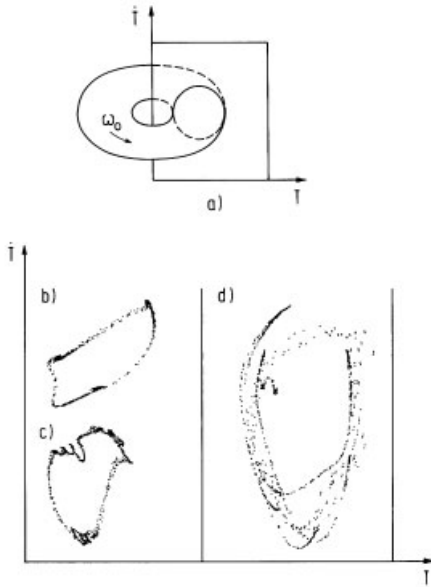


Figure 101: Poincaré sections for the Bénard experiment: a) Schematic section through torus; b)–d) experiments showing with increasing Rayleigh number a transition from quasiperiodic motion (b) to substructures indicating the destruction of the torus (c) and then to a strange attractor (d). (After Dubois, Berge and Croquette, 1982.)

Dubois and Berge (1982) observed experimentally the emergence of a strange attractor in a Bénard experiment. They measured the time series of temperature $T(t)$ and reconstructed a two-dimensional Poincaré section by plotting $[T(t), \dot{T}(t)]$ at intervals $t = n\tau$, where $\omega_0 = 2\pi/\tau$ was determined from an independent measurement of the velocity. (This is another method of reconstructing an attractor from the measurement of one variable; note that in our example from chapter 6.3 $\vec{x}(t) = [\sin(2\pi t), \cos(2\pi t)]$ [eq. (6.43)] the y component $y = \cos(2\pi t)$ could be obtained by differentiation, i. e., $y \propto \dot{x}$.) Figure 101 shows how the Poincaré section, which consists of a closed loop (as expected for a section of a torus), develops into a strange attractor.

Another example for the emergence of chaos after two Hopf bifurcations has been observed after a Taylor instability by Swinney and Gollub (1978). The Taylor instability occurs in a fluid layer between an inner cylinder rotating with an angular velocity Ω and a stationary outer cylinder (see Fig. 102 and Plate III at the beginning of the book). For small Ω , angular momentum fed to the inner cylinder is transported outside by viscosity (a). Above a critical angular velocity Ω_c , this state becomes unstable, and momentum is transported by annular convection cells (b). At still higher Ω s, periodic and multiply periodic oscillations of these cells occur which merge into chaos after two Hopf bifurcations.

The following results in Fig. 103 have been obtained by reconstructing the phase space for a Taylor experiment from a time series of the radial velocity $\{v(t_k), \dots, v(t_k + m\tau)\}$ with $t_k = k \cdot \tau_0$, $k = 0, 1, 2, \dots$, ($\tau_0 < \tau$):

- a) The Poincaré section shows the break-up of a torus similar to Fig. 101.

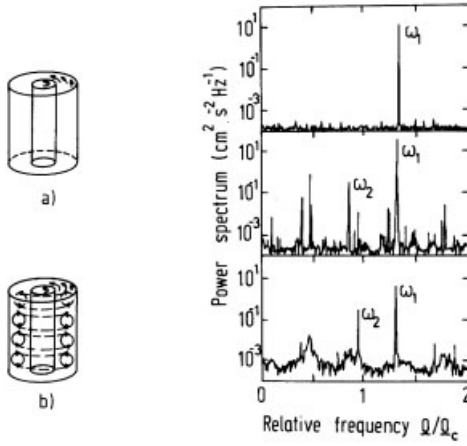


Figure 102: The Taylor instability and power spectrum of the velocity (after Swinney and Gollub, 1978).

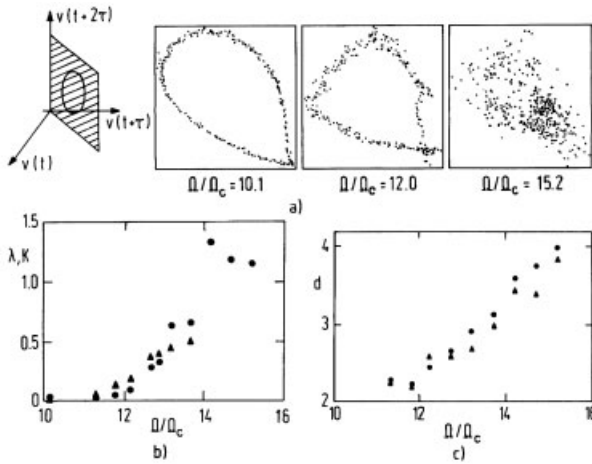


Figure 103: Experimental properties of a strange attractor which occurs in a Taylor experiment: a) Plane of the Poincaré section and break-up of the torus with increasing Ω . b) K -entropy (\blacktriangle) and largest Liapunov exponent (\bullet) vs. Ω/Ω_c . c) Hausdorff dimension D (\bullet) and correlation dimension D_2 (\blacktriangle) vs. Ω/Ω_c . (After Brandstätter *et al.*, 1983.)

- b) The K -entropy [obtained via eq. (6.109)] and the largest Liapunov exponent λ (obtained from the separation of nearby orbits in five-dimensional phase space) become positive for $\Omega > \Omega^*$. This proves experimentally the existence of a *strange* attractor.
- c) The Hausdorff dimension D (obtained via eq. (6.49)) and D_2 (obtained via eq. (6.76)) increase slowly with Ω/Ω_c . This shows that there are only a *few relevant degrees of freedom* even at Ω -values that are 30% above the critical value $\Omega^* = 120$, at the onset of chaos.

7.2 Universal Properties of the Transition from Quasiperiodicity to Chaos

The transition from quasiperiodic motion on a two-torus to chaotic motion has also been investigated by studying simple maps (Feigenbaum and Kadanoff, 1982; Rand *et al.*, 1982, 1983; Jensen *et al.*, 1984).

Figure 104 shows that the motion on an unperturbed unit torus can be described in polar coordinates by the Poincaré map

$$\theta_{n+1} = f(\theta_n) \equiv \theta_n + \Omega \bmod 1. \quad (7.9)$$

The parameter $\Omega = \omega_1/\omega_2$ determines the winding number

$$w = \lim_{n \rightarrow \infty} \frac{f^n(\theta_0) - \theta_0}{n} \quad (7.10)$$

which measures the average shift of the angle θ per iteration in eq. (7.10), the modulo in f has to be omitted. We find from eqs. (7.9–7.10) $w = \Omega$. But it should be noted that the definition of the winding number w given in eq. (7.10) holds for all maps of the unit circle onto itself.

In order to obtain an idea of how eq. (7.9) should be modified to describe the break-up of a torus in a physical system, we reconsider our kicked rotator from Chapter 2, eq. (2.18), for the case when a constant torque $\Gamma\Omega$ has been added to the driving force. If we make, in eqs. (2.18a,b), the following simplifying substitutions for $T = 1$:

$$x_n \rightarrow \theta_n; \quad \frac{e^\Gamma - 1}{\Gamma} y_n - \Omega \rightarrow r_n; \quad e^{-\Gamma} = b \quad (7.11a)$$

$$Kf(\theta_n) \rightarrow \frac{\Gamma}{1 - e^{-\Gamma}} \frac{K}{2\pi} \sin(2\pi\theta_n) + \Gamma\Omega \quad (7.11b)$$

we obtain

$$\theta_{n+1} = \theta_n + \Omega - \frac{K}{2\pi} \sin(2\pi\theta_n) + br_n \bmod 1, \quad (7.12a)$$

$$r_{n+1} = br_n - \frac{K}{2\pi} \sin(2\pi\theta_n), \quad (7.12b)$$

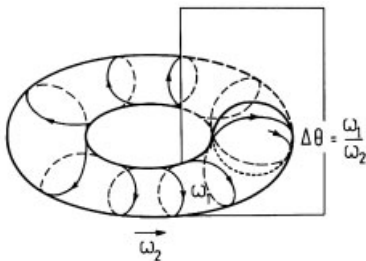


Figure 104: Motion on a unit torus. For rational $\omega_1/\omega_2 = p/q$, the trajectory closes after q -cycles. This is called a *mode-locked* state. For irrational ω_1/ω_2 , the motion is called *quasiperiodic*; the trajectory never closes and covers the whole torus.

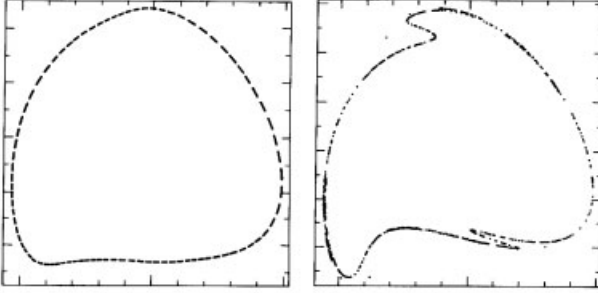


Figure 105: Break-up of a torus as described by the dissipative circle map [eqs. (7.12a,b)] (after Bauer, priv. comm.).

where θ_n is the angle of the kicked rotator at time n , $r_n = y_n[(e^\Gamma - 1)/\Gamma] - \Omega$ is – apart from a constant shift – proportional to the angular velocity $y_n = \dot{\theta}(t = n)$. Equations (7.12a–7.12b) define the so-called *dissipative circle map*. For vanishing nonlinearity ($K = 0$) and finite damping rate $b = e^{-\Gamma} < 1$, eqs. (7.12a–7.12b) reduce to the unperturbed map eq. (7.9) where Ω sets the rate of rotation.

Figure 105 shows that the dissipative circle map indeed describes the break-up of a torus if the parameter K which measures the strength of the nonlinearity $\sin(2\pi\theta_n)$ is increased from $K = 0.814$ to $K = 1.2$. In both pictures, we plotted $y_n = (1 + 4r_n)\sin\theta_n$ versus $x_n = (1 + 4r_n)\cos\theta_n$ with θ_n and r_n from eq. (7.12) and $\Omega = 0.612$, $b = 0.5$.

These pictures should be compared to Figs. 101 and 103 which show the destruction of a torus in experimentally measured Poincaré maps. For strongly dissipative systems ($b \rightarrow 0$), the radial motion of the trajectory disappears in eqs. (7.12a, b), and they reduce to the one-dimensional circle map:

$$\theta_{n+1} = f(\theta_n) \equiv \theta_n + \Omega - \frac{K}{2\pi} \sin(2\pi\theta_n) \bmod 1, \quad (7.13)$$

which describes the transition from quasiperiodicity to chaos only by the motion of the angles θ_n . Here θ_n is again understood modulo 1; K provides, in analogy to the Reynold's number, a measure for the nonlinearity $\sin(2\pi\theta_n)$ (which must be added to obtain a transition to chaos), and Ω again sets the rate of rotation [see eq. (7.10)]. In the following section, we study the break-up of the torus into a strange attractor via this map. It will be shown below that (by analogy to the logistic map for the period-doubling route) the special form of $f(\theta)$ is rather unimportant, and, of more importance, are the following general features of $f(\theta)$:

- $f(\theta)$ has the property $f(\theta + 1) = 1 + f(\theta)$.
- For $|K| < 1$, $f(\theta)$ (and its inverse) exists and is differentiable (i. e., $f(\theta)$ is a diffeomorphism).
- At $K = 1$, $f^{-1}(\theta)$ becomes nondifferentiable, and for $|K| > 1$, no unique inverse to $f(\theta)$ exists.

To obtain an overview of the behavior of the circle map (7.13), we show in Plate XVI (at

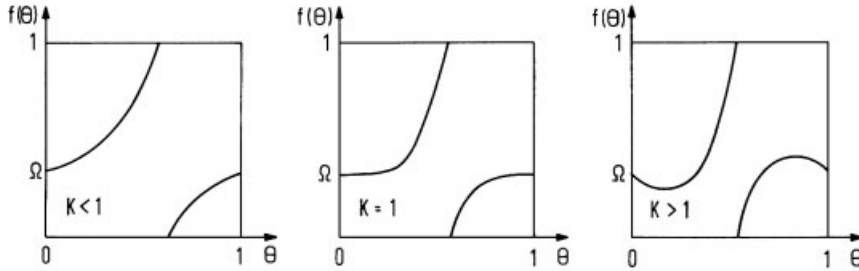


Figure 106: Variation of the map $f(\theta)$ with the parameter K . Note, that for $K > 1$, the map becomes noninvertible.

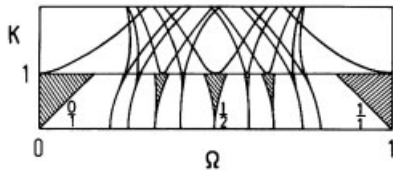


Figure 107: Phase diagram of the circle map (schematically). $K < 1$: Within the Arnold's tongues (hatched) the winding number w is rational, and one has mode locking. $K = 1$: the Arnold's tongues moved together, the remaining nonmode-locked "holes" form a Cantor set. $K > 1$: Chaos becomes possible, but coexists with order. The lines correspond to the parameter values for superstable, that is, nonchaotic cycles which are associated with the mode-locking regimes.

the beginning of this book) its Liapunov exponent λ depicted in colors as a function of the two control parameters K and Ω . We distinguish three regimes (cf. Fig. 106):

- For $|K| < 1$, one finds the so-called Arnold's tongues (Arnold, 1965) where the motion is mode-locked; that is, the winding number w [see eq. (7.10)] is rational. Between these tongues, the winding number is irrational. Both areas in the $K - \Omega$ plane, the mode-locking and the non-mode-locking one, are finite (see Fig. 107).
- At $K = 1$, the Arnold's tongues moved together in such a way that the non-mode-locked Ω intervals form a self-similar Cantor set with zero measure.
- For $|K| > 1$, the map becomes noninvertible, chaotic behavior becomes possible, but chaotic and nonchaotic regions are densely interwoven in parameter space (i. e., the $K - \Omega$ plane).

In the following section, we will investigate these different regimes in more detail. In the first part of this section, we study the nonchaotic mode-locking behavior. Mode locking means, according to eq. (7.10), that the ratio between the number of cycles, which the system executes divided by the number of oscillations of the driving force (think of a kicked rotator), is a rational number. Thus, mode locking with winding number $w = 1$ corresponds to complete synchronization between the external force and the system. Since this phenomenon occurs very often in nature – already in the 17th century the Dutch physicist Ch. Huyghens observed

synchronization between two clocks hanging back-to-back on a wall – the understanding of mode locking in nonlinear systems is of considerable interest.

In the second part of this section, we investigate universal properties at the transition from quasiperiodicity to chaos using different renormalization group formalisms. Since one has two control parameters K and Ω one has to distinguish between *local* scaling behavior, which occurs *near a point* in the $K - \Omega$ plane, and *global* scaling behavior, which occurs *for a whole set of Ω values* and describes the merging together of the Arnold tongues as the line $K = 1$, is approached in Fig. 107.

It will be shown that the local transition from quasiperiodicity to chaos near an irrational winding number displays, as a function of the control parameter Ω in its renormalization group description, some formal analogies to the period-doubling route. In contrast, the numerically found global scaling requires a different normalization group approach, and we will only calculate the universal Hausdorff dimension of the Cantor set which is formed by the non-mode-locked Ω intervals at $K = 1$ (see Fig. 107).

7.2.1 Mode Locking and the Farey Tree

In this subsection, we investigate the mode locking which occurs in the iterates of the circle map. It will be shown that for fixed K the width of an Arnold tongue decreases if the denominator q in the corresponding rational winding number $w = p/q$ increases. The resulting hierarchy of tongues at $K = 1$ can be conveniently represented by a Farey tree which orders all rationals in $[0, 1]$ according to their increasing denominators (see Hardy and Wright, 1938).

For a general mode-locked state with $w = p/q$, the corresponding Ω interval $\Omega = \Omega(K)$ can be calculated from the condition that a q -cycle with elements $\theta_1^*, \dots, \theta_q^*$ occurs in the circle map (7.13):

$$f_{\Omega, K}^q(\theta_i^*) = p + \theta_i^* \quad (7.14)$$

which is stable, i. e.,

$$f_{\Omega, K}^q(\theta_i^*) = \left| \prod_{i=1}^q f'_{\Omega, K}(\theta_i^*) \right| = \left| \prod_{i=1}^q [1 - K \cos(2\pi\theta_i^*)] \right| < 1. \quad (7.15)$$

(Here the indices K and Ω indicate that the left hand side in eqs. (7.14, 7.15) is still a function of both variables.) Equations (7.13–7.15) yield, e. g., for $w = 1$:

$$f_{\Omega, K}(\theta_0) = \theta_0 \rightarrow \Omega = \frac{K}{2\pi} \sin(2\pi\theta_0) \quad (7.16)$$

and

$$|f'_{\Omega, K}(\theta_0)| = |1 - K \cos(2\pi\theta_0)| < 1. \quad (7.17)$$

For $|K| < 1$, the boundaries $|f'_{\Omega, K}(\theta_0)| = 1$ are reached for $\theta_0 = \pm\pi/4$ which implies, via eq. (7.16), that the first Arnold tongue is a triangle with a width Ω

$$\Omega = \pm \frac{K}{2\pi} \quad (7.18)$$

as shown in Fig. 107.

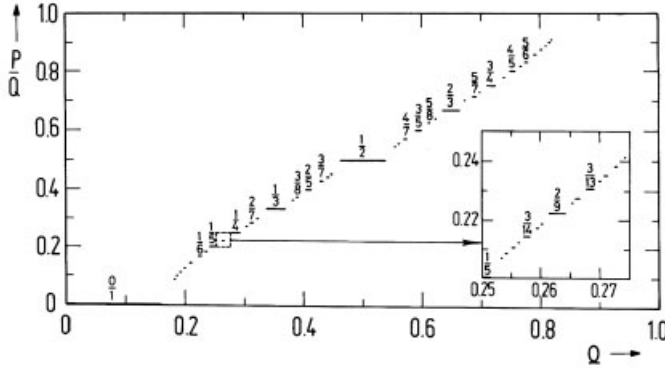


Figure 108: The mode-locking structure of the circle map, eq. (7.13) at $K = 1$. The devil’s staircase is complete; the numbers denote the rational winding numbers (after Jensen *et al.*, 1984).

The general eqs. (7.13–7.15) have been solved numerically by P. Bak and T. Bohr (1984) who found that for $0 < K < 1$ a whole interval $\Delta\Omega(p/q, K)$ of Ω values is associated to every rational winding number. For $K = 1$, these intervals form a complete self-similar devil’s staircase as shown in Fig. 108. The staircase for $K = 1$ is termed complete because the sum S of all Ω intervals is equal to 1, i. e.,

$$S = \sum_{p,q} \Delta\Omega(p/q, 1) = 1 . \tag{7.19}$$

For $0 < K < 1$, the staircase becomes incomplete, i. e., $S < 1$.

Figure 108 shows that the widths of the steps become smaller if the denominator in the corresponding winding number increases. Furthermore, if we have two steps with winding numbers p/q and p'/q' , then the largest step in between has a winding number $(p + p')/(q + q')$. If we list a few examples: $0/1 < 1/2 < 1/1$; $1/2 < 2/3 < 1/1$; $1/2 < 3/5 < 2/3$, etc., we see that $(p + p')/(q + q')$ is the rational number with the smallest denominator which lies between p/q and p'/q' . Thus the Farey tree, shown in Fig. 109, which orders all rationals p/q in $[0, 1]$ with increasing denominators q , orders also all mode-locking steps with $w = p/q$ in the circle map according to their decreasing widths.

Up to now, our observations were only based on numerical evidence shown in Fig. 108; however, there exists also a simple analytical result that establishes the relation between the devil’s staircase and the Farey tree.

The monotony of the circle map (and its iterates) in Ω implies that to every winding number in the Farey tree belongs exactly one mode-locking step in the devil’s staircase. Suppose one has a superstable q -cycle $f_{\Omega(p,q)}^q(\theta) = p + \theta$ and a q' -cycle $f_{\Omega(p',q')}^{q'}(\theta')$. If we combine both iterations we obtain:

$$f_{\Omega(p,q)}^q[f_{\Omega(p',q')}^{q'}(\theta)] = p + p' + \theta \tag{7.20}$$

that is, a cycle with the winding number $(q + q')/(p + p')$. Increasing $\Omega(p, q)$ in $f_{\Omega(p,q)}^q$ overshoots this cycle. This can be compensated by reducing $\Omega(p', q')$ in $f_{\Omega(p',q')}^{q'}$. Due to the fact that both iterates are monotonous in Ω , one can repeat this procedure until both Ω values

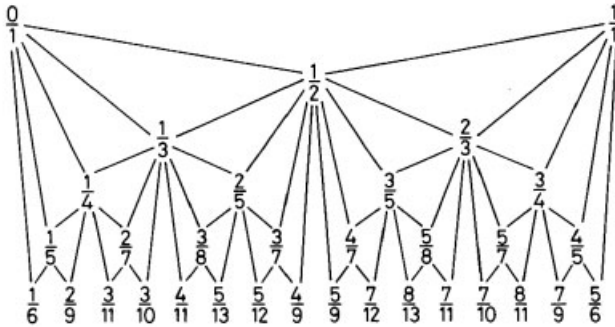


Figure 109: The Farey tree orders all rationals in $[0, 1]$ with increasing denominators according to the rule that the largest rational between p/q and p'/q' is $(p+p')/(q+q')$ (after Cvitanovic and Soderberg, 1985a).

coincide. Hence, the Ω interval between the p/q and p'/q' cycles, always contains an Ω value which corresponds to a $(p+q')/(q+q')$ cycle as claimed above.

The Farey tree construction has a universal importance because it orders not only the mode-locking regions for the circle map, but also for real systems such as a driven pendulum, Josephson junctions, and sliding charge density waves. This of course means that the dynamics of these systems can be reduced to circle maps as will be shown in Section 7.3.

7.2.2 Local Universality

The transition from quasiperiodicity to chaos is characterized by two types of universality. One is associated with the transition from quasiperiodicity to chaos for a special, that is, local winding number, and it shows close parallels to the period-doubling route. Its experimental verification is difficult because minute changes in winding numbers lead to large changes in scaling behavior. The second type is called global universality and pertains to a whole range of winding numbers. It describes the scaling behavior of the set of Ω values, complementary to the Arnold tongues on which the dynamical system is mode-locked, and it has been observed experimentally in several systems.

We begin with an investigation of the transition from quasiperiodicity to chaos for the golden mean winding number, because it also forms the basis for the investigation of the global universality for the circle map. In order to observe a transition from quasiperiodicity to chaos in the iterates of (7.13), two parameters have to be adjusted. If we increase, for example, the nonlinearity via K , Ω must always be balanced to keep the winding number w fixed to a given irrational value (this guarantees quasiperiodicity). But how can this be performed for a winding number which still gives the average shift of θ per iteration, and which, however, for general maps has to be defined as the limit [see eq. (7.10)]:

$$w = \lim_{n \rightarrow \infty} \frac{f^n(\theta_0) - \theta_0}{n} \quad (7.21)$$

(where the modulo in f has to be omitted)? We use the following method which has been suggested by Greene (1979) (in a similar context for Hamiltonian systems). One calculates

for fixed K the value $\Omega_{p,q}(K)$ which a) belongs to a q -cycle of the map $f(\theta)$, b) contains $\theta = 0$ as an element, and c) provides a shift by p . Thus, $\Omega_{p,q}$ which generates a rational winding number $w = p/q$, is defined by

$$f_{K,\Omega}^q(0) = p. \quad (7.22)$$

Next, the irrational winding number is approximated by a sequence of truncated continued fractions, i. e., rationals. If we consider, for example, the winding number $w^* = (\sqrt{5} - 1)/2$ which has as a continued fraction of the simple form

$$w^* = \frac{1}{1 + \frac{1}{\dots}} \quad (7.23)$$

then the so-called *Fibonacci numbers* F_n which are defined by

$$F_{n+1} = F_n + F_{n-1}; \quad F_0 = 0; \quad F_1 = 1; \quad n = 0, 1, 2, \dots \quad (7.24)$$

via

$$w_n = \frac{F_n}{F_{n+1}} = \frac{F_n}{F_n + F_{n-1}} = \quad (7.25a)$$

$$= \frac{1}{1 + \frac{F_{n-1}}{F_n}} = \frac{1}{\underbrace{1 + \frac{1}{\dots}}_{n \text{ times}}} \quad (7.25b)$$

yield a sequence of rationals w_n which converges towards

$$w^* = \lim_{n \rightarrow \infty} w_n. \quad (7.26)$$

For $n \rightarrow \infty$ eqs. (7.25a, b) yield

$$w^* = \frac{1}{1 + w^*} \rightarrow w^{*2} + w^* - 1 = 0 \rightarrow w^* = (\sqrt{5} - 1)/2. \quad (7.27)$$

This number is the so-called *golden mean*, which is defined in geometry by sectioning a straight line segment in such a way that the ratio of the longer segment l to the total length L equals the ratio of the shorter segment to the longer segment, i. e., $w^* = l/L = (L - l)/l$. In the following, we confine ourselves to this special winding number $w^* = (\sqrt{5} - 1)/2 = 0.6180339$, which is the “worst” irrational number in the sense that it is least well approximated by irrationals [see eqs. (7.23–7.25)]. Although any given irrational number has a unique representation by continued fractions, the renormalization scheme has, up to now, only been applied to the so-called quadratic irrationals, which are the solutions of a quadratic equation with integer coefficients, and for which the continued fraction representation is periodic.

Using the procedure described above, Shenker (1982) obtained the following numerical results for the circle map (7.13):

- a) The values of the parameters $\Omega_n(K)$ (7.13) which via (7.22) generate the winding numbers w_n in (7.25), geometrically tend to a constant, i. e.,

$$\Omega_n(K) = \Omega_\infty(K) - \text{const} \cdot \tilde{\delta}^{-n} \quad (7.28a)$$

where

$$\tilde{\delta} = \begin{cases} -2.6180339\dots & = -w^*-2 & \text{for } |K| < 1 \\ -2.83362\dots & & \text{for } |K| = 1 \end{cases} \quad (7.28b)$$

is a universal constant that, however, depends on w^* .

- b) The distances d_n from $\theta = 0$ to the nearest element of a cycle which belongs to w_n

$$d_n = f_{\Omega_n}^{F_n}(0) - F_{n-1} \quad (7.29a)$$

scale like

$$\lim_{n \rightarrow \infty} \frac{d_n}{d_{n+1}} = \tilde{\alpha} \quad (7.29b)$$

where $\tilde{\alpha}$ is again a universal constant with values

$$\tilde{\alpha} = \begin{cases} -1.618\dots & = -w^{*-1} & \text{for } |K| < 1 \\ -1.28857\dots & & \text{for } |K| = 1 \end{cases} \quad (7.29c)$$

(Note, that $f_{\Omega_n}^{F_{n+1}}(0) - F_n = 0$).

- c) Figure 110 shows the periodic function

$$u(t_j) = \theta^n(t_j) - t_j; \quad j = 0, 1, 2, \dots \quad (7.30)$$

that measures the time dependence of the cycle elements

$$\theta^n(t_j) = \theta(j \cdot w_n) \equiv f^j(0) \quad (7.31)$$

for times $t_j \equiv j \cdot w_n$ in the limit $n \rightarrow \infty$. (Here, $f^j(0)$ is taken at $\Omega_n(K)$, and $u(t_j)$ is periodic since the property $f(\theta + 1) = f(\theta) + 1$ leads to $\theta(t_j + 1) = \theta(t_j) + 1$). For $|K| < 1$ and $\Omega_n \rightarrow \Omega_\infty$, the variable $u(t)$ varies smoothly with t , but its behavior becomes “bumpy” for $|K| = 1$, which signals the transition from quasiperiodicity to chaos.

- d) The power spectrum

$$A(\omega) = \frac{1}{F_{n+1}} \sum_{j=0}^{F_{n+1}-1} u(t_j) e^{2\pi i \omega j} \quad (7.32)$$

for $\omega = 0, \dots, F_{n+1}$ is shown for $n \rightarrow \infty$ in Fig. 110e. It displays self-similarity (the major structure between any two adjacent peaks is essentially the same), and the main peaks occur at powers of the Fibonacci numbers reflecting the fact that the motion is almost periodic after F_n iterations.

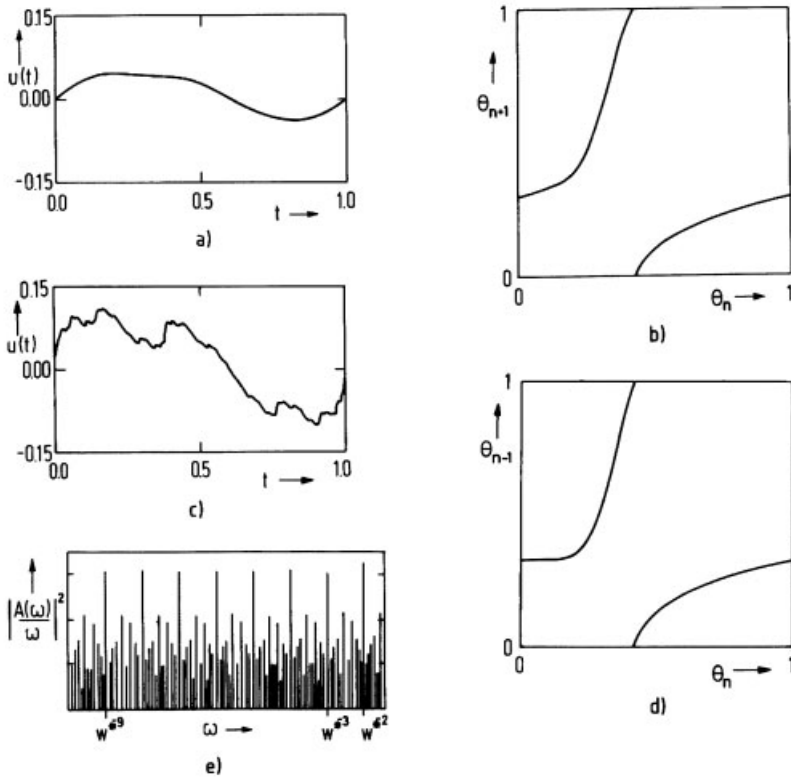


Figure 110: a) $u(t)$ for $K = 0.5$ (after Shenker, 1982); b) the map (6.57) at $K = 0.5$ and $w = w^*$ is a diffeomorphism (after Jensen *et al.*, 1983a); c) $u(t)$ becomes bumpy for $K = 1$ (after Shenker, 1982); d) the map (6.57) at $K = 1$ and $w = w^*$ becomes noninvertible $f'(0) = 0$ (after Jensen *et al.*, 1983a); e) the power spectrum for $K = 1$ (after Rand *et al.*, 1983). Note that indeed for $n \rightarrow \infty$, $u(t_j)$ converges to a function in $0 \leq t \leq 1$ because the periodicity of u implies that its argument is taken mod 1 and $j \cdot w^* \bmod 1$, $j = 0, 1, 2, \dots, n$ covers $[0, 1]$.

These results [especially a) and b)] appear very similar to those found for the period-doubling route, and it is therefore natural to attempt a *renormalization-group treatment* of this transition which establishes its universal features. The formal parallels between the transitions to chaos via period doubling and quasiperiodicity are summarized in Table 11. (Note, that $\tilde{\alpha}$ and $\tilde{\delta}$ in eqs. (7.28–7.29) are different from the Feigenbaum constants.) To derive the corresponding functional equations, we define [see eq. (7.29b)] the functions

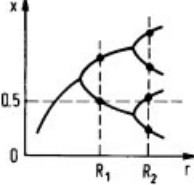
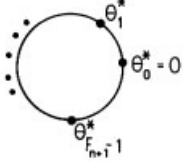
$$f_n(x) = \tilde{\alpha}^n f^n(\tilde{\alpha}^{-n} x) \quad \text{where} \tag{7.33}$$

$$f^n(x) = f^{F_{n+1}}(x) - F_n \tag{7.34}$$

such that eq. (7.29b) becomes

$$\lim_{n \rightarrow \infty} \tilde{\alpha}^n d_n \propto \lim_{n \rightarrow \infty} \tilde{\alpha}^n f^n(0) = \lim_{n \rightarrow \infty} f_n(0) = \text{const.} \tag{7.35}$$

Table 11: Parallels between the transitions to chaos via period doubling and quasiperiodicity.

Period Doubling	Quasiperiodicity
Logistic map $x_{n+1} = f_r(x_n) = r(1 - x_n)$	Circle map $\theta_{n+1} = f_{K\Omega}(\theta_n)$ $\equiv \theta_n + \Omega - \frac{K}{2\pi} \sin(2\pi\theta_n) \pmod 1$
One control parameter r	Two control parameters K, Ω
At $r = R_n$ superstable cycle of length 2^n	At $\Omega = \Omega_n$ superstable cycle of length F_{n+1}
	
R_n is calculated from $f_{R_n}^{2^n}(0) = 0$ (cycle closes)	Ω_n is calculated from $f_{K, \Omega_n}^{F_{n+1}}(0) - F_n = 0$ (ensures $w_n = \frac{F_n}{F_{n+1}}$)
Parameter scaling $R_{n+1} - R_n \sim \delta^{-n}$ for $n \gg 1$	$\Omega_{n+1} - \Omega_n \sim \tilde{\delta}^{-n}$ for $n \gg 1$
Scaling of distances between cycle elements $d_n \equiv f_{R_n}^{2^{n-1}}(0)$ (compare to $f_{R_n}^{2^{n-1}}(0) = 0$)	$d_n = f_{K, \Omega_n}^{F_n}(0) - F_{n-1}$ (compare to $f_{K, \Omega_n}^{F_{n+1}}(0) - F_n = 0$)
$\frac{d_n}{d_{n+1}} = -\alpha$ for $n \gg 1$	$\frac{d_n}{d_{n+1}} = \tilde{\alpha}$ for $n \gg 1$

As in the case of period doubling [see eq. (4.14)], this relation indicates that the sequence $\{f_n(x)\}$ converges towards a universal function

$$\lim_{n \rightarrow \infty} f_n(x) = f^*(x) \tag{7.36}$$

where $f^*(x)$ is again the solution of a fixed-point equation which we shall now derive. More precisely, we consider f_n at $\Omega = \Omega_\infty$, which corresponds to $i \rightarrow \infty$ in eq. (4.20).

The function f^{n+1} can be obtained from f^n and f^{n-1} by a rule which is dictated by the recursion of the Fibonacci numbers (7.24) and the property $f(x+1) = f(x) + 1$:

$$\begin{aligned} f^{n+1}(x) &= f^{F_{n+2}}(x) - F_{n+1} \\ &= f^{F_{n+1}}[f^{F_n}(x)] - (F_{n+1} + F_n) \\ &= f^n[f^{n-1}(x)]. \end{aligned} \tag{7.37}$$

Because the operation of iteration is commutative, we also have

$$f^{n+1}(x) = f^{n-1}[f^n(x)]. \tag{7.38}$$

According to eqs. (7.37–7.38), there are now two ways of calculating $f_{n+1}(x)$:

$$f^{n+1}(x) = \tilde{\alpha} f_n[\tilde{\alpha} f_{n-1}(\tilde{\alpha}^{-2}x)] \quad (7.39a)$$

and

$$f_{n+1}(x) = \tilde{\alpha}^2 f_{n-1}[\tilde{\alpha}^{-1} f_n(\tilde{\alpha}^{-1}x)] . \quad (7.39b)$$

Both equations become equivalent for the initial conditions

$$f_0[\tilde{\alpha}^{-1} f_1(\tilde{\alpha}x)] = \tilde{\alpha}^{-1} f_1[\tilde{\alpha} f_0(x)] . \quad (7.40)$$

Taking the limit $n \rightarrow \infty$ in (7.39a), we obtain for the fixed point function

$$f^*(x) = \tilde{\alpha} f^*[\tilde{\alpha} f^*(\tilde{\alpha}^{-2}x)] . \quad (7.41)$$

One can immediately verify that

$$\tilde{f}^*(x) = -1 + x \quad (7.42)$$

is a rigorous solution to this equation. If we substitute $\tilde{f}^*(x)$ into (7.41), we obtain

$$-1 + x = -\tilde{\alpha}^2 - \tilde{\alpha} + x \rightarrow \tilde{\alpha} = -w^{*-1} . \quad (7.43)$$

This value for $\tilde{\alpha}$ [which is equal to the second solution of eq. (7.27)] agrees with the numerical result for $|K| < 1$ [see eq. (7.29c)].

For $|K| = 1$, we expect that (7.41) has a different solution because the linear term is then absent in our model equation (7.13):

$$f(0) = \Omega + \theta^3 \cdot \text{const.} , \quad \text{for } \theta \rightarrow 0 ; \quad |K| = 1 . \quad (7.44)$$

If for $|K| = 1$ we try the ansatz

$$f^*(x) = 1 + ax^3 + bx^6 \dots \quad (7.45)$$

a value for $\tilde{\alpha}$ is found which is consistent with eq. (7.29c). This establishes the universality of the α s for $|K| \leq 1$.

By analogy to period doubling, the $\tilde{\delta}$ s appear as eigenvalues of the linearized fixed-point equation. These equations are somewhat more complicated than in the Feigenbaum route because the recursion relations are of *second* order; that is, f_n and f_{n-1} are required to produce f_{n+1} (for more details see, e. g., the article of Feigenbaum, Kadanoff and Shenker, 1982).

7.2.3 Global Universality

Let us now consider the globally universal properties of the set of Ω values that is complementary to the Arnold tongues and corresponds to irrational winding numbers. The following numerical results have been obtained by Jensen, P. Bak and T. Bohr (1984):

- For $K \rightarrow 0$ (from below), the complement C of the total length of the steps in the (incomplete) devil's staircase, i. e., $C = 1 - \sum_{p,q} \Delta\Omega(p/q, K)$, decreases to zero with a power law

$$C \propto (1 - K)^\beta$$

where the exponent $\beta \cong 0.34$ is the same for all $f(\theta)$ in eq. (7.13) which have a cubic inflection point at $K = 1$.

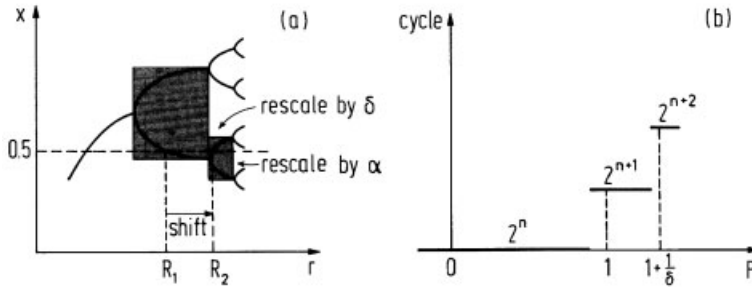


Figure 111: a) Self-similarity of the bifurcation tree; b) stability intervals of 2^n , 2^{n+1} , and 2^{n+2} cycles of $g_p(x)$ with n “arbitrarily high”. (After Cvitanovic, 1984.)

- At $K = 1$, the Ω values belonging to irrational winding numbers form a self-similar thin cantor set (of zero measure) whose Hausdorff dimension $D^* = 0.87$ is again universal.

Whereas there exists up to now no theoretical explanation for the value of β , we will follow the work of Cvitanovich *et al.* (1985b) and calculate D^* by introducing a whole family of universal functions that maintains a dependence on Ω [which was lost in the previous R.G. formulation where we put $\Omega = \Omega_\infty$ in eq. (7.36)]. For simplicity, we explain this method first for the period-doubling route and transfer it then to the circle map. Figure 111 shows again the self-similar structure of the bifurcation tree from Section 4.1.

In order to capture the change in x and r , we follow the procedure of Cvitanovic (1984) and introduce the modified doubling operator \hat{T} . It denotes the operation of iteration twice, rescaling x by α , shifting r to the corresponding values (with the same slope at the cycle points) at the next bifurcation, and rescaling it by δ :

$$\begin{aligned} \hat{T}f_{R_n+p\Delta_n}(x) &\equiv -\alpha f_{R_{n+1}+p\Delta_{n+1}}(-x/\alpha) \\ &= -\alpha f_{R_n+\Delta_n(1+p/\delta_n)}^{(n)} [f_{R_n+\Delta_n(1+p/\delta_n)}^{(n)}(-x/\alpha)] \end{aligned} \tag{7.46}$$

where

$$f^{(n)}(x) = f^{2^n}(x) \quad \Delta_n = R_{n+1} - R_n, \quad \delta_n = \Delta_n/\Delta_{n+1} \tag{7.47}$$

and $0 \leq p \leq 1$ is a parameter which interpolates the r s between a 2^n and a 2^{n+1} cycle. If we call $\lim_{n \rightarrow \infty} \delta_n = \delta$ and

$$\lim_{n \rightarrow \infty} \hat{T}^n f_{R_0+p\Delta_0}(x) \equiv g_p(x), \tag{7.48}$$

we obtain from the definitions (7.46–7.48) an equation for the universal family of functions $g_p(x)$:

$$g_p(x) = \hat{T}g_p(x) = -\alpha g_{1+p/\delta} [g_{1+p/\delta}(-x/\alpha)] \tag{7.49}$$

with boundary conditions:

$$g_0(0) = 0 \quad \text{and} \quad g_1(0) = 1. \tag{7.50}$$

The first condition means that the origin of p corresponds to the superstable fixed point. The second condition sets the scale of x and p by the superstable two-cycle (see Fig. 112).

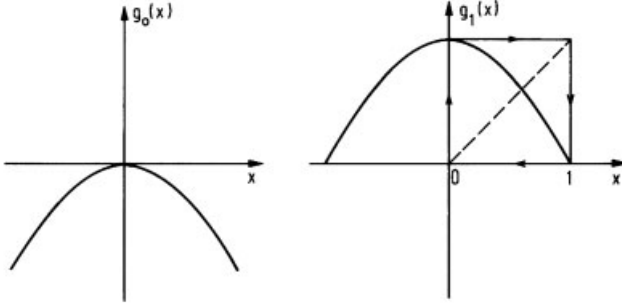


Figure 112: Boundary conditions for the functions $g(x)$ and $g_1(x)$ defined in the text (after Cvitanovic, 1984).

Note that our fixed-point equation (4.21) for the usual doubling operator can be obtained by choosing $p = p^*$ such that $g_{p^*} = g_{1+p^*}/\delta$, i. e., $p^* = \delta/(\delta - 1)$. The family of universal functions $g_p(x)$ in eq. (7.49) is called the unstable manifold (Vul and Khanin, 1982) because operation with \hat{T} drives $g_p(x)$ away from the fixed-point values $g_{p^*}(x)$.

The advantage of eq. (7.49) with respect to the usual fixed-point equation (4.21) is twofold. First, one could obtain *both* Feigenbaum constants α and δ from eq. (7.49) by expanding $g_p(x)$ into a double power series in p and x and comparing the coefficients of equal powers, that is one needs no linearization around the fixed point.

Since we have calculated their values already in Section 4.2, we now concentrate on the second aspect of eq. (7.49), namely its stability interpretation. It follows from Fig. 111b and eq. (7.49) that if $g_p(x)$ has a stable 2^n cycle (with n “arbitrarily high”) in the interval $-p_0 < p < p_0$, then $g_{1+p/\delta}(x)$ has a stable 2^{n+1} cycle in the p -interval around 1 whose width is reduced by a factor of $1/\delta$.

This somewhat trivial looking statement becomes rather powerful if we translate eqs. (7.46–7.49) to the circle map where they will allow us to obtain some insight into the self-similarity of the width of the mode-locking regions. The period-doubling operation [eq. (4.21)] translates according to eqs. (7.37–7.39) into:

$$\mathbf{T}[f^{n-1}, f^{n-2}] = \tilde{\alpha} f^{n-1}[f^{n-2}(x/\tilde{\alpha}^2)] \quad (7.51)$$

where $f^n(x) \equiv f^{F_{n+1}}(x) - F_n$. Accordingly, the doubling plus x, r rescaling transformation \hat{T} from eq. (7.46) changes into:

$$\begin{aligned} \hat{T}[f_{\Omega_{n-1}+p\Delta_{n-1}}^{n-1}(x), f_{\Omega_{n-2}+p\Delta_{n-2}}^{n-2}(x)] &\equiv \tilde{\alpha} f_{\Omega_n+p\Delta_n}^{n-1}[\tilde{\alpha} f_{\Omega_n+p\Delta_n}^{n-2}(x/\tilde{\alpha}^2)] \\ &= \tilde{\alpha} f_{\Omega_{n-1}+(1+p/\delta_n)\Delta_{n-1}}^{n-1}[\tilde{\alpha} f_{\Omega_{n-2}+(1+p/\delta_{n-1}+p/\delta_{n-1}\delta_n)\Delta_{n-2}}^{n-2}(\tilde{x}/\alpha^2)] \end{aligned} \quad (7.52)$$

where

$$\Delta_n = \Omega_{n-1} - \Omega_n; \quad \tilde{\delta}_n = \Delta_n/\Delta_{n-1} + 1$$

and $0 \leq p \leq 1$ interpolates the Ω s between an F_n and an F_{n+1} cycle. Calling

$$\lim_{n \rightarrow \infty} \hat{T}^n[f_{\Omega_0+p\Delta_0}^{n-1}, f_{\Omega_{-1}+p\Delta_{-1}}^{n-2}] = \tilde{g}_p(x) \quad (7.53)$$

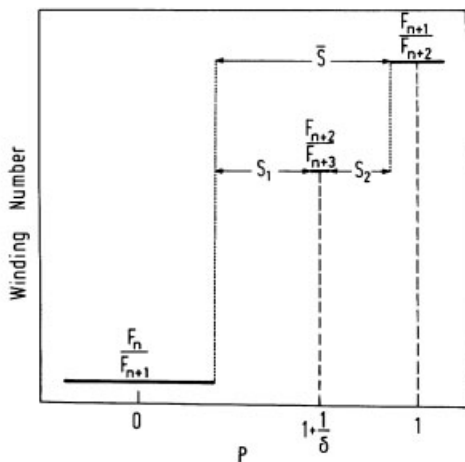


Figure 113: Three steps in the universal devil’s staircase as generated by the stability intervals of $\tilde{g}_p(x)$ and eq. (7.54). The widths of the steps are p^* , $p^*/\tilde{\delta}$ and $p^*/\tilde{\delta}^2$ for F_n/F_{n+1} , F_{n+1}/F_{n+2} , F_{n+2}/F_{n+3} , respectively, where n is “arbitrarily high”. Also indicated are the widths of the “holes” used in eq. (7.55) (after Cvitanovic *et al.*, 1985).

eqs. (7.52–7.53) yield [in analogy to eq. (7.49)]:

$$\tilde{g}_p(x) = \tilde{\alpha} \tilde{g}_{1+p/\tilde{\delta}}[\tilde{\alpha} \tilde{g}_{1+p/\tilde{\delta}+p/\tilde{\delta}^2}(x/\tilde{\alpha}^2)] \tag{7.54}$$

where the normalization conditions are again $\tilde{g}_0(0) = 0$, $\tilde{g}_1(0) = 1$.

One could again determine from eq. (7.54) the parameters $\tilde{\alpha}$ and $\tilde{\delta}$ for the route from quasiperiodicity to chaos. But we will use here the universal object $\tilde{g}_p(x)$ to investigate the structure of mode lockings. For $p = 0$, $\tilde{g}_p(x)$ has, by construction, a superstable fixed point at $x = 0$. Our arguments are now closely parallel to those which we used to interpret eq. (7.49) in connection with Fig. 107. The range of p around zero, for which $\tilde{g}_p(x)$ still has a fixed point, is the range of parameters for which the original map is locked (in some winding number w_n with “infinitely large” n (see Fig. 113). However, around $p = 1$, there is another locked state which corresponds to the next locked region in the sequence, and the width of this region is scaled down by a factor of $1/\tilde{\delta}$ compared to the first (note $\tilde{\delta} < 0$ for the transition from quasiperiodicity to chaos). Around $p = 1 + 1/\tilde{\delta}$, there is another mode-locked region scaled down by $1/\tilde{\delta}^2$ compared to the first, etc. Thus, by studying the stability of the fixed point of $\tilde{g}_p(x)$, one can find an infinity of mode-locked states which are universally located. Although these are not all mode-locked regions (see Cvitanovic *et al.*, 1985b), they are sufficient to yield an estimate for the Hausdorff Dimension D^* of the “holes” in the devil’s staircase at $K = 1$.

Generally, the Hausdorff Dimension of a self-similar fractal can be computed from the equation (Hentschel and Procaccia, 1983):

$$\sum_i \left(\frac{s_i}{\bar{s}}\right)^D = 1 \tag{7.55}$$

where \bar{s} is the length of a box that covers the whole set of points and s_i are the linear dimension of smaller boxes that also provide a complete coverage. Equation (7.55) can be derived by

noting that the number N of points of a fractal, which can be partitioned into boxes of size s_i containing N_i points, can be written as

$$N = \sum_i N_i. \quad (7.56)$$

Dividing this by N and using $(N_i/N) = (s_i/\bar{s})^D$ (which generalizes the formula that the number of points in an ordinary cube of linear dimension l grows like l^3), one obtains eq. (7.55). The values s_i and \bar{s} , which are needed to compute D^* , can be read from Fig. 113. The range of parameter values, for which $\tilde{g}_p(x)$ has a stable fixed point, follows from $\tilde{g}_{p^*}(x^*) = x^*$ and $|\tilde{g}'_{p^*}(x^*)| = 1$. Since $\tilde{g}_p(x)$ is universal, so is p^* and, therefore, D^* , which is computed from the universal quantities p^* and $\tilde{\delta}$. If we estimate p^* crudely by $p^* = 1/2\pi$ [which is just the width of the first Ω step in the circle map, see eq. (7.17)], we obtain from eq. (7.55) and Fig. (113) the value $D^* \cong 0.92$ which is less than 10% off the numerical result $D^* = 0.87$ found by Jensen *et al.* (1983b). More accurate theoretical values for D^* can be obtained by considering better approximations to $\tilde{g}_p(x)$ and p^* (see Cvitanovic *et al.*, 1985b).

7.3 Experiments and Circle Maps

There exists a large variety of real systems (see below) whose dynamical behavior can be modeled by circle maps. Usually an analysis to detect circle-map behavior proceeds as follows:

- The power spectrum of the (Fourier transformed) measured signal shows two or three incommensurate frequencies before the onset of broadband noise. This indicates a transition from quasiperiodicity to chaos.
- A reconstruction of the trajectory in phase space, from the measurement of a single variable, shows the destruction of a torus in favour of a strange attractor. By choosing a proper plane in phase space, the torus section appears (before the transition to chaos) as a closed curve which can be parametrized by θ_n . A plot of θ_{n+1} versus θ_n reveals the existence (or nonexistence) of a circle map $\theta_{n+1} = f(\theta_n)$ with $f(\theta+1) = f(\theta) + 1$.
 - An analysis of the time series of the measured angles θ_n as a function of the experimental control of parameters reveals universal properties near the transition such as:
 - Devil's staircase for the mode-locking intervals which is ordered by the Farey tree.
 - Hausdorff dimension $D_0 = 0.87$ for the unlocked intervals at the critical line which corresponds to $K = 1$ in the circle map.
 - Nontrivial scaling ($\tilde{\alpha} = -1.289$) near the golden mean winding number.

In the following examples, we will show how this program actually works.

7.3.1 Driven Pendulum

One of the simplest physical systems whose dynamical description has been reduced to a circle map (Jensen *et al.*, 1983a, 1984) is a periodically driven pendulum with an additional constant external torque B which is described by the differential equation:

$$\ddot{\theta} + \gamma \dot{\theta} + \sin \theta = A \cos(\omega t) + B \quad (7.57)$$

Naive discretization of the time derivative in eq. (7.57) yields for $\theta_n = \theta(t = (2\pi/\omega) \cdot n)$:

$$\theta_{n+1} - 2\theta_n + \theta_n + (1-b)(\theta_n - \theta_{n-1}) + K \sin \theta_n = (1-b)\Omega \quad (7.58)$$

where

$$(1-b) = \gamma \frac{2\pi}{\omega}; \quad \Omega = \frac{2\pi}{\omega}(A+B)/\gamma; \quad K = \frac{2\pi}{\omega}.$$

This is, for $r_n = \theta_n - \theta_{n-1} + \Omega$, equivalent to the dissipative circle map:

$$\theta_{n+1} = \theta_n + \Omega - K \sin \theta_n + br_n \quad (7.59a)$$

$$r_{n+1} = br_n - K \sin \theta_n. \quad (7.59b)$$

Equations (7.58–7.59) make it plausible that the pendulum has something to do with the circle map, but they do not, of course, establish a rigorous connection. A numerical proof has been given by Jensen *et al.* (1983a, 1984) who solved eq. (7.57) by using a computer. Figure 114 shows that subsequent values of the angles $\theta_n = \theta(t = (2\pi/\omega)n)$; $n = 0, 1, 2 \dots$ taken at integer multiples of the driving period $2\pi/\omega$ yield, for special parameter values, a one-dimensional circle map.

Let us briefly comment on how mode locking shows up in the solutions of eq. (7.57). Mode locking implies:

$$\theta(t_0 + qT) - \theta(t_0) = 2\pi \cdot p \quad (7.60)$$

where $T = 2\pi/\omega$. This yields

$$\langle \dot{\theta} \rangle \equiv \frac{1}{qT} \int_{t_0}^{t_0+qT} dt \dot{\theta} = \frac{p}{q} \cdot \omega \quad (7.61)$$

i. e., the mode locking state of the pendulum is characterized by the fact that its averaged angular velocity $\langle \dot{\theta} \rangle$ is a rational multiple of the external driving frequency ω .

Furthermore, the universal Hausdorff dimension $D = 0.87$ of the Cantor set derived from the space between mode-locked plateaus has also been measured directly in an electronic simulation of a driven pendulum by Yeh *et al.* (1984). They evaluated the following quantities:

$$S(l) = \text{total length of all mode-locking steps larger than } l$$

$$[1 - S(l)]/l = N(l) = \text{number of intervals of size } l \text{ needed to cover the unlocked holes.}$$

From $N(l)$ they obtained, via $\lim_{l \rightarrow 0} N(l) \propto l^{-D}$, the Hausdorff dimension D_0 shown in Figure 115.

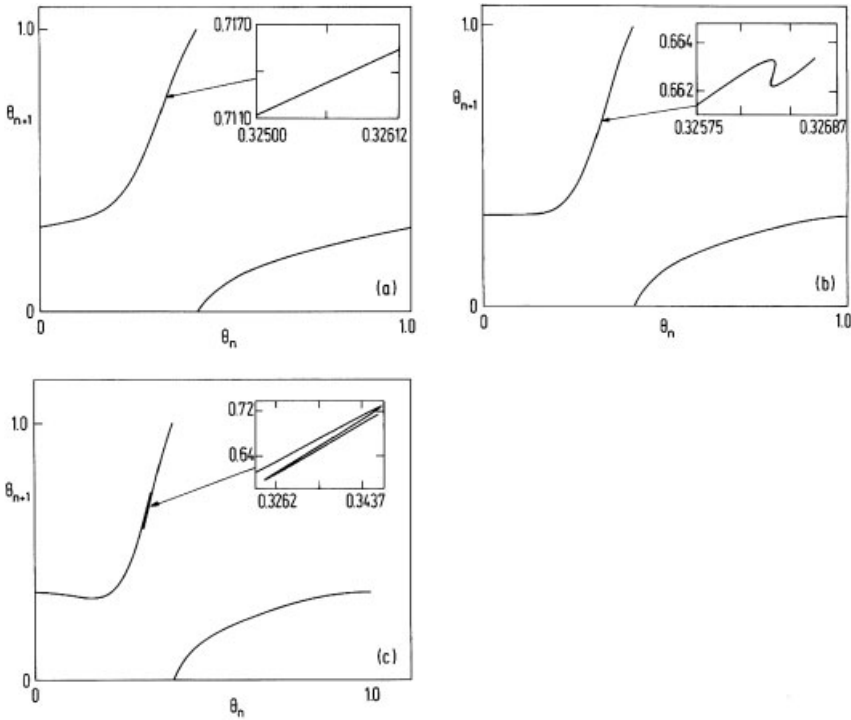


Figure 114: Poincaré maps obtained by numerical integration of the pendulum equation (7.57), $\theta_n = \theta(t = (2\pi/\omega)n)$. 25 000 consecutive points have been plotted; the first 1 000 points have been omitted. Parameters: $A = 1.0$, $\omega = 1.76$. a) $\gamma = 1.576$, $\Omega = 1.4$, the function $f(\theta_n)$ increases monotonically, and the inset is a magnification emphasizing the one dimensional character of the map. b) $\gamma = 1.253$, $\Omega = 1.2$, the map develops a cubic inflection point, indicating the transition to chaos. The inset shows an enlargement around the inflection point. c) $\gamma = 1.081$, $\Omega = 1.094$, the map develops a local minimum and wiggles (insets) indicating chaotic behavior. (After Jensen *et al.*, 1984.)

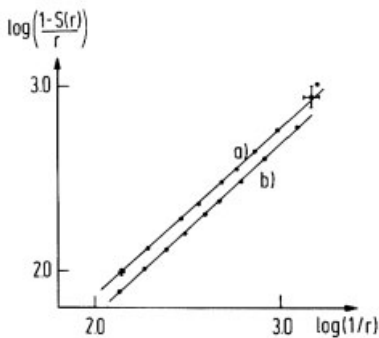


Figure 115: Plots of $\log\{[1 - S(r)]/r\}$ versus $\log(1/r)$, the slopes give the fractal dimension D_0 . a) $\omega = 2.9$, $A = 1.06$, $1/8 < B < 1/5$ yields $D_0 = 0.91$ based on 91 steps. b) $\omega = 1.58$, $A = 0.63$, $1/5 < B < 1/3$ yields $D_0 = 0.92$ based on 45 steps. (After Yeh *et al.*, 1984.)

Let us also call attention to the colored plates, XVI and XVII, at the beginning of this book which show the parameter dependence of the largest Liapunov exponents of a driven pendulum and the corresponding quantity for the circle map. One sees how, in both cases, the Arnold tongues develop and finally merge together as the nonlinearity parameter is increased.

Since eq. (7.57) also describes externally driven Josephson junctions and charge-density waves under the influence of a dc and ac electric field (Jensen *et al.*, 1984), one expects that the dynamical behavior of these systems can also be modeled by one-dimensional circle maps. This has indeed been partly confirmed experimentally (see References to this section).

7.3.2 Electrical Conductivity in Barium Sodium Niobate

Another fine example, where the circle map and the devil's staircase (associated to mode locking) have been observed experimentally, is the Barium Sodium Niobate crystal that we already described on page 132 (Martin and Martienssen, 1986). The voltage across the crystal displays, under the influence of a constant dc current, spontaneous oscillations that can be modulated by an additional ac current as shown in Fig. 116.

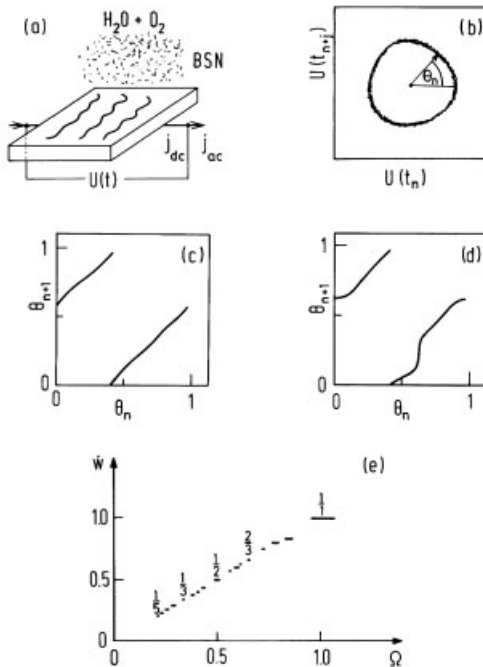


Figure 116: a) BSN crystal in humidified oxygen atmosphere at a temperature of 535 °C with an ac current density j_{ac} superimposed onto a constant dc current density j_{dc} . Also indicated are the “domains” shown in plate V at the beginning of this book. b) Poincaré map constructed from the measured voltage signal. c) and d): the circle map (c) constructed from the measured voltage (a) becomes nonlinear (d) if the dc current density is increased. e) Mode-locked states, measured by varying the driving frequency, display a devil's-staircase behavior near the transition to chaos. (After Martin and Martienssen, 1986.)

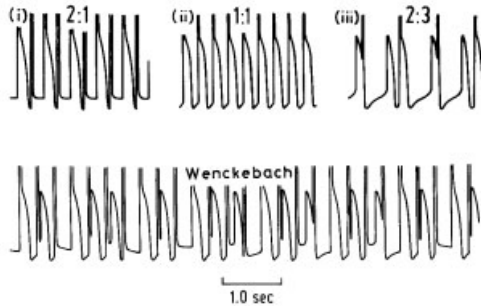


Figure 117: Influence of periodic stimulation as a function of the interstimulus interval t_s : a) Stable phase-locked pattern (i) 2:1 $t_s = 210$ ms; (ii) 1:1 $t_s = 240$ ms; (iii) 2:3 $t_s = 600$ ms. b) Irregular dynamics displaying the Wenckebach phenomenon, $t_s = 280$ ms. (After Guevara *et al.*, 1981; copyright 1981 by the AAAS.)

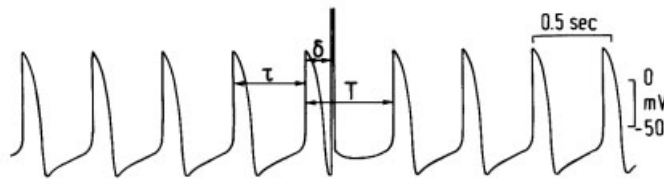


Figure 118: Time course of the transmembrane electrical potential from an aggregate of embryonic heart cells. Left: Spontaneous pulses. Right: After administration of a brief depolarizing stimulus (off-scale response) which occurs 8 ms after the action potential upstroke. The graph sharply rises, and the spontaneous-state period τ is shifted to a new value T . (From Guevara *et al.*, 1981; copyright 1981 by the AAAS.)

7.3.3 Dynamics of Cardiac Cells

It has been found by M. R. Guevara, L. Glass, and A. Shrier (1981) that circle maps are also relevant for explaining the dynamics of cardiac cells. Figure 117 shows the temporal behavior of the transmembrane electric potential from an aggregate of embryonic chick heart cells, which beat spontaneously. If the system is periodically stimulated via a current pulse through a microelectrode, the nature of the response depends on the interstimulus interval. The main idea is to reduce this response to a single stimulus by constructing an appropriate circle map.

Figure 118 shows that the influence of a single pulse changes the period of the spontaneous beats from τ to T . The assumption is now that their ratio T/τ depends only on the phase shift $\theta = \delta/\tau$ of the stimulus with respect to the natural signal, that is,

$$T/\tau = g(\theta) . \quad (7.62)$$

This assumption is supported by the experimentally determined function $g(\theta)$ displayed in Fig. 119.

Next we consider a train of stimuli separated by a uniform time interval t_s . Consultation of Fig. 120 leads to the relation

$$\delta_{i+1} + T_i = \delta_i + t_s . \quad (7.63)$$

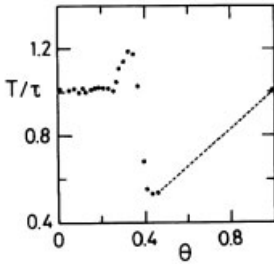


Figure 119: The function $g(\theta)$ defined in eq. (7.62), as experimentally determined for embryonic chick heart cell aggregates (from Guevara *et al.*, 1981; copyright 1981 by the AAAS).

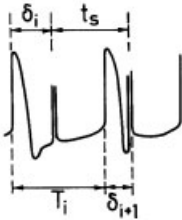


Figure 120: Graphical demonstration of the relation $T_i + \delta_{i+1} = \delta_i + t_s$ for $T_i < \delta_i + t_s < T_i + \tau$.

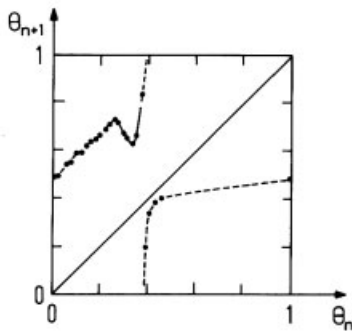


Figure 121: Experimentally determined circle map that describes the dynamics of beating chicken heart cell aggregates. This graph is obtained by using $g(\theta)$ from Fig. 119 in eq. (7.64). (From Guevara *et al.*, 1981; copyright 1981 by the AAAS.)

Division by τ , and assuming that the influence of a single stimulus decays sufficiently fast such that eq. (7.62) holds for every i , yields the phase relationship:

$$\theta_{i+1} = \theta_i + \Omega - g(\theta_i); \quad \Omega \equiv t_s/\tau \quad (7.64)$$

which has the form of a circle map (see Fig. 121) where the rate of rotation $\Omega = t_s/\tau$ is set by the interstimulus distance t_s .

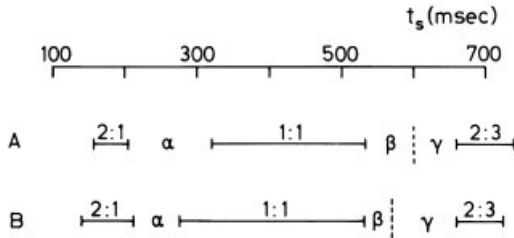


Figure 122: Experimentally determined and theoretically computed responses to periodic stimulation of period t_s with the same pulse durations and amplitudes as in Fig. 117a). a) Experimentally determined dynamics: 2:1, 1:1, 2:3 mode-locking regions and three zones α , β , γ of complicated dynamics. b) Theoretically predicted dynamics obtained via eq. (7.64). (After Guevara *et al.*, 1981; copyright 1981 AAAS.)

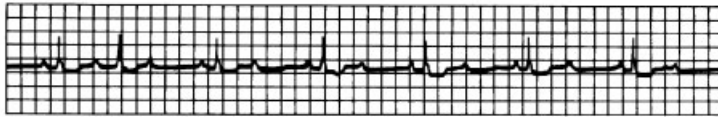


Figure 123: Human electrocardiogram showing one 3:2 Wenckebach cycle followed by five 2:1 cycles (after Glass *et al.*, 1981).

Using $g(\theta)$ from Fig. 119, eq. (7.64) has been used to successfully predict the response to a train of stimuli as a function of t_s (see Fig. 122). The so-called Wenckebach phenomenon in Fig. 117c (i. e., the gradual prolongation of the time between a stimulus and the subsequent action potential until an active potential is skipped either irregularly or in a phase-locked pattern) occurs also in human electrocardiograms (Fig. 123). There the external stimulus is replaced by the stimulus provided by the sinoatrial node. It appears, therefore, from the results in Fig. 122 that circle maps provide a promising tool for the investigation of human cardiac dysrhythmia.

7.3.4 Forced Rayleigh–Bénard Experiment

Another example where the global metric properties of the attractor which occurs at the transition from quasiperiodicity to chaos at the golden mean winding number have been measured in some detail is a forced Rayleigh–Bénard experiment by Jensen *et al.* (1985). One uses mercury as a fluid in a small Rayleigh–Bénard cell that supports two convection rolls. The Rayleigh number is chosen in a range where the convection is oscillatory in time. A second frequency is introduced by passing an ac current through the fluid whose amplitude and frequency serve as control parameters. Figure 124a shows the reconstructed experimental orbit obtained at the point of the breakdown of the torus, which has a golden mean winding number. The dots in Fig. 124b are the experimental points derived from the data shown in Fig. 124a, and the full line is the $f(\alpha)$ curve obtained from the time series of the circle map at $K = 1$, $w^* = (\sqrt{5} - 1)/2$.

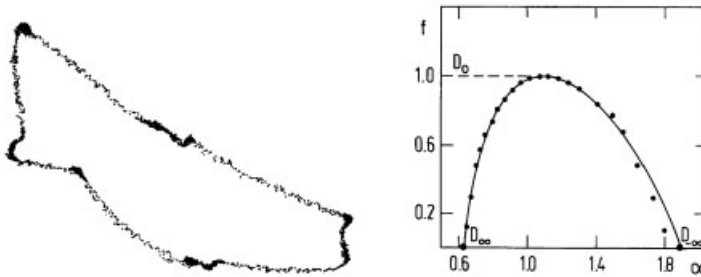


Figure 124: a) The experiment attractor of a forced Rayleigh–Bénard system in two dimensions. 2500 points are plotted. Note the variation in the density of points on the attractor. Part of this variation is, however, due to the projection of the attractor onto the plane. The attractor is nonintersecting in three dimensions, in which it was embedded for the numerical analysis. In the absence of experimental noise, the points should fall on a single curve. The smearing of the observed data set is mostly due to the slow drift in the experimental system during the run over about 2 hours. b) full line: $f(\alpha)$ curve obtained from the iterates of the circle map eq. (7.13) at $K = 1$ and the golden mean winding number; dots: $f(\alpha)$ values obtained from the experimental data in a). (After Jensen *et al.*, 1985.)

The agreement between both sets of data is rather obvious and leads to the conclusion that the experimental data in Fig. 124 a, which look not at all like a smooth circle, and the iterates of the circle map (7.13) belong, from the metric point of view, to the same universality class.

We note that this experiment yields also via $D_{-\infty}$ the first measurement of the nontrivial scaling parameter $\tilde{\alpha}$ of the circle map. $D_{-\infty}$ has, at the transition from quasiperiodicity to chaos, the value

$$D_{-\infty} = -\frac{\log w^*}{\log \tilde{\alpha}} = 1.8980\dots \quad (7.65)$$


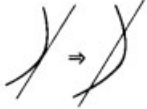
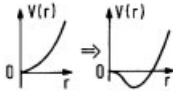
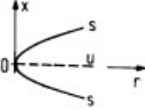
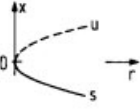
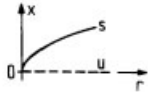
which is obtained for circle maps, in analogy to eq. (6.81), by replacing the ratio in the number of subsequent cycles (which is 2 for period doubling) by $F_{n+1}/F_n = 1/w^*$ and using $\tilde{\alpha}$ instead of α .

7.4 Routes to Chaos

Table 12 summarizes the three different routes to chaos which we have discussed up to now. But this table should only be considered as a first approximation to the true variety of transition scenarios. (Let us only recall that we have already discussed three types of intermittency). While it is natural to focus on common features, it would be premature to make sweeping generalizations about routes to chaos, and it should be emphasized that the range of dynamical behavior observed is quite large.

This situation arises, on the one hand, because experiments on hydrodynamic systems (Bénard and Taylor instability) depend sensitively on the aspect ratios (i. e., the ratio of the cell dimensions in the Bénard experiment, and the ratio of the width between the inner and outer cylinder and the height of the cylinder in the Taylor experiment) such that, for a given set of control parameters, one can have more than one stable state. On the other hand, new types of transitions are possible when one has more than one control parameter (Swinney, 1983). Let us finally present a transition to chaos not mentioned above.

Table 12: Summary of three main routes to chaos.

Feigenbaum	Manneville–Pomeau	Ruelle–Takens–Newhouse
<i>Pitchfork bifurcation</i>	<i>Tangent bifurcation</i>	<i>Hopf bifurcation</i>
		
<i>Bifurcation diagrams</i>		
		
<i>Main phenomena</i>		
Infinite cascade of period doublings with universal scaling parameters	Intermittent transition to chaos. The laminar phase has a duration $(r - r_c)^{-1/2}$	After three bifurcations, strange attractor “probable”.
<i>Experiments</i>		
Bénard experiment	Bénard experiment	Bénard experiment
Taylor experiment	Josephson junction	Taylor experiment
Driven nonlinear oscillator	Chemical reactions	Nonlin. conductors
Chemical reactions	Lasers	
Optical instabilities		

7.4.1 Crises

Crises are collisions between a chaotic attractor and a coexisting unstable fixed point or periodic orbit. Grebogi, Ott and York (1983b) were the first to observe that such collisions lead to sudden changes in the chaotic attractor. A simple example occurs in the period-three window of the logistic map in Fig. 51, where three stable and three unstable fixed points are generated by tangent bifurcations. Figure 125 shows that the unstable fixed points, having entered the chaotic regions, immediately repel the trajectory out of the sub-band in such a way that the regions between the bands are also filled chaotically. Similar crises also occur in two- and three-dimensional maps and in three-dimensional flows.

As the discontinuity is approached, one often finds transient chaos, i. e., seemingly chaotic orbits which decay exponentially towards periodic orbits with a decay rate that follows a power law of the distance (in parameter space) from the discontinuity. It has been conjectured by Grebogi *et al.* (1983b) that “almost all” sudden changes in chaotic attractors are due to crises.

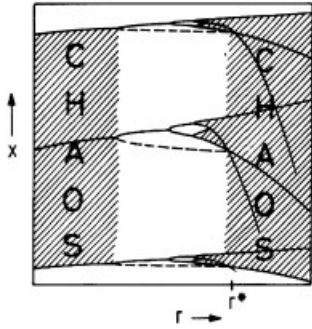


Figure 125: Detail of the bifurcation diagram in the region of the period-three tangent bifurcation. The dashed curves denote the unstable period-three orbit created at the tangent bifurcation; the crises occur at r^* (schematic, after Grebogi *et al.*, 1983 b).

8 Regular and Irregular Motion in Conservative Systems

Up to now we have exclusively studied dissipative systems for which volume elements in phase space shrink with increasing time. Although there are many physical realizations of dissipative systems, which range from the onset of turbulence in fluids to electronic circuits, there exists another large class of physical systems for which chaotic motion has been found (by Poincaré, 1982) before the discovery of the strange attractor for dissipative systems (Lorenz, 1963): These are the conservative systems which encompass all dynamical systems of classical mechanics.

Because there already exist excellent review articles by Berry (1978) and Helleman (1980) and a recent book by Lichtenberg and Liebermann (1982) on this subject, our presentation will be rather brief (as compared with six chapters on dissipative systems).

In the following, conservative systems are considered to be either systems that follow Hamilton's equations of motion,

$$\dot{q} = \frac{\partial H}{\partial p}, \quad \dot{p} = -\frac{\partial H}{\partial q} \quad (8.1)$$

and for which, volume elements in phase space are conserved because of Liouville's theorem,

$$\operatorname{div} \vec{j} = \operatorname{div}(\dot{q}, \dot{p}) = \sum_i \left(\frac{\partial^2 H}{\partial q_i \partial p_i} - \frac{\partial^2 H}{\partial p_i \partial q_i} \right) = 0 \quad (8.2)$$

or, in a more general sense, volume preserving, discrete maps.

The fact that volumes do not change in conservative systems implies immediately that they display (in contrast to dissipative systems) no attracting regions in phase space, i. e., no attracting fixed points, no attracting limit cycles, and no strange attractors (see Fig. 126 and Appendix G). Nevertheless, in conservative systems one also finds chaos with a positive K -entropy, i. e., there are "strange" or "chaotic" regions in phase space, but they are not attractive and can be densely interweaved with regular regions.

We now present some motivation for the study of conservative systems and then give an overview of the rest of this chapter.

For some time, attention has shifted from the calculation of individual orbits to consideration of the qualitative properties of families of orbits, as shown in Fig. 127. Today, we are mainly interested in the long-time behavior of conservative systems. There are several reasons for this:

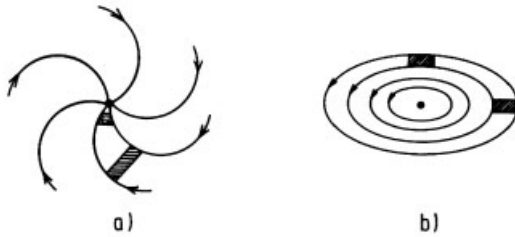


Figure 126: a) In dissipative systems trajectories are attracted to a fixed point, and the volume shrinks. b) In conservative systems the points rotate around an elliptic fixed point, and the volume is conserved.

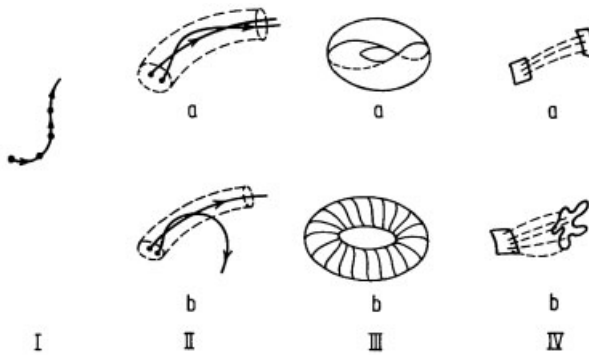


Figure 127: Problems of increasing globality in classical mechanics. I. Step by step integration of the equations of motion. II. a) Local stability; b) local instability. III. Topological nature of complete trajectories: a) periodic motion on a torus; b) motion on a torus with irrational frequency ratios. IV. Types of flow in phase space: a) non mixing; b) mixing. (After Balescu, 1975.)

- a) We should, for example, be able to answer the question whether the solar systems and the galaxy are stable under mutual perturbations of their constituents, or whether they will eventually collapse or disperse to infinity. The long-time limit involved here is of the order of the age of the universe. But “long” times are much shorter in the storage rings used for high-energy physics or in fusion experiments, where the particles make many revolutions in fractions of a second. In such systems irregular or chaotic motion is to be avoided at all costs, and this is only possible if the long-time behavior of these (conservative) systems is known.
- b) Another point concerns the foundations of statistical mechanics, where no attempt is made to follow the detailed motion of all constituents of a complicated many-body problem. Instead, the ergodic hypothesis is made, i. e., one assumes that in the course of time the system explores the entire region of phase space allowed (the energy surface) and eventually covers this region uniformly. Time averages can then be replaced by simpler phase-space averages. But is the ergodic hypothesis correct? To answer this question, the long-time behavior of Hamiltonian systems with N degrees of freedom in the limit $N \rightarrow \infty$ (and $N/\text{volume} = \text{constant}$) must be known.

In the first part of this section, we consider the classical mechanics of simple Hamiltonian systems with a few degrees of freedom and show that in most cases their motion in phase space is extremely complicated and neither regular nor simply ergodic. In other words, it will be shown that the regular motion treated in most textbooks on classical mechanics is an exception and rather uncommon.

In the second part, we discuss some simple model systems which behave ergodically although they have only a few degrees of freedom. Finally, a classification scheme for chaotic behavior in conservative systems is described.

8.1 Coexistence of Regular and Irregular Motion

In the following, we investigate the stability of the trajectories of a nonintegrable Hamiltonian system in the long-time limit. For this purpose, we start from an integrable Hamiltonian and consider the effect of a small nonintegrable perturbation.

8.1.1 Integrable Systems

A Hamiltonian $H'_0(\vec{p}, \vec{q})$ is called integrable if one can find a canonical transformation $S(\vec{q}, \vec{J})$ to new variables $\vec{\theta}, \vec{J}$:

$$\vec{q}, \vec{p} = \frac{\partial S(\vec{q}, \vec{J})}{\partial \vec{q}} \leftrightarrow \vec{J}, \vec{\theta} = \frac{\partial S(\vec{q}, \vec{J})}{\partial \vec{J}} \quad (8.3)$$

such that in the new coordinates the Hamiltonian depends only on the new momenta \vec{J} , i. e., $S(\vec{q}, \vec{J})$ is a solution of the *Hamilton–Jacobi equation* (see, e. g., Arnold, 1978):

$$H'_0 = \left[\vec{q}, \frac{\partial S(\vec{q}, \vec{J})}{\partial \vec{q}} \right] = H_0(\vec{J}) \quad (8.4)$$

and the equations of motion in the action-angle variables \vec{J} and $\vec{\theta}$

$$\dot{\vec{J}} = -\frac{\partial H_0}{\partial \vec{\theta}} = 0 \quad (8.5)$$

$$\dot{\vec{\theta}} = -\frac{\partial H_0}{\partial \vec{J}} = \vec{\omega}(\vec{J}) \quad (8.6)$$

can easily be integrated to

$$\begin{aligned} \vec{J} &= \text{const.} \\ \vec{\theta} &= \vec{\omega} \cdot t + \vec{\delta}. \end{aligned} \quad (8.7)$$

One of the simplest examples for an integrable system is a harmonic oscillator that has the Hamiltonian

$$H'_0 = \frac{1}{2}(p^2 + \omega^2 q^2). \quad (8.8)$$

The Hamilton–Jacobi equation (8.4) then becomes

$$\frac{1}{2} \left[\left(\frac{\partial S}{\partial q} \right)^2 + \omega^2 q^2 \right] = H_0(J) \quad (8.9)$$

$$\rightarrow \frac{\partial S}{\partial q} = \sqrt{2H_0 - \omega^2 q^2} \quad (8.10)$$

and J is determined by

$$J = \frac{1}{2\pi} \oint \frac{\partial S}{\partial q} dq = \frac{H_0(J)}{\omega} \quad (8.11)$$

$$\rightarrow H_0(J) = J\omega \quad (8.12)$$

where the integral has been taken over one cycle of q .

The equations of motion in the action-angle variables are

$$J = \frac{\partial H_0}{\partial \theta} = 0 \rightarrow J = \text{const.} \quad (8.13a)$$

$$\dot{\theta} = \frac{\partial H_0}{\partial J} = \omega \rightarrow \theta = \omega t + \delta. \quad (8.13b)$$

The motion in the variables p and q is obtained from

$$\theta = \frac{\partial S}{\partial J} = \frac{\partial}{\partial J} \int dq \sqrt{2H_0 - \omega^2 q^2} = \arccos \left(q \sqrt{\frac{\omega}{2J}} \right) \quad (8.14)$$

$$\rightarrow q = \sqrt{\frac{2J}{\omega}} \cos \theta \quad (8.15)$$

and

$$p = \frac{\partial S}{\partial q} = -\sqrt{2J\omega} \sin \theta. \quad (8.16)$$

The corresponding trajectory in phase space is an ellipse that becomes a circle with polar coordinates \sqrt{J} and θ after proper rescaling. Comparing eqs. (8.7) and (8.13) one sees that the equations of motion (in action-angle variables) of any integrable system with n degrees of freedom are practically the same as those of a set of n uncoupled harmonic oscillators. The only difference is that in a general integrable system the frequencies ω_i are still functions of the actions J_i whereas they are independent of J_i for harmonic oscillators. The existence of n integrals of the motion (J_1, \dots, J_n) confines the trajectory in the $2n$ -dimensional phase space ($q_1 \dots q_n, p_1 \dots p_n$) of an integrable system to an n -dimensional manifold which has – in analogy to a circle for a harmonic oscillator with $n = 1$ and a torus for two harmonic oscillators with $n = 2$ – the topology of an n -torus.

In the following, we will confine ourselves to $n = 2$, but most results can be extended to more degrees of freedom. Figure 128 shows the motion of an integrable system with two degrees of freedom (i. e., with a four-dimensional phase space) on a torus. Closed orbits occur only if

$$n\Delta\theta_2 = 2\pi \cdot m, \quad \text{i. e.,} \quad \frac{\omega_2}{\omega_1} = \frac{m}{n} = \text{rational}; \quad m, n = 1, 2, 3 \dots \quad (8.17)$$

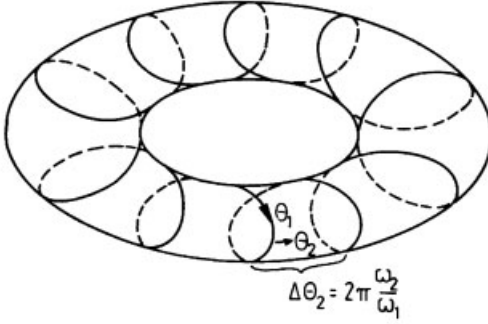


Figure 128: Torus in phase space.

For irrational frequency ratios, the orbit never repeats itself but approaches every point on the two-dimensional manifold infinitesimally close in the course of time. In other words, the motion is ergodic on the torus. (Note that the dimension 2 of the torus is different from the dimension 3 of the manifold defined by $H(\vec{p}, \vec{q}) = E = \text{const.}$)

8.1.2 Perturbation Theory and Vanishing Denominators

Let us now add to H_0 a perturbation εH_1 and see how it affects the previously regular motion; that is, we consider the Hamiltonian

$$H(\vec{J}, \vec{\theta}) = H_0(\vec{J}) + \varepsilon H_1(\vec{J}, \vec{\theta}) \quad (8.18)$$

(where we expressed H_1 in the action-angle variables $\vec{J} = (J_1, J_2)$, $\vec{\theta} = (\theta_1, \theta_2)$ of the unperturbed system), and we try to solve the Hamilton–Jacobi equation

$$H \left[\frac{\partial S}{\partial \vec{\theta}}, \vec{\theta} \right] = H_{00}(\vec{J}). \quad (8.19)$$

Writing the generating function S as

$$S(\vec{J}, \vec{\theta}) = \vec{\theta} \cdot \vec{J} + \varepsilon S_1(\vec{J}, \vec{\theta}) \quad (8.20)$$

and expanding M to order ε , we obtain

$$H_0(\vec{J}) + \varepsilon \frac{\partial H_0}{\partial \vec{J}} \cdot \frac{\partial S_1(\vec{J}, \vec{\theta})}{\partial \vec{\theta}} + \varepsilon H_1(\vec{J}, \vec{\theta}) + O(\varepsilon^2) = H_{00}(\vec{J}) \quad (8.21)$$

S_1 is determined by requiring that the left-hand side in (8.21) is independent of θ , i. e.,

$$\vec{\omega} \cdot \frac{\partial S_1(\vec{J}, \vec{\theta})}{\partial \vec{\theta}} = -H_1(\vec{J}, \vec{\theta}) \quad (8.22)$$

where $\vec{\omega} = \partial H_0 / \partial \vec{J}$ are the frequencies of the unperturbed system. Equation (8.21) can be solved by expanding S_1 and H_1 (both being periodic in the components of $\vec{\theta}$) into Fourier series:

$$S_1(\vec{J}, \vec{\theta}) = \sum_{\vec{k} \neq 0} S_{1,\vec{k}}(\vec{J}) e^{i\vec{k} \cdot \vec{\theta}} \quad (8.23a)$$

$$H_1(\vec{J}, \vec{\theta}) = \sum_{\vec{k} \neq 0} H_{1,\vec{k}}(\vec{J}) e^{i\vec{k} \cdot \vec{\theta}} \quad (8.23b)$$

with $\vec{k} = 2\pi(n_1, n_2)$; n_1, n_2 integers.

Using both expressions in (8.22) and comparing equal Fourier components, finally yields

$$S(\vec{J}, \vec{\theta}) = \vec{\theta} \cdot \vec{J} + i\varepsilon \sum_{\vec{k} \neq 0} \frac{H_{1,\vec{k}}(\vec{J})}{\vec{k} \cdot \vec{\omega}(\vec{J})} e^{i\vec{k} \cdot \vec{\theta}}. \quad (8.24)$$

Equation (8.24) shows that S diverges for

$$\omega_1 n_1 + \omega_2 n_2 = 0, \quad \text{i. e.,} \quad \frac{\omega_1}{\omega_2} = -\frac{n_2}{n_1} = \text{rational}. \quad (8.25)$$

This is the famous problem of vanishing denominators. It shows that the system cannot be integrated by perturbation theory for rational frequency ratios because of strong resonances, and it seems that it can at most be integrated for irrational values of ω_1/ω_2 if the perturbation series in ε converges.

In the following we consider two problems:

- What happens if an integrable system with ω_1/ω_2 close to an *irrational* value is perturbed by εH_1 ?
- What happens under a perturbation εH_1 to the tori of a system for which ω_1/ω_2 has a *rational* value?

8.1.3 Stable Tori and KAM Theorem

The first question is answered by a celebrated theorem of Kolmogorov (1954), Arnold (1963), and Moser (1967), the so-called KAM theorem which we quote here for $n = 2$, without proof. (The theorem holds for an arbitrary number n of degrees of freedom and proofs can be found in the quoted references.) The theorem states that if, among other technical conditions, the Jacobian of the frequencies is nonzero, i. e.,

$$\left| \frac{\partial \omega_i}{\partial J_j} \right| \neq 0 \quad (8.26)$$

then those tori, whose frequency ratio ω_2/Ω_1 is sufficiently irrational such that

$$\left| \frac{\omega_1}{\omega_2} - \frac{m}{s} \right| > \frac{k(\varepsilon)}{s^{2.5}} \quad (k(\varepsilon \rightarrow 0) \rightarrow 0) \quad (8.27)$$

holds (m and s are mutually prime integers), are stable under the perturbation εH_1 in the limit $\varepsilon \ll 1$.



Figure 129: Intervals of lengths $k(\varepsilon)/s^{2.5}$ contributing to L .

It is important to note that the set of frequency ratios, for which (8.27) holds and for which the motion is therefore regular, even after the perturbation, has a nonzero measure. This follows because the total length L of all intervals in $0 \leq \omega_1/\omega_2 \leq 1$, for which (8.27) *does not hold* can be estimated as

$$L < \sum_{s=1}^{\infty} \frac{k(\varepsilon)}{s^{2.5}} \cdot s = k(\varepsilon) \sum_{s=1}^{\infty} s^{-1.5} = \text{const.} \cdot k(\varepsilon) \rightarrow 0 \quad \text{for } \varepsilon \rightarrow 0. \quad (8.28)$$

Here $k(\varepsilon)/s^{2.5}$ is the length of an interval around the rational m/s where (8.27) does not apply, and s is the number of m values with $m/s \leq 1$ (see Fig. 129).

Equation (8.28) means that the set of frequency ratios, for which (under a perturbation by εH_1) the original motion on the torus is only slightly disturbed into the motion of a deformed torus, has the finite measure $1 - \text{const.} \cdot k(\varepsilon)$. But, on the ω_1/ω_2 axis, this set has holes around every rational ω_1/ω_2 .

For large enough ε the perturbation εH_1 destroys all tori. The last KAM torus which will be destroyed is the one for which the frequency ratio is the “worst irrational number“ $\omega_1/\omega_2 = (\sqrt{5} - 1)/2$ (see Section 7.2). The destruction of this KAM torus shows some similarity to the Ruelle–Takens route to chaos in dissipative systems. It has indeed been found by Shenker and Kadanoff (1982) and McKay (1983) who studied the conservative version ($b = 1$) of the map (7.12) of the annulus onto itself that the decay of the last KAM trajectory shows scaling behavior and universal features.

8.1.4 Unstable Tori and Poincaré–Birkhoff Theorem

Let us now discuss the situation when ω_1/ω_2 is rational. We will show that in this case the original torus decomposes into smaller and smaller tori. Some of these newly created tori are again stable according to the KAM theorem. But, between the stable tori, the motion is completely irregular.

It is convenient to visualize what happens (to H_0 under a perturbation εH_1) in a Poincaré map that is, in general, defined by the intersection points of the orbit with a hyperplane in phase space. For the case in hand, we consider the intersections with the q_1, p_1 plane S shown in Fig. 130, which define an area-preserving two-dimensional map

$$r_{i+1} = r_i; \quad r_i = r \left(t = i \cdot \frac{2\pi}{\omega_2} \right) \quad (8.29)$$

$$\theta_{i+1} = \theta_i + 2\pi \frac{\omega_1}{\omega_2}$$

since the point in phase space hits S after a period $2\pi/\omega_2$ during which θ changes by $2\pi\omega_1/\omega_2$.

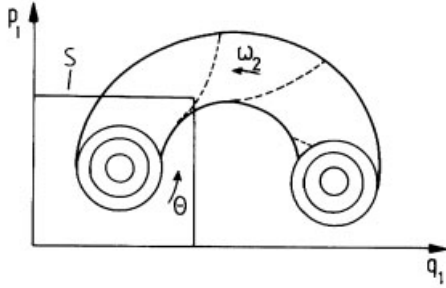


Figure 130: Poincaré map of orbits on the torus in the plane (q_1, p_1) .

The frequency ratio ω_1/ω_2 depends only on the radius r because

$$\left. \begin{aligned} \frac{\omega_1}{\omega_2} &= \frac{\frac{\partial H_0(J_1, J_2)}{\partial J_1}}{\frac{\partial H_0(J_1, J_2)}{\partial J_2}} = f(J_1, J_2) \\ H_0(J_1, J_2) &= E \rightarrow J_2 = J_2(J_1) \\ J_1 &= \frac{1}{2\pi} \oint p_1 dq_1 = \frac{r^2}{2} \end{aligned} \right\} \frac{\omega_1}{\omega_2} = a(r) \tag{8.30}$$

Equation (8.30) can therefore be written as

$$\left. \begin{aligned} r' &= r \\ \theta' &= \theta + 2\pi a(r) \end{aligned} \right\} \equiv T \left(\begin{matrix} r \\ \theta \end{matrix} \right). \tag{8.31}$$

This is Moser's twist map (Moser, 1973).

We note that for a rational frequency ratio $r/s = a(r_0)$ every point on the circle r_0 , θ_0 is a fixed point of T^s since

$$T^s \left(\begin{matrix} r_0 \\ \theta_0 \end{matrix} \right) = \left\{ \begin{matrix} r_0 \\ \theta_0 + 2\pi \frac{r}{s} \cdot s = \theta_0 + 2\pi r. \end{matrix} \right. \tag{8.32}$$

If we now perturb H_0 by ϵH_1 , the twist map becomes

$$\left. \begin{aligned} r_{i+1} &= r_i + \epsilon f(r_i, \theta_i) \\ \theta_{i+1} &= \theta_i + 2\pi a(r_i) + \epsilon g(r_i, \theta_i) \end{aligned} \right\} \equiv T_\epsilon \left(\begin{matrix} r_i \\ \theta_i \end{matrix} \right) \tag{8.33}$$

where f and g depend on H_1 . As a consequence of Liouville's theorem (which also holds for the Hamiltonian $H_0 + \epsilon H_1$), the map T_ϵ is area-preserving.

What can we say now about the fixed points of T_ϵ ? Consider two circles C_+ and C_- between which lies the circle C on which $a = r/s$. On C_+ , $a > s$ and on C_- , $a < r/s$. T^s therefore maps C_+ anti-clockwise, C_- clockwise, and C not at all (see Fig. 131).

Under the perturbed map T_ϵ^s these relative twists are preserved if ϵ is small enough. Thus, on any radius from 0 there must be one point whose angular coordinate is unchanged by T_ϵ^s . These radially mapped points make up a curve R_ϵ close to C .

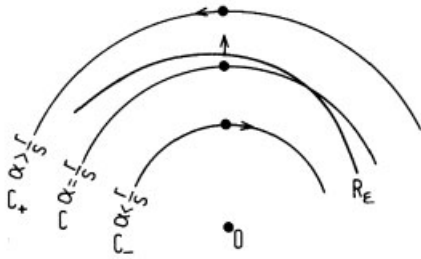


Figure 131: Action of T^s and T_ϵ^s on C_+ and C_- .

Figure 132 shows the curve R_ϵ formed by these points, and its image $T_\epsilon^s(R_\epsilon)$ which cuts R_ϵ in an even number of points because the area enclosed by R_ϵ and $T_\epsilon^s(R_\epsilon)$ must be the same.

The points common to R_ϵ and $T_\epsilon^s(R_\epsilon)$ are the fixed points of T_ϵ^s and we can see in Fig. 133 that an alternating sequence of elliptic and hyperbolic fixed points emerges. This means that the original torus with rational frequency ratio is not completely destroyed under a perturbation, but there remains an even number of fixed points. This is the ‘‘Poincaré–Birkhoff theorem’’ (Birkhoff, 1935).

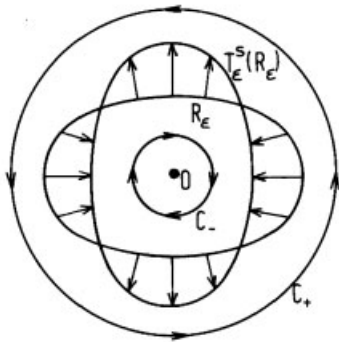


Figure 132: The curve of radially mapped points R_ϵ , and its image $T_\epsilon^s(R_\epsilon)$.

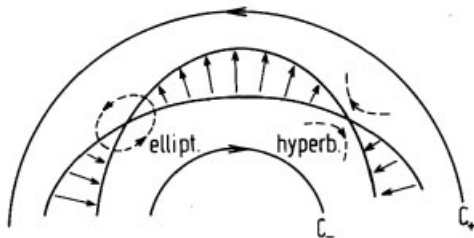


Figure 133: Alternating hyperbolic and elliptic fixed points of T_ϵ^s .

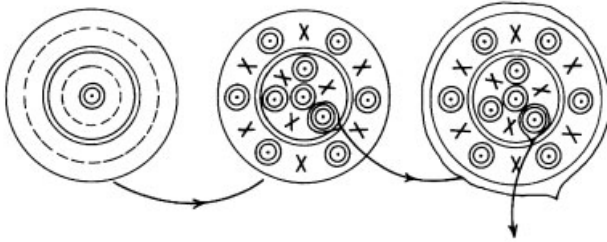


Figure 134: Tori with rational frequency ratio decay into smaller and smaller tori, and the pattern of newly created elliptic and hyperbolic fixed points shows self-similarity.

Let us first consider the elliptic fixed points which are surrounded by rotating points (see Figs. 126, 133). The corresponding orbits are the Poincaré sections of smaller tori for which all our arguments can be repeated; that is, some of these smaller tori are again stable according to the KAM theorem and other tori decompose into smaller ones according to the Poincaré–Birkhoff theorem. This gives rise to the self-similar structure in Fig. 134.

8.1.5 Homoclinic Points and Chaos

Which role do the hyperbolic fixed points play? Fig. 135 shows that, near a hyperbolic fixed point H , the motion becomes unstable, and orbits are driven away from it, in contrast to the stable rotational motion around an elliptic fixed point.

The stable (W_s) and unstable (W_u) lines which lead to or emanate from H behave highly irregularly since:

- They cannot intersect themselves (otherwise the motion on a trajectory in phase space would not be unique for a given set of initial conditions),
- but W_u can intersect W_s at a so-called homoclinic point (see Fig. 136).

Because the map T_ε^s is continuous, and a homoclinic point is not a fixed point, repeated application of T_ε^s produces new homoclinic points. Furthermore, T_ε^s must be applied an infinite number of times to approach the hyperbolic fixed point H along W_s (Appendix G). Between each homoclinic point H_0 and H_1 there is, therefore, an infinite number of other homoclinic points; that is, the curves W_u and W_s form an extremely complex network.

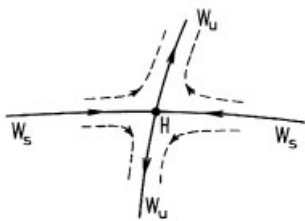


Figure 135: Hyperbolic fixed point H with stable (W_s) and unstable (W_u) lines.

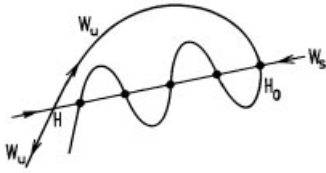


Figure 136: Homoclinic points H_0 are the intersections of W_u and W_s .

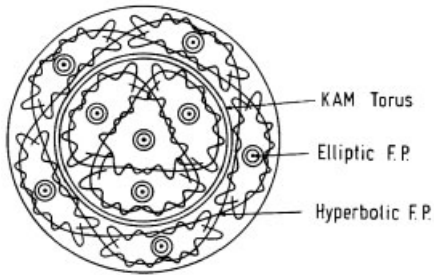


Figure 137: Regular and irregular motion in the phase space of a nonintegrable system.

Summarizing: If we disturb the regular orbits of an integrable system on a torus in phase space by adding a nonintegrable perturbation, then, depending on the different initial conditions [different \vec{J} , $\vec{\delta}$ in (7.7) imply different ω_1/ω_2 , since $\vec{\omega} = \vec{\omega}(\vec{J})$], regular or completely irregular motion results. Although the measure of initial conditions, which lead to regular motion, is nonzero due to the KAM theorem, for every rational frequency ratio (which are densely distributed along the real axis) one obtains smaller and smaller stable tori and irregular orbits due to the hyperbolic fixed points. Thus, an arbitrarily small change in the initial conditions leads to a completely different long-time behavior; and for the motion in phase space, one obtains the complicated pattern in Fig. 137. It shows that in conservative systems regular and irregular motion are densely interweaved.

Finally, we also mention that for area-preserving maps one finds “period doubling”, i. e., a successive creation of new pairs of elliptic fixed points (Greene *et al.*, 1981). We shall discuss this scenario in Appendix G and show that the corresponding Feigenbaum constants are larger than in the dissipative case.

8.1.6 Arnold Diffusion

So far in this section we have only dealt with systems having two degrees of freedom for which the two-dimensional tori stratify the three-dimensional energy surface S_E . The irregular orbits which traverse regions where rational tori have been destroyed are therefore trapped between irrational tori. They can only explore a region of the energy surface which, while three-dimensional, is nevertheless restricted and, in particular, disconnected from other irregular regions, as shown in Fig. 138.

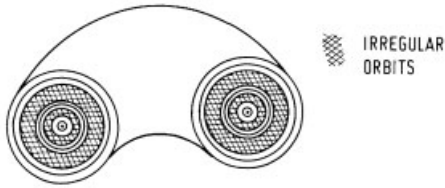


Figure 138: Trapping of irregular orbits between stable KAM tori for a system with two degrees of freedom.

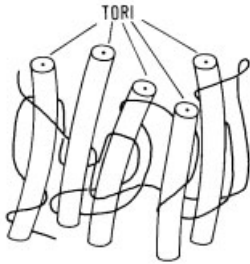


Figure 139: Arnold diffusion for Hamiltonian systems with more than two degrees of freedom (schematically).

For more degrees of freedom, however, the tori do not stratify S_E (e. g., for three degrees of freedom the tori are three-dimensional, and the energy surface is five-dimensional). The gaps then form one single connected region. This offers the possibility of so-called “Arnold diffusion” of irregular trajectories (Arnold, 1964). The existence of invariant tori for perturbed motion is, therefore, not a guarantee of stability of motion for systems with more than two degrees of freedom because irregular wandering orbits that are not trapped exist arbitrarily close to the tori (cf. Fig. 139).

8.1.7 Examples of Classical Chaos

Finally, we present some experimental evidence for the coexistence of regular and irregular motion. Figure 140 shows the Poincaré map in S for the nonintegrable Hénon–Heiles system,

$$H = \frac{1}{2}p_1^2 + q_1^2 + p_2^2 + q_2^2 + \left[q_1^2 q_2 - \frac{q_2^3}{3} \right] \quad (8.34)$$

which consists of an integrable pair of harmonic oscillators coupled by nonintegrable cubic terms (Hénon, Heiles, 1964). The left-hand column shows the surfaces of section generated by eighth-order perturbation theory for various energies (after Gustavson, 1966). The right-hand side are the computed intersections of the trajectory with S . For $E = 1/24$ and $E = 1/12$, the mapping plane is covered with the intersections of (somewhat deformed) tori which signal regular motion and which are identical with those given by perturbation theory. Above $E = 1/9$, however, most, but not all, tori are destroyed, and all the dots which appear to be

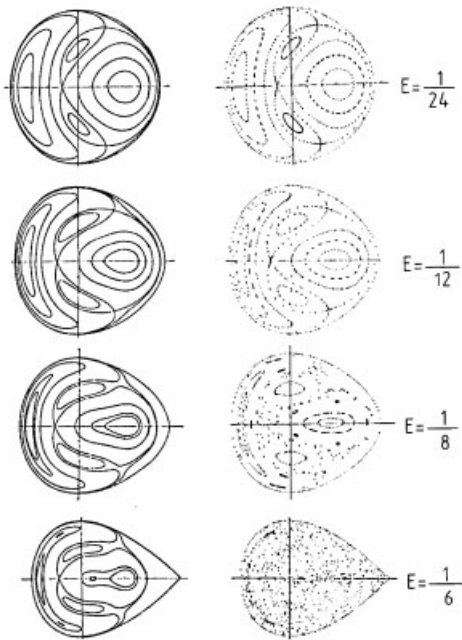


Figure 140: Poincaré maps for the Hénon–Heiles system (after Berry, 1978).

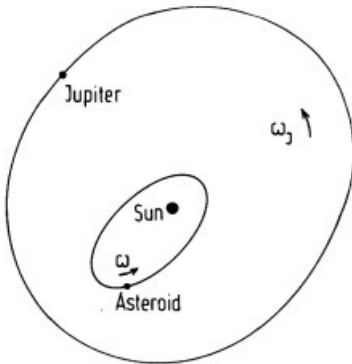


Figure 141: Perturbation of an asteroid's motion by Jupiter.

random are generated by one trajectory as it crosses S . The figure for $E = 1/8$ clearly shows the coexistence of regular and irregular motion. As a further example, we consider the motion of an asteroid around the sun, perturbed by the motion of Jupiter, as shown in Fig. 141.

This three-body problem is nonintegrable, and according to eqs. (8.24–8.25) we expect that the asteroid motion becomes unstable if the ratio of the unperturbed frequency of the

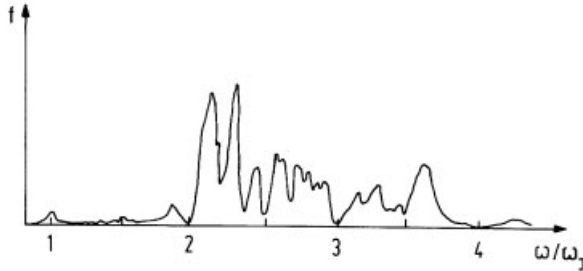


Figure 142: Fraction f of asteroids in the belt between Mars and Jupiter as a function of ω/ω_j (after Berry, 1978).

asteroid motion ω and the angular frequency of Jupiter ω_j becomes rational. Figure 142 illustrates that, in fact, gaps occur in the asteroid distribution for rational ω/ω_j . On the other hand, the existence of stable asteroid orbits ($f \neq 0$) can be considered as a confirmation of the KAM theorem.

A second sort of solar-system gap occurs in the rings of Saturn. In this system Saturn is the attractor; the perturber is any of the inner satellites, and the rest masses are the ring particles. One major resonance occurs within the “Cassini division” shown on Plate VII at the beginning of the book.

8.2 Strongly Irregular Motion and Ergodicity

In the previous section, we linked the origin of irregular motion in Hamiltonian systems to hyperbolic fixed points in the associated area-preserving maps. If we, therefore, want to construct models for strongly irregular motion, it is natural to search for maps for which all fixed points are hyperbolic.

8.2.1 Cat Map

One example of such a system is Arnold’s cat map on a torus which is defined by

$$\left. \begin{aligned} x_{n+1} &= x_n + y_n \bmod 1 \\ y_{n+1} &= x_n + 2y_n \bmod 1 \end{aligned} \right\} \equiv T \begin{pmatrix} x_n \\ y_n \end{pmatrix} \quad (8.35)$$

This map is area-preserving because the Jacobian of T is unity, and it has the eigenvalues

$$\lambda_1 = (3 + \sqrt{5})/2 > 1 \quad \text{and} \quad \lambda_2 = \lambda_1^{-1} < 1 \quad (8.36)$$

so that all fixed points of T^n ($n = 1, 2, 3 \dots$) are hyperbolic. Any point on the torus for which x_0 and y_0 are rational fractions is a fixed point of T^n for some n (e. g., $(0, 0)$ is a fixed point of T , and $(2/5, 1/5)$ and $(3/5, 4/5)$ are fixed points of T^2 , etc.), and these are the only fixed points because T has integral coefficients. The action of the cat map is illustrated in Fig. 143. After just one iteration the cat is wound around the torus in complicated filaments; its dissociation arises from the hyperbolic nature of T which causes initially close points to map far apart.

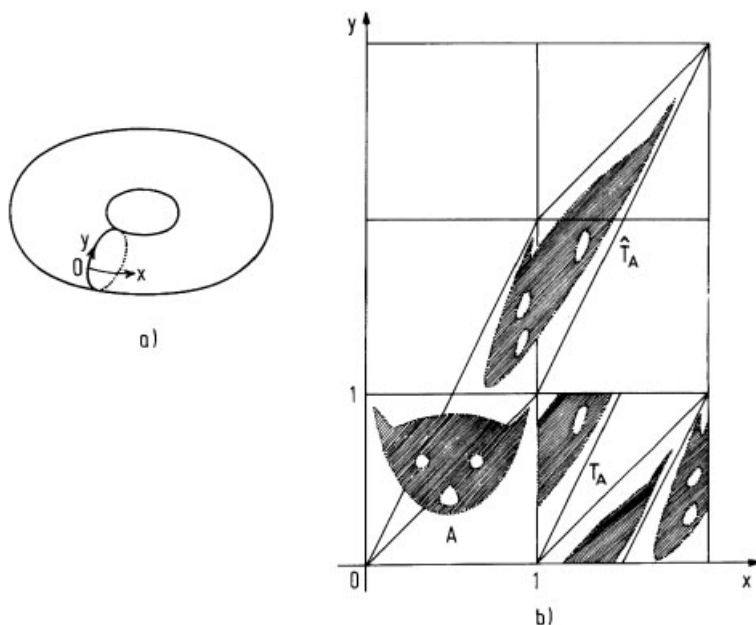


Figure 143: Action of the map T on a cat on a torus. The torus a) is transposed into the unit square of b). \hat{T} is the map T without restriction to the torus. (After Arnold and Avez, 1968.)

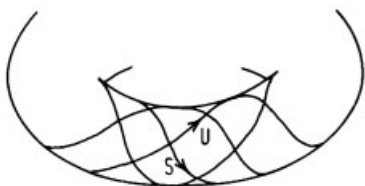


Figure 144: Motion of W_u and W_s under the cat map.

The axes of stretch (W_u) and compression (W_s) from $(0, 0)$ lie along irrational directions and so wrap densely around the torus, never intersecting themselves but intersecting one another infinitely often, as shown in Fig. 144.

Since any set of iterates [which starts from a point (x_0, y_0) with $x_0/y_0 = \text{irrational}$] eventually covers the torus, “time” averages over the iterates are equal to “space” averages over the torus, and the motion generated by the cat map is ergodic.

However, the cat map has even a stronger property – mixing. In other words, the map distorts any area element so strongly, that it is eventually spread over the whole torus, just as a drop of ink (its volume corresponds to an area element in the cat map) is homogeneously distributed throughout a glass of water after it has been stirred (see Fig. 145).

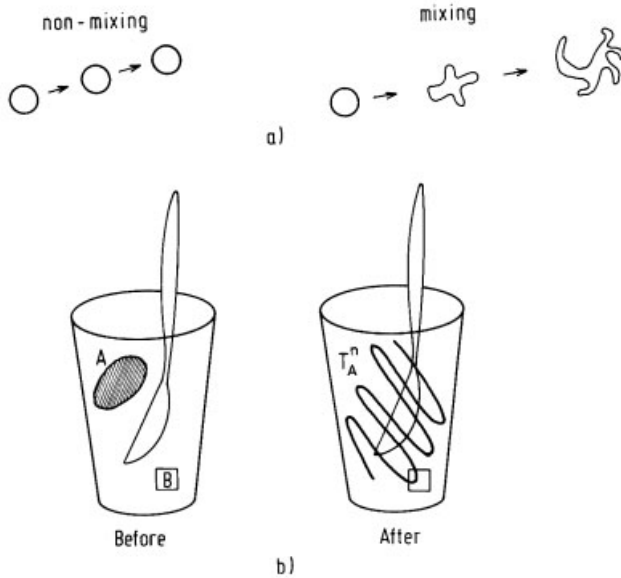


Figure 145: a) Behavior of a volume element for nonmixing and for mixing transformations. b) Mixing of a drop of ink in a glass of water. (After Arnold and Avez, 1968.)

8.2.2 Hierarchy of Classical Chaos

Table 13 gives an overview of the hierarchy of properties which indicates increasingly chaotic motion.

The first entry in Table 13 contains the well-known Poincaré recurrence theorem for Hamiltonian systems. It is simply a consequence of area-preserving motion in a finite region. We can draw an analogy to what happens if we take a walk in a snow-covered finite square: eventually the area will be covered with footprints; and after some time, one is forced to walk on one's own prints (again and again).

Recurrence does not imply ergodicity because the allowed areas need not be connected (there could be two squares). If the phase space is divided, the trajectory is confined to the region in which it started and does not cover the whole phase space.

More formally, a map f is called mixing, if

$$\lim_{n \rightarrow \infty} \rho[f^n(A) \cap B] = \rho(A)\rho(B) \quad (8.37)$$

for every pair of measurable sets A and B . Here ρ is the invariant measure of f . We used the abbreviation

$$\rho(A) \equiv \int_A dx \rho(x) \quad (8.38)$$

and assumed that the measure of the allowed phase space Γ , on which f acts, is normalized to unity, i. e., $\int_{\Gamma} dx \rho(x) = 1$.

Table 13: Hierarchy of classical chaos.

Property	Definition	Example
Recurrent	The trajectory returns to a given neighborhood of a point an infinite number of times	Any Hamiltonian system (or area-preserving map) which maps a finite region of phase space onto itself
Ergodic	Time averages can be replaced by averages over phase space \leftrightarrow Zero is a simple eigenvalue of the Liouville operator L .	$x_{n+1} = x_n + b \bmod 1$ $b =$ irrational
Mixing	Correlation functions decay to zero in the infinite time limit $\leftrightarrow L$ has one simple eigenvalue 0 and the rest of the spectrum is continuous.	Cat map
K -system	The map has a positive K -entropy, i. e., close orbits separate exponentially $\leftrightarrow L$ has a Lebesgue spectrum with denumerably infinite multiplicity.	Cat map

If A and B correspond to the same point, eq. (8.37) reduces to

$$\lim_{n \rightarrow \infty} \int_{\Gamma} dx \rho(x) f^n(x) x \equiv \langle x_n x_0 \rangle = \left[\int_{\Gamma} dx \rho(x) x \right]^2 = \langle x_0 \rangle^2 \quad (8.39)$$

i. e., *mixing means that the autocorrelation function* $\langle (x_n - \langle x_0 \rangle)(x_0 - \langle x_0 \rangle) \rangle = \langle x_n x_0 \rangle - \langle x_0 \rangle^2$ *decays to zero* and “the system relaxes to thermal equilibrium”. (The general proof can be found in the book by Arnold and Avez (1968) who actually show that a system is mixing if, and only if, $\lim_{n \rightarrow \infty} \langle F^n[f^n(x)]G(x) \rangle = \langle F^n(x) \rangle \langle G(x) \rangle$ for any square integrable complex-valued functions F and G .)

Although ergodicity (of course) implies recurrence, it does not imply mixing. Consider, for example, the map

$$x_{n+1} = x_n + b \bmod 1 \equiv f(x_n) \quad (8.40)$$

which shifts a point x_0 on a unit circle by b .

The map is ergodic for irrational values of b , because then a given starting point x_0 never returns to itself, as it does for rational $b = p/q$, (p, q integers) after q steps, and the images of x_0 cover the circle uniformly. The Liapunov exponent for this map is

$$\lambda = \lim_{n \rightarrow \infty} \frac{1}{n} \log \left| \frac{dx_n}{dx_0} \right| = 0 \quad (8.41)$$

i. e., (8.40) is an example that shows a) ergodicity without sensitive dependence on the initial conditions, and b) ergodicity without mixing. The last statement follows because the overlap

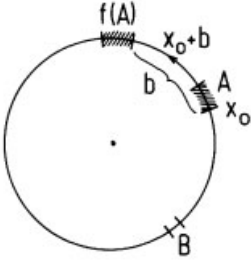


Figure 146: Translations on a circle show ergodicity but they are not mixing.

of the images $f^n(A)$ of a line element A with another (line) element B is either finite or zero (according to the number of iterations) and never reaches a finite equilibrium value as required by eq. (8.37) (see Fig. 146). (Note that for simplicity we have replaced in this example “area” elements by “line” elements.)

Typical systems that show mixing are the cat map (Fig. 143) and the baker’s transformation (Fig. 70a). In both cases a given volume element becomes distorted into finer and finer filaments that eventually cover the whole phase space uniformly. But, the rate at which volume elements become stretched need not be exponential (as in the examples quoted above), i. e., a system that shows mixing need not be a K -system. These examples show that the properties in Table 13 indeed characterize increasingly chaotic motion.

We have also indicated in this table that the hierarchy of classical chaos is mirrored by the spectrum of eigenvalues of the Liouville operator. Let us briefly explain this fundamental relation which allows a characterization of classical chaos without considering individual trajectories.

The Liouville operator L determines the time evolution of the density $\rho(\vec{p}, \vec{q})$ in phase space:

$$\frac{d}{dt}\rho(\vec{p}, \vec{q}) = \dot{\vec{q}} \frac{\partial \rho}{\partial \vec{g}\dot{\vec{q}}} + \dot{\vec{p}} \frac{\partial \rho}{\partial \vec{p}} = \quad (8.42)$$

$$= \left[\frac{\partial H}{\partial \vec{p}} \frac{\partial}{\partial \vec{q}} - \frac{\partial H}{\partial \vec{q}} \frac{\partial}{\partial \vec{p}} \right] \rho \equiv -iL\rho \quad (8.43)$$

$$\rightarrow \rho(t) = e^{-itL}\rho(0). \quad (8.44)$$

Here we used Hamilton’s equations, and (8.43) defines L . It is useful to introduce the eigenvalues λ of L via

$$e^{-itL}\varphi(\vec{x}) = e^{i\lambda t}\varphi(\vec{x}); \quad \vec{x} = (\vec{p}, \vec{q}) \quad (8.45)$$

where $\varphi(\vec{x})$ is a complex, square integrable function in phase space. According to Table 13, different degrees of classical chaos correspond to different spectra of λ (the arrows indicate the direction of the statement). We explain this correspondence by two examples and refer to the cited literature for the general proofs.

First we consider two uncoupled harmonic oscillators whose Hamiltonian reads in action-angle variables:

$$H_{\text{osc}} = \omega_1 J_1 + \omega_2 J_2 \quad (8.46)$$

where ω_1, ω_2 are the oscillator frequencies. Equations (8.43–8.45) then become

$$-iL_{\text{osc}}\rho = \left[\omega_1 \frac{\partial}{\partial \theta_1} + \frac{\partial}{\partial \theta_2} \right] \rho \quad (8.47)$$

$$e^{-iL_{\text{osc}}}\varphi(\theta_1, \theta_2) = e^{i\lambda}\varphi(\theta_1, \theta_2) \quad (8.48)$$

where φ is periodic in the angles θ_1 and θ_2 . These equations have the obvious solutions

$$\varphi(\theta_1, \theta_2) \propto e^{2\pi i(n_1\theta_1 + n_2\theta_2)} \quad (8.49)$$

$$\rightarrow \lambda = 2\pi(n_1\omega_1 + n_2\omega_2) \quad (8.50)$$

where n_1 and n_2 are integers.

The motion of the two oscillators on the torus (see Fig. 128) is only ergodic if ω_1/ω_2 is irrational, i. e., $\lambda \propto n_1\omega_1 + n_2\omega_2 = 0$ only for $n_1 = n_2 = 0$, and $\lambda = 0$ is a simple eigenvalue. For nonergodic motion $\omega_1/\omega_2 = \text{rational}$, and $\lambda = 0$ is degenerate. It is quite plausible that ergodicity and a nondegenerate eigenvalue $\lambda = 0$ correspond to each other because only then the equation for the time invariant density ρ ,

$$e^{-iL}\rho = \rho \quad (8.51)$$

has a unique solution. Equation (8.44) can be extended to maps $\vec{x}_{n+1} = \vec{G}(x_n)$ by

$$e^{-iL}\varphi(\vec{x}) \equiv \varphi[\vec{G}^{-1}(\vec{x})] = e^{i\lambda}\varphi(\vec{x}) . \quad (8.52)$$

As a further example, we consider the cat map (8.35) which acts on a torus so that we can expand φ as

$$\varphi(\vec{x}) = \sum_{\vec{m}} e^{2\pi i\vec{m}\cdot\vec{x}} \tilde{\varphi}(\vec{m}) \quad (8.53)$$

where $\vec{m} = (m_1, m_2)$; m_1, m_2 integers. Using the fact that the transformation matrix T is symmetric, we obtain from (8.52–8.53) after straightforward manipulations

$$\tilde{\varphi}(T\vec{m}) = e^{i\lambda}\tilde{\varphi}(\vec{m}) . \quad (8.54)$$

The point $m = 0$ yields the only fixed point in (8.54), i. e., $\lambda = 0$ is again a simple eigenvalue that corresponds to a constant invariant density. The action of T on the other \vec{m} -values is explained in Fig. 147. If we relabel the m s according to their hyperbolas (α) and their place on it (j), i. e., $\vec{m} \hat{=} (\alpha, j)$, then eq. (7.54) can be written as

$$e^{-iL}\tilde{\varphi}(\alpha, j) \equiv \tilde{\varphi}(\alpha, j+1) = e^{i\lambda}\tilde{\varphi}(\alpha, j) \quad (8.55)$$

i. e., e^{-iL} is a translation operator in the variable j . The corresponding spectrum of L is continuous (note that the j s are not limited) and denumerably infinite degenerate (via the α 's). A spectrum λ , which contains every real number with the same multiplicity and for which the spectral weight is just $d\lambda$, is called the Lebesgue spectrum. The cat map is an example for a K -system. These systems have (also in general) Lebesgue spectra with denumerably infinite multiplicity.

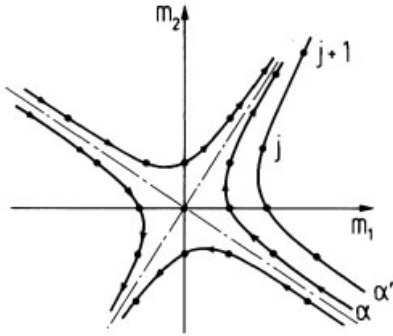


Figure 147: Except for the origin, all points in the \vec{m} -plane are mapped under the action of the matrix T along hyperbolas because the eigenvalues of T are $\lambda_1 = (3 + \sqrt{5})/2 > 1$ and $\lambda_2 = 1/\lambda_1 < 1$.

8.2.3 Three Classical K -Systems

Let us now present some physical examples of K -systems that exhibit ergodic and mixing behavior.

First, we consider the famous hard-sphere fluid whose mixing was rigorously established by Sinai (1970). Because of the infinite contact potential, this is clearly not a perturbation to a simple system (e. g., of noninteracting particles). Figure 148 a shows how exponential separation of the trajectories results from collisions between the spheres' convex surfaces. It is worth emphasizing that Sinai's proof is valid for two discs moving on a torus, i. e., it does not require the thermodynamic limit of infinitely many particles.

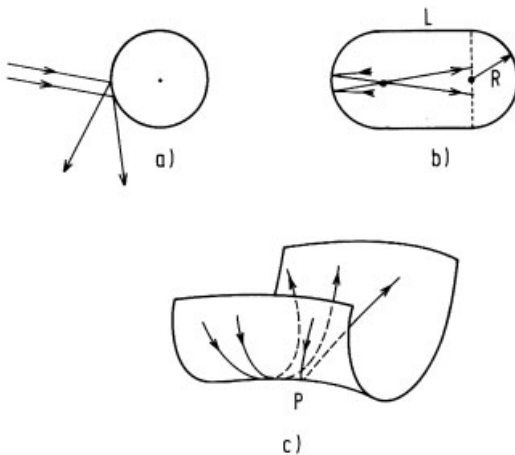


Figure 148: Separation of trajectories for three chaotic systems: a) Sinai's billiards, b) a free particle in a stadium, c) a free particle on a surface with negative curvature.

Another system, which has only a few degrees of freedom, but which nevertheless exhibits ergodicity and mixing, is a free particle in a stadium, as shown in Fig. 148b. The exponential separation of trajectories is generated by the particular form of the boundary (Bunimovich, 1979).

Finally, we mention that the geodesic motion of a mass point on a compact surface with *overall* negative Gaussian curvature is also mixing and ergodic (Anosov, 1969). It can be already seen from the saddle-shaped surface in Fig. 148c (which has a negative curvature at *one* point P) how nearby trajectories separate along geodesics.

9 Chaos in Quantum Systems?

The existence of chaotic motion in classical conservative systems naturally leads to the question of how this irregularity manifests itself in the corresponding quantum systems. In a broader context, one might inquire about the nature of the solutions to the wave equations that arise, e. g., in plasma physics, optics, or acoustics, whose ray trajectories (WKB solution, geometric optics) are stochastic.

The question about the behavior of quantum systems whose classical limit exhibits chaos has been posed since the early days of quantum mechanics (Einstein, 1917) because it raises the problem of how to quantize a system which executes nonperiodic motion (at that time, periodic system were quantized via the Bohr–Sommerfeld quantization rule $\oint p dq = nh$, where h is Planck's constant). Since the discovery and the establishment of wave mechanics, we know how to proceed if we wish to learn about the time evolution of any quantum system: solve the time-dependent Schrödinger equation

$$\hat{H}\Psi = -\frac{\hbar}{i} \frac{\partial}{\partial t} \Psi \quad (9.1)$$

where \hat{H} is the Hamiltonian of the system, Ψ is its wave function, and $\hbar = h/2\pi$. In order to develop some intuition for the changes which will arise if we pass from a classically chaotic system to its quantum mechanical version, we recall several major differences between classical and quantum systems:

- In contrast to classical mechanics (where a statistical description is only necessary if the system becomes chaotic in time), quantum mechanics allows only statistical predictions. Although the Schrödinger equation is linear in Ψ and can, e. g., be solved exactly for a harmonic oscillator with the result that Ψ depends regularly on time (i. e., there is no chaotic time behavior), this does not mean that the motion is completely deterministic, since $|\Psi(\vec{x}, t)|^2$ is only the probability density to find an electron at a space-time point (\vec{x}, t) .

- Because of Heisenberg's uncertainty principle

$$\Delta p \Delta q > \hbar/2 \quad (9.2)$$

there are no trajectories in quantum mechanics [if one measures q with precision Δq , one disturbs the momentum p by Δp according to (9.2)]. Therefore, the characterization of chaos based on the exponentially fast separation of nearby trajectories becomes useless for quantum systems.

- The uncertainty principle (9.2) implies also that points in $2n$ -dimensional phase space within a volume \hbar^n cannot be distinguished, i. e., the phase space becomes coarse grained. This means that regions in phase space in which the motion is classically chaotic (see

Fig. 140), but which have volumes smaller than \hbar^n , are not “seen” in quantum mechanics; and for the corresponding quantum system, we expect a regular behavior in time. Thus the finite value of Planck’s constant tends to suppress chaos. On the other hand, the limit $\hbar \rightarrow 0$ becomes difficult (for quantum systems which have a classical counterpart which displays chaos) because if \hbar becomes smaller, more and more irregular structures will appear.

In the following, we *distinguish* between (time-independent) *stationary Hamiltonians* and *time-dependent Hamiltonians*, which appear, for example, in the quantum version of the kicked rotator.

For systems with stationary Hamiltonians \hat{H} , the Schrödinger equation (9.1) can be reduced [with $\Psi = \Psi_0 \exp(-iEt/\hbar)$] to a linear eigenvalue problem for the energy levels E :

$$\hat{H}\Psi_0 = E\Psi_0. \quad (9.3)$$

As long as the levels are discrete, Ψ behaves regularly in time and there is no chaos. But, there remain the fundamental questions: under what circumstances will this be the case and are there still differences between the energy spectra of a quantum system with a regular classical limit and a quantum system whose classical version displays chaos?

Information about the behavior of systems with time-dependent Hamiltonians are, for example, relevant for the problem of how energy is distributed in the energy ladder of a molecule excited by a laser beam, i. e., they are related to the practical problem of laser photochemistry.

More specifically, the answers to the following questions are sought: Does quantum chaos exist? How can one characterize it? Is there an equivalent to the hierarchy shown in Table 13 in quantum mechanics? What happens to the KAM-theorem for quantized motion, etc.? Up to now there are more questions than answers.

To get at least some insight into these problems, we consider several model systems. In Section 9.1 we investigate the quantized version of the cat map (whose classical motion is purely chaotic) and show that it displays no chaos because the finite value of Planck’s constant, together with the doubly periodic boundary conditions, restrict the eigenvalues of the time-evolution operator to a discrete set, such that the motion becomes completely periodic.

In the subsequent section we describe a calculation by McDonald and Kaufmann (1979), which shows that the energy spectrum of a free quantum particle in a stadium (for which the classical motion is chaotic) differs drastically from that of a free (quantum) particle in a circle (for which the classical motion is regular).

Finally, in the last section we demonstrate (by mapping the system to an electron localization problem) that a kicked quantum rotator shows no diffusion, whereas its classical counterpart displays deterministic diffusion above a certain threshold.

9.1 The Quantum Cat Map

To see how a conservative system, which classically behaves completely chaotically, changes its behavior for nonzero values of Planck’s constant, we quantize a modification of Arnold’s cat map. (The familiar cat map (8.35) cannot be quantized because the corresponding time-evolution operator does not preserve the periodicity of the wave function of the torus, see Hannay and Berry, 1980.)

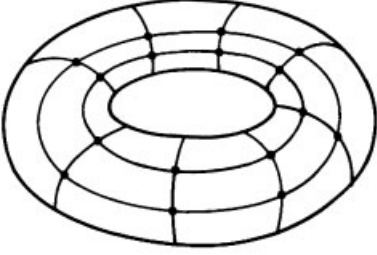


Figure 149: Allowed phase points for the quantized version of a cat map (schematic).

Let us recall that the allowed phase space of a classical cat map is the unit torus. In this example, the phase points develop according to the dynamical law

$$\begin{pmatrix} p_{n+1} \\ q_{n+1} \end{pmatrix} = \begin{pmatrix} 1 & 2 \\ 2 & 3 \end{pmatrix} \begin{pmatrix} p_n \\ q_n \end{pmatrix}. \quad (9.4)$$

In quantum mechanics, eq. (9.4) becomes the Heisenberg equation of motion for the coordinate and momentum operators \hat{q}_n, \hat{p}_n at time n , and the restriction of the classical phase space to a torus implies periodic boundary conditions for the quantum-mechanical wave function in coordinate and momentum space. In other words, the eigenvalues of *both* operators \hat{p} and \hat{q} only have discrete values which cover the torus by a lattice of allowed phase points, as shown in Fig. 149.

We will now show that the unit cell of this lattice is a square with a lattice constant, which is just Planck's quantum of the action h .

If the eigenvalues of \hat{q} have a spacing $\Delta q = \frac{1}{N}$ i. e.,

$$q = 0, \frac{1}{N}, \dots, 1 \quad \text{where } N = \text{integer} \quad (9.5)$$

this implies (via the double periodicity of the wave function) the maximum momentum eigenvalue

$$p_{\max} = \hbar 2\pi / \left(\frac{1}{N} \right) = Nh \quad (9.6)$$

and a spacing $\Delta p = h$, i. e., the eigenvalues of \hat{p} are

$$p = 0, h, 2h, \dots, Nh. \quad (9.7)$$

Because the allowed phase space has unit area, we have

$$1 = q_{\max} p_{\max} = Nh \quad (9.8)$$

$$\text{i. e., } h = \frac{1}{N} \rightarrow \Delta p = \Delta q = h. \quad (9.9)$$

This requirement makes the quantum version of the cat map somewhat unrealistic. But if we assume for a moment that Planck's constant h is a free parameter and the quantum case is only defined by $h \neq 0$ such that eq. (9.9) makes sense, then it follows from (9.5) and (9.7) that

in quantum mechanics only phase points with a rational ratio p/q are allowed. This means that the points with irrational ratios, which were the only ones in the classical cat maps which lead to chaotic trajectories, are forbidden in quantum mechanics. It is therefore reasonable to expect that the quantum version of the cat map will not exhibit chaos.

It has indeed been found by Hannay and Berry (1980) that the time-evolution operator \hat{U} for the quantum cat map is periodic (i. e., for every N there exists an $n(N)$ such that $\hat{U}^{n(N)} = 1$) and has a discrete spectrum of eigenvalues. This implies that all expectation values for the cat map are periodic in time. In other words, the finite values of Planck's constant and the doubly periodic boundary conditions restrict the eigenvalues (of the time-evolution operator) in the quantum version of Arnold's cat map such that chaotic motion becomes impossible.

9.2 A Quantum Particle in a Stadium

Although we have seen in the previous section that a quantum system with a chaotic classical limit does not necessarily also behave chaotically, one nevertheless expects some difference between a quantum system having a classical counterpart, which shows irregular motion, and a quantum version of an integrable classical system having regular trajectories. To cast some light on this problem, McDonald and Kaufmann (1979) calculated numerically the wave functions and spectra of a free particle in a stadium and in a circular disc by solving the Schrödinger equation for a free particle in two dimensions

$$\vec{\nabla}^2 \psi = E \psi \tag{9.10}$$

with the boundary condition $\psi(x, y) = 0$ at the "walls".

Their results are summarized in Fig. 150:

1. The eigenfunctions of the stadium problem show irregular nodal curves (where $\psi(x, y) = 0$) in contrast to the regular curves for the circle.
2. The distribution $N(\Delta E)$ of the eigenvalue spacings ΔE for the circle shows a maximum at $\Delta E = 0$, i. e., there is a high probability of level degeneracies, and one finds *level clustering*. It has been proved by Berry and Tabor (1977) that for integrable systems $N(\Delta E) \propto \exp(-\Delta E \cdot \text{const})$. (An exception is a quantum mechanical oscillator for which $N(\Delta E)$ is a delta function at $\Delta E = \hbar\omega_0$.) For the stadium $N(\Delta E)$ has a maximum at $\Delta E \neq 0$, i. e., there is *level repulsion*.

This level repulsion has also been found for the quantum version of Sinai's billiard (Berry, 1983, Bohigas *et al.*, 1984), and it seems to be a characteristic feature of a quantum system, whose classical limit shows chaos. It is related to the fact that no symmetries exist in these systems, i. e., there are no degeneracies (and no selection rules which prevent mutual interaction of the levels) such that $\lim_{\Delta E \rightarrow 0} N(\Delta E) = 0$. Several theoretical explanations for this phenomenon have been offered, and an interesting connection to random matrix theory (which is used to explain level repulsion in nuclear spectra) has been suggested (Zaslavski, 1981, Berry, 1983, Bohigas *et al.*, 1984). Note that the distribution of level spacings is related to the eigenvalue spectrum of the quantum version of the Liouville operator \hat{L} because $\hat{L}|n\rangle \propto \langle m| \propto [\hat{H}, |n\rangle\langle m|] = (E_n - E_m)|n\rangle\langle m|$, where \hat{H} is the Hamiltonian, and $|n\rangle, |m\rangle$ are its eigenfunctions.

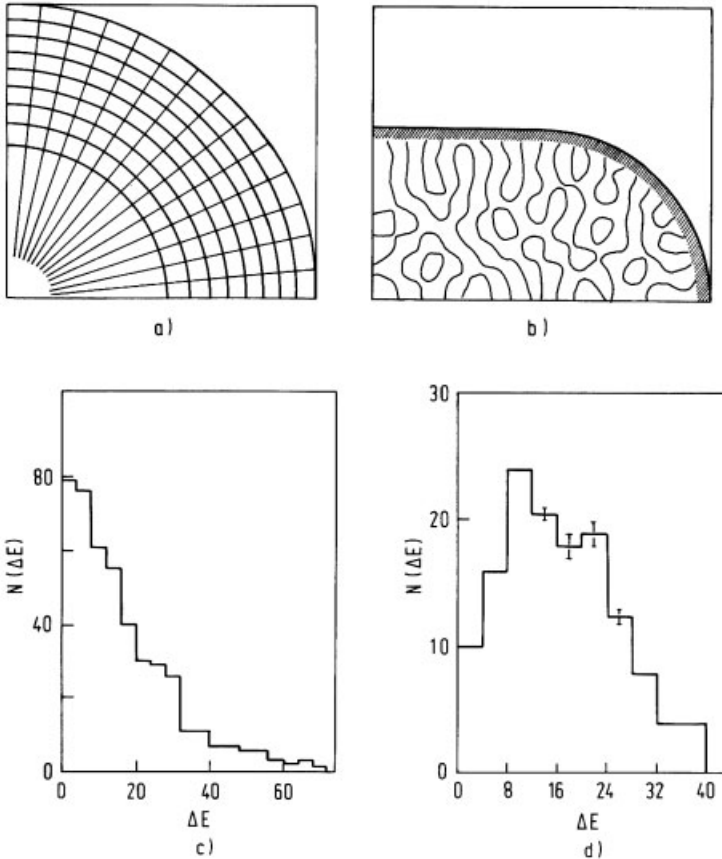


Figure 150: Nodal curves $[\psi(x, y) = 0]$ for one quadrant of the (odd-odd parity) eigenfunctions in a disc (a) and in a stadium (with dimensions $R = a$) (b). Distribution $N(\Delta E)$ of (odd-odd parity) energy level spacings for a circular boundary (c) and for a stadium boundary (d). (After McDonald and Kaufmann, 1979.) Note that $\Delta E = E_{j+1} - E_j$ is the spacing between neighboring levels, and j increases with energy.

9.3 The Kicked Quantum Rotator

We have already seen in Chapter 3 that deterministic diffusion serves as an indicator of chaos. It is, therefore, interesting to see whether this phenomenon also exists in quantum systems. (If the answer is yes, then we know that there is chaos in the quantum system). We show first that a classical kicked rotator, without damping, displays (for strong enough kicking forces) deterministic diffusion, and subsequently investigate its quantum version.

According to eq. (2.26), the equations of motion for the angle θ and the angular momentum p of a classical kicked rotator are

$$p_{n+1} = p_n - V'(\theta_n) \quad n = 0, 1, 2 \dots \quad (9.11a)$$

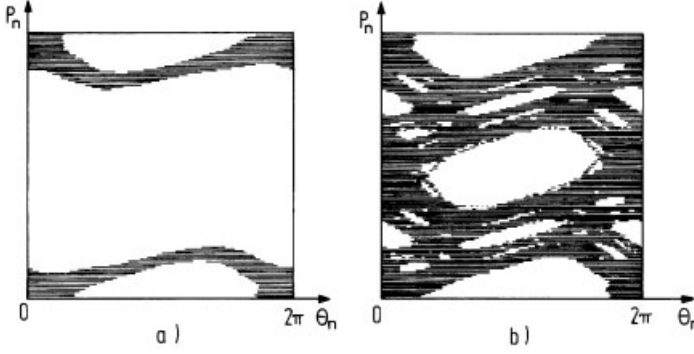


Figure 151: A phase portrait of a classical kicked rotator with a potential function $K \cos \theta$, obtained by iterating eq. (8.11) and plotting successive points. a) For $K = 0.96$ different orbits in the shaded regions are still separated. b) For $K = 1.13$ the islands overlap and the angular momentum can diffuse. (After Chirikov, 1979.)

$$\theta_{n+1} = \theta_n + p_{n+1} = \theta_n - V'(\theta_n) + p_n \quad (9.11b)$$

where $V(\theta) = V(\theta + 2\pi)$ is the potential function of the kicking force.

Summation of (9.11a) over n yields

$$\langle (p_{n+1} - p_0)^2 \rangle = \sum_{i,j}^n \langle V'(\theta_i) V'(\theta_j) \rangle \quad (9.12)$$

where $\langle \dots \rangle$ denotes the average over all initial points θ_0 . If the correlations between the $V'(\theta_i)$ are short-ranged (with range n_0), eq. (9.12) becomes

$$\langle (p_{n+1} - p_0)^2 \rangle = n \sum_j^{n_0} \langle V'(\theta_j) V'(\theta_0) \rangle \propto n \quad \text{for } n \gg 1 \quad (9.13)$$

i. e., the angular momentum of the kicked rotator diffuses.

It has, for example, been found numerically that a kicking potential of the form $V(\theta) = K \cdot \cos \theta$ generates deterministic diffusion (of the angular momentum) above a threshold $K_c \simeq 0.972$ (see Fig. 151).

Another example is the “open cat map” in which the restriction of periodicity of the p_n is lifted. This can be viewed as a kicked rotator with a potential function $V(\theta) = -(K/2) \cdot (\theta \bmod 2\pi)^2$ and has the equations of motion

$$p_{n+1} = p_n + K\theta_n \quad (9.14a)$$

$$\theta_{n+1} = \theta_n(1+K) + p_n \quad (9.14b)$$

where θ_n is always modulo 2π . Including the modulo restriction, eq. (9.14b) appears (apart from p_n , which does not seriously disturb our argument, and after division by 2π , which changes $\bmod 2\pi$ to $\bmod 1$) similar to the map (3.1) that produced the Bernoulli shift. This means that for $K > 0$, eq. (9.14b) generates chaotic motion of the angles which leads via (9.12) to deterministic diffusion.

We now show that the quantum version of the kicked rotator does not diffuse. Instead, one finds either quantum resonance, i. e., the square of the angular momentum increases quadratically in time, or almost periodicity, thus the angular momentum is limited and recurs repeatedly arbitrarily close to its original value.

To understand this result, we use the idea of Fishman, Grempel, and Prange (1982) and map the kicked quantum rotator into a one-dimensional electron localization problem (about which several results are known). [The following derivation is due to V. Emery (private communication).] The time-dependent Hamiltonian of a kicked rotator can be written as

$$\hat{H} = \begin{cases} \frac{\hat{V}(\theta)}{1-\gamma} & \text{for } 0 < t < 1-\gamma \\ \frac{\hat{T}}{\gamma} & \text{for } 1-\gamma < t < 1, \quad \text{with } \hat{T} = -\tau \frac{\partial^2}{\partial \theta^2} \end{cases} \quad (9.15)$$

where we have ignored the kinetic energy \hat{T} during the delta kick which corresponds to the limit $\gamma \rightarrow 1$ in (9.15).

The time-evolution operator from time $t = n$ to time $t = n + 1$, i. e., before and after one kick, therefore becomes

$$\hat{U} = e^{-i\hat{T}} e^{-i\hat{V}} \quad (9.16)$$

and its eigenstates $|\psi_\lambda\rangle$ are determined by

$$\hat{U}|\psi_\lambda\rangle = e^{-i\lambda}|\psi_\lambda\rangle \quad (9.17)$$

where λ is the eigenvalue. This equation governs the time dependence of any state $|\varphi\rangle$ that develops with \hat{U} , because

$$|\varphi(n)\rangle = \hat{U}^n|\varphi\rangle = \sum_\lambda e^{-in\lambda} c_\lambda |\psi_\lambda\rangle; \quad c_\lambda = \langle \psi_\lambda | \varphi \rangle. \quad (9.18)$$

We rewrite (9.17) now in the form of a Schrödinger equation for an electron in a one-dimensional random chain. By using the explicit expression (9.16) for \hat{U} , (9.17) reads

$$e^{-i\hat{T}} e^{-i\hat{V}}|\psi_\lambda\rangle = e^{-i\lambda}|\psi_\lambda\rangle \quad (9.19)$$

which for $\hat{E} \equiv \lambda\hat{1} - \hat{T}$ becomes

$$e^{-i\hat{E}} e^{-i\hat{V}}|\psi_\lambda\rangle = |\psi_\lambda\rangle. \quad (9.20)$$

With $|\psi_\lambda\rangle \equiv e^{i(\hat{V}/2)}|\omega\rangle$ this can be rewritten as:

$$e^{i(\hat{V}/2)}|\omega\rangle = e^{i\hat{E}} e^{-i(\hat{V}/2)}|\omega\rangle = 0 \quad (9.21)$$

or

$$\left[(1 - e^{i\hat{E}}) \cos \frac{\hat{V}}{2} + i(1 + e^{i\hat{E}}) \sin \frac{\hat{V}}{2} \right] |\omega\rangle = 0 \quad (9.22)$$

from which we obtain

$$i(1 + e^{i\hat{E}}) \left[\frac{1 - e^{i\hat{E}}}{i} + \frac{\sin(\hat{V}/2)}{\cos(\hat{V}/2)} \right] \cos \left(\frac{\hat{V}}{2} \right) |\omega\rangle = 0. \quad (9.23)$$

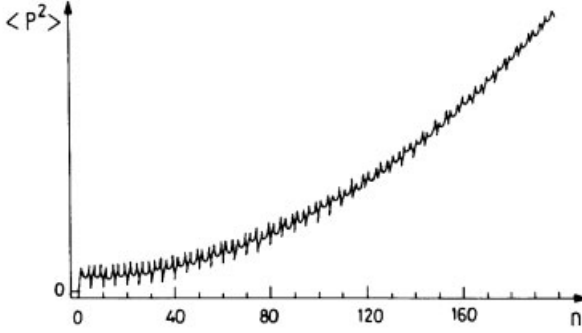


Figure 152: Numerically determined quantum resonance for a kicked rotator at $\tau = 8\pi/5$ (after Izraelev and Shepelyanskii, 1980).

We, therefore, have to find the solutions of

$$\left[\tan \frac{\hat{E}}{2} - \tan \frac{\hat{V}}{2} \right] |u\rangle = 0 \quad \text{when} \quad |u\rangle = \cos \frac{\hat{V}}{2} |\omega\rangle. \quad (9.24)$$

The periodic boundary conditions $\psi_\lambda(\theta + 2\pi) = \psi_\lambda(\theta)$ yield $u(\theta + 2\pi) = u(\theta)$, i. e., $u(\theta)$ can be expanded in a Fourier series:

$$u(\theta) = \sum_m u(m) e^{im\theta}. \quad (9.25)$$

Note that $e^{im\theta}$ is simply the eigenfunction of the angular momentum operator. Thus, (9.24) can be written as

$$T_m u_m + \sum_{r \neq 0} W_r u_{m+r} = \varepsilon u_m; \quad \varepsilon = W_0 \quad (9.26)$$

where

$$T_m \equiv \tan \left[\frac{1}{2} (\lambda - \tau m^2) \right] \quad \text{and} \quad W_r = \frac{1}{2\pi} \int_{-\pi}^{\pi} d\theta e^{ir\theta} \tan \left[\frac{\hat{V}(\theta)}{2} \right].$$

Equation (9.26) is the Schrödinger equation for an electron on a chain with on-site potentials T_m and hopping matrix elements W_r . The integer eigenvalues m of the angular momentum of the kicked rotator correspond to the lattice sites in the conduction problem. Two cases must be distinguished:

- a) For rational values of $\tau/(2\pi) = p/q$, where p and q are both mutually prime integers, the electrons described by (9.26) move freely in a periodic potential and are completely delocalized. For the rotator problem this means that its angular momentum is unbounded in time, i. e., all eigenvalues m can be achieved. In fact the square of the angular momentum increases quadratically in time (see Fig. 152). This phenomenon is termed quantum resonance and occurs for all rational values of $\tau/(2\pi)$. We will explain this phenomenon

for the simplest case $p/q = 1$. The effect of the time-evolution operator on any periodic wave function ψ then becomes

$$\hat{U}|\psi\rangle \doteq e^{2\pi i(\partial^2/\partial\theta^2)} e^{-iV(\theta)}\psi(\theta) = e^{-iV(\theta)}\psi(\theta) \quad (9.27)$$

since we can expand e^{-iV} in a Fourier series:

$$e^{-iV(\theta)}\psi(\theta) = \sum_{m=-\infty}^{\infty} A_m e^{im\theta} \quad (9.28)$$

and

$$(e^{-2\pi i(\partial^2/\partial\theta^2)}) e^{im\theta} = e^{-2\pi im^2} e^{im\theta} = e^{im\theta}. \quad (9.29)$$

For the expectation value of the square of the angular momentum with any periodic wave function after n kicks, we therefore find:

$$\begin{aligned} \langle p^2 \rangle &\propto \langle \psi | (\hat{U}^+)^n \frac{\partial^2}{\partial\theta^2} \hat{U}^n | \psi \rangle \propto \int_{-\pi}^{\pi} d\theta \psi^*(\theta) e^{inV(\theta)} \frac{\partial^2}{\partial\theta^2} e^{-inV(\theta)} \psi(\theta) \\ &\propto n^2 \langle \psi | \left(\frac{\partial V}{\partial\theta} \right)^2 | \psi \rangle + O(n). \end{aligned} \quad (9.30)$$

This quadratic increase in time is clearly a quantum effect because (9.27) holds only for integer values of m , i. e., for a quantized angular momentum.

- b) Next we consider the case where $\tau/(2\pi)$ is irrational. The potential $T_m = \tan[(\lambda - m^2\tau)/2]$ then becomes random instead of periodic because $[(\lambda - m^2\tau)/2] \bmod \pi$ behaves like a random number generator. (Note that $\tan x$ is periodic with period π and its argument can, after division by π , be written as $x_m = [\lambda/(2\pi) - m^2\tau/(\pi)] \bmod 1$. If $\tau/(2\pi)$ is expressed in binary representation and one considers, for example, values $m^2 = 2^n$, then it is seen that the $x_{m=2^n}$ are generated by a Bernoulli shift from a irrational number and are, hence, truly random.)

Intuitively, one expects that an electron in a one-dimensional random potential has a strong tendency to localize since there is (in contrast to higher dimensions) only one way to move from one point to the next, and this could be easily blocked by a potential barrier. It is in fact well known from the work of Anderson (1958) and Ishii (1973) (but by no means trivial to prove) that all electrons in a one-dimensional random potential are localized (for short-ranged hopping matrix elements). The physical reason for this is that, in the one-dimensional case, the random potential changes the phase of the wave function at every site, and this random dephasing eventually leads to localization.

The electron is, therefore, confined to a finite range of ms , i. e., the angular momentum of the rotator is bounded and does not increase in time; in other words, there is no diffusion of momentum in contrast to the classical case. Figure 153 shows the time dependence of the energy of a periodically kicked rotator, numerically calculated for an irrational value of $\tau/2\pi$. It can be seen that the oscillations in energy are not only bounded but recur many times.

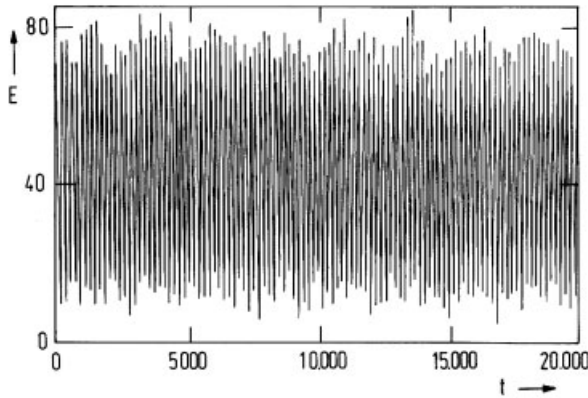


Figure 153: Numerical result for the expectation value of the energy $E \propto \langle p^2 \rangle$ (of a kicked quantum rotor) as a function of the number n of pulses for an irrational value of $\tau/(2\pi)$ (after Hogg and Hubermann, 1982).

It has been proved by Hogg and Hubermann (1982) that if the wave function can be normalized (i. e., if we know that the angular momentum does not diffuse) then both the wave function and the energy return arbitrarily close to their initial values arbitrarily often. This time dependence is called *almost periodic* in contrast to the quasiperiodic motion mentioned in Chapter 7. (For almost periodic functions $f(t)$ there exists a relatively dense set $\{\tau_\epsilon\}$ such that $|f(t + \tau_\epsilon) - f(t)| < \epsilon$ for any $\epsilon > 0$. $\{\tau_\epsilon\}$ is relatively dense if there exists a T_ϵ such that each interval of length T_ϵ on the real axis contains at least one τ_ϵ .)

We have seen, above, that up to now no quantum system seems to exist which exhibits deterministic chaos (indicated either by a continuous power spectrum or deterministic diffusion). Nevertheless, there is a difference in the behavior of quantum systems with a chaotic classical counterpart and those (quantum systems) with a regular classical limit.

Let us finally mention an interesting calculation of Gutzwiller (1983) for an electron which is scattered from a non-compact surface with negative curvature. It shows that the phase shift as a function of momentum is essentially given by the phase angles of the Riemann zeta function on the imaginary axis, at a distance 0.5 from the famous critical line. This phase shift displays features of chaos because it is able to mimic any given smooth function. It, therefore, seems that the chaotic nature of quantum systems which are described by wave mechanics is of a rather subtle and “softer” kind than the chaos in classical mechanics.

These comments indicate that the question of stochasticity in quantum mechanics is still far from being solved.

10 Controlling Chaos

Around 1950, the famous mathematician and father of the computer John v. Neumann had already remarked (cited after Dyson, 1988) that dynamical systems can be divided into two classes: stable systems whose behavior can be predicted by computers, and unstable systems which display a sensitive dependence on initial conditions and therefore can be easily stabilized and controlled by computers. He proposed the control of local weather by distributing chemicals from airplanes. Therefore the idea of controlling chaotic systems by small time-dependent perturbations is not completely new.

In 1987 the space agency NASA (Farquhar *et al.*, 1985) made use of the sensitive dependence on initial conditions in the classical three-body problem to manoeuvre a space-craft towards a comet by means of small corrections which required only a small amount of fuel (see Fig. 154). This would never have been possible for a non-chaotic system where one needs large forces to bring the space-craft into a new orbit.

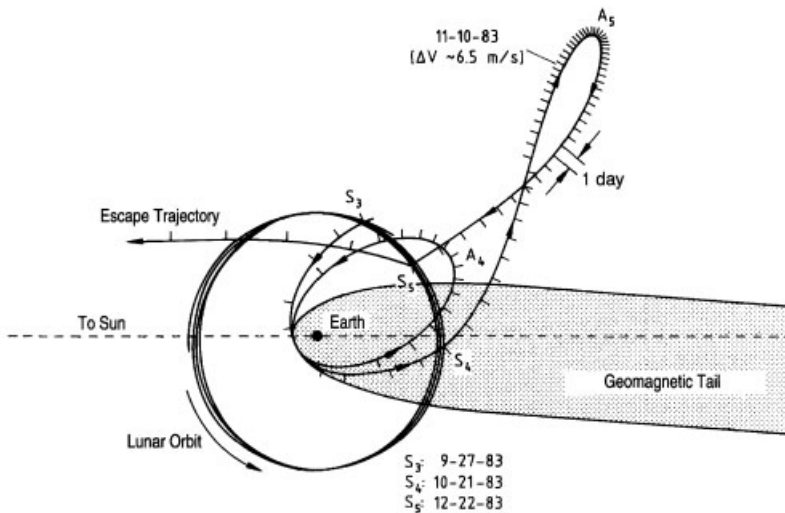


Figure 154: The trajectory of the space-ship ISEE 3 (International Sun Earth Explorer 3) was changed in order to leave the earth–moon system in the direction of the comet Giacobini–Zinner. On October 10, 1983, the velocity of the space-ship was changed by the tiny amount of 6.5 m s^{-1} . By exploiting the gravitation of the moon in a clever fashion, this small change was sufficient to send the space-ship in the direction of the comet (after Farquhar *et al.*, 1985).

Then in 1990 the seminal article of Ott, Grebogi and Yorke was published in which they demonstrated that small time-dependent changes in the control parameter of a system can change the chaotic motion on the strange attractor into periodic motion.

The chaotic motion on a strange attractor can be viewed as a dance of the trajectory between different unstable periodic orbits. This can easily be seen when we recall the period-doubling route. In this route, cycles of different lengths become unstable one after the other if the control parameter r is increased. At the culmination point r_∞ one has an infinitely long cycle, and in the chaotic regime $r > r_\infty$ the trajectory moves between unstable cycles (see Fig. 155). During this movement the trajectories become repelled from the cycles; otherwise the motion would again be periodic (see Appendix H).

10.1 Stabilization of Unstable Orbits

In 1990 Grebogi, Ott and Yorke showed that small variations in the control parameter can change unstable cycles into stable cycles in such a way that the chaotic trajectory becomes periodic.

In the following we will demonstrate this for the simple example of the logistic map. Figure 156 shows that the fixed point x^* becomes unstable for $r > r_\infty$ because $|f'(x^*)| > 1$. This means that a starting point x_0 will move away from x^* (see Fig. 156 a). But if we change the parameter r for a moment by an amount δr , in such a way that the parabola is shifted upwards, we could choose δr such that x_0 falls after one iteration onto the unstable fixed point x^* (Fig. 156b). Since we also have, for an unstable fixed point, the equation $x^* = f(x^*)$, the trajectory remains located on x^* if we put $\delta r = 0$. Therefore, the system becomes trapped on an unstable fixed point and shows no longer any chaos.

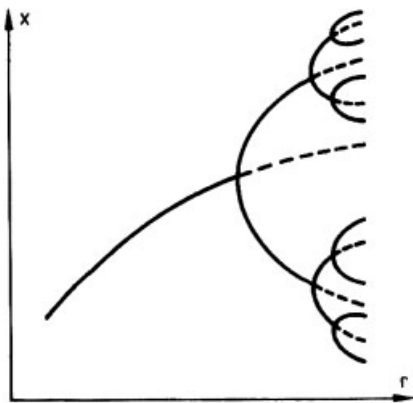


Figure 155: The period doubling route generates unstable periodic orbits (schematically).

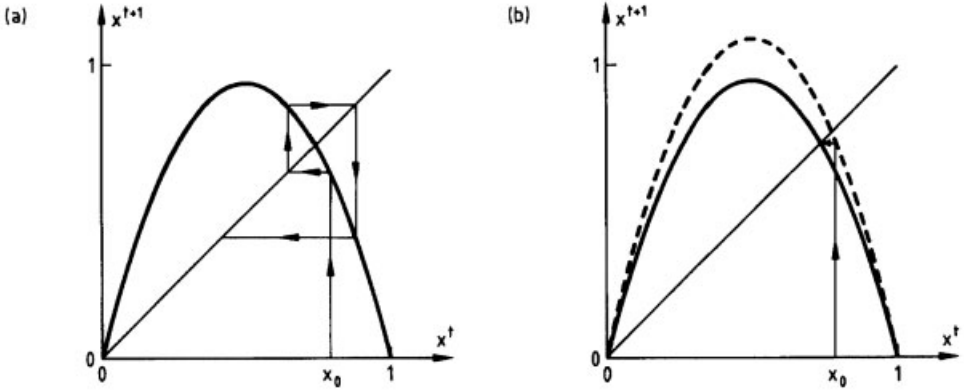


Figure 156: Stabilization of a fixed point by a change in the control parameter. (a) The fixed point x^* of the logistic map at $r = 3.78$ is unstable, and the trajectory which starts at x_0 becomes repelled from it. (b) Small changes in the control parameter r lead to the dotted map, which drives x_0 , after the next time step, back to the fixed point.

To compute the change in the control parameter that is needed to stabilize the fixed point, we linearize the map $f_r(x)$ in the vicinity of x^* . With $\delta x^t = x^t - x^*$ one obtains:

$$\begin{aligned} x^{t+1} &= f_r(x^t) = f_r(x^* + x^t - x^*) \\ &= f_r(x^*) + f'_r(x^*)\delta x^t + O((\delta x^t)^2). \end{aligned} \quad (10.1)$$

By changing $r \rightarrow r + \delta r^t$ we get an additional term

$$x^{t+1} = f_r(x^*) + f'_r(x^*)\delta x^t + \frac{\partial f}{\partial r}(x^*)\delta r^t, \quad (10.2)$$

and we have neglected contributions of order $(\delta x^t)^2$, $(\delta r^t)^2$ and $\delta x^t \delta r^t$.

With $f_r(x^*) = x^*$ we can write equation (10.2) as

$$\delta x^{t+1} = f'_r(x^*)\delta x^t + \frac{\partial f}{\partial r}(x^*)\delta r^t. \quad (10.3)$$

Since we require that the system ends up at time $t + 1$ on the unstable fixed point x^* , this means $\delta x^{t+1} = 0$, we obtain according to eq. (10.3)

$$\delta r^t = -\frac{f'_r(x^*)}{\frac{\partial f}{\partial r}(x^*)}\delta x^t. \quad (10.4)$$

This means that, to stabilize the fixed point, the change in the control parameter must be proportional to the distance δx^t between the fixed point and the trajectory. The change in the control parameter becomes small if the initial distance between the trajectory and the fixed point, i. e., $(x^* - x_0)$ is small. This condition can always be fulfilled: Since the motion of the trajectory on the strange attractor is ergodic, the trajectory in the course of time approaches every unstable fixed point arbitrarily closely. Therefore, one has to wait until the trajectory comes very close to x^* . A change in control parameter $\delta r^t \propto \delta x^t$ which is needed to stabilize

the fixed point can then be made arbitrarily small. The whole procedure recalls somehow the Japanese art of self-defense where one uses the motion of the opponent in a clever way to send him to the floor with a tiny twist.

To floor the chaotic motion on a strange attractor onto a fixed point we have to do the following:

1. Localize the fixed point.
2. Wait until the trajectory comes close to the fixed point (this can take some time).
3. Change the control parameter in proportion to the distance between the trajectory and the fixed point.

We can already see at this stage that one has some freedom in the choice of the proportionality factor ε between δr^t and δx^t , which has in eq. (10.4) the form $\varepsilon = -f'_r(x^*)/(\partial f(x^*)/\partial r)$. With $\delta r^t = \varepsilon \delta x^t$, eq. (10.3) becomes

$$\delta x^{t+1} = (f'_r(x^*) + \varepsilon) \delta x^t. \quad (10.5)$$

If we require only that the system becomes attracted to the fixed point after a long time, i. e., $\lim_{t \rightarrow \infty} \delta x^t \rightarrow 0$, any ε which ensures

$$|f'_r(x^*) + \varepsilon| < 1 \quad (10.6)$$

will do (see eq. (3.17) on page 24). This means that one has for fixed $f'(x^*)$ a whole range of ε values for which the system converges to the fixed point (Schuster *et al.*, 1996), cf. Fig. 157. Since one needs only very little information about the nonlinear system to stabilize a fixed point it becomes understandable that this type of chaos control has been performed successfully in many experimental systems (Shinbrot *et al.*, 1993). One has only to wait until the trajectory comes into the vicinity of a fixed point and then switch on the change in the control parameter which is proportional to the distance between the fixed point and the trajectory. Figure 158 shows how this procedure works for a Belousov–Zhabotinsky reaction (introduced on page 11), whose nonlinear dynamics can be reduced to a one-dimensional map.

The ideas which have been outlined for a fixed point in the previous paragraph can be generalized in a straightforward fashion to longer unstable cycles. For example, if we want to stabilize a cycle of period 2 for the logistic map, we have only to replace $f(x)$ by $f^2(x)$ in eq. (10.1) and linearize around one of the two fixed points $f^2(x_{1,2}^*) = x_{1,2}^*$. Everything runs through as for a simple fixed point, one must only check that the control parameter is switched on in even time steps in order to stabilize the correct fixed point x_1^* or x_2^* .

The ideas described so far are quite well known to engineers and applied mathematicians, as these concepts are at the heart of control theory (Chen, 1999; Slotine and Li, 1991). In fact, quite elaborate approaches have been developed but, from the point of view of applications, most ideas are confined to the linearized regime as, e. g., sketched above. It is the essentially new idea of chaos control that the nonlinear dynamical system provides a huge number of unstable periodic orbits. Each of them can be stabilized with tiny control forces. In the wake of these observations control of chaos became one of the most popular branches in applied nonlinear science. Meanwhile reviews are available in the literature (Schuster, 1999). Here we focus on a more detailed description of two quite popular and important control schemes.

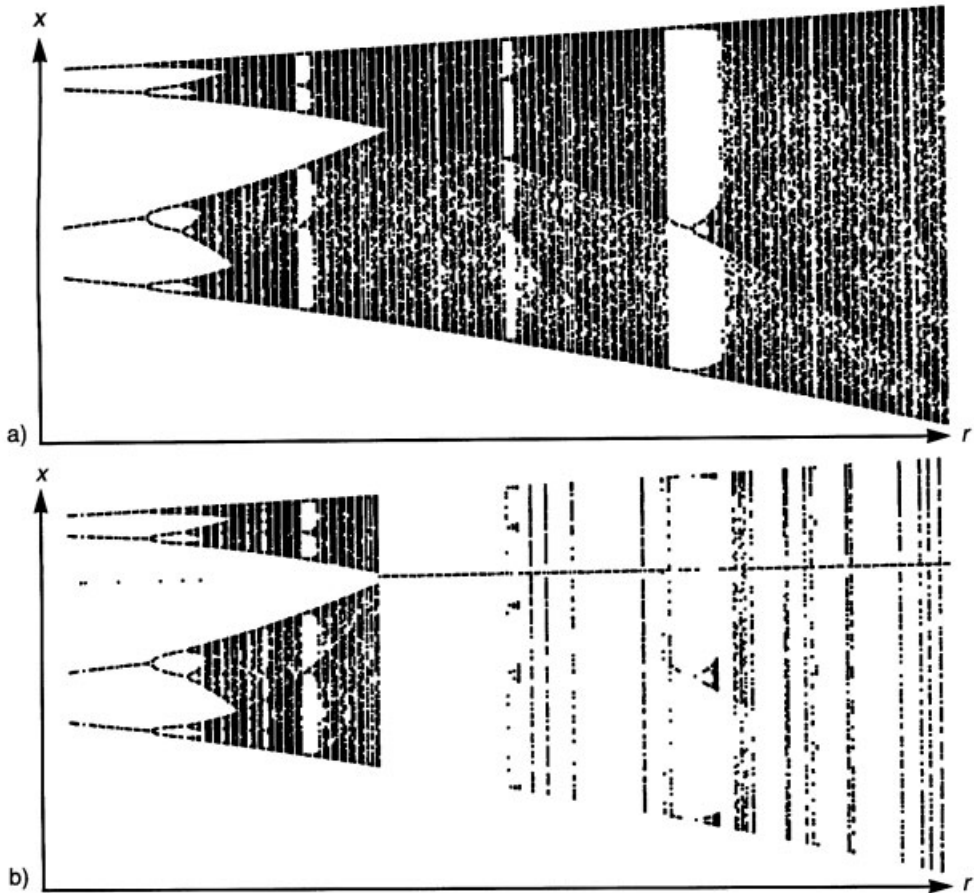


Figure 157: Stabilization of the unstable fixed point $x^* = (r-1)/r$ of the logistic map for $r > r_\infty$ by a change in the control parameter as $\delta r^j = \epsilon(\partial f(x^*)/\partial r) \cdot (x^* - x)$. This change is only switched on if $|x^* - x| < 10^{-2}$ for $\epsilon = 2$. (a) Normal bifurcation diagram (compare with Fig. 36 on page 53), (b) bifurcation diagram when the time-dependent parameter change has been switched on.

10.2 The OGY Method

For higher-dimensional maps one has only to stabilize the unstable directions (which are given by the eigenvectors of the local Jacobi matrix which belong to eigenvalues with modulus > 1). Thus the number of parameters needed to adjust the phase space point properly are given by the dimension of the unstable manifold. Figure 159 shows how the trajectory is driven onto a stable manifold by a small change in the control parameter. Once it is on the stable manifold, no more changes in the control parameter are needed and the trajectory is pulled onto the fixed point.

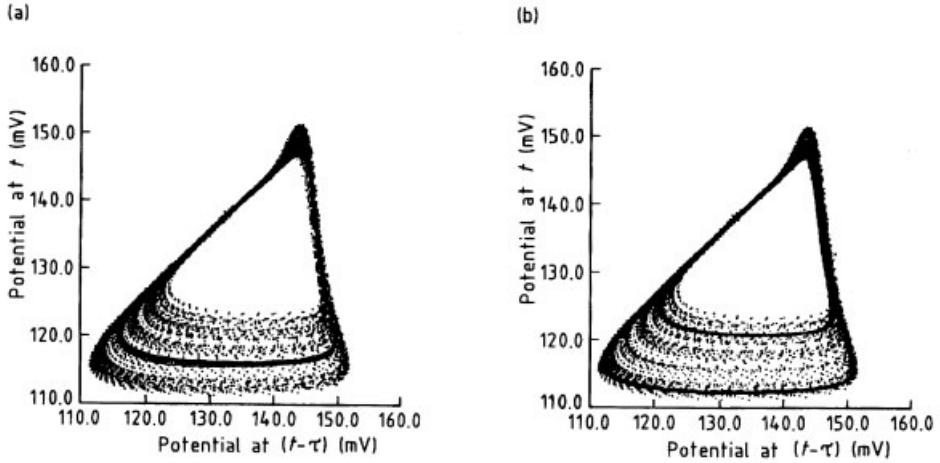


Figure 158: Cycles of period 1 and 2, which have been stabilized in a Belousov–Zhabotinsky reaction by changing the flow rate in the previously chaotic region. The figure shows the phase portraits, which have been obtained by reconstructing phase space via time delay from the measured potential of a bromide electrode (the potential is proportional to the concentration of BrO_3^- , see also page 11, after Petrov *et al.*, 1993).

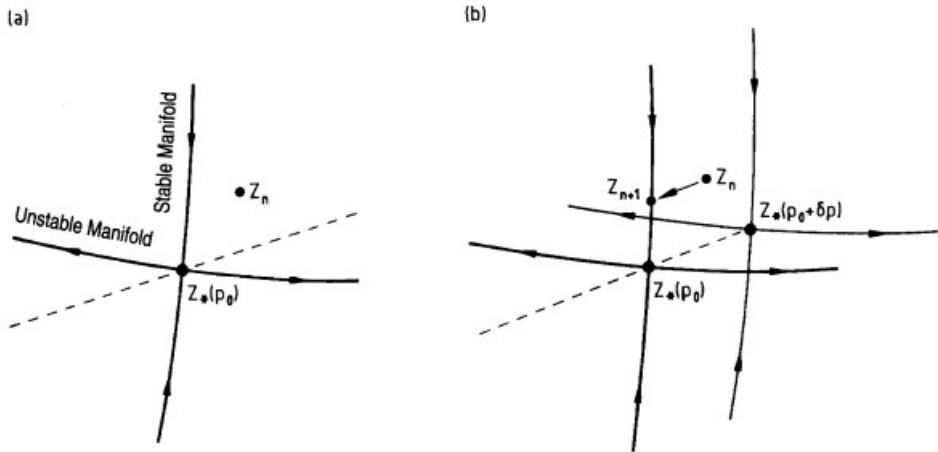


Figure 159: Stabilization of a previously unstable fixed point in two dimensions. (a) The fixed point $Z_*(p_0)$ and its stable and unstable manifolds can be shifted along the dotted line by a change in the control parameter p_0 . (b) p_0 is changed by δp , the point Z_n moves in the following time step onto the stable manifold on which Z_{n+1} becomes attracted to the fixed point (after Shinbrot *et al.*, 1993).

This method for controlling chaos has been applied to many systems, especially to lasers, hydrodynamic systems and coupled cardiac cells (compare Table 2 on page 10). Since chaotic systems contain an infinite number of periodic orbits, they offer the possibility to stabilize completely different types of dynamical behavior. If one wants to stabilize a technical system it would therefore be advantageous to drive it into the chaotic region in order to control it with tiny variations in the control parameter. To perform this control it is not necessary to know the equation of motion of the system in explicit form. It is sufficient to know the location of the fixed points and the local Jacobian. This information could be extracted from measured data, for example, by the method of delay coordinates (see Chapter 6, eq. (6.44) and Shinbrot *et al.*, 1993; Hubinger, Doerner and Martienssen, 1993). Since one just needs to obtain the local phase-space structure in a neighborhood of the unstable orbit, the requirements concerning the amount of data are less severe than for the global reconstruction of the whole attractor.

10.3 Time-Delayed Feedback Control

As pointed out in the preceding sections, control is achieved by a suitable time-dependent change in a system parameter $r \rightarrow r + \delta r^t$. With an appropriate choice of δr^t the target state, e. g., an unstable fixed point x^* , becomes stable. The simple scheme introduced at the beginning of this chapter, $\delta r^t = x^t - x^*$, requires the a priori knowledge of the target state x^* . Following an idea of Pyragas (1992) one may obtain a crude estimate by replacing the unknown fixed point by a previous iterate, i. e., by deriving the control force from a time-delayed difference $\delta r^t = K(x^t - x^{t-1}) = K(\delta x^t - \delta x^{t-1})$. It is often convenient to introduce a linear amplification factor K as well. In order to figure out whether such a simple control scheme works one considers the motion in a neighborhood of the target state. Using eq. (10.3) the dynamics is governed by the higher order difference equation

$$\delta x^{t+1} = f'_r(x^*)\delta x^t + \frac{\partial f}{\partial r}(x^*)K(\delta x^t - \delta x^{t-1}). \quad (10.7)$$

As usual the time evolution follows the typical exponential law $\delta x^t = \gamma^t \delta x^0$ where the so-called Floquet multiplier γ obeys

$$\gamma^2 = \left(f'_r(x^*) + K \frac{\partial f}{\partial r}(x^*) \right) \gamma - K \frac{\partial f}{\partial r}(x^*). \quad (10.8)$$

Stabilization is achieved for those values of K where eq. (10.8) yields only solutions with modulus lower than one, $|\gamma| < 1$.

Conditions for successful control may be either derived from the explicit solution for γ or through conditions which do not require the computation of the roots of eq. (10.8) (the Schur–Cohn–Jury criterion). Finally we obtain three constraints for the stability of the controlled fixed point

$$0 < 1 - f'_r(x^*) \quad (10.9a)$$

$$0 < 2 \left(1 + K \frac{\partial f}{\partial r}(x^*) \right) - 1 + f'_r(x^*) \quad (10.9b)$$

$$1 > \left| K \frac{\partial f}{\partial r}(x^*) \right|. \quad (10.9c)$$

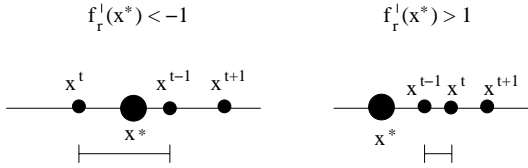


Figure 160: Successive iterates in the neighborhood of the unstable fixed point for negative (left) and positive (right) Floquet multiplier. The size of the time-delayed difference $x^t - x^{t-1}$ from which the control force is derived is also indicated.

Condition (10.9a) does not involve the control amplitude K . It just poses a constraint on the unstable fixed point. Since unstable fixed points obey $|f_r'(x^*)| > 1$ we recognize that only unstable orbits with negative Floquet multipliers, i. e., $f_r'(x^*) < -1$, are accessible for time-delayed feedback control. Such a constraint has a simple geometric meaning. When $f_r'(x^*) < -1$ the dynamics oscillates in a neighborhood of the fixed point. Actually such a type of motion is generated in period-doubling bifurcations (cf. Fig. 155). The control force is derived from a time-delayed difference $x^t - x^{t-1}$. To keep this force finite when stabilization sets in, one needs a finite difference between successive iterates as otherwise the control force will vanish. Thus, as sketched in Fig. 160, the oscillatory part of the motion is required. Only target states with oscillating dynamics, i. e., with negative (or complex) Floquet multipliers are accessible for time-delayed feedback control.

Conditions (10.9b) and (10.9c) yield constraints for the control amplitude. In fact, eq. (10.9c) tells us that control fails for large values of the amplification K . In view of eq. (10.9a) it is quite straightforward to work out that conditions (10.9b) and (10.9c) yield a finite interval of K values for successful control provided $f_r'(x^*) > -3$. No such control interval is obtained if $f_r'(x^*) < -3$. Thus time-delayed feedback control fails for strongly unstable orbits.

10.3.1 Rhythmic Control

The original Pyragas scheme suffers from the constraint that only orbits with oscillating dynamics in their neighborhood, i. e., complex Floquet exponents, are accessible. To overcome such a severe limitation, modifications have been proposed which essentially result in an effective enlargement of the phase space (Schuster and Stemmler, 1997). A simple implementation consists of a time-dependent modulation of the control amplitude. Consider a period-two modulation of the control amplitude, i. e., K takes the value K_0 on even time steps and K_1 on odd time steps. Then condition (10.7) determining the stability reads

$$\delta x^{2t+1} = f_r'(x^*)\delta x^{2t} + \frac{\partial f}{\partial r}(x^*)K_0(\delta x^{2t} - \delta x^{2t-1}) \quad (10.10a)$$

$$\delta x^{2t+2} = f_r'(x^*)\delta x^{2t+1} + \frac{\partial f}{\partial r}(x^*)K_1(\delta x^{2t+1} - \delta x^{2t}). \quad (10.10b)$$

Since the time evolution at even and odd time steps is governed by different control amplitudes, one effectively ends up with a higher-dimensional dynamics, eqs. (10.10). With the usual exponential law, $\delta x^{2t} = \gamma^{2t}\delta x_0$, $\delta x^{2t+1} = \gamma^{2t+1}\delta x_1$ one obtains for the multiplier γ the

characteristic equation

$$\left(\gamma^2 + \frac{\partial f}{\partial r}(x^*)K_0\right) \left(\gamma^2 + \frac{\partial f}{\partial r}(x^*)K_1\right) \quad (10.11)$$

$$= \gamma^2 \left(f'_r(x^*) + \frac{\partial f}{\partial r}(x^*)K_0\right) \left(f'_r(x^*) + \frac{\partial f}{\partial r}(x^*)K_1\right). \quad (10.12)$$

Of course, eq. (10.11) without modulation, $K_0 = K_1 = K$, is nothing else but the original characteristic equation (10.8) squared in a suitable way. Evaluation of the stability criteria results now in the three constraints

$$0 < (1 - f'_r(x^*)) \left(1 + f'_r(x^*) + \frac{\partial f}{\partial r}(x^*)K_0 + \frac{\partial f}{\partial r}(x^*)K_1\right) \quad (10.13a)$$

$$0 < \left(1 - \frac{\partial f}{\partial r}(x^*)K_0\right) \left(1 - \frac{\partial f}{\partial r}(x^*)K_1\right) \\ + \left(f'_r(x^*) + \frac{\partial f}{\partial r}(x^*)K_0\right) \left(f'_r(x^*) + \frac{\partial f}{\partial r}(x^*)K_1\right) \quad (10.13b)$$

$$1 > \left|K_0 \frac{\partial f}{\partial r}(x^*)K_1 \frac{\partial f}{\partial r}(x^*)\right|. \quad (10.13c)$$

Now, even in the case $f'_r(x^*) > 1$, i. e., without oscillating motion in the vicinity of the target state, these three conditions can be satisfied thanks to the second factor in eq. (10.13a) (cf. eq. (10.9a)). One just takes an appropriate negative value for, say, $K_1 \partial f / \partial r$ and chooses K_0 so small that the condition (10.13c) is still valid. For instance the choice $K_0 = 0$, $K_1 \partial f / \partial r \lesssim -(1 + f'_r)$ works nicely.

Apart from rhythmic control there exist alternatives to increase the effective phase space dimension and to stabilize orbits with positive Floquet multipliers, e. g., by directly adding unstable degrees of freedom to the control loop (Pyragas, 2001).

10.3.2 Extended Time-Delayed Feedback Control

To overcome the second limitation of the original Pyragas scheme mentioned above, namely the inability to stabilize strongly unstable periodic orbits, an extended version of time-delayed feedback control has been proposed (Socolar *et al.*, 1994) using multiple time delay. Within the framework of the previous paragraphs such an approach amounts to a parameter modulation according to

$$\delta r^j = K \sum_{\tau=0}^{\infty} R^\tau (x^{j-\tau} - x^{j-\tau-1}) = K(x^j - x^{j-1}) + R\delta r^{j-1}. \quad (10.14)$$

Here the filter parameter R , $|R| < 1$, determines how sensitively the control depends on the history of time-delayed differences. Using $\delta x^j = \gamma \delta x^0$ and $\delta r^j = \gamma \delta r^0$ stability is determined through the condition [cf. eqs. (10.3) and (10.14)]

$$\gamma^2 = \gamma \left(f'_r(x^*) + \frac{\partial f}{\partial r}(x^*)K + R\right) - \frac{\partial f}{\partial r}(x^*)K - Rf'_r(x^*) \quad (10.15)$$

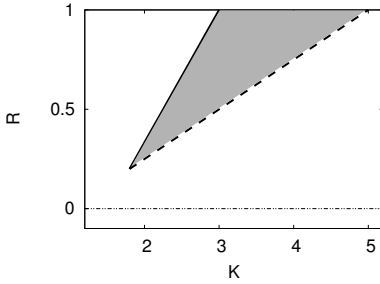


Figure 161: Control domain for extended time-delayed feedback control according to the conditions (10.16) for $f'_r(x^*) = -4$ and $\partial f/\partial r = 1$. K: control amplitude, R: filter parameter.

which of course in the limit $R = 0$ reduces to eq. (10.8). Stability conditions result in

$$0 < (1 - f'_r(x^*))(1 - R) \quad (10.16a)$$

$$0 < 2 \left(1 + K \frac{\partial f}{\partial r}(x^*) + R f'_r(x^*) \right) - (1 - f'_r(x^*))(1 - R) \quad (10.16b)$$

$$1 > \left| K \frac{\partial f}{\partial r}(x^*) + R f'_r(x^*) \right|. \quad (10.16c)$$

Thanks to the factor $1 - R$ in condition (10.16b), stabilization can be achieved even if the orbit is strongly unstable, $f'_r(x^*) < -3$, by taking positive values for the filter parameter. Figure 161 shows the typical triangular shape of the control domain in the K - R control parameter space. Even when the original Pyragas scheme $R = 0$ fails to produce a finite control interval, successful stabilization can be achieved by choosing positive values for the filter parameter.

10.3.3 Experimental Realization of Time-Delayed Feedback Control

While the OGY scheme requires some data processing like, e. g., determination of the periodic target state, analysis of invariant manifolds, or the construction of a Poincaré cross-section time-delayed feedback control can be implemented with less effort. One just needs to measure a signal $s(t)$ and modulate one of the accessible systems parameters, e. g., the amplitude of a driving field, according to the time-delayed difference, $s(t) - s(t - \tau)$. A typical experimental setup is sketched in Fig. 162. In order to keep the scheme non-invasive, the delay time τ is chosen to be an integer multiple of the period of the target state (cf., e. g., Kittel *et al.*, 1995 for suitable schemes to adapt the delay time properly). But one has to pay a price, namely that no a priori estimate is available as to whether the control will work and what the appropriate parameter values could be.

As pointed out in the previous paragraphs, the simple time-delayed feedback scheme suffers from constraints, in particular:

1. Torsion in the phase space is a necessary condition for the control to work, i. e., only orbits with complex Floquet exponents are accessible for time-delayed feedback control.
2. Orbits with a large Liapunov exponents, i. e., strongly unstable orbits, cannot be stabilized by the Pyragas scheme.

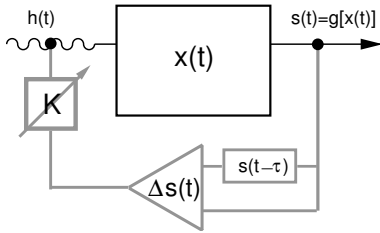


Figure 162: Diagrammatic view of an experimental setup for time-delayed feedback control: $x(t)$, internal degrees of freedom; $h(t)$, system parameter; $s(t)$, signal. The control loop with time-delayed feedback device is displayed in grey. The control force is derived from a time-delayed difference and a linear amplification, $K[s(t) - s(t - \tau)]$. The force is used to modulate a system parameter.

These constraints are not confined to simple one-dimensional maps but apply to the general case as well and thus constitute a universal feature of time-delayed feedback control (Just *et al.*, 2003). Fortunately, one may overcome these limitations either by rhythmic control, i. e., periodic modulation of the control amplitude and by extended control schemes employing multiple delays. One should mention that for the implementation of the latter scheme no additional delay device is required.

Since time-delayed feedback schemes are extremely simple to implement they have been successfully applied in quite diverse experimental contexts, e. g., in laser systems (Bielawski *et al.*, 1994), discharge gas tubes (Pierre *et al.*, 1996), Taylor–Couette flows (Lüthje, 2001), electrochemical reactions (Parmananda *et al.*, 1999), high-power ferromagnetic resonance experiments (Benner and Just, 2002), and even for arrhythmic cardiac control (Hall *et al.*, 1997). Rhythmic control has been employed in a laser experiment (Bielawski *et al.*, 1993). The success of extended time-delayed feedback has been demonstrated in fast diode resonator experiments (Gauthier *et al.*, 1994).

10.4 Parametric Resonance from Unstable Periodic Orbits

The very existence of unstable periodic orbits in chaotic systems leads to resonances, from which one can determine the location of the cycles on the attractor and their local stability (Schuster *et al.*, 1996).

Figure 163 shows the lifetime τ of a trajectory of the logistic map within the interval $x_0 \pm \delta$ (where x_0 is a freely chosen point on the attractor) for the case when the control parameter r has been modulated as $\delta r^t = \varepsilon(x^t - x_0)$. The inverse lifetime τ^{-1} displays as a function for ε a minimum, this means that the lifetime of the most stable unstable cycle, which has a point within the interval $x_0 \pm \delta$, diverges.

In order to understand this phenomenon we compute as an example the lifetime of the unstable fixed point x^* of the logistic map as a function of ε . The linearized equation of motion (10.3) becomes, with $\gamma = \frac{\partial f}{\partial x}(x^*) + \varepsilon \frac{\partial f}{\partial r}(x^*)$:

$$\delta x^t = \gamma \delta x^{t-1} = \gamma^t \delta x^0. \quad (10.17)$$

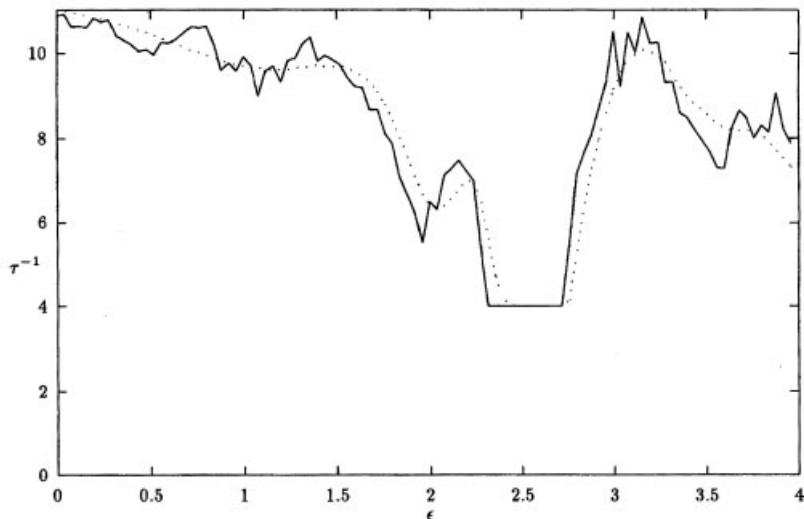


Figure 163: The inverse lifetime τ^{-1} of the trajectory of the logistic map with $r = 3.79$ in the interval $x^* + \delta$ ($x^* = 0.6$, $\delta = 0.03$) as a function of the control parameter ϵ . For $2.32 \leq \epsilon \leq 2.76$ an unstable cycle with period 4 becomes stabilized. The dotted line shows τ^{-1} for the same parameter values for the case when white noise with amplitude 10^{-2} has been added to the logistic map, i. e., the observed resonance phenomenon is stable against noise (Schuster *et al.*, 1996).

The lifetime τ is determined by the requirement that the trajectory leaves the interval at $x_0 \pm \delta$, i. e.,

$$\delta x^\tau = \gamma^\tau \delta x^0 = \delta. \quad (10.18)$$

This yields

$$\tau^{-1} \propto \log |\gamma| = \log \left| \frac{\partial f}{\partial x}(x^*) + \epsilon \frac{\partial f}{\partial r}(x^*) \right|. \quad (10.19)$$

The lifetime τ diverges in the interval $\epsilon_- \leq \epsilon \leq \epsilon_+$, where

$$\epsilon_\pm = [f'(x_0^*) \pm 1] / \frac{\partial f}{\partial r}(x^*). \quad (10.20)$$

Since ϵ_\pm can be measured, one can compute via eq. (10.20) the unknown $\frac{\partial f}{\partial x}(x^*)$ and $\frac{\partial f}{\partial r}(x^*)$, i. e., the local Liapunov exponents $\lambda(x^*) = \log \left| \frac{\partial f}{\partial x}(x^*) \right|$.

Parametric resonances of unstable periodic orbits can also be observed for higher-dimensional maps. As an example we consider the Hénon map

$$x^{t+1} = r + 0.3y^t - (x^t)^2 \quad (10.21a)$$

$$y^{t+1} = x^t, \quad (10.21b)$$

whose control parameter is modulated as $\delta r^t = \epsilon_1(x^* - x^t) + \epsilon_2(y^* - y^t)$ (where $x^* = y^*$ is the fixed point of the Hénon map [10.21 a–b]).

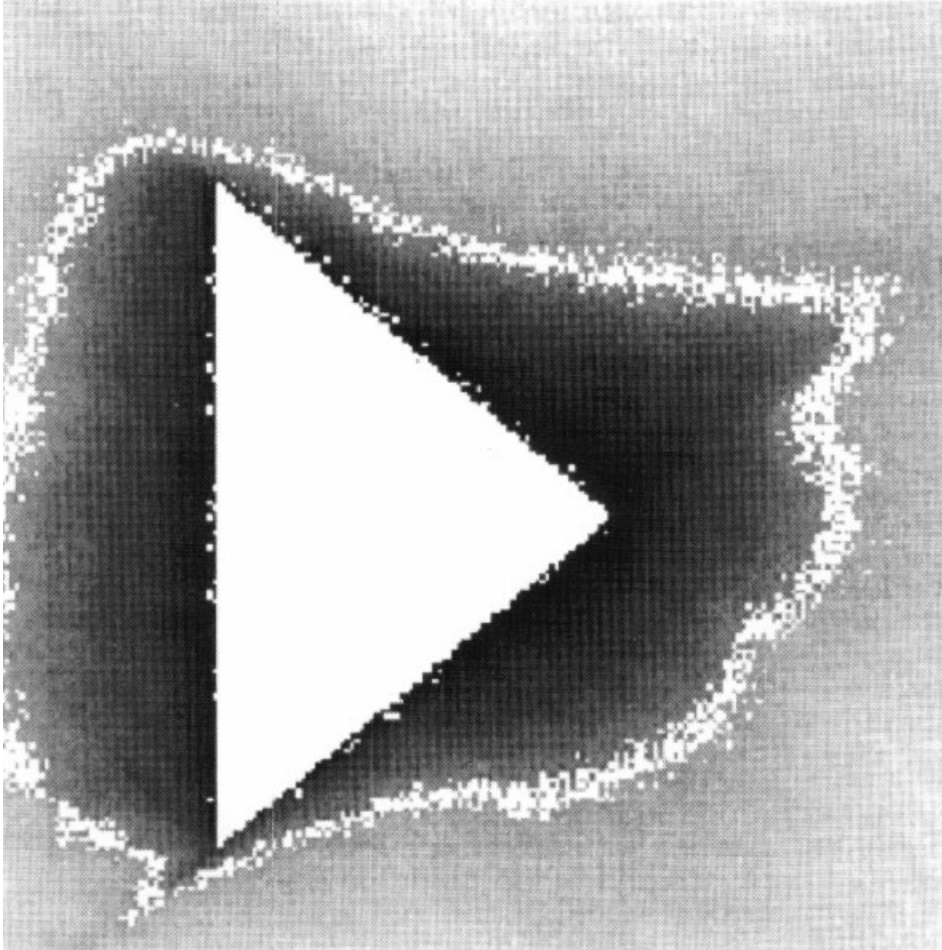


Figure 164: The lifetime of the fixed point of the Hénon map (10.21 a–b) for $r = 1.4$ in the $(\varepsilon_1, \varepsilon_2)$ -plane of control parameters for $\delta = 10^{-3}$, $-2.5 \leq \varepsilon_1 \leq 2.5$ and $-1 \leq \varepsilon_2 \leq 5$. Within the white triangle, τ becomes infinite, and the fixed point becomes completely stabilized. The white line is determined by those $(\varepsilon_1, \varepsilon_2)$ -values for which τ remains unchanged (Schuster *et al.*, 1996).

Figure 164 shows the region in parameter space ($\vec{\varepsilon}$ -space), where the lifetime of the stabilized fixed point diverges (white region). Outside of this region τ becomes gradually smaller (grey shades). The white line in Fig. 164 characterizes the $\varepsilon_1, \varepsilon_2$ -values, for which τ does not change. From the corners of the white triangle one can again determine the local instability rates of the fixed point (Schuster *et al.*, 1996). This leads to the conclusion that parametric resonance in chaotic systems allows for a new means of attractor spectroscopy, whereby one can determine the location length and stability of unstable periodic orbits on a strange attractor by measuring the lifetime of the cycle (e. g., via the power spectrum or the invariant density) as a function of the parametric feedback parameter ε .

11 Synchronization of Chaotic Systems

Synchronization is a common phenomenon in nature, e. g., in coupled nonlinear oscillator systems. The first empirical report dates back to the seventeenth century where Christiaan Huygens observed that clocks hanging from the same wooden rod tend to synchronize their motion. An excellent recent review of various synchronization phenomena is contained in the book of Pikovsky *et al.* (1993). Here we address particular synchronization phenomena for coupled chaotic systems. Systems with symmetric coupling show a novel type of intermittency as a precursor of the synchronization whereby one has to distinguish between weak and strong synchronization. In addition, these models emphasize that a proper notion of a chaotic attractor might be quite subtle. Apart from complete synchronization notions like generalized and phase synchronization are also discussed. In particular, we will demonstrate that certain unidirectionally coupled models display strange nonchaotic motion.

11.1 Identical Systems with Symmetric Coupling

In 1985 Fujisaka and Yamada discovered an unusual type of intermittent behavior when two identical chaotic systems are coupled. This observation gives rise to phenomena which are nowadays called on–off intermittency and blowout bifurcation. In addition, it illustrates why the concept of a chaotic attractor might be quite subtle.

For pedagogical purpose let us consider a simple model (Pikovsky and Grassberger, 1991; Glendinning, 2001) consisting of two one-dimensional maps coupled in symmetric way

$$x_{n+1} = (1 - \varepsilon)f(x_n) + \varepsilon f(y_n) \quad (11.1a)$$

$$y_{n+1} = (1 - \varepsilon)f(y_n) + \varepsilon f(x_n) . \quad (11.1b)$$

Here ε denotes the coupling constant. For the map f we take a skewed tent map (cf. eq. (6.89) and Fig. 165)

$$f(x) = \begin{cases} ax & \text{if } 0 \leq x \leq 1/a \\ a(1-x)/(a-1) & \text{if } 1/a < x \leq 1 \end{cases} \quad (11.2)$$

with slope $1 < a < 2$. The coupled system (11.1) admits a chaotic synchronized solution $x_n = y_n \equiv z_n$, where the dynamics of the synchronized state is given by the map (11.2), $z_{n+1} = f(z_n)$. In the two-dimensional x - y plane the synchronized state is confined to the diagonal. It is natural to ask for which values of the coupling strength ε the synchronized state is stable.

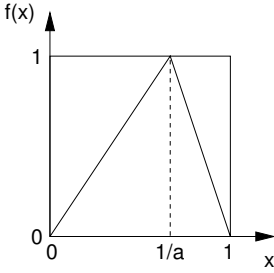


Figure 165: The skewed tent map, eq. (11.2), for $1 < a < 2$.

The stability of the synchronized state is investigated by observing transverse fluctuations through the variable $\Delta_n = y_n - x_n$. Using $x_n = z_n - \Delta_n/2$ and $y_n = z_n + \Delta_n/2$ where the mean $z_n = (x_n + y_n)/2$ describes the motion on the synchronized manifold we obtain in linear order from eq. (11.1)

$$\Delta_{n+1} = (1 - 2\varepsilon)f'(z_n)\Delta_n. \quad (11.3)$$

Thus the transverse coordinate obeys

$$\Delta_n = (1 - 2\varepsilon)^n \prod_{k=0}^{n-1} f'(z_k) \Delta_0. \quad (11.4)$$

If we take the definition of the Liapunov exponent of the map f into account [cf. eq. (3.9)] we obtain an exponential growth for the product in eq. (11.4) if a typical orbit of the synchronized state is considered

$$\left| \prod_{k=0}^{n-1} f'(z_k) \right| \simeq \exp(n\lambda). \quad (11.5)$$

Thus, the modulus of the transverse fluctuation obeys

$$|\Delta_n| \simeq (1 - 2\varepsilon)^n \exp(n\lambda) |\Delta_0|. \quad (11.6)$$

Fluctuations decay if the coupling exceeds a threshold value

$$\varepsilon > \varepsilon_{bo} = (1 - \exp(-\lambda))/2. \quad (11.7)$$

For the simple piecewise linear model, the Liapunov exponent can be calculated quite easily since the corresponding invariant density is constant, $\rho(x) = 1$ (cf. Section 3.2)

$$\lambda = \int_0^1 \ln |f'(x)| \rho(x) dx = \ln a - (1 - 1/a) \ln(a - 1) \quad (11.8)$$

11.1.1 On–Off Intermittency

If the coupling falls short of the critical value ε_{bo} , the synchronized state $x_n = y_n$ becomes unstable and a characteristic intermittent dynamics is observed. Figure 166 shows the dynamics close to the threshold. While for $\varepsilon > \varepsilon_{bo}$ the motion settles on the diagonal, i. e., on the synchronized state, one observes a blow-up of the attractor when the coupling crosses the

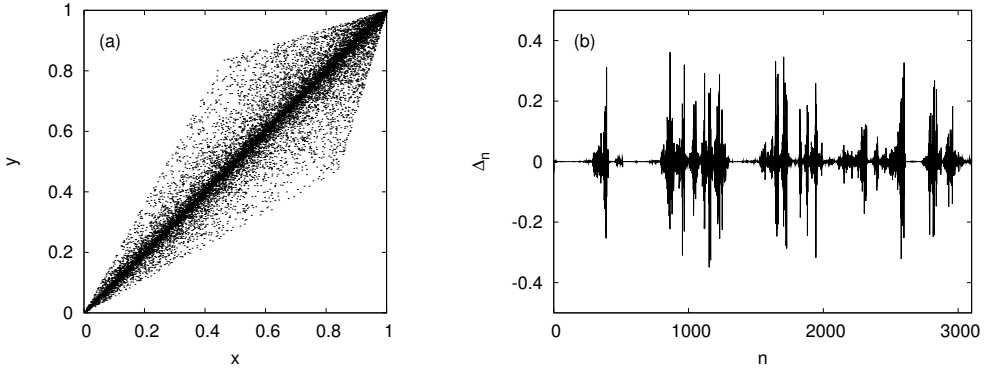


Figure 166: *Left:* Attractor of the coupled system (11.1) for $a = 1.5$ and $\varepsilon = 0.23$ in the supercritical regime ($\varepsilon < \varepsilon_{bo} = 0.235\dots$). *Right:* Time evolution of the transverse coordinate $\Delta_n = y_n - x_n$.

critical value (left in Fig. 166). This type of transition is called, for obvious reason, a blow-out bifurcation. In the supercritical regime, i. e., just below the transition point, intermittent motion of Δ_n is observed (right in Fig. 166). This type of intermittency is quite different from the classical scenarios introduced in Chapter 5. Laminar phases $|\Delta_n| \ll 1$ are interrupted by chaotic bursts $|\Delta_n| \sim 1$, and the temporal series shows a spiky characteristic. This type of intermittency has been termed on–off intermittency. Its statistical properties have been studied in detail (Yamada and Fujisaka, 1986). The main mechanism causing intermittency is already visible in eq. (11.3) which governs the dynamics of the transverse dynamics. While on average the factor $|f'(z_k)|$ is larger than one (for $\varepsilon < \varepsilon_{bo}$) its chaotic fluctuations determine the distribution and correlations of the transverse coordinate Δ_n . The basic intermittency mechanism comes from the competition between the trajectory instability of chaotic elements and the synchronization tendency due to the diffusion-type coupling.

In particular, Heagy *et al.* (1994) have investigated the statistical properties of the length ℓ of the laminar phases. In view of eq. (11.4) the length of a laminar phase is determined by the condition $|\prod_{k=0}^{\ell-1} f'(z_k)| \sim 1$. Reformulating this condition as an exit-time problem, a scaling law for the distribution of laminar phases has been obtained

$$P(\ell) \simeq \ell^{-3/2} \exp(-\alpha\ell) \quad (11.9)$$

where the exponential cutoff scales linearly with the coupling strength $\alpha \sim 1 - \varepsilon/\varepsilon_{bo}$. Close to the blow-out bifurcation one observes a power law with exponent $3/2$.

11.1.2 Strong vs. Weak Synchronization

On–off intermittency and blow-out bifurcations are closely linked phenomena and are both caused by the peculiar stability properties of the synchronized state. Actually the crucial relation (11.5) is valid for typical orbits only. For instance, it is quite simple to check that the “nontrivial” synchronized fixed point $x = y = a/(2a - 1)$ is transversally stable for $\varepsilon > \varepsilon_+ = (1 - \exp(-\lambda_+))/2$ [cf. eq. (11.7)] while the trivial synchronized fixed point is stable if $\varepsilon > \varepsilon_- = (1 - \exp(-\lambda_-))/2$ where λ_{\pm} just denotes the stability exponent of the corresponding

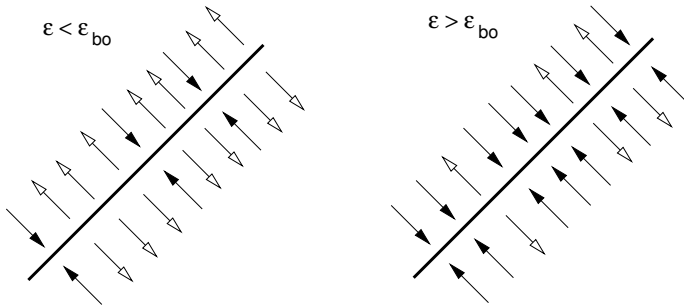


Figure 167: Diagrammatic view of the synchronized state and its local stability properties in the vicinity of the blow-out bifurcation: unstable weakly synchronized state (left), stable weakly synchronized state (right).

fixed point. Since $\lambda_- < \lambda < \lambda_+$ holds, the former fixed point is unstable throughout the blow-out transition, while the latter fixed point is transversally stable. Similar arguments apply to all the other unstable periodic states. Roughly speaking, synchronization sets in when the majority of synchronized periodic states becomes transversally stable leaving a minority (i. e., a set of measure zero) transversally unstable, as sketched in Fig. 167. The values ε_{\pm} mark the limiting values where all synchronized orbits become stable or unstable, respectively. Thus one refers to these thresholds sometimes as the onset of strong synchronization or strong desynchronization, respectively, while the onset of synchronization according to the condition (11.7) is called weak synchronization.

In the regime of weak synchronization, $\varepsilon > \varepsilon_{bo}$, there are still (infinitely many) initial conditions which are arbitrarily close to the synchronized state, but which do not converge towards this stable solution (Glendinning, 2001). These initial conditions are just related to those unstable orbits which are still transversally unstable. Thus when dealing with chaotic dynamics, the notion of an attractor becomes quite subtle. In addition, the just mentioned mechanism can cause basins of a particularly wired shape, so-called riddled basins (Ott *et al.*, 1994). Such basins do not contain any open disk, i. e., if one considers any point in the basin then arbitrarily close there are points which do not belong to the basin.

All the features which we have reported in this section for the simple model (11.1) have a quite generic character. Thus it is not surprising that topics in synchronization recently became one of the most active branches in nonlinear dynamics.

11.2 Master–Slave Configurations

Despite the fact that chaotic systems display sensitive dependence on the initial condition, synchronization can be achieved without great effort. A particularly simple demonstration of this feature can be achieved in the so-called master–slave configuration where a systems output, the drive, drives an identical copy, the response system (Pecora and Carroll, 1990). The setup is easily demonstrated by considering, e. g., a two-dimensional map as the driving

system

$$x_{n+1} = f(x_n, y_n) \quad (11.10a)$$

$$y_{n+1} = g(x_n, y_n). \quad (11.10b)$$

The output y_n of the second equation is used to drive an identical copy of eq. (11.10b)

$$\xi_{n+1} = f(\xi_n, y_n). \quad (11.11)$$

The question arises whether the response system (11.11) synchronizes with the drive, eq. (11.10), i. e., whether ξ_n tends towards x_n , even if the drive shows chaotic motion. The problem is easily addressed by considering the Liapunov exponent of the response. In linear order one obtains for the difference $\delta x_n = x_n - \xi_n$ between the master and the slave from eqs. 11.10) and (11.11)

$$\delta x_{n+1} = \frac{\partial f(x_n, y_n)}{\partial x_n} \delta x_n. \quad (11.12)$$

The deviation obeys as usual an exponential law, $\delta x_n \sim \exp(\lambda_{\perp} n)$, where the so-called conditional Liapunov exponent of the response system is determined by [cf. eq. (3.9)]

$$\lambda_{\perp} = \lim_{N \rightarrow \infty} \sum_{k=0}^{N-1} \ln \left| \frac{\partial f(x_k, y_k)}{\partial x_k} \right|. \quad (11.13)$$

Synchronization occurs if λ_{\perp} is negative.

There is in general no simple relation between the quantity (11.13) and the Liapunov exponents of the master system (11.10). Synchronization may occur even if the dynamics of the drive system is chaotic. For the purpose of illustration let us consider as a trivial example the dissipative baker's transformation [cf. eq. (6.7)]

$$x_{n+1} = f(x_n, y_n) = \begin{cases} ax_n & \text{if } 0 \leq y_n < 1/2 \\ 1/2 + ax_n & \text{if } 1/2 \leq y_n \leq 1 \end{cases} \quad (11.14a)$$

$$y_{n+1} = g(x_n, y_n) = 2y_n \bmod 1 \quad (11.14b)$$

where $0 < a < 1$. For the response system we take the x -subsystem eq. (11.11). Since the derivative $\partial f(x, y)/\partial x = a$ is constant one obtains from eq. (11.12) for the conditional Liapunov exponent $\lambda_{\perp} = \ln |a| < 0$. Thus synchronization works successfully, $\xi_n \rightarrow x_n$, despite the chaotic dynamics of the drive. This simple example shows clearly the underlying mechanism. Because of the special choice of the response system, the dynamics of ξ is essentially governed by the stable manifold, i. e., by the contraction of the baker's transformation (cf. Fig. 70, recall that the coordinate axis have been interchanged in the present example). The expanding part of the master's motion, i. e., those directions corresponding to the positive Liapunov exponent, are entirely contained in the output used for driving the response system. In fact, using the y -system as a response system does not result in synchronization, as can be checked easily. In general master–slave configurations the situation might be more involved since drive and response systems do not decompose nicely in terms of stable and unstable directions. But the essential mechanism for synchronization is the same as in this simple example. Master–slave configurations and the corresponding synchronization features have been proposed as a method for secure communication (Cuomo and Oppenheim, 1993).

11.3 Generalized Synchronization

So far we have considered synchronization where coordinates of the different subsystems coincide, e. g., $x_n = \xi_n$ in the previous setup. This type of behavior can only be expected when identical copies of the subsystems are involved. Already the use of different physical units in the drive and the response systems will prohibit the just-mentioned complete synchronization in a strict sense. Thus the notion of generalized synchronization has been introduced (Rulkov *et al.*, 1995) which can even cope with nonidentical subsystems. For the purpose of illustration consider a drive system given in terms of a map f , which drives a different response system

$$x_{n+1} = f(x_n) \quad (11.15a)$$

$$y_{n+1} = g(x_n, y_n). \quad (11.15b)$$

Generalized synchronization between the systems (11.15a) and (11.15b) is said to prevail if there is a functional relation between both variables, x and y , i. e., $y_n = h(x_n)$ holds for all times and some function h . Unlike for the case of complete synchronization, the function entering this relation is in general not the identity $h(x) = x$. The concept of generalized synchronization is indeed quite general. Our setup just states that the dynamics of the unidirectionally coupled system (11.15) settles onto a smaller set given by the condition $y = h(x)$. Provided the synchronization manifold $y = h(x)$ is known, the stability of the synchronized state is again given in terms of the appropriate conditional Liapunov exponent [cf. eq. (11.13)].

11.3.1 Strange Nonchaotic Attractors

A very important example of generalized synchronization, which by the way demonstrates the flexibility of this notion, is given in terms of quasiperiodically forced systems. Such systems can be described in terms of appropriate Poincaré maps. A prototype is the quasiperiodically forced logistic equation (cf. Prasad *et al.*, 1998)

$$x_{n+1} = x_n + \omega \bmod 1 \quad (11.16a)$$

$$y_{n+1} = a - y_n^2 + \varepsilon \cos(2\pi x_n). \quad (11.16b)$$

Here the variable x , with trivial dynamics, describes the drive and the variable y the response system. Quasiperiodic forcing is expressed by the choice that the frequency ω is irrational (cf. Section 7.2). Obviously the model (11.16) fits in the general scheme (11.15). Figure 168 shows the attractor of the mapping (11.16) for small and large coupling ε while the parameter value a corresponds to nonchaotic behavior of the logistic map. In both cases generalized synchronization is observed, $y = h(x)$. While for small coupling (Fig. 168 a) the function $y = h(x)$ results in a “smooth” dependence a much more intricate behavior is observed for larger coupling strength (Fig. 168 b). Actually the dependence results in a fractal function where the graph has a nontrivial Hausdorff dimension. The dynamics on this type of strange attractor is however still nonchaotic since the Liapunov exponents are nonpositive, as can be already inspected from the value of the parameter a . Such behavior, which is quite typical for quasiperiodically force systems, has been termed strange nonchaotic motion (Grebogi *et al.*, 1984). Observations of such strange nonchaotic attractors have been reported in different types of experiment (Ditto *et al.*, 1990, Ding *et al.*, 1997)

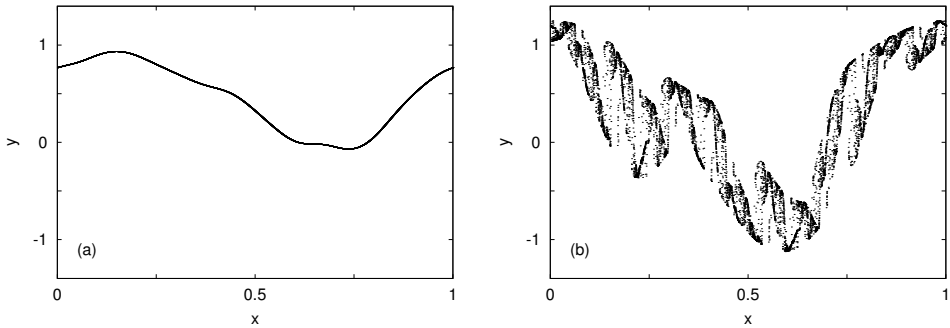


Figure 168: Attractor of the quasiperiodically forced logistic map (11.16) for $\omega = (\sqrt{5} - 1)/2$ and (a): $a = 0.8$, $\varepsilon = 0.3$, (b): $a = 0.8$, $\varepsilon = 0.45$ (after Pikovsky *et al.*, 2001).

11.4 Phase Synchronization of Chaotic Systems

For the investigation of synchronization phenomena in oscillatory systems, the notion of a phase variable plays a crucial role. While the phase is well defined in regular, nonchaotic systems (cf. the action-angle variables introduced in Section 8.1) the concept requires some additional comments for chaotic motion. As a paradigm for a chaotic oscillator let us consider the Rössler model

$$\dot{x} = -y - z \quad (11.17a)$$

$$\dot{y} = x + ay \quad (11.17b)$$

$$\dot{z} = b + z(x - c) \quad (11.17c)$$

originally introduced as a toy model describing a simple chemical reaction. For a wide range of parameter values, chaotic behavior is observed. Phase-space plots and the time evolution is displayed in Fig. 169.

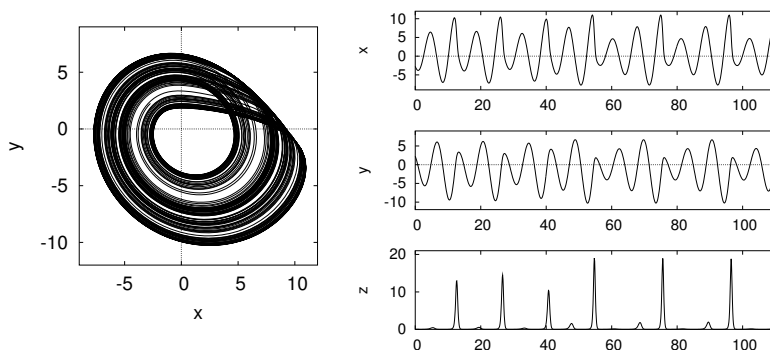


Figure 169: Dynamics of the Rössler model, eq. (11.17), for $a = b = 0.2$, $c = 5.7$. *Left:* Projection of the phase space trajectory onto the x - y subspace. *Right:* Time trace of the three coordinates.

As a characteristic feature the solutions display oscillatory behavior but with time-dependent and chaotic amplitudes. Inspecting the x - y projection of the phase-space plot (Fig. 169 a) several definitions of a chaotic phase seem to be promising (Pikovsky *et al.*, 2001). One may, e. g., take the corresponding angle in the phase plane, $\tan \theta = y/x$, where of course the angle is lifted by 2π each time a revolution is completed. As an alternative definition we may use the recurrence time with respect to a Poincaré surface of section and interpolate the phase continuously between successive hits. Finally a very elegant and universal way of introducing a phase is based on the Hilbert transform of a real-valued signal $s(t)$, say a component of the Rössler model (11.17). One constructs from the real-valued signal a complex process $\zeta(t)$ according to

$$\begin{aligned}\zeta(t) = A(t) \exp(i\phi(t)) &= \lim_{\varepsilon \rightarrow 0^+} \frac{i}{\pi} \int_{-\infty}^{\infty} \frac{s(\tau)}{t - \tau + i\varepsilon} d\tau \\ &= s(t) + \frac{i}{\pi} \mathcal{P} \int_{-\infty}^{\infty} \frac{s(\tau)}{t - \tau} d\tau\end{aligned}\quad (11.18)$$

where the last integral denotes the principal value. Thus converting the real-valued signal into a complex number, the complex phase $\phi(t)$ is taken to be the phase of the signal $s(t)$. Definition (11.18) is motivated by the observation that it just generalizes the notion of the phase for a purely periodic signal. Considering, e. g., a harmonic signal $s(t) = a \cos(\omega t + \varphi)$. Then by contour integration we have

$$\begin{aligned}\frac{i}{\pi} \int_{-\infty}^{\infty} \frac{a \cos(\omega\tau + \varphi)}{t - \tau + i\varepsilon} d\tau &= \frac{i}{2\pi} \int_{C_+} \frac{ae^{i(\omega z + \varphi)}}{t - z + i\varepsilon} dz + \frac{i}{2\pi} \int_{C_-} \frac{ae^{-i(\omega z + \varphi)}}{t - z + i\varepsilon} dz \\ &= ae^{i(\omega t + \varphi) - \varepsilon t} + 0\end{aligned}\quad (11.19)$$

where C_{\pm} denotes the contour in the complex plane consisting of the real axis and the semi-circle (with infinite radius) in the upper/lower half-plane. Thus eq. (11.18) yields, for the complex phase, the usual result $\phi(t) = \omega t + \varphi$. Altogether, eq. (11.18) generalizes the phase to cases where the amplitudes are fluctuating, e. g., chaotically. But one should keep in mind that these definitions require a signal with nice oscillatory features such as those displayed in Fig. 169.

The just-mentioned three definitions of the phase are not identical but qualitatively similar. In fact, the fine structure of the phase is not really relevant. One may instead concentrate on the mean frequency (or the winding number, cf. Section 7.2)

$$\Omega = \lim_{t \rightarrow \infty} \frac{\phi(t)}{t} . \quad (11.20)$$

Such a characteristic is independent of the particular definition of the phase and may serve as a quantifier for the chaotic oscillatory motion. Mean frequencies are useful to characterize the phase synchronization of chaotic oscillators. A nice demonstrative example is given by two nonidentical coupled Rössler models (Pikovsky *et al.*, 2001)

$$\begin{aligned}\dot{x}_1 &= -(1 + \nu)y_1 - z_1 & \dot{x}_2 &= -(1 - \nu)y_2 - z_2 \\ &+ \varepsilon(x_2 - x_1) & &+ \varepsilon(x_1 - x_2) \\ \dot{y}_1 &= (1 + \nu)x_1 + ay_1 & \dot{y}_2 &= (1 - \nu)x_2 + ay_2 \\ \dot{z}_1 &= b + z_1(x_1 - c) & \dot{z}_2 &= b + z_2(x_2 - c)\end{aligned}\quad (11.21)$$

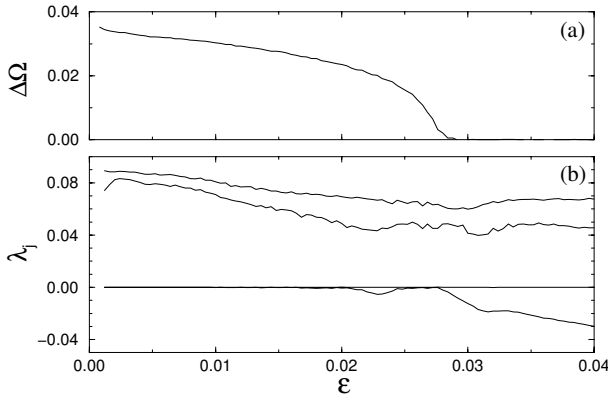


Figure 170: (a) Phase difference of the coupled Rössler system (11.21) in dependence on the coupling strength. (b) Corresponding Liapunov exponents (after Pikovski *et al.*, 2001).

where ϵ denotes the coupling parameter and v takes a parameter mismatch into account, resulting in a frequency mismatch of the uncoupled model. The analysis of coupled oscillator systems suggests (cf. Section 7.3) that, for finite coupling, a synchronized regime exists, i. e., that the mean frequencies of the two subsystems become identical, $\Omega_1 = \Omega_2$. Indeed such a transition is observed for finite coupling strength (cf. Fig. 170 a). The nature of such a phase synchronization transition can be easily understood when looking at the corresponding Liapunov spectrum, Fig. 170 b. For weak coupling two positive Liapunov exponents exist, corresponding to the chaotic fluctuations of each amplitude. In addition two zero exponents are visible, reflecting the phase dynamics of each chaotic oscillator. These exponents are just caused by the two Goldstone modes of the uncoupled model. When the critical coupling strength is crossed, the two independent phases are locked and only one Goldstone mode survives, turning the second vanishing Liapunov exponent negative.

Apart from the just-mentioned 1:1 resonance higher order resonances may take place as well. The interaction between the heart beat and the respiration cycles provides a nice experimental demonstration of such a feature (see Pikovsky *et al.*, 2001 for details).

12 Spatiotemporal Chaos

While there is nowadays a quite concise description of chaos in systems with few degrees of freedom, the problem of adequate approaches for complex dynamics in high-dimensional chaotic systems is still unsolved. For each experimental problem one may of course tailor appropriate tools, but a concise pattern is still missing. We are trying to describe some common features, concerning model systems, characteristic quantities, and paradigmatic experiments. But our presentation is selective and far from being exhaustive. Even after 20 years of development in Nonlinear Dynamics, a comprehensive presentation of spatiotemporal chaos has to be postponed to the future.

12.1 Models for Space–Time Chaos

Within a physical description of dynamical systems, time is a continuous variable. The spatial degree of freedom is either discrete or continuous depending on whether one deals with lattice dynamics or an effective hydrodynamic description in terms of continuous fields. Thus, depending on the properties of the variables, one may introduce the classification of dynamical systems shown in Table 14 where, in addition, we have taken time discrete dynamics into account. In each case one ends up with a different model class, either partial differential equations, systems of coupled differential equations, or coupled map lattices. For each class we will discuss typical examples which have proven to be fruitful for investigating spatiotemporal complex dynamics. But our discussion is far from being exhaustive and just focuses on some selected features.

12.1.1 Coupled Map Lattices

As demonstrated in the previous chapters, time discrete dynamical systems, i. e., maps, have proven to be fruitful for understanding features of low-dimensional dynamical systems. In order to investigate fundamental aspects of the interaction between local chaotic motion and spatial coupling, models of coupled maps have been proposed (cf. Kaneko, 1993, or Chazottes

Table 14: Classification of spatiotemporal chaotic models.

space	time	
discrete	discrete	coupled map lattice
discrete	continuous	system of differential equations
continuous	continuous	partial differential equation

and Fernandez, 2005, for recent overviews). A particularly simple example is given by a spatially one-dimensional diffusively coupled map lattice

$$x_{n+1}^{(v)} = (1 - \varepsilon)f(x_n^{(v)}) + \frac{\varepsilon}{2} \left[f(x_n^{(v+1)}) + f(x_n^{(v-1)}) \right] \quad (12.1)$$

where $0 \leq v \leq L - 1$ denotes the lattice sites, n the discrete time, $f(x)$ the single site map, and ε the coupling constant. The coupling derives from a spatially discrete Laplace operator. But one should not overestimate such an argument since no meaningful continuum limit exists. Although no derivation of such models from first principles is available, coupled map lattices have proven to be useful for modelling quite diverse dynamical phenomena (cf., e. g., Kaneko, 1989, for a detailed numerical study of coupled logistic maps or Yanagita and Kaneko, 1995, for the modelling of a hydrodynamical problem). Thus, coupled map lattices are a testing ground for approaches in studying spatiotemporal chaos mainly because the effort for numerical simulations even on large lattices is quite small. Apart from plain numerical approaches coupled map lattices are among those few spatially extended systems where even analytical approaches in the space–time chaotic regime can be applied. Such studies mainly rely on symbolic dynamics along the lines of Section 3.1 and link dynamical systems with models from statistical mechanics, such as probabilistic cellular automata (Gielis and MacKay, 2000).

12.1.2 Coupled Oscillator Models

Systems of coupled differential equations, e. g., a lattice of nonlinear oscillators, are in particular used for testing hypothesis of extended nonlinear systems by numerical means. Following an idea of Kuramoto (1984) one may concentrate on fundamental aspects by emphasizing the general structure of such models. Assuming that the individual oscillators are described in terms of a phase variable, one ends up with a kind of minimal model

$$\dot{\phi}_v(t) = \omega_v - \sum_{\mu=0}^{N-1} J_{v\mu} \sin(\phi_v(t) - \phi_\mu(t)) \quad (12.2)$$

where ϕ_v denotes the 2π -periodic phase of the oscillator at lattice site v , ω_v its free frequency, and $J_{v\mu}$ the spatial coupling. The trigonometric coupling function takes the periodicity into account. Models of this type may be derived from general arguments and thus possess some degree of universality.

If one considers the simplest case of global coupling, $J_{v\mu} = J/N$, $J > 0$ then even analytical solutions are available in the limit of large system size $N \rightarrow \infty$. The essential idea uses arguments borrowed from traditional mean-field theories. Introducing a complex valued order parameter

$$Z = R \exp(i\Psi) = \frac{1}{N} \sum_{\mu=0}^{N-1} \exp(i\phi_\mu) \quad (12.3)$$

the coupled system (12.2) is written as an effective one-oscillator model

$$\dot{\phi}_v(t) = \omega_v - JR \sin(\phi_v(t) - \Psi) \quad (12.4)$$

which can be integrated without great effort. Actually just two types of solutions are possible. If $|\omega_v| < JR$ then the phase locks onto a fixed point, while for $|\omega_v| > JR$ a continuous rotation

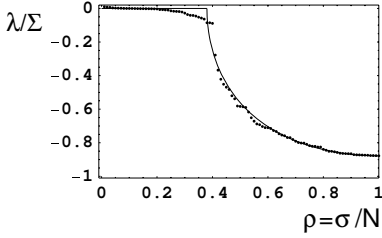


Figure 171: Liapunov exponents of the Kuramoto model in the partially synchronized state, $J = 1.75\Sigma$. Frequencies ω_ν are distributed according to a Gaussian distribution of variance Σ . *Full line:* analytical result; *dots:* numerical simulation of a system of size $N = 100$. (After Radons, 2004.)

prevails. The actual value of the order parameter may be worked out self-consistently. As on average the rotating solutions do not contribute to eq. (12.3), only the oscillators locking on the fixed points will determine Z for large system size N . Let us, e. g., assume that the frequencies ω_ν are distributed according to a symmetric single humped distribution $g(\omega) = \lim_{N \rightarrow \infty} \sum_\nu \delta(\omega - \omega_\nu)/N$. If we recall that the stable fixed point of eq. (12.4) obeys $\sin(\phi_\mu - \Psi) = \omega_\mu/(JR)$ and $\cos(\phi_\mu - \Psi) = \sqrt{1 - \sin^2(\phi_\mu - \Psi)}$ then, taking the sum over all lattice sites which lock onto the fixed-point solution, the self-consistency condition reads

$$\begin{aligned} R &= \frac{1}{N} \sum_{\mu \in \text{fix}} \exp(i(\phi_\mu - \Psi)) = \int_{-JR}^{JR} \left(\sqrt{1 - \left(\frac{\omega}{JR}\right)^2} + i \frac{\omega}{JR} \right) g(\omega) d\omega \\ &= JR \int_{-1}^1 \sqrt{1 - x^2} g(JRx) dx. \end{aligned} \quad (12.5)$$

There are two different solutions of this self-consistency condition. If the coupling J is small then only the trivial solution $R = 0$ exists, meaning that all oscillators rotate incoherently. When the coupling exceeds a critical value $J > J_c = 2/(\pi g(0))$ then it is quite straightforward to check that a nontrivial solution $R > 0$ is born. Thus there appears a transition towards a partially synchronized state where a fraction of oscillators rotate coherently. The scenario is similar to the synchronization phenomena described in Chapter 11.

The two different phases can be distinguished on the basis of their Liapunov exponents, too. Since the Kuramoto model essentially boils down to a single oscillator dynamics, eq. (12.4) the Liapunov exponents can even be computed analytically in the limit of large N (Radons, 2004). Within the partially synchronized state, the negative Liapunov exponents reflect the dynamics of the synchronized oscillators, while the vanishing exponents correspond to the nonsynchronized part of the system, cf. Fig. 171.

Generalizations of the approach, e. g., for other distributions of the frequencies and to some extent even for nonglobal coupling, are available in the literature. But already the simple model described above shows rather subtle features if stability properties of the partially synchronized phase are addressed (Strogatz, 2001). Above all, the observed phenomenon displays a phase-transition-like characteristic, in particular, since the limit of large system size is involved.

12.1.3 Complex Ginzburg–Landau Equation

The dynamics of complex patterns close to stability thresholds leads to features which can be described by universal equations of motion. A particularly important example is the complex Ginzburg–Landau equation (cf. Aranson and Kramer, 2002, for a recent review). In one spatial dimension it takes the form, using dimensionless variables

$$\frac{\partial A}{\partial t} = A + (1 + ib) \frac{\partial^2 A}{\partial x^2} - (1 + ic) |A|^2 A. \quad (12.6)$$

Here the complex field $A(x, t)$ describes amplitude and phase modulations of an underlying regular structure close to some stability threshold. The two real-valued parameters b and c characterize the linear and nonlinear dispersion.

When starting from physical equations of motion, e. g., a reaction diffusion equation describing a concentration field $c(x, t)$ an effective description in terms of the complex Ginzburg–Landau equation can be obtained when a regular structure, e. g., a plane wave becomes unstable. The pattern in the neighborhood of the stability threshold is described by a modulated structure

$$c(x, t) = A(x, t) \exp(i\omega t + ikx) + c.c. \quad (12.7)$$

where the space–time dependence of the amplitude A is slow with respect to the underlying regular structure. The amplitude equation (12.6) is derived by a formal perturbation scheme (cf. Cross and Hohenberg, 1993). Its structure is essentially determined by symmetries of the underlying dynamics. In that respect, equations like eq. (12.6) yield a quite universal description of spatiotemporal dynamics close to instability thresholds. These concepts are the generalizations of bifurcation analysis to spatially extended systems.

The dynamics of the complex Ginzburg–Landau equation is highly nontrivial. While the investigation of different regular stationary and periodic structures can still be done by analytical tools, one relies on numerical simulations for studying spatiotemporal chaotic states. There are at least two qualitatively different chaotic regimes. Whenever the amplitude A vanishes a defect occurs since the complex phase is not well defined at such a point. Thus, dynamics without defects can be described only in terms of the phase variable [cf. eq. (12.8)]. Chaotic motion of the phase without defects is called phase turbulence, whereas defect chaos is generated by chaotic motion of point defects of a pattern. Occurrence and stability of the different states depends of course on the choice of the two parameters b and c .

12.1.4 Kuramoto–Sivashinsky Equation

Phase turbulent dynamics can be described in terms of a the local phase $\phi(x, t)$ or the local wave vector $u(x, t) = \partial\phi/\partial x$, which is just the spatial derivative of the phase. According to Kuramoto and Tsuzuki (1976) an appropriate equation of motion can be derived from the Ginzburg–Landau equation. In terms of dimensionless variables it reads

$$\frac{\partial u}{\partial t} = -\frac{\partial^2 u}{\partial x^2} - \frac{\partial^4 u}{\partial x^4} + u(x, t) \frac{\partial u}{\partial x}. \quad (12.8)$$

Equation (12.8) contains no parameter, apart from the system size. Thus it may be considered as a kind of universal model for space–time chaos. The spatiotemporal chaotic motion which

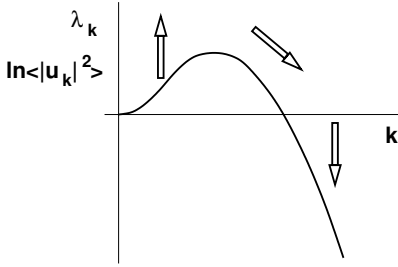


Figure 172: Diagrammatic view of the energy transport in the Kuramoto–Sivashinsky equation, (12.10). The dispersion relation $\lambda_k = k^2 - k^4$ and the logarithm of the temporal average of the Fourier amplitude, $\ln\langle|u_k|^2\rangle$, show qualitatively similar dependence on the wavenumber k . Arrows indicate the transport processes in the integral, inertial, and dissipation range, respectively.

appears in systems of sufficiently large size may be understood qualitatively by arguments which originate from hydrodynamics (cf. Section 12.3.1). Rewriting the equation of motion in terms of Fourier modes

$$u_k(t) = \frac{1}{L} \int_0^L \exp(ikx) u(x, t) dx \quad (12.9)$$

one obtains

$$\dot{u}_k = (k^2 - k^4)u_k - i \sum_{k'} k' u_{k-k'} u_{k'} . \quad (12.10)$$

This equation of motion contains linear contributions which are governed by the dispersion relation $\lambda_k = k^2 - k^4$ and a coupling of Fourier modes stemming from the nonlinear part. Decomposition in terms of Fourier modes usually does not help to compute the solution. But on that level one may understand qualitatively the mechanism for the generation of spatiotemporal chaos. The linear contribution tends to amplify Fourier amplitudes in the large-wavelength regime, $k < 1$, while modes with small wavelengths, $k > 1$ are damped. If only the nonlinear part of the equation of motion were present then it is quite straightforward to check that the total “energy” $\int_0^L |u(x, t)|^2 dx / L = \sum_k |u_k|^2$ would be preserved. Thus the nonlinear part just redistributes the “energies” of the modes, $|u_k|^2$. Such a mechanism is dominant in the so-called “inertial range”, which is the wavenumber regime between the “dissipation range” $k \gg 1$ and the “integral range” $k \ll 1$. Thus the whole dynamics may be viewed as an energy transfer process from large to small scales while, on average, the individual energies $\langle|u_k|^2\rangle$ develop a k -dependence which is determined by the linear dispersion. Such arguments which are summarized in Fig. 172 are at the heart of a phenomenological explanation of turbulence.

12.2 Characterization of Space–Time Chaos

Traditional characterization of spatiotemporal dynamics relies to some extent on spatiotemporal correlation functions and Fourier spectra. Different types of correlation function may be introduced, depending on the space–time pattern under consideration (cf. e. g., Eckmann and Ruelle, 1985, and Cross and Hohenberg, 1993). In addition quantities like dimensions,

entropies, and Liapunov exponents which have been discussed in Sections 6.2 and 6.3 can be applied as well. A formulation in terms of corresponding densities is more suitable when extensive properties are considered. There is still no generally accepted characterization of space–time chaos available. Here we focus on the question of how the concept of Liapunov exponents can be generalized to take the particular aspect of spatial extension into account. Similar ideas may be applied to other characteristic quantities as well.

12.2.1 Liapunov Spectrum

Liapunov exponents quantify the sensitivity of the motion with respect to changes of the initial condition. When considering a spatially extended system, i. e., a system with many degrees of freedom, then many exponents exist which measure the sensitivity with respect to different modes. To be definite, when considering a coupled map lattice, eq. (12.1), then the equation of motion for small disturbances $\delta x_n^{(v)}$ is obtained by linearization with respect to the reference trajectory $x_n^{(v)}$ (cf. Section 6.2 for the case of multi-dimensional maps)

$$\delta x_{n+1}^{(v)} = (1 - \varepsilon) f' \left(x_n^{(v)} \right) \delta x_n^{(v)} + \frac{\varepsilon}{2} \left[f' \left(x_n^{(v+1)} \right) \delta x_n^{(v+1)} + f' \left(x_n^{(v-1)} \right) \delta x_n^{(v-1)} \right]. \quad (12.11)$$

Exponential growth of these perturbations determines the different Liapunov exponents λ_σ , $0 \leq \sigma \leq L - 1$. When considering the limit of large lattices $L \rightarrow \infty$ then these exponents behave like intensive quantities and are described in terms of a smooth spectrum $\ell(\rho)$, $0 \leq \rho \leq 1$

$$\lambda_\sigma = \ell(\sigma/L), \quad 0 \leq \sigma \leq L - 1. \quad (12.12)$$

Such Liapunov spectra are cumbersome to compute because of the time-dependent fluctuations, $f' \left(x_n^{(v)} \right)$, appearing in eq. (12.11). But some of the essential features can already be observed when considering the trivial example of generalized Bernoulli maps

$$f(x) = rx \bmod 1, \quad r > 1. \quad (12.13)$$

Then the derivatives in eq. (12.11) are time independent and the solution for the perturbations may be written in terms of plane waves

$$\delta x_n^{(v)} = \exp(\lambda_\sigma n) \exp(ik_\sigma v) \quad (12.14)$$

where the wavenumbers due to periodic boundary conditions obey $k_\sigma = 2\pi\sigma/L$. The different Liapunov exponents are obtained from eq. (12.11)

$$\exp(\lambda_\sigma) = (1 - \varepsilon)r + \varepsilon r \cos(k_\sigma). \quad (12.15)$$

Strictly speaking, such an expression is only correct if $\varepsilon \leq 1/2$, since Liapunov exponents are by definition real-valued. For larger values of the coupling, the modulus of the right-hand side of eq. (12.11) has to be considered. Finally, the Liapunov spectrum according to eq. (12.12) reads

$$\ell(\rho) = \ln r + \ln |1 - \varepsilon + \varepsilon \cos(2\pi\rho/L)|. \quad (12.16)$$

Equation (12.14) tells us that a plane wave is related with each Liapunov exponent. Such Liapunov modes describe the spatial pattern associated with the corresponding growth rate. In general Liapunov modes are far more complicated and even their definition allows for some degree of ambiguity.

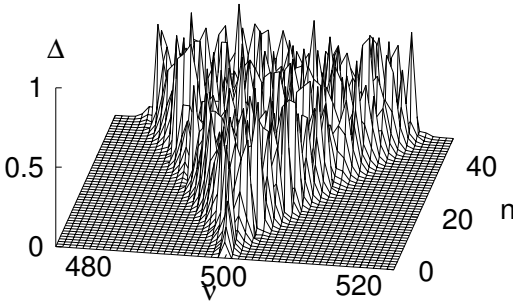


Figure 173: Propagation of a perturbation in a system of coupled Bernoulli maps, eqs. 12.1) and (12.13) for $\varepsilon = 0.1$ and $r = 2$. Space–time plot of the difference $\Delta = |y_n^{(v)} - x_n^{(v)}|$ of two replicas with initial condition differing at site $v = 500$ only.

12.2.2 Co-moving Liapunov Exponent

Propagation of signals is one of the ubiquitous features of spatially extended systems. Within a spatiotemporal chaotic system, this property has been studied, e. g., by observing how localized structures of the initial condition propagate in the course of time. Figure 173 shows a simple example generated from a coupled map lattice. The difference of two patterns, which are obtained from two initial conditions differing at one lattice site only, is displayed. The propagation of the error at a finite speed is clearly visible.

In order to quantify the propagation of disturbances, a velocity-dependent Liapunov exponent has been proposed by Deissler and Kaneko (1987). This exponent measures the exponential growth of perturbations in a co-moving reference frame. Starting from a localized disturbance at one lattice site, say v , $\delta x_0^{(v)} = \delta_{v,0}$ the exponential growth is observed in a moving reference frame through the law

$$|\delta x_n^{(v)}| \simeq \exp(\Lambda(v)n) \quad (12.17)$$

where the reference velocity $v = v/n$ determines the relative scaling between position v and time n . By definition $\Lambda(v = 0)$ coincides with the maximal Liapunov exponent of the system, while $\Lambda(v) > 0$ indicates that perturbations with velocity v tend to propagate. Thus the maximal propagation speed obeys $\Lambda(v) = 0$.

While a numerical evaluation of this idea is fairly straightforward, a direct analytical computation is quite difficult even for the simple model of coupled Bernoulli maps. Although an analytical solution for $\Lambda(v)$ is still available we refer to the next paragraph for a simpler but indirect determination of the co-moving Liapunov exponent. Figure 174 summarizes the result. As expected, the maximal propagation speed increases when the coupling strength is increased. Because of the diffusive coupling, eq. (12.1), speeds are limited to the range $v \leq 1$.

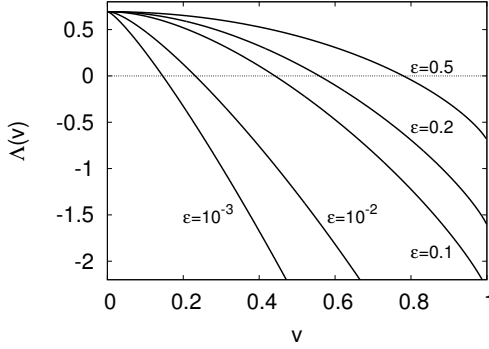


Figure 174: Co-moving Liapunov exponent for a system of coupled Bernoulli maps, eqs. (12.1) and (12.13), with $r = 2$ and different values of the coupling strength ε (after Kaneko, 1992).

12.2.3 Chronotopic Liapunov Analysis

Fronts, propagating in a chaotic medium as displayed in Fig. 173, may have an exponentially decaying spatial profile. This property is already implicitly assumed in the definition of the co-moving Liapunov exponent, eq. (12.17), when keeping the scaling $n = v/\nu$ in mind. Thus propagation of signals may be analyzed from the very beginning by taking this profile into account (Politi and Torcini, 1992). Using the ansatz

$$\delta x_n^{(v)} = \exp(\gamma\nu)\delta z_n^{(v)} \quad (12.18)$$

the equation of motion (12.11) reads

$$\begin{aligned} \delta z_{n+1}^{(v)} = & (1 - \varepsilon)f'(x_n^{(v)})\delta z_n^{(v)} + \frac{\varepsilon}{2} \left[f'(x_n^{(v+1)})\exp(\gamma)\delta z_n^{(v+1)} \right. \\ & \left. + f'(x_n^{(v-1)})\exp(-\gamma)\delta z_n^{(v-1)} \right]. \end{aligned} \quad (12.19)$$

When analyzing the temporal evolution of eq. (12.19), we have essentially changed the boundary conditions which originally apply to $\delta x_n^{(v)}$ but which are now imposed on the new variables $\delta z_n^{(v)}$. It is, in fact, this change which is the whole clue to the analysis.

Equation (12.19) describes the propagation of a spatially exponential profile where the decay rate γ of the profile enters explicitly as a parameter. As in the previous sections we may just compute the largest Liapunov exponent $L(\gamma)$ of the equation of motion (12.19). It depends, of course, on the shape of the profile, i. e., on γ .

For the purpose of illustration we again resort to the case of coupled Bernoulli maps, eq. (12.13). As in the previous case the exponential growth rate is computed straightforwardly from eq. (12.19) using $\delta z_n^{(v)} = \exp(L(\gamma)n)$, since the time-dependent derivatives turn out to be constant, $f'(x_n^{(v)}) = r$

$$\exp(L(\gamma)) = (1 - \varepsilon)r + \varepsilon r \cosh(\gamma). \quad (12.20)$$

For $\gamma = 0$ we obtain of course the largest Liapunov exponent, $\lambda_{\sigma=0}$ [cf. eq. (12.15)].

The growth rate $L(\gamma)$ and the co-moving Liapunov exponent $\Lambda(v)$ are related through a Legendre transformation. If we evaluate the definition (12.17) of the co-moving Liapunov exponent for a neighboring lattice site $v + \Delta v$, we have

$$\delta x_n^{(v+\Delta v)} \simeq \exp[\Lambda(v + \Delta v/n)n] \simeq \exp[\Lambda(v)n + \Lambda'(v)\Delta v] \quad (12.21)$$

where a Taylor series expansion has been employed. Thus the front has a spatial profile with exponential decay rate

$$\gamma = \Lambda'(v) . \quad (12.22)$$

On the other hand, eq. (12.18) in connection with the exponent $L(\gamma)$ tells us that

$$\delta x_n^{(v)} \simeq \exp(\gamma v) \exp[L(\gamma)n] = \exp([\gamma v + L(\gamma)]n) \quad (12.23)$$

where we used the scaling in terms of the front velocity, $v = v/n$. Hence, comparison with the definition (12.17) of the co-moving Liapunov exponent yields

$$\Lambda(v) = \gamma v + L(\gamma) . \quad (12.24)$$

Equations (12.22) and (12.24) constitute a Legendre transformation. Using the inverse transformation $L'(\gamma) = -v$ it is, in principle, straightforward to compute explicitly the co-moving Liapunov exponent of the coupled Bernoulli maps from eq. (12.20)

One may develop a whole consistent theory for spatiotemporal exponents following the ideas presented in this paragraph. Such an approach is sometimes called chronotopic analysis (Lepri *et al.*, 1997). To some extent it is based on the same formal concepts which we have already described in Section 6.3 in the context of the multifractal analysis.

12.3 Nonlinear Nonequilibrium Space–Time Dynamics

Although high-dimensional chaotic behavior still poses one of the major challenges for Nonlinear Dynamics, it is quite well established that the understanding of spatiotemporal chaotic motion is at the heart of several physical phenomena. We briefly describe here three illustrative examples, mainly from nonequilibrium physics, where application of such concepts is potentially fruitful and experimentally relevant.

12.3.1 Fully Developed Turbulence

Hydrodynamic turbulence is the classical example of nonlinear complex dynamics. In its simplest form the underlying physical equations of motion, i. e., the Navier–Stokes equation and the continuity equation for a simple, incompressible, viscous fluid, are nonlinear partial differential equations for the velocity field $\vec{u}(\vec{r}, t)$. Written in dimensionless units the free parameter, apart from the geometry of the boundary conditions and the driving force, is given by the Reynolds number $Re = LU/v$. Here L denotes the lateral extension of the system, e. g., the tube diameter, U the order of magnitude of the velocity field, e. g., the mean velocity or the square-root of the second moment, and v the kinematic viscosity. Due to scaling properties, flows with the same Reynolds number and the same geometry of boundary conditions are similar.

Properties of the turbulent state may already be understood by simple dimension and statistical arguments (see, e. g., Frisch, 1995, for a comprehensive exposition). Energy is injected into the flow on large length scales of order L , the integral scale, either due to boundary conditions or stirring forces. Let ε denote the energy injection rate per unit mass and time. This process induces the velocity of order U at the length scale L . As the physical dimension of the energy rate is given by $[\varepsilon] = \text{m}^2/\text{s}^3$ these quantities are related by $\varepsilon \sim U^3/L$. In a stationary turbulent state the same amount of energy is dissipated by viscosity at a length scale η , the dissipation scale. As the only physical relevant parameters are the energy rate ε and the viscosity ν with dimension $[\nu] = \text{m}^2/\text{s}$ the unique way to obtain such a dissipation scale is $\eta \sim (\nu^3/\varepsilon)^{1/4}$. Combining these expressions, the ratio of the two length scales obeys $L/\eta \sim \text{Re}^{3/4}$. Thus the scales are well separated for high Reynolds number flows, i. e., in the regime of fully developed turbulence. Energy is injected on the integral scale and dissipated on the dissipation scale. In between, i. e., in the inertial range $\eta \ll R \ll L$, a ballistic transport takes place. From a qualitative point of view the dynamics looks similar to that in the Kuramoto–Sivashinsky equation (cf. Section 12.1.4), which sometimes serves as a toy model for fully-developed turbulence.

Quantitative characterization of hydrodynamic turbulence is usually done by suitable correlation functions of the velocity field. In order to get rid of large scale features like the mean flow rate, which are nonuniversal and depend on the particular stirring mechanism, one considers spatial velocity differences, $\vec{u}(\vec{r} + \vec{R}, t) - \vec{u}(\vec{r}, t)$, with \vec{R} chosen in the inertial range. The statistical characterization is done in terms of moments of such differences which in its simplest form reads

$$M_q(R) = \langle |\vec{u}(\vec{r} + \vec{R}, t) - \vec{u}(\vec{r}, t)|^q \rangle. \quad (12.25)$$

Within the inertial range the moment (12.25) shows a power-law dependence on R , due to the energy transport process from large to small scale. The law can be obtained by an heuristic dimensional argument which has been developed independently by Kolmogorov and Obukov, Heisenberg and Weizsäcker, and Onsager. One assumes that, in the limit of large Reynolds numbers, the energy transport at scale R , i. e., the statistical properties of Fourier modes of wavenumber $k \sim 1/R$, depends only on the energy transfer rate ε and on the local scale R . Then, the only dimensionally correct expression for the moment (12.26) reads

$$M_q(R) \sim \varepsilon^{q/3} R^{q/3}. \quad (12.26)$$

One obtains a power law with an exponent $\zeta_q = q/3$ in the inertial range $\eta \ll R \ll L$. Such a law can be derived even analytically from the Navier–Stokes equation for $q = 3$. It is also confirmed experimentally. But small deviations appear which are amplified when large exponents q are considered. Such “intermittency corrections” are attributed to nonuniform features of the dissipation process which have been implicitly neglected when deriving the result (12.26) with the simple dimensional argument. Actually it is one of the main purposes of the multifractal approach introduced in Section 6.3 to model such deviations. But the derivation of intermittency corrections from the full Navier–Stokes equation still poses one of the major challenges of Nonlinear Dynamics.

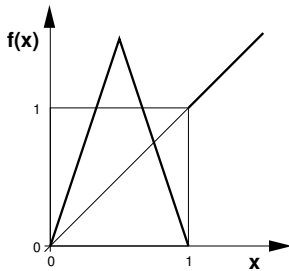


Figure 175: Single site map of the minimal spatiotemporal intermittent coupled map lattice (after Chaté and Manneville, 1988).

12.3.2 Spatiotemporal Intermittency

Onset of turbulence is one of the most intense fields of research. A possible scenario based on intermittency in spatially extended systems which goes beyond the investigation of low-dimensional chaotic systems has been proposed by Kaneko (1985) on the basis of coupled map lattices. Competition between local turbulent and laminar dynamics and spatial coupling yields characteristic space–time patterns of turbulent and laminar phases.

A minimal model which captures all the essential ingredients has been introduced by Chaté and Manneville (1988). The single site map (cf. Fig. 175)

$$f(x) = \begin{cases} r(1/2 - |x - 1/2|) & \text{if } 0 \leq x \leq 1 \\ x & \text{if } x > 1 \end{cases} \quad (12.27)$$

has a quite trivial dynamics. After a chaotic transient in the domain $x < 1$ the motion settles on a “laminar” state in the range $x > 1$. Due to spatial diffusive coupling, eq. (12.1), the motion becomes nontrivial. Below a critical coupling strength $\varepsilon < \varepsilon_c$ typical initial conditions finally settle in the laminar domain. But beyond that critical value a persistent space–time chaotic motion is observed, while close to the threshold, intermittency characteristics appear in the space–time pattern (cf. Fig. 176). Such space–time intermittent scenarios share some features with phase transitions, e. g., if one considers the statistical properties of laminar and turbulent sites. But the problem concerning universality, scaling behavior, and critical exponents is quite subtle and still not completely settled (Bohr *et al.*, 2001).

Spatiotemporal intermittency is apparently a common mechanism for the generation of turbulence as it has been found in a wide class of dynamical models, such as the Ginzburg–Landau equation, as well as in hydrodynamic experiments.

12.3.3 Molecular Dynamics

Concepts of Nonlinear Dynamics have been applied to investigate the motion of many-particle systems, i. e., solids, fluids and gases, subjected to equilibrium and nonequilibrium conditions. It is the main scope of such approaches to understand the fundamentals of Statistical Physics from a dynamical point of view. In addition, the relation between quantifiers of chaotic motion, like Liapunov exponents and fractal dimension spectra, and quantities of Statistical Physics, like thermodynamical modules and transport coefficients, is of particular interest.

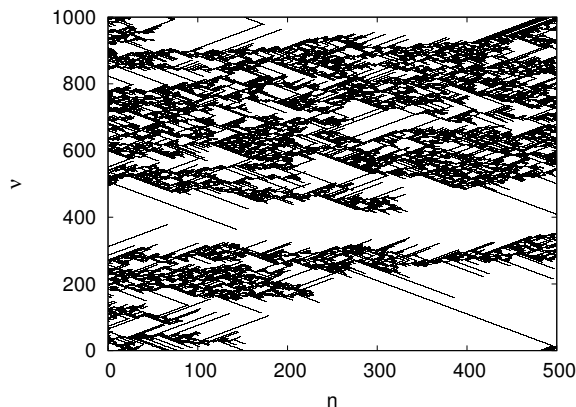


Figure 176: Space–time plot of a spatiotemporal intermittent state of the Chaté–Manneville model for $r = 3$ and $\varepsilon = 0.361$: *black*: turbulent sites $x_n^{(v)} < 1$; *white*: laminar sites $x_n^{(v)} > 1$.

As a prototype the equations of motion of classical mechanics are usually considered. Without external driving forces, i. e., for the investigation of equilibrium states, they read

$$\dot{\vec{q}}_i = \vec{p}_i/m \quad (12.28a)$$

$$\dot{\vec{p}}_i = - \sum_{j=1}^N \vec{\nabla} u(\vec{q}_i - \vec{q}_j). \quad (12.28b)$$

In particular, Liapunov spectra have been investigated recently. Because of the Hamiltonian structure of the equations of motion (12.28) the $6N$ Liapunov exponents obey a pairing rule, $\lambda_k + \lambda_{6N+1-k}$, since each expanding exponent possesses a contracting counterpart (cf. Fig. 177).

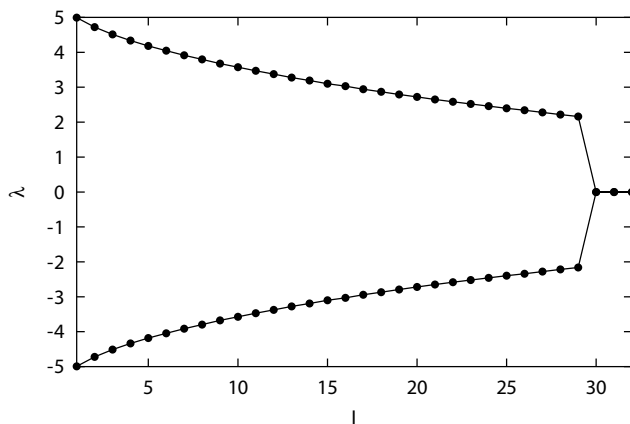


Figure 177: Liapunov spectrum of a two-dimensional hard disk system (cf. Posch and Forster, 2004, for details).

Such Liapunov spectra typically display exponents with small modulus. These exponents are related to the slow dynamics of the system. This a part of the motion is typically attributed to hydrodynamic behavior which can be described in terms of macroscopic densities and the corresponding hydrodynamic equations of motion. In fact, the Liapunov vectors reflect this behavior. While Liapunov vectors corresponding to large exponents are highly localized (i. e., only a small part of the components have appreciable size) the Liapunov vectors of the small exponents show wave-like characteristics (Forster *et al.* 2004).

To investigate nonequilibrium features of the system (12.28), one applies driving forces and appropriate damping terms to keep, e. g., the energy constant. The corresponding stationary states of the dynamical system can be linked with the nonequilibrium physics of the corresponding many-particle system (cf., e. g., Ruelle, 1999). In particular, transport coefficients and entropy production can be related to properties of the Liapunov spectrum. But the matter is currently not completely understood.

Outlook

Within this book we have tried to present a comprehensible introduction to deterministic chaos from the theoretical as well as experimental point of view. In particular, we have stressed the importance of self-similar structures, renormalization-group ideas, and universality. Several aspects, which are still in their infancy and which have been barely touched in the last chapters of the book, concern recent developments in that field.

First of all, even after several decades of research in nonlinear dynamics, the role of deterministic chaos in systems with many degrees of freedom is not really understood. Such topics are of utmost relevance when dealing, e. g., with interacting oscillator dynamics in biological systems, nonequilibrium pattern formation in chemistry, or even the classical example of fully developed turbulence and the significance of intermittency. There is still a considerable lack of understanding of the fundamental aspects of the dynamics in high-dimensional phase spaces, e. g., the concept of attractors and related ergodic properties. Furthermore proper tools for analyzing high-dimensional motion are still missing since the standard concepts of nonlinear data analysis are essentially confined to low-dimensional chaos.

Fundamental aspects of statistical physics, i. e., the foundations of nonequilibrium statistical mechanics may benefit from recent developments in nonlinear dynamics. Some of these ideas have been briefly sketched in the last chapters of the book. But there are still many open questions. One puzzle, e. g., concerns the curious properties of heat transport in simple nonlinear chains. Since quantum mechanics is at the heart of microscopic theories of many particle systems, developments from quantum chaos are also expected to play a crucial role in understanding nonlinear nonequilibrium physics properly.

Within the present book we focused entirely on deterministic dynamical systems. But the interplay between stochastic forces and randomness with chaotic motion becomes increasingly relevant. Nonlinear stochastic systems have been investigated for decades but the role of chaotic motion is barely understood in this context. A prominent physical example are glass-like phase transitions and aging which can be modelled by simple random chaotic systems.

The list is by no means complete. We have skipped all aspects related to mathematical approaches. While even low-dimensional chaotic motion still poses a considerable challenge from the rigorous point of view, the investigation of high-dimensional dynamics, i. e., on infinite-dimensional phase spaces, is just beginning. Here, links between dynamical systems and equilibrium statistical mechanics which are mediated by symbolic dynamics may give new insight into the ergodic properties as qualitative changes of the motion can be mapped onto equilibrium phase transitions.

Above all, the major conclusion stays the same as we had already stated one decade ago in the previous edition: *Since nature is nonlinear, one has always to reckon with deterministic chaos.* This means, however, that predictions about future developments in the field of deterministic chaos are as difficult or short-ranged as predictions of chaotic motion itself, i. e., there is (fortunately) much scope for the unexpected. Interestingly enough, about 100 years ago, James Clerk Maxwell (the founder of the theory of electromagnetism) wrote the following far-sighted remark about the predictability of nonlinear, i. e., unstable, systems (quoted after Berry, 1978): *“If, therefore, those cultivators of the physical science from whom the intelligent public deduce their conception of the physicist . . . are led in pursuit of the arcana of science to the study of the singularities and instabilities, rather than the continuities and stabilities of things, the promotion of natural knowledge may tend to remove that prejudice in favor of determinism which seems to arise from assuming that the physical science of the future is a mere magnified image of that of the past.”*

Appendix

A Derivation of the Lorenz Model

For References see References to Chapter 2 on p. 260.

In the following we present a somewhat short derivation of the Lorenz model that should provide the reader with a feeling for the approximations involved. For a more rigorous treatment, we refer the reader to the original articles by Saltzman (1962) and Lorenz (1963) and the monograph by Chandrasekhar (1961).

Consider the Rayleigh–Bénard experiment as depicted in Fig. 119. The liquid is described by a velocity field $\vec{v}(\vec{x}, t)$ and a temperature field $T(\vec{x}, t)$. The basic equations which describe our system are

- a) the Navier–Stokes equations:

$$\rho \frac{d\vec{v}}{dt} = \vec{F} - \vec{\nabla} p + \mu \vec{\nabla}^2 v \quad (\text{A.1})$$

- b) the equation for heat conduction:

$$\frac{dT}{dt} = \kappa \vec{\nabla}^2 T \quad (\text{A.2})$$

- c) the continuity equation:

$$\frac{d\rho}{dt} + \text{div}(\rho \vec{v}) = 0 \quad (\text{A.3})$$

with the boundary conditions

$$\begin{aligned} T(x, y, z = 0, t) &= T_0 + \Delta T \\ T(x, y, z = h, t) &= T_0 . \end{aligned} \quad (\text{A.4})$$

Here ρ is the density of the fluid, μ is its viscosity, p is the pressure, κ is the thermal conductivity, and $F = \rho g \vec{e}_z$ is the external force in the \vec{e}_z -direction due to gravity. The *fundamental nonlinearity in hydrodynamics* comes from the term $\dot{\vec{v}} = (\vec{v} \cdot \vec{\nabla})\vec{v} + \partial\vec{v}/\partial t$ (which is quadratic in \vec{v}) in the Navier–Stokes equation (A.1).

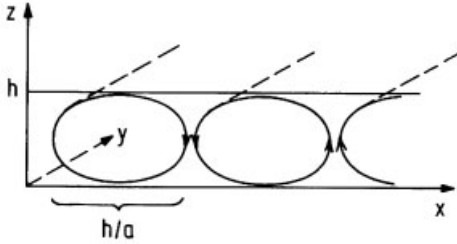


Figure 178: Convection rolls and geometry in the Bénard experiment.

To simplify the calculation, it is assumed a) that the system is translationally invariant in the y -direction so that convection rolls extend to infinity as shown in Fig. 178, and b) that the ΔT -dependence of all coefficients – except in $\rho = \bar{\rho}(1 - \alpha\Delta T)$ – can be neglected (Boussinesq approximation). The continuity equation thus becomes

$$\frac{\partial u}{\partial x} + \frac{\partial w}{\partial z} = 0 \quad \text{with} \quad u = v_x \quad \text{and} \quad w = v_z \quad (\text{A.5})$$

and, it is, therefore, convenient to introduce a function $\psi(x, z, t)$ with

$$u = -\frac{\partial \psi}{\partial z} \quad \text{and} \quad w = \frac{\partial \psi}{\partial x} \quad (\text{A.6})$$

such that (A.5) is automatically fulfilled.

As a next step we introduce the deviation $\theta(x, z, t)$ from the linear temperature profile via

$$T(x, z, t) = T_0 + \Delta T - \frac{\Delta T}{h}z + \theta(x, z, t). \quad (\text{A.7})$$

Using (A.6) and (A.7) the basic equations can, according to Saltzmann, be written as

$$\frac{\partial}{\partial t} \vec{\nabla}^2 \psi = -\frac{\partial(\psi, \vec{\nabla}^2 \psi)}{\partial(x, z)} + \nu \vec{\nabla}^4 \psi + g\alpha \frac{\partial \theta}{\partial x} \quad (\text{A.8})$$

$$\frac{\partial}{\partial t} \theta = -\frac{\partial(\psi, \theta)}{\partial(x, z)} + \frac{\Delta T}{h} \frac{\partial \psi}{\partial x} + \kappa \vec{\nabla}^2 \theta \quad (\text{A.9})$$

where

$$\begin{aligned} \frac{\partial(a, b)}{\partial(x, z)} &= \frac{\partial a}{\partial x} \cdot \frac{\partial b}{\partial z} - \frac{\partial a}{\partial z} \cdot \frac{\partial b}{\partial x}, \\ \vec{\nabla}^4 &= \frac{\partial^4}{\partial x^4} + \frac{\partial^4}{\partial z^4} \end{aligned} \quad (\text{A.10})$$

$\nu = \mu/\bar{\rho}$ is the kinematic viscosity, and the pressure term was eliminated by taking the curl in the Navier–Stokes equations. In order to simplify (A.8) and (A.9), Lorenz used free boundary conditions:

$$\begin{aligned} \theta(0, 0, t) &= \theta(0, h, t) = \psi(0, 0, t) = \psi(0, h, t) \\ &= \vec{\nabla}^2 \psi(0, 0, t) = \vec{\nabla}^2 \psi(0, h, t) = 0 \end{aligned} \quad (\text{A.11})$$

and retained only the lowest-order terms in the Fourier expansions of ψ and θ , and proposed the following ansatz:

$$\frac{a}{1+a^2} \frac{1}{\kappa} \Psi = \sqrt{2} X(t) \sin\left(\frac{\pi a}{h} x\right) \sin\left(\frac{\pi h}{z}\right) \tag{A.12}$$

$$= \sqrt{2} Y(t) \cos\left(\frac{\pi a}{h} x\right) \sin\left(\frac{\pi h}{z}\right) - Z(t) \sin\left(\frac{2\pi z}{h}\right) \tag{A.13}$$

where $R \equiv (g\alpha h^3 / \chi \nu) \Delta T$ is the Rayleigh number, a is the aspect ratio (see Fig. 178) and $R_c \equiv \pi^4 a^{-2} (1+a^2)^3$. By inserting (A.12) and (A.13) into (A.8) and (A.9) and neglecting higher harmonics, one finally obtains the Lorenz model:

$$\dot{X} = -\sigma X + \sigma Y \tag{A.14a}$$

$$\dot{Y} = -XZ + rX - Y \tag{A.14b}$$

$$\dot{Z} = XY - bZ \tag{A.14c}$$

where the dot denotes the derivative with respect to the normalized time $\tau = \pi^2 h^{-2} (1+a^2) \kappa t$; $\sigma = \nu / \kappa$ is the Prandtl number, $b \equiv 4(1+a^2)^{-1}$, and $r = R/R_c \propto \Delta T$ is the external control parameter.

B Stability Analysis and the Onset of Convection and Turbulence in the Lorenz Model

For References see References to Chapter 2 on p. 260.

Let us write the Lorenz equations (A.14) in the compact form

$$\dot{\vec{X}} = \vec{F}(\vec{X}) \tag{B.1}$$

and linearize around the fixed points

$$\vec{X}_1 = 0; \quad \vec{X}_2 = (\pm\sqrt{b(r-1)}; \pm\sqrt{b(r-1)}; r-1), \tag{B.2}$$

which are determined by

$$\vec{F}(\vec{X}_{1,2}) = 0. \tag{B.3}$$

The first fixed point $\vec{X}_1 = \vec{0}$ corresponds to thermal conductivity without motion of the liquid, and its stability matrix

$$\left. \frac{\partial F_i}{\partial X_j} \right|_{\vec{x}_1} = \begin{pmatrix} -\sigma & \sigma & 0 \\ r & -1 & 0 \\ 0 & 0 & -b \end{pmatrix} \tag{B.4}$$

has the eigenvalues

$$\lambda_{1,2} = -\frac{\sigma+1}{2} \pm \frac{1}{2} \sqrt{(\sigma+1)^2 + 4(r-1)\sigma}; \quad \lambda_3 = -b. \tag{B.5}$$

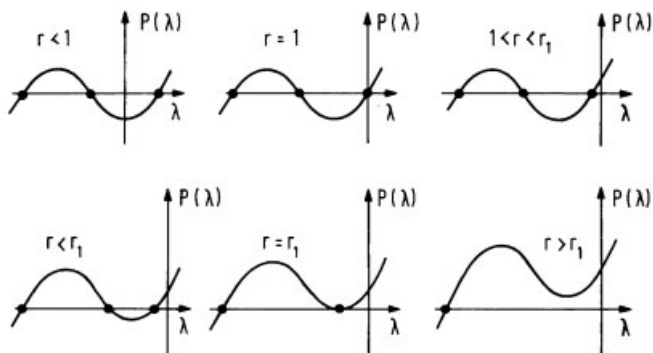


Figure 179: Qualitative behavior of the polynomial $P(\lambda)$.

Thus, $\vec{X}_1 = \vec{0}$ is stable, i. e., all eigenvalues are negative for $0 < r < 1$. The Bénard convection starts at $r = 1$ because then $\lambda_1 = 0$, and this is just where the second fixed point \vec{X}_2 (which corresponds to moving rolls, as shown in Fig. 179) takes over. The stability matrix for \vec{X}_2 is

$$\left. \frac{\partial F_i}{\partial X_j} \right|_{\vec{X}_2} = \begin{pmatrix} -\sigma & \sigma & 0 \\ 1 & -1 & c \\ c & c & -b \end{pmatrix}; c \equiv \pm \sqrt{b(r-1)}. \quad (\text{B.6})$$

Its eigenvalues are the roots of the polynomial

$$P(\lambda) = \lambda^3 + (\sigma + b + 1)\lambda^2 + b(\sigma + r)\lambda + 2b\sigma(r - 1) = 0. \quad (\text{B.7})$$

One sees immediately that for $r = 1$ we have $\lambda_1 = 0$, $\lambda_2 = -b$, and $\lambda_3 = -(\sigma + 1)$, i. e., the convection fixed point is marginally stable, and Fig. 179 shows that it is stable for $1 < r < r_1$. At $r_1 < r_c$ two of the eigenvalues become complex, i. e., two limit cycles result which are stable so long as the real part of the complex eigenvalues is smaller than zero. For $r = r_c$ these real parts become zero, i. e., we have two eigenvalues $\lambda = \pm i\lambda_0$, which lead via (B.7) to

$$r_c = \sigma \frac{\sigma + b + 3}{\sigma - b - 1} \left(= 24.7368 \quad \text{for } a = 10, \quad b = \frac{8}{3} \right).$$

Above r_c the limit cycles become unstable (the complex eigenvalues have positive real parts), and chaos sets in. This analysis is consistent with the numerical result obtained by Lorenz, who found chaotic behavior for $\sigma = 10$, $b = 8/3$ above $r_c = 24.74$.

C The Schwarzian Derivative

For References see References to Chapter 2 on p. 260.

Not all unimodal functions (i. e., continuously differentiable maps f that map the unit interval $[0, 1]$ onto itself with a single maximum at $x = 1/2$ and are monotonic for $0 \leq x \leq 1/2$ and $1/2 < x \leq 1$) display an infinite sequence of pitchfork bifurcations.

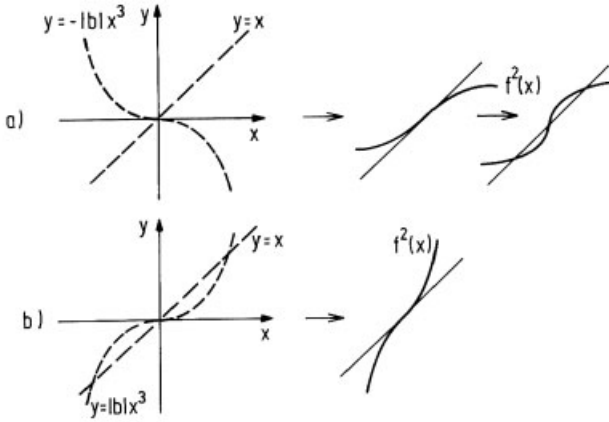


Figure 180: Behavior of $f^2(x) = f^{2'}(x_0)x + bx^3$, $b \equiv f^{2'''}(x_0)/3!$ near $x_0 = 0$ for a) $Sf < 0$, i. e., $b < 0$, and b) $Sf > 0$, i. e., $b > 0$.

In addition to being unimodular, the Schwarzian derivative of f

$$Sf \equiv \frac{f'''}{f'} - \frac{3}{2} \left(\frac{f''}{f'} \right)^2 \propto \frac{d^2}{dx^2} [f'(x)]^{-1/2} \tag{C.1}$$

must be negative over the whole interval $[0, 1]$. This is, for example, true for the logistic map, since $f'''(x) = 0$.

To make this requirement, which at first sight appears unusual, more plausible, we note the important property that $Sf < 0$ implies a negative Schwarzian derivative for all iterates of f , i. e., $Sf^n < 0$. This can be verified by direct calculation. As a consequence, it is found that at a fixed point x_0 of f that just becomes unstable, i. e.,

$$f'(x_0) = -1 \tag{C.2}$$

and

$$\begin{aligned} f^{2'}(x_0) &= [f'(x_0)]^2 = 1 \\ f^{2''}(x_0) &= f''(x_0)\{[f'(x_0)]^2 + f'(x_0)\} = 0 \end{aligned} \tag{C.3}$$

the third derivative of $f^2(x_0)$ becomes negative for $Sf < 0$, and, near $x_0 = 0$, $f^2(x)$ behaves as shown in Fig. 180, which can lead to a pitchfork bifurcation. The same figure shows that a pitchfork bifurcation becomes impossible for $Sf > 0$.

The importance of the Schwarzian derivative had first been noted by Singer, who showed that unimodal maps with $Sf < 0$ cannot have more than one periodic attractor. Later Guckenheimer and Misurewicz proved that, in this case, all points in $[0, 1]$ (i. e., with the exception of a set of measure zero) become attracted to it. The proofs and references can be found in the monograph by Collet and Eckmann (1980).

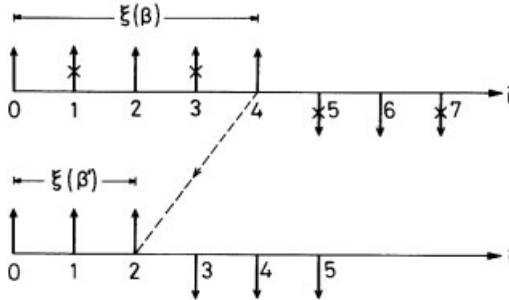


Figure 181: Renormalization-group steps for the one-dimensional Ising Model. *Top:* Spins with odd indices are integrated out. *Bottom:* The correlation length in the renormalized system becomes smaller.

D Renormalization of the One-Dimensional Ising Model

For References see References to Chapter 2 on p. 260.

The functional renormalization group which is used in this book has been constructed in analogy to the renormalization-group method for critical phenomena. This section explains the method for critical phenomena (which is simpler than the functional renormalization method) for the example of the one-dimensional Ising model. Although the one-dimensional Ising model has several strange features (its transition temperature is zero, etc., see below), these are outweighed by the fact that every renormalization-group step can be performed explicitly. It is assumed that the reader is familiar with the usual exact solution of this model that can be found in most textbooks on statistical mechanics.

The partition function of the one-dimensional Ising model has the well-known form

$$Z = \sum_{\{\sigma_i\}} e^{\sum_i \sigma_i \sigma_{i+1}} \quad (\text{D.1})$$

where $\beta = J/T$ is the ratio of coupling constant J and temperature T ; the spin variables σ_i take the values $\sigma_i = \pm 1$, and the sites are $i = 0 \dots N$. The renormalization-group steps are visualized in Fig. 181: First, we sum in (D.1) over all spin variables σ_i with odd i . Then we relabel the remaining variables with even i :

$$\sigma_{2i} \rightarrow \sigma_i / \alpha \quad (\text{D.2})$$

(for our simple example, we have $\alpha = 1$; but for the two-dimensional Ising model, one needs $\alpha \neq 1$). Figure 181 shows that the system of residual spins exhibits the same pattern as before and only two factors have changed: all lengths are reduced by a factor of two and the coupling between the residual spins becomes renormalized ($\beta \rightarrow \beta'$). At the transition temperature $T = T_c = 0$, the correlation length is infinite and the spin pattern is self-similar for all length scales, i. e., repeated applications of the renormalization-group procedure always lead to similar results.

To perform these steps explicitly, we consider a typical sum over an odd variable in (D.1):

$$Z_3 = \sum_{\sigma_3} e^{\beta(\sigma_2\sigma_3 + \sigma_3\sigma_4)} = 2[(\cosh \beta)^2 + \sigma_2\sigma_4(\sinh \beta)^2]. \quad (\text{D.3})$$

This can be written as

$$Z_3 = c \cdot e^{\beta' \sigma_2 \sigma_4} = c [\cosh \beta + \sigma_2 \sigma_4 \sinh \beta] \tag{D.4}$$

with

$$\tanh \beta' = (\tanh \beta)^2 . \tag{D.5}$$

Equation (D.5) is obtained by comparing the right-hand sides of (D.3) and (D.4), keeping in mind that σ_2 and σ_4 have only the values ± 1 .

In the next step, we relabel the spins according to (D.2) and obtain the renormalized version of Z :

$$Z(\beta) = Z(\beta') = c^{N/2} \sum_{\{\sigma_i\}} e^{\beta' \sum_i^{N/2} \sigma_i \sigma_{i+1}} . \tag{D.6}$$

(The constant c will not be further considered because it cancels in all thermodynamic averages). The renormalized coupling β' , between the residual spins is, according to (D.6):

$$\beta' = \operatorname{artanh} [(\tanh \beta)^2] \equiv R_2(\beta) . \tag{D.7}$$

Iteration of the renormalization procedure yields

$$\beta'' = R_2[R_2(\beta)] = R_4(\beta) . \tag{D.8}$$

The last equal sign means that two repeated renormalizations are equivalent to one renormalization where only every fourth spin is retained, i. e., the renormalization-group operators R form a semigroup (“semi” because no inverse element exists). The fixed points of (D.7) are

$$\beta^* = \infty \quad \text{and} \quad \beta^* = 0 \tag{D.9}$$

i. e., they occur at zero temperature (the transition temperature of the one-dimensional Ising model) and at infinite temperature. In both limits, the spin pattern is self-similar (the spin system is completely disordered at $T = \infty$, and at $T = 0$ all spins are aligned). For $\beta > 0$, the system is always driven (by repeated applications of R_2) to the stable fixed point $\beta^* = \infty$.

Because the correlation length ξ is reduced by a factor of two, after one renormalization step, we can immediately determine the temperature dependence of ξ via the following scaling argument:

$$\xi(\beta) = 2\xi(\beta') \tag{D.10}$$

$$\rightarrow \xi(\beta) = 2 \{ \operatorname{artanh} [(\tanh \beta)^2] \} = 2^n \xi \{ \operatorname{artanh} (\tanh \beta)^{2^n} \} . \tag{D.11}$$

For $\beta \gg 1$, the variable n can be chosen such that

$$(\tanh \beta)^{2^n} = \text{const.} \tag{D.12}$$

$$\rightarrow 2^n \propto 1 / \log(\tanh \beta) \tag{D.13}$$

$$\rightarrow \xi \propto 1 / \log(\tanh \beta) \tag{D.14}$$

This last relation can be verified by direct computation of the correlation function:

$$\langle \sigma_{j+r} \sigma_j \rangle \equiv \sum_{\{\sigma_i\}} e^{\beta \sum_i \sigma_i \sigma_{i+1}} \sigma_{j+1} \sigma_j / \left(\sum_{\{\sigma_i\}} e^{\beta \sum_i \sigma_i \sigma_{i+1}} \sigma_{j+1} \sigma_j \right) \tag{D.15}$$

$$= (\tanh \beta)^r \equiv e^{-r/\xi} \tag{D.16}$$

where we used

$$\sum_{\sigma_{i+1}} e^{\beta\sigma_i\sigma_{i+1}} = 2 \cosh \beta \quad (\text{D.17})$$

and

$$\sum_{\sigma_{i+1}} e^{\beta\sigma_i\sigma_{i+1}} \sigma_{i+1} = 2 \sinh \beta. \quad (\text{D.18})$$

It should be noted that for more complicated systems (e.g., the two- or three-dimensional Ising model), the elimination of spin variables in one renormalization step leads to next-nearest-neighbor and higher-order couplings (between the spins), and it is part of the art of renormalization to keep track of them.

E Decimation and Path Integrals for External Noise

For References see References to Chapter 2 on p. 260.

Here we present a derivation of the scaling form of the Liapunov exponent (4.90) that follows an important article by Feigenbaum and Hasslacher (1982). Our main aim is to explain their decimation method which has, on the one hand, a wide range of potential applications (for example to the transition from quasi-periodicity to chaos in Chapter 7), and, on the other hand, close parallels to the renormalization of the one-dimensional Ising model (explained in Appendix D).

As a first step, we write the iterates of (4.86)

$$x_{n+1} = f(x_n) + \xi_n \quad (\text{E.1})$$

as integrals over δ -functions:

$$x_1 = f(x_0) + \xi_0 = \int dx_1 x_1 \delta[x_1 - f(x_0) - \xi_0] \quad (\text{E.2a})$$

$$\begin{aligned} x_2 &= f[f(x_0) + \xi_0] + \xi_1 & (\text{E.2b}) \\ &= \int dx_1 dx_2 x_2 \delta[x_2 - f(x_1) - \xi_1] \delta[x_1 - f(x_0) - \xi_0] \end{aligned}$$

\vdots

$$x_n = \int \prod_{j=1}^n dx_j x_n \delta[x_{j+1} - f(x_j) - \xi_j] \quad (\text{E.2c})$$

The ξ_j are independent random variables with Gaussian probability distributions:

$$P_0\{\xi_j\} = \prod_j P[\xi_j; \sigma^2] \equiv \prod_j \frac{1}{\sqrt{2\pi\sigma}} e^{-\xi_j^2/2\sigma^2}. \quad (\text{E.3})$$

If we use eqs. (E.2c), (E.3) and integrate over $\{\xi_i\}$, the average of x_n becomes

$$\langle x_n \rangle = \int \prod_j d\xi_j P_0\{\xi_j\} x_n \quad (\text{E.4})$$

$$= \int \prod_{j=1}^n dx_j x_n \prod_{i=0}^{n-1} P[x_{i+1} - f(x_i); \sigma^2]. \quad (\text{E.5})$$

This average has the form of a path integral that is (if the time variable i is interpreted as a site index) reminiscent of the thermodynamic average of a magnet and, therefore, well-suited for a renormalization-group treatment. The idea is to perform the integration over the x_i *step by step*, i. e., the renormalization-group treatment consists of integrating out all x_i with odd i s (this is called “decimation”) and rescaling the variables such that the whole operation can be repeated.

Let us choose $n = 2^q$, q integer, and separate variables with even and odd indices in (E.4):

$$\langle x_n \rangle = \int \prod_1^{n/2} dx_{2i} x_n \prod_1^{n/2} dx_{2i-1} \prod_0^{n/2-1} P[x_{2i+2} - f(x_{2i+1}); \sigma^2] \times P[x_{2i+1} - f(x_{2i}); \sigma^2].$$

The relevant integrals over the odd variables,

$$I = \int dx_{2i+1} \exp\{-[x_{2i+2} - f(x_{2i+1})]^2/2\sigma^2 - [x_{2i+1} - f(x_{2i})]^2/2\sigma^2\}^2 \tag{E.6}$$

are evaluated using the saddle-point approximation that is valid for small noise amplitudes $\sigma \ll 1$.

If we have an integral over a function which is sharply peaked at x^* , the simplest form of the saddle-point approximation consists of replacing the integral by the integrand taken at x^* .

Consider, for example, for $N \gg 1$ the integral

$$I_0 = \int dx e^{-NF(x)}. \tag{E.7}$$

Using the saddle-point approximation this becomes

$$I_0 \approx \int dx \exp\left\{-N \left[F(x^*) + \frac{1}{2} F''(x^*)(x-x^*)^2 \right]\right\} = e^{-NF(x^*)} \cdot \sqrt{\frac{2\pi}{NF''(x^*)}} \tag{E.8}$$

where the “saddle point” x^* is determined by the condition that $e^{-NF(x)}$ has a maximum at x^* , i. e.,

$$F'(x^*) = 0. \tag{E.9}$$

If we apply this approximation to (E.6), we obtain instead of (E.9):

$$-[x_{2i+2} - f(x_{2i+1}^*)]f'(x_{2i+1}^*) + x_{2i+1}^* - f(x_{2i}) = 0 \tag{E.10a}$$

$$\rightarrow (x_{2i+1}^*) \approx f(x_{2i}) + [x_{2i+2} - f^2(x_{2i})]f'[f(x_{2i})] \tag{E.10b}$$

and

$$I \approx \exp\{[x_{2i+2} - f^2(x_{2i})]^2/2\bar{\sigma}^2\} \tag{E.11}$$

(where we have omitted all pre-exponential factors because they will cancel out in $\langle x_n \rangle$) and

$$\bar{\sigma}^2 = \sigma^2 + \{f'[f(x_{2i})]\}^2 \sigma^2. \tag{E.12}$$

Thus, $\bar{\sigma}$ depends on x_{2i} after one integration, i. e., when we repeat this procedure (see below) we will always encounter x -dependent σ s and instead of (E.6), we should therefore consider from the very beginning

$$I = \int dx_{2i+1} \exp\{-[x_{2i+2} - f(x_{2i+1})]^2/2\sigma^2(x_{2i+1}) - [x_{2i+1} - f(x_{2i})]^2/2\sigma^2(x_{2i})\}. \quad (\text{E.13})$$

In analogy to our previous calculation, we also obtain eq. (E.11) for this I , but with (E.12) replaced by

$$\bar{\sigma}^2(x_{2i}) = \sigma^2[f(x_{2i}) + \{f'[f(x_{2i})]\}^2 \cdot \sigma^2[x_{2i}]]. \quad (\text{E.14})$$

If we combine eqs. (E.5), (E.11) and (E.14) and rescale and relabel the variables, i. e.,

$$x_{2i} \equiv \bar{x}_i/a, \quad (a = -|a|) \quad (\text{E.15})$$

we obtain

$$\langle x_n \rangle \propto \int \prod_1^{n/2} d\bar{x}_i \bar{x}_{n/2} \prod_0^{n/2-1} P[\bar{x}_{i+1} - \text{T}f(\bar{x}_i); \bar{\sigma}^2(\bar{\sigma}_i)] \quad (\text{E.16})$$

where T is again the doubling operator

$$\text{T}f(x) = af \left[f \left(\frac{x}{a} \right) \right] \quad (\text{E.17})$$

and

$$\bar{\sigma}^2(x) = a^2 \left\{ \sigma^2 \left[f \left(\frac{x}{a} \right) \right] + \left[f' \left[f \left(\frac{x}{a} \right) \right] \right]^2 \cdot \sigma^2 \left(\frac{x}{a} \right) \right\} \equiv \hat{\text{L}}_f \sigma^2(x) \quad (\text{E.18})$$

i. e., $\bar{\sigma}^2(x)$ is obtained by acting on $\sigma^2(x_n)$ with a linear operator $\hat{\text{L}}_f$. We note that the rescaling and relabeling were necessary to bring the expression (E.16) for $\langle x_n \rangle$ (after the odd variables had been integrated out) back into the *old form* (E.4) such that the whole renormalization-group transformation can be iterated.

After m renormalization steps we obtain finally

$$\langle x_n \rangle \propto \prod_1^{n/2^m} d\bar{x}_i \bar{x}_{n/2^m} \prod_0^{n/2^m-1} P[\bar{x}_{i+1} - \text{T}^m f(\bar{x}_i); \hat{\text{L}}_{\text{T}^{m-1}f} \dots \hat{\text{L}}_{\text{T}f} \cdot \hat{\text{L}}_f \sigma^2(\bar{x}_i)]. \quad (\text{E.19})$$

For $m \gg 1$ we have again [see (4.52)]

$$\text{T}^m f_R(x) = g(x) + r\delta^m ah(x) \quad \text{with} \quad r = R_\infty - R \quad (\text{E.20})$$

and in analogy to (4.35)–(4.42)

$$\hat{\text{L}}_{\text{T}^{m-1}f} \dots \hat{\text{L}}_f \sigma^2(x) \cong \hat{\text{L}}_g^m \sigma^2(x) \cong \hat{\beta}^{2m} \hat{\sigma}^2(x) \quad (\text{E.21})$$

where $\hat{\beta}^2$ and $\hat{\sigma}^2$ denote the largest eigenvalue and eigenfunction of $\hat{\text{L}}_g$, respectively.

Thus, $\langle x_n \rangle$ can be written as

$$\langle x_n \rangle \propto \prod_1^{n/2^m} d\bar{x}_i \bar{x}_{n/2^m} \prod_0^{n/2^m-1} P[\bar{x}_{i+1} - g(\bar{x}_i) - r\delta^m ah(\bar{x}_i); \hat{\beta}^{2m} \hat{\sigma}^2(\bar{x}_i)]. \quad (\text{E.22})$$

For the Liapunov exponent λ , this yields

$$\exp[n\lambda(r; \sigma)] = \left| \frac{d}{dx_0} \langle x_n \rangle \right| = \exp[(n/2^m)\lambda[r\delta^m; \sigma \cdot \hat{\beta}^m]] \tag{E.23}$$

where σ denotes the initial noise amplitude. If we set $\hat{\beta}^m \cdot \sigma = 1$ and $\lambda(x; 1) = L(x)$, we obtain the desired scaling behavior for λ :

$$\lambda(r, \sigma) = \sigma^\theta L[r\sigma^{-\gamma}] \tag{E.24}$$

with

$$\theta = \log 2 / \log \hat{\beta} = 0.367 \quad \text{and} \quad \gamma = \log \delta / \log \hat{\beta} = 0.815 . \tag{E.25}$$

Note that the numerical value for $\hat{\beta}$ ($\hat{\beta} = 6.618$) that was obtained as the solution of the eigenvalue equation

$$\hat{L}_g \hat{\sigma}^2(x) = \hat{\beta}^2 \hat{\sigma}^2(x) \tag{E.26}$$

agrees closely with the best value for μ ($\mu = 6.557$). This justifies our earlier treatment of external noise.

F Shannon's Measure of Information

For References see References to Chapter 6 on p. 266.

This short heuristic introduction into Shannon's measure of information should enable the reader to understand Chapters 3 and 6. For a more detailed treatment we recommend the book by Shannon and Weaver (1949).

F.1 Information Capacity of a Store

Figure 182 a shows a system with two possible states. If the position of the points is unknown, a priori, and we learn that it is in the left box, say, we gain by definition information amounting to one bit. If we obtain this information, we save one question (with possible answer yes or

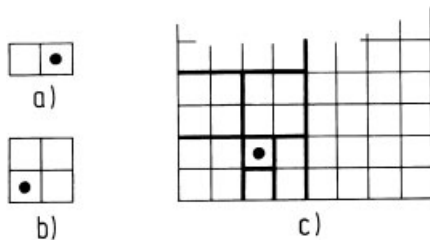


Figure 182: Information capacity of a store. a) A box with two states. b) It takes two questions (and their answers) to locate a point in a system with four states: right or left? up or down? c) In order to locate a point on a checkerboard with $64 = 2^6$ states, one needs six questions.

no, which we would have needed to locate the point). Thus, the maximum information content of a system with two states is one bit.

For a box with four possible states, one needs two questions to locate the point, i. e., its maximum information content I is

$$I = 2 \text{ (bits)} \quad (\text{F.1})$$

(we will drop the unit “bit” in the following).

This can be written as the logarithm to the base two (ld) of the number of possible states:

$$I = \text{ld}4 . \quad (\text{F.2})$$

According to Fig. 182 c, this logarithmic relation between the maximum information content I and the number of states N ,

$$I = \text{ld}N \quad (\text{F.3})$$

is true in general.

F.2 Information Gain

Let us now calculate the average gain in information if one learns the outcome of statistical events. Suppose we toss a coin such that heads or tails occur with equal probabilities

$$p_1 = p_2 = \frac{1}{2} . \quad (\text{F.4})$$

The information I acquired by learning that the outcome of this experiment is heads, say, is

$$I = 1 \quad (\text{F.5})$$

because there are two equally probable states, as in Fig. 182 a. This result can be expressed via the $\{p_i\}$ as

$$I = - \left(\frac{1}{2} \text{ld} \frac{1}{2} + \frac{1}{2} \text{ld} \frac{1}{2} \right) \quad (\text{F.6})$$

or

$$I = - \sum_i p_i \text{ld} p_i . \quad (\text{F.7})$$

Equation (F.7) can be generalized to situations where the p_i s are different:

$$p_1 \neq p_2 = 1 - p_1 . \quad (\text{F.8})$$

It then gives the average gain in information if we toss a deformed coin many times.

Let $p_1 = r/q$, where r and q are mutually prime integers, and let us choose the number m of events such that mr/q is again an integer. The total number of distinct states which occur if one tosses a (deformed) coin m times is

$$N = \frac{m!}{(p_1 m)! (p_2 m)!} \quad (\text{F.9})$$

where we eliminated, by division, the permutations that correspond to a rearrangement of equal events. The sequences hht and hht with h = head and t = tail, where the hs have been

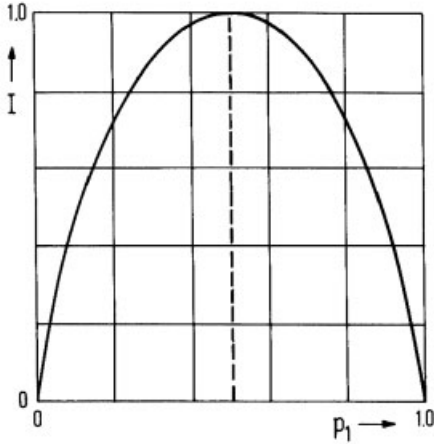


Figure 183: $I(p)$ for an experiment with two possible outcomes. If $p_1 = 0$, we are sure that the outcome will be event 2, and we gain no information. The maximum information I is acquired for $p_1 = p_2 = 1/2$, where the uncertainty of the outcome has its maximum and one learns most from the experiment.

interchanged, correspond to the same state. In the limit $m \rightarrow \infty$ we can use Stirling's formula, and, for the average information gain, eq. (F.3) yields (cf. Fig. 183)

$$\begin{aligned}
 I &= \frac{1}{m} \text{ld} N = \frac{1}{m} \text{ld} \left[\left(\frac{m}{e} \right)^m \left(\frac{e}{p_1 m} \right)^{p_1 m} \left(\frac{e}{p_2 m} \right)^{p_2 m} \right] = \\
 &= -(p_1 \text{ld} p_1 + p_2 \text{ld} p_2) .
 \end{aligned}
 \tag{F.10}$$

This confirms eq. (F.7) and can be generalized to Shannon's result: If we, a priori, know only that $1 \dots n$ events (or states of a system) occur with probabilities $\{p_i\}$ (such that $\sum_{i=1}^n p_i = 1$) and we learn by a measurement that a certain event j has taken place (or the system actually occupies a certain state), then (if we repeat this measurement many times) we gain the average information

$$I = - \sum_{i=1}^n p_i \text{ld} p_i .
 \tag{F.11}$$

G Period Doubling for the Conservative Hénon Map

For References see References to Chapter 7 on p. 269.

Let us consider the quadratic area-preserving Hénon map

$$x_{n+1} = 1 - ax_n^2 - y_n
 \tag{G.1a}$$

$$y_{n+1} = x_n
 \tag{G.1b}$$

that describes (as we have seen in Chapter 2) a periodically kicked rotator for zero damping and small amplitudes. We want to show that this map (which represents a whole class of two-

dimensional maps with a quadratic maximum) also leads to a cascade of period doublings, but with Feigenbaum constants that are larger than those for one-dimensional maps.

It is convenient to transform (G.1 a,b) using

$$x_n = -\frac{2}{a}\bar{x}_n + \beta; \quad a\beta^2 + 2\beta - 1 = 0; \quad C = -a\beta \quad (\text{G.2})$$

into the form

$$\left. \begin{aligned} y_{n+1} &= x_n \\ x_{n+1} &= 2Cx_n + 2x_n^2 - y_n \end{aligned} \right\} \equiv T \begin{pmatrix} x_n \\ y_n \end{pmatrix} \quad (\text{G.3})$$

(where we have omitted the bar notation).

We will first discuss the fixed points of T and T^2 and their stability, and finally introduce Helleman's renormalization scheme (Helleman, 1980), which sheds some light on the doubling mechanism and allows a convenient estimate of the relevant Feigenbaum constants.

The fixed points of T are

$$x_1^* = y_1^* = 0 \quad \text{and} \quad x_2^* = y_2^* = 1 - C \quad (\text{G.4})$$

and those of the second iterate T^2 where

$$T^2 \begin{pmatrix} x_n \\ y_n \end{pmatrix} = \begin{cases} x_{n+2} = 2C[2Cx_n + 2x_n^2 - y_n] + 2[2Cx_n + 2x_n^2 - y_n]^2 - x_n \\ y_{n+2} = 2Cx_n + 2x_n^2 - y_n \end{cases} \quad (\text{G.5})$$

are the solution of

$$(Cx + x^2)^2 + C(Cx + x^2) - x = 0. \quad (\text{G.6})$$

To solve this equation it is noted that the fixed points (G.4) of T are also fixed points of T^2 , i. e., (G.6) can be reduced to a quadratic equation with the solutions:

$$x_{3,4}^* = y_{3,4}^* = \frac{1}{2} \left[-(C+1) \pm \sqrt{(C+1)(C-3)} \right]. \quad (\text{G.7})$$

The stability of the fixed points is (by analogy to the one-dimensional case) determined by the eigenvalues $\lambda_{1,2}$ of the matrix of derivatives

$$L(x^*, y^*) = \begin{pmatrix} \frac{\partial T_x}{\partial x} & \frac{\partial T_x}{\partial y} \\ \frac{\partial T_y}{\partial x} & \frac{\partial T_y}{\partial y} \end{pmatrix}_{x^*, y^*} = \begin{pmatrix} 2C + 4x^* & -1 \\ 1 & 0 \end{pmatrix} \quad (\text{G.8})$$

which are

$$\lambda_{1,2} = \frac{1}{2} \left[\text{Tr} L \pm \sqrt{(\text{Tr} L)^2 - 4} \right], \quad \text{Tr} L = 2C + 4x^*. \quad (\text{G.9})$$

Since T is an area-preserving map, $\det L = 1$, i. e., $\lambda_2 = 1/\lambda_1$. This leaves (apart from parabolic fixed points that we do not consider here because they are not generic) only two essentially different types of fixed point:

- a) Hyperbolic fixed point: The λ s are real and $\lambda_1 > 1$ implies $\lambda_2 = 1/\lambda_1 < 1$, i. e., along the directions of the eigenvectors e_1, e_2 the behavior shown in Fig. 184 is found, which can be described by

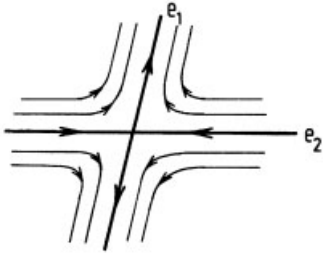


Figure 184: Trajectories around a hyperbolic fixed point with eigenvectors e_1 and e_2 .

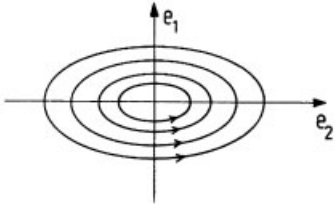


Figure 185: Trajectories around an elliptic fixed point.

$$\begin{aligned}
 T \begin{bmatrix} x \\ y \end{bmatrix} &= \begin{bmatrix} x^* \\ y^* \end{bmatrix} + L \begin{bmatrix} \Delta x \\ \Delta y \end{bmatrix} \\
 L \begin{bmatrix} \Delta x \\ \Delta y \end{bmatrix} &= \begin{bmatrix} \lambda_1 & \Delta x \\ 1/\lambda_1 & \Delta y \end{bmatrix}
 \end{aligned}
 \tag{G.10}$$

i. e., this fixed point is unstable since all points which are not on the stable manifold along e_2 are driven away from (x^*, y^*) , and an infinite number of iterations is required to approach the fixed point along e_2 :

$$\lim_{n \rightarrow \infty} L^n \begin{bmatrix} 0 \\ \Delta y \end{bmatrix} = \lim_{n \rightarrow \infty} L^n \begin{bmatrix} 0 \\ (1/\lambda_1^n) \Delta y \end{bmatrix} = \begin{bmatrix} 0 \\ 0 \end{bmatrix}
 \tag{G.11}$$

b) Elliptic fixed point: The λ 's, as solutions of a quadratic equation, are complex conjugates and can be written as

$$\lambda_{1,2} = e^{\pm i\varphi} \quad \text{because} \quad \det L = \lambda_1^* \lambda_1 = 1 .
 \tag{G.12}$$

After an appropriate coordinate transformation, L can be written as a simple rotation:

$$L \begin{bmatrix} \Delta x \\ \Delta y \end{bmatrix} = \begin{bmatrix} \cos \varphi, & -\sin \varphi \\ \sin \varphi, & \cos \varphi \end{bmatrix} \begin{bmatrix} \Delta x \\ \Delta y \end{bmatrix}
 \tag{G.13}$$

and the fixed point is stable as shown in Fig. 185 because every point in its close vicinity remains there and is never driven away by applying L .

Because, according to (G.9), the eigenvalues depend only on the trace of the linearized transformation matrix, we obtain the following criterion for stability:

$$\begin{aligned} |\operatorname{Tr}L| < 2 &\rightarrow \text{stable} \\ |\operatorname{Tr}L| > 2 &\rightarrow \text{unstable} \end{aligned} \quad \text{fixed point.} \quad (\text{G.14})$$

The stability of the fixed points (G.4) of T , therefore, becomes

$$x^* = y^* = 0 \quad \rightarrow \quad |\operatorname{Tr}L| = |2C| \quad \rightarrow \quad \text{stable for } |C| < 1 \quad (\text{G.15a})$$

$$x^* = y^* = 1 - C \quad \rightarrow \quad |\operatorname{Tr}L| = 2|2 - C| \quad \rightarrow \quad \text{unstable for } |C| > 1 \quad (\text{G.15b})$$

For T^2 we have by analogy to the chain rule $df^2(x)/dx = f'[f(x)]f'(x)$ in the one-dimensional case:

$$\begin{aligned} \operatorname{Tr}L_{T^2} &= \operatorname{Tr}[L_T(x_3^*, y_3^*) \cdot L_T(x_4^*, y_4^*)] \\ &= 2[-2(C+1)(C+3) + 1] = \begin{cases} +1 & \text{for } C = -1 \\ -1 & \text{for } C = 1 - \sqrt{5} \end{cases} \end{aligned} \quad (\text{G.16})$$

where we denoted the functional matrix of T^2 by L_{T^2} and used $(x_3^*, y_3^*) = T(x_4^*, y_4^*)$.

Collecting (G.15)–(G.16) together, we find: (x_1^*, y_1^*) is an attractor of period 1 and is stable for $-1 < C < 1$, and $(x_{3,4}^*, y_{3,4}^*)$ is an attractor of period 2 and stable for $1 - \sqrt{5} < C < -1$. We therefore see the beginning of a bifurcation cascade.

Let us now demonstrate the self-similarity which leads to the whole sequence of period doublings by introducing Hellemann's renormalization scheme.

It starts from (G.3) which can be written as

$$x_{n+1} + x_{n-1} = 2Cx_n + 2x_n^2. \quad (\text{G.17})$$

A linearization of this equation around the fixed points of period two,

$$x_n^* = \frac{1}{2} \left[-(C+1) + (-1)^n \sqrt{(C+1)(C-3)} \right]; \quad n = 0, 1, 2, 3 \quad (\text{G.18})$$

yields

$$\Delta x_{n+1} + \Delta x_{n-1} = (2C + 4x_n^*)\Delta x_n - 2(\Delta x_n)^2. \quad (\text{G.19})$$

If we add (G.19), then for $n = 2m + 1$ and $n = 2m - 1$ we obtain

$$\begin{aligned} \Delta x_{2m+2} + \Delta x_{2m-2} &= -2\Delta x_{2m} + (2C + 4x_0^*)[\Delta x_{2m-1} + \Delta x_{2m-1}] \\ &\quad + 2[(\Delta x_{2m-1})^2 + (\Delta x_{2m+1})^2]. \end{aligned} \quad (\text{G.20})$$

Now we take (G.19) at $n = 2m$,

$$\Delta x_{2m+1} + \Delta x_{2m-1} = (2C + 4x_1^*)\Delta x_{2m} + 2(\Delta x_{2m})^2 \quad (\text{G.21})$$

and add it to (G.20):

$$\Delta x_{2m+2} + \Delta x_{2m-2} = 2C'\Delta x_{2m} + 2\alpha(\Delta x_{2m})^2 + O[(\Delta x)^3]. \quad (\text{G.22})$$

This equation can be put into the same form as (G.17) by rescaling $x'_m \equiv \alpha\Delta x_{2m}$:

$$x'_{m+1} + x'_{m-1} = 2C'x'_m + 2x'^2_m \quad (\text{G.23})$$

where

$$C' = 2(C + 2x_1^*)(C + 2x_0^*) - 1 = 2C^2 + 4C + 7 \quad (\text{G.24})$$

$$\alpha = 2(C + 2x_1^*) + 2(C + 2x_0^*)^2. \quad (\text{G.25})$$

The meaning of eq. (G.23) is as follows: If the two-dimensional map is developed to second order around the two-cycle and the result is rescaled, one obtains the old map, i. e., the stability of $x^* = y^* = 0$ for $|C| < 1$ implies [because of the similarity of (G.17) and (G.23)] the stability of $x^{*f} = y^{*f} = \Delta x = \Delta y = 0$, i. e., of the two-cycle for $|C| = |-2C^2 + 4C + 7| < 1$ or $1 - \sqrt{5} < C < -1$.

Repeating this argument we see that (G.23) also holds for the derivatives around a four-cycle, etc. A cascade of bifurcations with cycles of period 2^n is obtained which are stable for $C_{n-1} < C < C_n$ where

$$C_{n-1} = 2C_n^2 + 4C_n + 7. \tag{G.26}$$

The bifurcation points accumulate at C_∞ which is determined by

$$C_\infty = 2C_\infty + 4C_\infty + 7 \rightarrow C_\infty = -1.2656(1.266311\dots) \tag{G.27}$$

which yields

$$\alpha = \alpha(C_\infty) = -4.128(4.018077\dots) \tag{G.28}$$

and the Feigenbaum constant δ

$$C_n = C_\infty + A\delta^{-n} \quad \text{with} \quad \delta = 9.06(8.72109\dots) \tag{G.29}$$

where the numbers in parentheses give the best current numerical values for the constants.

Fig. 186 shows the orbits of the Hénon map (G.1 a, b) near a stable fixed point and after the first bifurcation.

H Unstable Periodic Orbits

For References see References to Chapter 10 on p. 275.

The simplest integrable conservative systems are harmonic oscillators, and the simplest chaotic systems are described by piecewise linear maps (see Chapter 3). Harmonic oscillators are the starting point for perturbation expansions in classical mechanics (see Chapter 8).

In the following we will show that, in an analogous fashion, the dynamics on strange attractors can be successively approximated by the dynamics of piecewise linear maps. The points on the attractor around which one linearizes are determined by the unstable periodic cycles. If we describe the dynamics on the attractor by the map

$$\vec{x}^{t+1} = \vec{f}(\vec{x}^t), \tag{H.1}$$

then the unstable cycles $\{\vec{x}^*\}$ of order n are just the unstable fixed points of order n of $\vec{f}(\vec{x})$:

$$\vec{x}^* = \vec{f}^{(n)}(\vec{x}^*). \tag{H.2}$$

Here $\vec{f}^{(n)}(\vec{x})$ is the n th iterate of the map and the cycle is unstable. This means that the Jacobian $J_{ij} = \partial f_i^{(n)}(\vec{x}^*) / \partial x_j^*$ has at least one eigenvalue with modulus larger than 1. If one takes the points of all unstable periodic orbits, they cover the attractor with a dense set. The trajectory on the attractor becomes repelled from these points (because they are unstable) and dances between them. The rhythm of this dance is determined by the unstable periodic orbits.

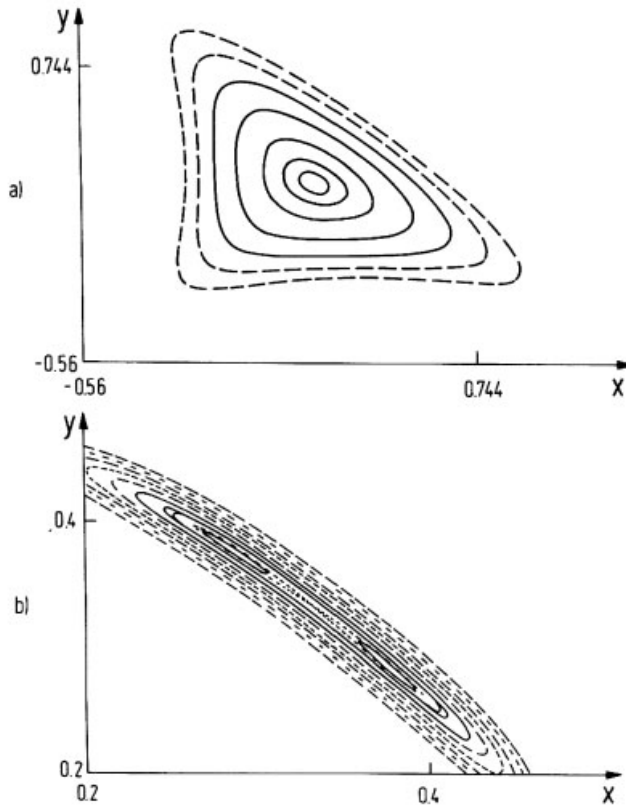


Figure 186: Orbits of the Hénon map. a) At $a = 0.95$; b) At $a = 3.02$ (after Bountis, 1981).

This metaphorical picture and the importance of unstable periodic orbits was already known to Poincaré. In his book *Statistical Mechanics, Thermodynamic formalism* (1978) Ruelle had already developed a method to expand physical averages in terms of unstable periodic orbits for expanding maps. During recent years Cvitanovich and his co-workers (Cvitanovich *et al.*, 1990) have shown how averages on strange attractors (for example generalized dimensions or generalized entropies) can be expanded in terms of unstable periodic orbits of increasing order.

In the following we want to explain the importance of unstable periodic orbits for the example of one-dimensional maps, further details and applications can be found in the cited literature. In the first step we show that the eigenvalues of the Frobenius–Perron operator (which determines the dynamics on the strange attractor) can be expanded in terms of unstable periodic orbits. Next we explain how a nonlinear map can be approximated in a hierarchical fashion by piecewise linear maps.

The linear Frobenius–Perron operator describes the time development of a dynamical system. It has for a one-dimensional map

$$x^{t+1} = f(x^t) \tag{H.3}$$

the form

$$K(x|y) = \delta[x - f(y)] . \tag{H.4}$$

The time development of an arbitrary function $p(x)$ under the influence of the map $f(x)$ is determined by

$$p^{t+1}(x) = \int dy K(x|y) p^t(y) . \tag{H.5}$$

Every linear operator (think of a matrix) can be written in terms of its left and right eigenfunctions (eigenvectors of the matrix) and its eigenvalues. Therefore, $K(x|y)$ can be written as:

$$K(x|y) = \sum_{\nu} \lambda_{\nu} \Phi_{\nu}^R(x) \Phi_{\nu}^L(y) . \tag{H.6}$$

Here λ_{ν} are the eigenvalues and $\Phi_{\nu}^L(x)$, $\Phi_{\nu}^R(y)$ are the left and right eigenfunctions of $K(x|y)$, which are defined by:

$$\int dy K(x|y) \Phi_{\nu}^R(y) = \lambda_{\nu} \Phi_{\nu}^R(x) \tag{H.7a}$$

$$\int dx \Phi_{\nu}^L(x) K(x|y) = \lambda_{\nu} \Phi_{\nu}^L(y) \tag{H.7b}$$

and

$$\int dx \Phi_{\nu}^L(x) \Phi_{\mu}^R(x) = \delta_{\mu\nu} . \tag{H.8}$$

Next we will show that the eigenvalues λ_{ν} of $K(x|y)$ can be written in terms of the unstable periodic orbits of $f(x)$. The eigenvalues of any linear operator are given by the zeros of the characteristic polynomial

$$\det[1 - zK] = 0 , \tag{H.9}$$

i. e., $z = \{\lambda_{\nu}^{-1}\}$. Since we have for any nonsingular matrix M the relation $\log \det M = \text{Tr} \log M$ (in terms of the eigenvalues Γ_i one has $\det M = \prod_i \Gamma_i$ and $\log \det M = \sum_i \log \Gamma_i = \text{Tr} M$). The logarithm of the determinant in eq. (H.9) can be written as

$$\log \det[1 - zK] = \text{Tr} \log[1 - zK] . \tag{H.10}$$

By expanding the logarithm ($\log(1 - x) = -\sum_{n=1}^{\infty} x^n/n$), we obtain:

$$\text{Tr} \log[1 - zK] = - \sum_{n=1}^{\infty} \frac{z^n}{n} \text{Tr} K^n . \tag{H.11}$$

Putting everything together we get:

$$\det(1 - zK) = \exp \left[- \sum_{n=1}^{\infty} \frac{z^n}{n} \text{Tr} K^n \right] . \tag{H.12}$$

The trace of K^n can be directly written in terms of unstable periodic orbits:

$$\text{Tr} K^n = \int dx \delta[x - f^n(x)] = \sum_{\text{fix}} \frac{1}{|1 - f^n'(x^*)|} . \tag{H.13}$$

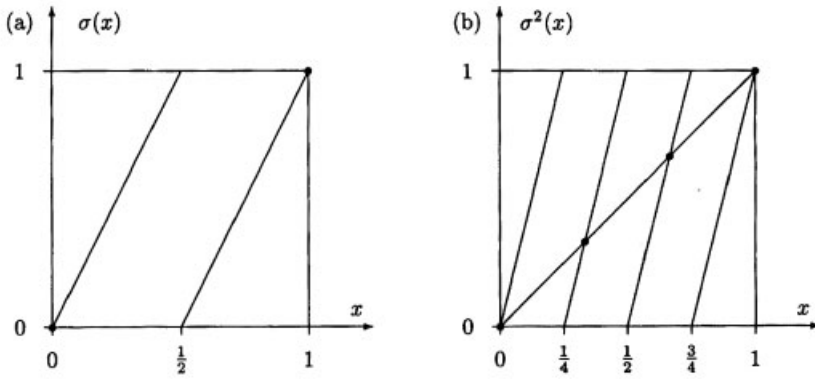


Figure 187: a) The Bernoulli shift $\sigma(x)$ with two unstable fixed points. b) The second iterate $\sigma^2(x)$ with four unstable fixed points.

The sum \sum_{fix} in eq. (H.13) runs over all fixed points of $f^n(x)$, i. e., we have

$$x^* = f^n(x^*) . \tag{H.14}$$

The solutions of eq. (H.14) are all one-cycles (= fixed points), two-cycles and cycles of higher order (up to length n) of $f(x)$ (see Chapter 4). Since the chaotic regime contains only unstable periodic orbits, we have

$$|f^{(n)'}(x^*)| > 1 . \tag{H.15}$$

Let us now compute as a simple example the eigenvalues of the Frobenius–Perron operator of the Bernoulli shift $\sigma(x) = 2x \bmod 1$ (see Chapter 3). The n th iterate of $\sigma(x)$ can be written as

$$\sigma^n(x) = (2^n x) \bmod 1 . \tag{H.16}$$

Figure 187 shows that $\sigma^n(x)$ has just 2^n fixed points. Therefore we obtain

$$\text{Tr } K^n = \sum_{\text{fix}} \left| \frac{1}{1 - f^{n'}(x^*)} \right| = 2^n \left| \frac{1}{1 - 2^n} \right| = \frac{1}{1 - 2^{-n}} . \tag{H.17}$$

If we use this result in eq. (H.12) for the characteristic polynomial, we get:

$$\log \det(1 - zK) = - \sum_{n=1}^{\infty} \frac{z^n}{n} \frac{1}{1 - 2^{-n}} . \tag{H.18}$$

Next we write $(1 - 2^{-n})^{-1}$ as a geometric series and obtain

$$- \sum_{n=1}^{\infty} \frac{z^n}{n} \sum_{m=0}^{\infty} (2^{-n})^m = - \sum_{m=0}^{\infty} \sum_{n=1}^{\infty} \frac{(z \cdot 2^{-m})^n}{n} = \sum_{m=0}^{\infty} \log(1 - z \cdot 2^{-m}) . \tag{H.19}$$

This yields

$$\det(1 - zK) = \prod_{m=0}^{\infty} (1 - z \cdot 2^{-m}) , \tag{H.20}$$

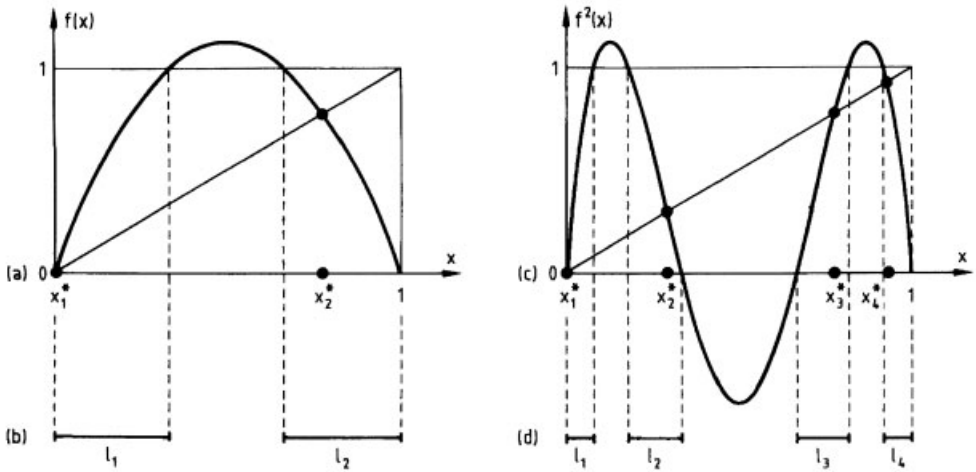


Figure 188: a) The logistic map for $r > 4$. b) Set of points which remain in the interval $[0, 1]$ after one iteration of $f(x)$. Each of the fixed points $x_1^* = 0$ and x_2^* of $f(x)$ is an element of the remaining intervals. c) The second iterate of the logistic map for $r > 4$. d) After two iterations of $f(x)$ only four smaller intervals remain. Again, the fixed points of $f^2(x)$ are contained in these intervals.

which has the zeros $z_m = 2^m$, i. e., the eigenvalues of K have the form

$$\lambda_\nu = z_\nu^{-1} = 2^{-\nu}. \tag{H.21}$$

We have shown that the eigenvalues of the Frobenius–Perron operator are uniquely determined by unstable periodic orbits. What is needed to compute these eigenvalues are the positions of the cycle elements and (because the chain rule allows us to express f^m by f') the derivatives of $f(x)$ at these positions, i. e., to calculate λ_ν , it is sufficient to know the piecewise linearized map where the linearization has been performed around the cycle points (this yields $\{f'(x^*)\}$ and $\{x^*\}$).

To make this geometrical picture even clearer, we consider the logistic map for $r > 4$ (see Fig. 188 a) and ask which points will remain within the unit interval, if we start from a homogeneous distribution of points within the interval $[0, 1]$ and iterate the map. The first iteration step eliminates all points with $f(x) > 1$ (Fig. 188 a–b). After the second iteration step all points with $f^2(x) > 1$ have left the interval (Fig. 188 c–d). How could we estimate the length of the remaining intervals?

First we note that all remaining intervals contain at least one point of an unstable periodic orbit (see Fig. 188).

As a second step we approximate the logistic map successively by piecewise linear maps, which touch the original map at the points which correspond to unstable periodic orbits (see Fig. 189 a). Thereby we obtain, to first order, the estimate

$$l'_1 \sim \left| \frac{1}{f'(x_1^*)} \right|, \quad l'_2 \sim \left| \frac{1}{f'(x_2^*)} \right| \tag{H.22}$$

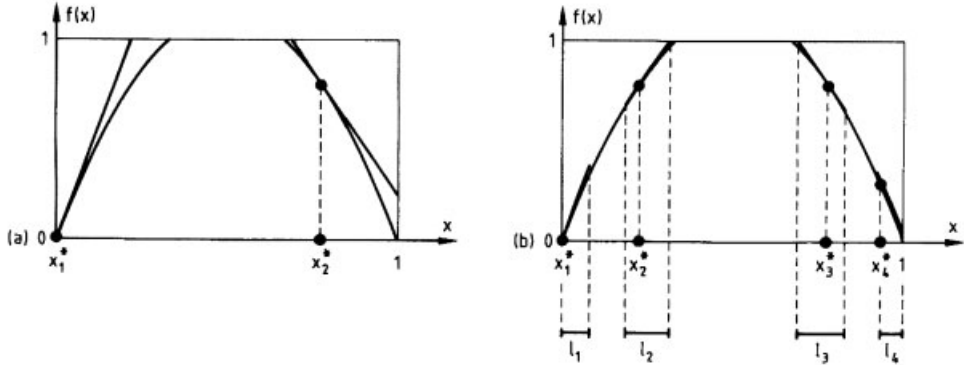


Figure 189: Approximation of $f(x)$ by piecewise linear maps (see Fig. 188). a) $f(x)$ is approximated by tangents to $f(x)$ in the two fixed points of $f(x)$. b) The next-order approximation of $f(x)$ is given by the tangents to $f(x)$ in the four fixed points of $f^2(x)$.

and to second order (see Fig. 189b):

$$l'_1 \sim \left| \frac{1}{f^{2'}(x_1^*)} \right|, \quad l'_2 \sim \left| \frac{1}{f^{2'}(x_2^*)} \right|, \quad l'_3 \sim \left| \frac{1}{f^{2'}(x_3^*)} \right|, \quad l'_4 \sim \left| \frac{1}{f^{2'}(x_4^*)} \right|. \quad (\text{H.23})$$

After n iteration steps the remaining set of points has a measure Γ^n which is proportional to

$$\Gamma^n \sim \sum_{\text{fix}} \left| \frac{1}{f^{n'}(x^*)} \right|. \quad (\text{H.24})$$

Here the sum runs again over all fixed points $f^n(x) = x^*$, and eq. (H.24) is an estimate for Γ^n , where we neglected factors of order 1 because $f^{n'}(x^*)$ diverges as $|f^{n'}(x^*)| \propto e^{n \cdot \text{const.}}$. By comparing eq. (H.24) with eq. (H.13), we see that Γ^n is just equal to the trace of K^n (note $f^{n'}(x) \gg 1$, i. e., $|1 - f^{n'}(x^*)| \approx |f^{n'}(x^*)|$):

$$\Gamma^n \sim \text{Tr} K^n. \quad (\text{H.25})$$

Therefore a computation of the trace of K^n via unstable periodic orbits corresponds to an approximation of the nonlinear map by piecewise linear maps which are located at the cycle points.

Figure 190 shows that this geometrical picture can also be generalized to higher-dimensional maps and attractors, and it represents, from the conceptual point of view, the main result of this chapter. Equation (H.25) can also be derived in a more direct fashion by writing Γ^n as:

$$\Gamma^n = \int dx' dx \delta[x' - f^n(x)]. \quad (\text{H.26})$$

Here we first summed over all points x within the unit interval and then considered only those points x' which remain after n iterations within the interval. To show that $\Gamma^n \propto \text{Tr} K^n$, we note that K^n can be written as

$$K^n(x|y) = \sum_v \lambda_v^n \Phi_v^R(x) \Phi_v^L(y) = \delta[x - f^n(y)]. \quad (\text{H.27})$$

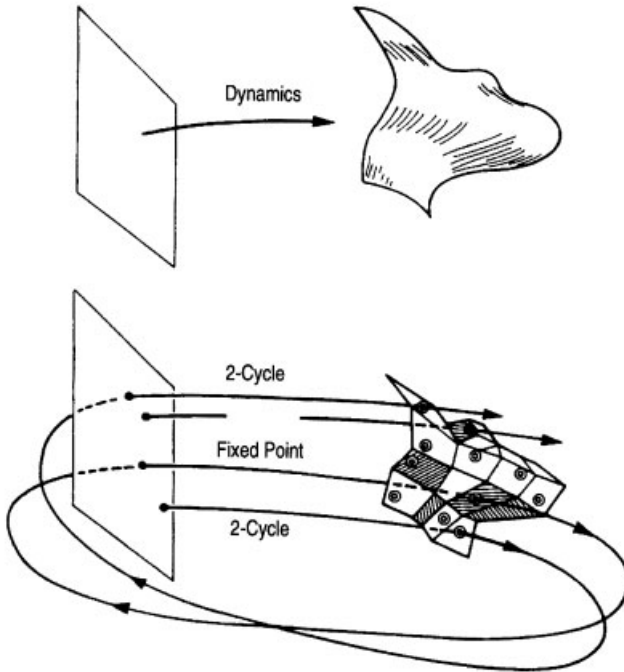


Figure 190: Approximation of a dynamical system by unstable periodic orbits. A continuous flow is approximated by piecewise linear maps (centered around the points that belong to the unstable periodic orbits), after Artuso *et al.*, (1990).

For $n \rightarrow \infty$ the sum is dominated by the largest eigenvalue, i. e., we have

$$K^n(x|y) \sim \lambda_{\max}^n \Phi_{\max}^R(x) \Phi_{\max}^L(y) . \tag{H.28}$$

Therefore

$$\Gamma^n \sim \lambda_{\max}^n , \tag{H.29}$$

and $\lambda_{\max}^n = \text{Tr} K^n$ for $n \rightarrow \infty$.

We have shown for the example of the Bernoulli shift $\sigma(x) = 2x \bmod 1$, that the sum over n in eq. (H.13) can be performed explicitly. This is of course not always possible. But it has been shown by Artuso *et al.*, (1990), that the sum over all fixed points in eq. (H.13) can be replaced by a simpler sum over so-called primitive unstable cycles in such a way that one obtains a systematic expansion of $\det(1 - zK)$ in terms of primitive cycles. In the following section we want to make this idea plausible (mathematical rigor is not intended) and we refer for more details to the original article (Artuso *et al.*, 1990).

The simplest primitive cycle is a fixed point for which we have $f^n(x^*) = [f'(x^*)]^n$, i. e., for this cycle we can perform the sum over n in complete analogy to eq. (H.17). In a similar fashion, cycles of higher order can be reduced to simpler cycles, and the corresponding n -sums can be performed.

With $|1 - f^{n'}(x^*)|^{-1} = |f^{n'}(x^*)|^{-1} \sum_{m=0}^{\infty} |f^{n'}(x^*)|^m$, it follows from eq. (H.13):

$$\text{Tr} K^n = \sum_{m=0}^{\infty} \sum_{\text{fix}} \sum_{n=0}^{\infty} \frac{z^n}{n} |f^{n'}(x^*)|^{-(m+1)}. \tag{H.30}$$

If one reduces the sum over the fixed points \sum_{fix} to the sum of the primitive fixed cycles \sum_p (we will refer for details to Artuso *et al.*, 1990), it becomes plausible that $\text{Tr} K^n$ can be written as

$$\begin{aligned} \text{Tr} K^n &= \sum_{m=0}^{\infty} \sum_p \sum_{n=0}^{\infty} [z^{n_p} |f'(x_p)|^{(m+1)n}]^n / n \\ &= \sum_{m=0}^{\infty} \sum_p \log[1 - z^{n_p} |f'(x_p)|^{-(m+1)}]. \end{aligned} \tag{H.31}$$

This yields:

$$\det(1 - zK) = \prod_{m=0}^{\infty} \prod_p \frac{1}{1 - z^{n_p} |f'(x_p)|^{-(m+1)}}. \tag{H.32}$$

Here n_p is an integer which determines the multiplicity of the corresponding cycle. The product of the primitive cycles \prod_p is the so-called Ruelle zeta function because it bears a formal analogy to the Euler representation of the Riemann zeta function $\zeta(z)$ (see, e.g., Edwards, 1974):

$$\zeta(z) = \sum_{m=0}^{\infty} \frac{1}{n^z} = \prod_{\{p_i\}} \frac{1}{1 - p_i^{-z}}. \tag{H.33}$$

The last equality sign becomes plausible if we recall that each integer can be written as a product of prime numbers p_i with different multiplicity, i. e., $n = \prod_{p_i} p_i^{m_i}$, and the summation over n corresponds to a summation over all m_i , i. e.,

$$\zeta(z) = \sum_{n=1}^{\infty} n^{-z} = \sum_{\{m_i\}} \prod_{p_i} (p_i^{-z})^{m_i} = \prod_{p_i} \frac{1}{1 - p_i^{-z}}. \tag{H.34}$$

Remarks and References

Since the introductory review articles and books mentioned below already contain extensive lists of original literature (e. g., there are 300 references in the articles by Helleman), no attempt has been made to cover all references. Authors whose work has inadvertently not been cited are asked for their forgiveness. The references and further reading material are listed according to the individual chapters.

Chapter 1: Introduction

Original articles and general sources::

- Abraham, R. H., and Shaw, C. D. (1981): *Dynamics – The Geometry of Behavior*. Aerial Press, Santa Cruz.
- Arnold, V. I. (1963): “Small Denominators II, Proof of a Theorem of A. N. Kolmogorov on the Preservation of Conditionally-Periodic Motions Under a Small Perturbation of the Hamiltonian”, *Russ. Math. Surveys* **18**, 5.
- Arnold, V. I., and Avez, A. (1968): *Ergodic Problems of Classical Mechanics*. Benjamin, New York.
- Balescu, R. (1975): *Equilibrium and Nonequilibrium Statistical Mechanics*. Wiley, New York.
- Berge, P., Pomeau, Y., and Vidal, Ch. (1984): *L’Ordre dans le Chaos*. Hermann, Paris.
- Campbell, D., and Rose, H. (eds.) (1983). “Proc. of the International Conference on Order in Chaos’ in Los Alamos”, *Physica* **7D**, 1.
- Chandrasekhar, S. (1961): *Hydrodynamic and Hydromagnetic Stability*. Clarendon Press, Oxford.
- Chirikov, B. V. (1980): “A Universal Instability of Many-Dimensional Oscillator Systems”, *Phys. Rep.* **52**, 463.
- Collet, P., and Eckmann, J. P. (1980): *Iterated Maps of the Interval as Dynamical Systems*. Birkhäuser, Boston.
- Couillet, P., and Tresser, J. (1978): “Iterations d’Endomorphismes et Groupe de Renormalisation”, *C. R. Hebd. Seances Acad. Sci., Ser. A* **287**, 577, and *J. Phys. (Paris) Coll.* **39**, C 5–25 (1978).
- Cvitanovich, P. (ed.) (1984): *Universality in Chaos*. A reprint selection, Adam Hilger, Bristol.
- Eckmann, J. P. (1981): “Roads to Turbulence in Dissipative Dynamical Systems”, *Rev. Mod. Phys.* **53**, 643.
- Feigenbaum, M. J. (1978): “Quantitative Universality for a Class of Nonlinear Transformations”, *J. Stat. Phys.* **19**, 25.
- Feigenbaum, M. (1980): *Universal Behavior in Nonlinear Systems*. Los Alamos Science.

- Garrido, L. (ed.) (1982): *Dynamical Systems and Chaos*. Lecture Notes in Physics **179**, Springer, Berlin-Heidelberg-New York-Tokyo.
- Gorel, D. G. and Roessler, O. E. (eds.) (1978): “Bifurcation Theory in Scientific Disciplines”, *Ann. N. Y. Acad. Sci.* **306**.
- Grossmann, S., and Thomae, S. (1977): “Invariant Distributions and Stationary Correlation Functions of One-Dimensional Discrete Processes”, *Z. Naturforsch.* **32 A**, 1353.
- Guckenheimer, J., and Holmes, P. (1983): *Nonlinear Oscillations, Dynamical Systems and Bifurcations of Vector Fields*. Springer, Berlin-Heidelberg-New York-Tokyo.
- Haken, H. (ed.) (1981): *Chaos and Order in Nature*. Springer, Berlin-Heidelberg-New York-Tokyo.
- Haken, H. (1982): *Synergetics*, 2nd Ed. Springer, Berlin-Heidelberg-New York-Tokyo.
- Haken, H. (ed.) (1982): *Evolution of Order and Chaos*. Springer, Berlin-Heidelberg-New York-Tokyo.
- Haken, H. (1984): *Advanced Synergetics*. Springer, Berlin-Heidelberg-New York-Tokyo.
- Hao Bai-Lin (1984): *Chaos*. World Scientific, Singapore.
- Hellemann, R. H. G. (1980): in E. G. D. Cohen (ed.): *Fundamental Problems in Statistical Mechanics*. Vol. V. North-Holland, Amsterdam-New York, p. 165.
- Hellemann, R. H. G. (ed.) (1980): “Proc. of the 1979 Int. Conf. on Nonlinear Dynamics”, *Ann. N. Y. Acad. Sci.* **603**.
- Hellemann, R. H. G., and Ioos, G. (eds.) (1983): Les Houches Summerschool on “Chaotic Behavior in Deterministic Systems”. North-Holland, Amsterdam.
- Hu, B. (1982): “Introduction to Real Space Renormalization Group Methods in Critical and Chaotic Phenomena”, *Phys. Rep.* **31**, 233.
- Kolmogorov, A. N. (1954): “On Conservation of Conditionally-Periodic Motions for a Small Change in Hamilton’s Function”, *Dokl. Akad. Nauk. USSR* **98**, 525.
- Landau, L. D. (1944): *C. R. Dokl. Acad. Sci. USSR* **44**, 311.
- Landau, L. D., and Lifshitz, E. M. (1959): *Fluid Mechanics*, Pergamon, Oxford.
- Lichtenberg, A. J., and Liebermann, M. A. (1983): *Regular and Stochastic Motion*. Springer, Berlin-Heidelberg-New York-Tokyo.
- Lorenz, E. N. (1963): “Deterministic Nonperiodic Flow”, *J. Atmos. Sci.* **20**, 130.
- Manneville, P., and Pomeau, Y. (1979): “Intermittency and the Lorenz Model”, *Phys. Lett.* **75 A**, 1.
- May, R. M. (1976): “Simple Mathematical Models With Very Complicated Dynamics”, *Nature* **261**, 459.
- Monin, A. S. and Yaglom, A. N. (1978): *Statistical Fluid Mechanics*. MIT Press, Cambridge, Mass.
- Moser, J. (1967): “Convergent Series Expansions of Quasi-Periodic Motions”, *Math. Ann.* **169**, 163.
- Moser, J. (1973): *Stable and Random Motion in Dynamical Systems*. Princeton Univ. Press.
- Moser, J. (1978): “Is the Solar System Stable?”, *Math. Intelligencer* **1**, 65.

- Newhouse, S., Ruelle, D., and Takens, F. (1978): “Occurrence of Strange Axiom-A Attractors Near Quasiperiodic Flow on T^m , $m \geq 3$ ”, *Commun. Math. Phys.* **64**, 35.
- Ott, E. (1981): “Strange Attractors and Chaotic Motions of Dynamical Systems”, *Rev. Mod. Phys.* **53**, 655.
- Peitgen, H. O., and Richter, P. H. (1986): *The Beauty of Fractals*. Springer, Berlin-Heidelberg-New York-Tokyo.
- Poincaré, H. (1892): *Les Methodes Nouvelles de la Mechanique Celeste*, Gauthier-Villars, Paris; in English (1967): *N.A.S.A Translation TTF-450/452*. U.S. Fed. Clearinghouse; Springfield, VA, USA.
- Ruelle, D., and Takens, F. (1971): “On the Nature of Turbulence”, *Commun. Math. Phys.* **20**, 167.
- Ruelle, D. (1980): “Strange Attractors”, *Math. Intelligencer* **2**, 126.
- Shaw, R. S. (1981): “Strange Attractors, Chaotic Behavior and Information Flow”, *Z. Naturforsch.* **36 A**, 80.
- Swinney, H. L. and Gollub, J. P. (1981): *Hydrodynamic Instabilities and the Transition to Turbulence*. Springer, Berlin-Heidelberg-New York-Tokyo.
- Vidal, C., and Pacault, A. (1981): *Nonlinear Phenomena in Chemical Dynamics*. Springer, Berlin-Heidelberg-New York-Tokyo.
- Zaslavsky, G. M. (1981): “Stochasticity in Quantum Systems”, *Phys. Rep.* **80**, 157.

More information about the systems quoted in Table 1 on p. 2 can be found in the following references::

- [1] D. D’Humierès, M. R., Beasley, B. A., Humberman and A. Libchaber, “Chaotic States and Routes to Chaos in the Forced Pendulum”, *Phys. Rev.* **26 A** (1982) 3483.
- [2] A. Libchaber and J. Maurer in T. Riste (ed.): *Nonlinear Phenomena at Phase Transitions and Instabilities*. NATO Adv. Study Inst., Plenum Press, New York 1982; see also the book edited by Swinney and Gollub, mentioned under “general sources” on p. 257.
- [3] H. Haken, “Analogy Between Higher Instabilities in Fluids and Lasers”, *Phys. Lett.* **53 A** (1975) 77.
- [4] F. A. Hopf, D. L. Kaplan, H. M. Gibbs and R. L. Shoemaker, “Bifurcations to Chaos in Optical Bistability”, *Phys. Rev.* **25 A** (1982) 2172.
- [5] M. Cirillo and N. F. Pedersen, “On Bifurcations and Transitions to Chaos in a Josephson Junction”, *Phys. Lett.* **90 A** (1982) 150.
- [6] R. H. Simoyi, A. Wolf and H. L. Swinney: “One Dimensional Dynamics in a Multicomponent Chemical Reaction”, *Phys. Rev. Lett.* **49** (1982) 245.
- [7–8] See the review article by Hellemann, mentioned under “general sources” on p. 257.
- [9] J. M. Wersinger, J. M. Finn and E. Ott in G. Laval and D. Gresillon (eds.): *Intrinsic Stochasticity in Plasmas*. Les Editions de Physique, Courtaboeuf, Orsay, France 1980.
- [10] See the article by May, mentioned under “general sources” on p. 257.
- [11] L. Glass, M. R. Guevara and A. Shrier, “Bifurcation and Chaos in a Periodically Stimulated Cardiac Oscillator”, *Physica* **7D** (1983) 89, and A. T. Winfree, *Sci. Am.* **248**, No. 5 (1983).

Chapter 2: Experiments and Simple Models

More information on the systems presented in Table 2 on p. 10 can be found in the following references:

- Dubois, M., and Berge, P. (1981). “Instabilities de Couche Limite dans un Fluide en Convection. Evolution vers la Turbulence”, *J. Phys. (Paris)* **42**, 167.
- Epstein, I. R., Kustin, K., de Kepper, P., and Orban, M. (1983): “Oscillating Chemical Reactions”, *Sci. Am.* **248**, No. 3.
- Haken, H. (1975): “Analogy Between Higher Instabilities in Fluids and Lasers”, *Phys. Lett.* **53 A**, 77.
- Haken, H. (1982): *Synergetics*, 2nd Edition. Springer, Berlin-Heidelberg-New York-Tokyo.
- Haken, H. (1984): *Advanced Synergetics*. Springer, Berlin-Heidelberg-New York-Tokyo.
- Hénon, M., and Heiles, C. (1964): “The Applicability of the Third Integral of the Motion: Some Numerical Results”, *Astron. J.* **69**, 73.
- D’Humières, D., Beasley, M. R., Huberman, B. A., and Libchaber, A. (1982): “Chaotic States and Routes to Chaos in the Forced Pendulum”, *Phys. Rev.* **A 26**, 3483.
- Libchaber, A., and Maurer, J. (1982) in Riste, T. (ed.): *Nonlinear Phenomena at Phase Transitions and Instabilities*. NATO Advanced Study Inst., Plenum Press, New York.
- Lorenz, E. N. (1963): “Deterministic Nonperiodic Flow”, *J. Atmos. Sci.* **20**, 130.
- Ma, S. (1976): *Modern Theory of Critical Phenomena*. Benjamin, New York.
- McLaughlin, J. B., and Martin, P. C. (1975): “Transition to Turbulence of a Statically Stressed Fluid System”, *Phys. Rev.* **A 12**, 186.
- Roux, J. C., Rossi, A., Bachelart, S., and Vidal, C. (1981): “Experimental Observations of Complex Behavior During a Chemical Reaction”, *Physica* **2 D**, 395.
- Saltzman, B. (1962): “Finite Amplitude Free Convection as an Initial Value Problem I”, *J. Atmos. Sci.* **19**, 329.
- Simoyi, R. H., Wolf, A., and Swinney, H. L. (1982): “One-Dimensional Dynamics in a Multicomponent Chemical Reaction”, *Phys. Rev. Lett.* **49**, 245.
- Swinney, H. L., and Gollub, J. P. (1978): “The Transition to Turbulence”, *Phys. Today* **31 (8)**, 41.
- Swinney, H. L., and Gollub, J. P. (eds.) (1980): *Hydrodynamic Instabilities and the Transition to Turbulence*. Springer, Berlin-Heidelberg-New York-Tokyo.
- Tyson, J. J. (1976): *The Belousov–Zhabotinsky Reaction*. Lecture Notes in Biomathematics 22, Springer, Berlin-Heidelberg-New York-Tokyo.
- Vidal, C., Roux, J. C., Bachelart, S., and Rossi, A., in Helleman, R. H. G. (ed.) (1980): “Proc. of the 1979 Int. Conf. on Nonlinear Dynamics”, *Ann. N.Y. Acad. Sci.* 603.
- Wegmann, K., and Roessler, O. E., (1978). “Different Kinds of Chaos in the Belousov–Zhabotinsky Reaction”, *Z. Naturforsch.* **33 a**, 1179.
- Wilson, K. G., and Kogut, J. (1974): “The Renormalization Group and the ϵ -Expansion”, *Phys. Rep.* **C 12**, 75.

The periodically kicked rotator and related topics are studied in the following articles:

- Campbell, D., and Rose, H., (eds.) (1983): “Proc. of the International Conference on ‘Order in Chaos’ in Los Alamos”, *Physica* **7D**, 1.
- Chandrasekhar, S. (1961): *Hydrodynamic and Hydromagnetic Stability*, Clarendon Press, Oxford.
- Chirikov, B. V. (1979): “A Universal Instability of Many Dimensional Oscillator Systems”, *Phys. Rep.* **52**, 463.
- Hénon, M. (1976): “A Two Dimensional Map With a Strange Attractor”. *Commun. Math. Phys.* **50**, 69.
- Ott, E. (1981): “Strange Attractors and Chaotic Motions of Dynamical Systems”, *Rev. Mod. Phys.* **53**, 655.
- Zaslavsky, G. M. (1978): “The Simplest Case of a Strange Attractor”, *Phys. Lett.* **69A**, 145.
- Zaslavski, G. M., and Rachki, Kh. R. Ya. (1979): “Singularities of the Transition to Turbulent Motion”, *Sov. Phys. J.E.T.P.* **49**, 1039.

Chapter 3: Piecewise Linear Maps and Deterministic Chaos

The Bernoulli shift is discussed in:

- Billingsley, O. (1964): *Ergodic Theory and Information*. Wiley, New York.
- Shaw, R. S. (1981): in Haken, H. (ed.): *Chaos and Order in Nature*. Springer, Berlin-Heidelberg-New York-Tokyo.

A proof that almost all irrational numbers in $[0, 1]$ in their binary representation contain any finite sequence infinitely many times, can be found in:

- Hardy, G. H., and Wright, E. M. (1938): *The Theory of Numbers*, Oxford University Press, Oxford, p. 125.

More on the behavior of piecewise linear maps can be found in:

- Eckmann, J. P., and Ruelle, D. (1985): “Ergodic Theory of Chaos and Strange Attractors”, *Rev. Mod. Phys.* **57**, 617.
- Grossmann, S., and Thornae, S. (1977): “Invariant Distributions and Stationary Correlation Functions of One-Dimensional Discrete Processes”, *Z. Naturforsch.* **32A**, 1353.
- Shaw, R. S. (1981): “Strange Attractors, Chaotic Behavior and Information Flow”, *Z. Naturforsch.* **36A**, 80.

Deterministic diffusion has been studied, for example, in the following papers:

- Geisel, T., and Nierwetberg, J. (1982). “Onset of Diffusion and Universal Scaling in Chaotic Systems”, *Phys. Rev. Lett.* **48**, 7.
- Grossmann, S., and Fujisaka, H. (1982): “Diffusion in Discrete Nonlinear Systems”, *Phys. Rev.* **26A**, 1779.
- Grossmann, S. (1982) in Haken, H. (ed.): *Evolution of Order and Chaos*. Springer, Berlin-Heidelberg-New York-Tokyo.
- Haken, H. (1982): *Synergetics*, 2nd Ed. Springer, Berlin-Heidelberg-New York-Tokyo.

Chapter 4: Universal Behavior of Quadratic Maps

Original articles and general sources:

- Collet, P., and Eckmann, J. P. (1980): *Iterated Maps of the Interval as Dynamical Systems*. Birkhäuser, Boston.
- Collet, P., Eckmann, J. P., and Lanford, O. E. (1980): “Universal Properties of Maps on an Interval”, *Commun. Math. Phys.* **76**, 211.
- Couillet, P., and Tresser, J. (1978): “Iterations d’Endomorphismes et Groupe de Renormalisation”, *C. R. Hebd. Seances Acad. Sci. Series A* **287**, 577, and *J. Phys. (Paris)* **C 5**, 25 (1978).
- Derrida, B., Gervois, A., and Pomeau, Y. (1979): “Universal Metric Properties of Bifurcations and Endomorphisms”, *J. Phys.* **12 A**, 269.
- Feigenbaum, M. J. (1978): “Quantitative Universality for a Class of Nonlinear Transformations”, *J. Stat. Phys.* **19**, 25.
- Feigenbaum, M. J. (1979): “The Universal Properties of Nonlinear Transformations”, *J. Stat. Phys.* **21**, 669.
- Grossmann, S., and Thomae, S. (1977): “Invariant Distributions and Stationary Correlation Functions of One-Dimensional Discrete Processes”, *Z. Naturforsch.* **32 A**, 1353.
- Hubermann, B. A., and Rudnick, J. (1980): “Scaling Behavior of Chaotic Flows”, *Phys. Rev. Lett.* **45**, 154.
- May, R. M. (1976): “Simple Mathematical Models With Very Complicated Dynamics”, *Nature* **261**, 459.
- Metropolis, M., Stein, M. L., and Stein, P. R. (1973): “On Finite Limit Sets for Transformations of the Unit Interval”, *J. Combinatorial Theory (A)* **15**, 25.
- Lanford, O. E., (1982): “A Computer-Assisted Proof of the Feigenbaum Conjectures”, *Bull. Am. Math. Soc.* **6**, 427.
- Peitgen, H. O., and Richter, P. H. (1984): *Harmonie in Chaos und Kosmos*, and *Morphologie komplexer Grenzen; Bilder aus der Theorie dynamischer Systeme*. Both catalogues can be obtained from: Forschungsschwerpunkt: Dynamische Systeme, Universität Bremen, D-2800 Bremen, F.R.G.

The Hausdorff dimension and related topics are discussed in:

- Grassberger, P. (1981): “On the Hausdorff Dimension of Fractal Attractors”, *J. Stat. Phys.* **19**, 25.
- Mandelbrot, B. B. (1982): *The Fractal Geometry of Nature*, Freeman, San Francisco.

The universal properties of the power spectrum are calculated in:

- Collet, P., and Eckmann, J. P. (1980): *Iterated Maps of Intervals as Dynamical Systems*. Birkhäuser, Boston.
- Feigenbaum, M. J. (1979): “The Onset Spectrum of Turbulence”, *Phys. Lett.* **74 A**, 375.
- Feigenbaum, M. J. (1980): “The Transition to Aperiodic Behavior in Turbulent Systems”, *Commun. Math. Phys.* **77**, 65.
- Nauenberg, M., and Rudnick, J. (1981): “Universality and the Power Spectrum at the Onset of Chaos”, *Phys. Rev.* **B 24**, 439.

The influence of external noise on period doubling is, e. g., discussed in:

- Crutchfield, J. P., Nauenberg, M., and Rudnick, J. (1981). “Scaling for External Noise at the Onset of Chaos”, *Phys. Rev. Lett.* **46**, 933.
- Crutchfield, J. P., Farmer, J. D., and Hubermann, B. A. (1982): “Fluctuations and Simple Chaotic Dynamics”, *Phys. Rep.* **92**, 45.
- Feigenbaum, M. J., and Hasslacher, B. (1982): “Irrational Decimations and Path Integrals for External Noise”, *Phys. Rev. Lett.* **49**, 605.
- Shraiman, B., Wayne, C. E., and Martin, P. C. (1981): “Scaling Theory for Noisy Period-Doubling Transition to Chaos”, *Phys. Rev. Lett.* **46**, 935.

The behavior of the logistic map for $r > r_\infty$ is investigated in:

- Derrida, B., Gervois, A., and Pomeau, Y. (1978): “Iteration of Endomorphisms on the Real Axis and Representation of Numbers”, *Ann. Inst. Henri Poincaré* **29 A**, 305.
- Farmer, J. D. (1985): “Sensitive Dependence on Parameters in Nonlinear Dynamics”, *Phys. Rev. Lett.* **55**, 351.
- Farmer, J. D. (1986): in G. Mayer Kress (ed.): *Dimensions and Entropies in Chaotic Systems*, p. 54. Springer, Berlin-Heidelberg-New York-Tokyo.
- Feigenbaum, M. J. (1978): “Quantitative Universality for a Class of Nonlinear Transformations”, *J. Stat. Phys.* **19**, 25.
- Geisel, T., and Nierwetberg, J. (1981): “Universal Fine Structure of the Chaotic Region in Period-Doubling Systems”, *Phys. Rev. Lett.* **47**, 975.
- Guckenheimer, J. (1980): “One Dimensional Dynamics”, *Ann. N.Y. Acad. Sci.* **357**, 343.
- Jacobson, M. V. (1981): “Absolutely Continuous Invariant Measure for One-Parameter Families of One-Dimensional Maps”, *Comm. Math. Phys.* **81**, 39.
- Li, T., and Yorke, J. A. (1975): “Period Three Implies Chaos”, *Ann. Math. Monthly* **82**, 985.
- Metropolis, N., Stein, M. L., and Stein, P. R. (1973): “On Finite Limit Sets for Transformations on the Unit Interval”, *J. Combinat. Theor.* **15**, 25.
- Sarkovskii, A. N. (1964): “Coexistence of Cycles of a Continuous Map of a Line Into Itself”, *Ukr. Mat. Z.* **16**, 61.
- Thomae, S., and Grossmann, S. (1981): “Correlations and Spectra of Periodic Chaos Generated by the Logistic Parabola”, *J. Stat. Phys.* **26**, 485.

More on Sarkovskii’s theorem and the Schwarzian derivative can be found in the book by Collet and Eckmann mentioned in the list of general references of the introduction and in:

- Lanford, O. E. (1980): “Smooth Transformations of Intervals”, *Seminaire BOURBAKI* No. 563.

The references for the experiments quoted in the text are:

- Lauterborn, W., and Cramer, E. (1981): “Subharmonic Route to Chaos Observed in Acoustics”, *Phys. Rev. Lett.* **47**, 1145.
- Lauterborn, W. (1982): “Cavitation Bubble Dynamics. New Tools for an Intricate Problem”, *Appl. Sci. Res.* **38**, 165.

- Lauterborn, W., and Mayer-Ilse, W. (1986): “Chaos”, *Phys. uns. Zeit* **17**, 177.
- Lauterborn, W., and Suchla, E. (1984): “Bifurcation Superstructure in a Model of Acoustical Turbulence”, *Phys. Rev. Lett.* **53**, 2304.
- Libchaber, A., and Maurer, J. (1980): “Une Experience de Rayleigh-Bénard de Géometrie Reduite; Multiplication, Accrochage et Démultiplication de Fréquences”, *J. Phys. (Paris) Coll.* **41**, C 3–51.
- Libchaber, A., and Maurer J. (1982) in Riste, T. (ed.): *Nonlinear Phenomena at Phase Transitions and Instabilities*. NATO Adv. Study Institute, Pergamon Press, New York.
- Linsay, P. S. (1981): “Period Doubling and Chaotic Behavior in a Driven Anharmonic Oscillator”, *Phys. Rev. Lett.* **47**, 1349.
- Rollins, R. W., and Hunt, E. R. (1982): “Exactly Solvable Model of a System Exhibiting Universal Chaotic Behavior”, *Phys. Rev. Lett.* **49**, 1295.
- Testa, J., Perez, J., and Jeffries, C. (1982): “Evidence for Universal Chaotic Behavior of a Driven Nonlinear Oscillator”. *Phys. Rev. Lett.* **48**, 714.

A renormalization-group treatment of second-order phase transitions can, e. g., be found in:

- Ma, S. K. (1976): *Modern Theory of Critical Phenomena*. Benjamin, New York.

The Feigenbaum route has been observed in many experiments. Some more references are:

- Arecchi, F. T., Meucci, R., Puccioni, G., and Tredice, J. (1982): “Experimental Evidence for Subharmonic Bifurcations, Multistability and Turbulence in a Q -switched Gas Laser”, *Phys. Rev. Lett.* **49**, 1217.
- Brun, E., Derighetti, D., Holzner, R., and Meier, D. (1983): “The NMR-Laser – A Nonlinear Solid-State System Showing Chaos”, *Helv. Phys. Acta* **56**, 852.
- Cirillo, M., and Pedersen, N. F. (1982): “On Bifurcations and Transition to Chaos in a Josephson Junction”, *Phys. Lett.* **90 A**, 150.
- Giglio, M., Musazzi, S., and Perine, V. (1981): “Transition to Chaotic Behavior via a Reproducible Sequence of Period-Doubling Bifurcations”, *Phys. Rev. Lett.* **47**, 243.
- Gollub, J. P., and Swinney, H. L. (1975): “Onset of Turbulence in a Rotating Fluid”, *Phys. Rev. Lett.* **35**, 927.
- Gollub, J. P., and Benson, S. V. (1980): “Many Routes to Turbulent Convection”, *J. Fluid Mech.* **100**, 499.
- Hopf, F. A., Kaplan, D. L., Gibbs, H. M., and Shoemaker, R. L. (1982): “Bifurcations to Chaos in Optical Bistability”, *Phys. Rev.* **25 A**, 2171.
- Klinker, T., Meyer-Ilse, W., and Lauterborn, W. (1984): “Period Doubling and Chaotic Behavior in a Driven Toda Oscillator”, *Phys. Lett.* **101 A**, 371.
- Libchaber, A., Laroche, C., and Fauve, S. (1982): “Period Doubling in Mercury, a Qualitative Measurement”, *J. Phys. (Paris) Lett.* **43**, L211.
- Pfister, G. (1984): “Period Doubling in Rotational Taylor–Couette Flow”, *Proc. 2nd Int. Symp. on Appl. of Laser Anemometry to Fluid Mechanics*. Lisboa.
- Simoyi, R. H., Wolf, A., and Swinney, H. L. (1982): “One-Dimensional Dynamics in a Multicomponent Chemical Reaction”, *Phys. Rev. Lett.* **49**, 245.
- Smith, C. W., Tejwani, M. J., and Farris, D. A. (1982): “Bifurcation Universality for First Sound Subharmonic Generation in Superfluid Helium-4”, *Phys. Rev. Lett.* **48**, 429.

Chapter 5: The Intermittency Route to Chaos

The intermittency route has been investigated in the following pioneering articles:

- Manneville, P., and Pomeau, Y. (1979): “Intermittency and the Lorenz Model”, *Phys. Lett.* **75 A**, 1.
- Manneville, P., and Pomeau, Y. (1980): “Different Ways to Turbulence in Dissipative Dynamical Systems”, *Physica* **1 D**, 219.
- Pomeau, Y., and Manneville P. (1979): in G. Laval, and D. Gresillon (eds.): *Intrinsic Stochasticity in Plasmas*. Ed. de Physique, Orsay, p. 239.
- Pomeau, Y., and Manneville, P. (1980): “Intermittent Transition to Turbulence in Dissipative Dynamical Systems“, *Comm.Math. Phys.* **74**, 189.

Influence of external noise on intermittency:

- Eckmann, J. P., Thomas, L., and Wittwer, P. (1981): “Intermittency in the Presence of Noise”, *J. Phys.* **14 A**, 3153.
- Hirsch, J. E., Hubermann, B. A., and Scalapino, D. J. (1982): “Theory of Intermittency”, *Phys. Rev.* **25 A**, 519.
- Hirsch, J. E., Nauenberg, M., and Scalapino, D. L. (1982): “Intermittency in the Presence of Noise: A Renormalization Group Formulation”, *Phys. Lett.* **87 A**, 391.
- Hu, B., and Rudnick, J. (1982): “Exact Solutions of the Feigenbaum Renormalization Group Equations for Intermittency”, *Phys. Rev. Lett.* **48**, 1645.

More on $1/f$ -noise can be found in:

- Ben-Mizrachi, A., Procaccia, I., Rosenberg, N., Schmidt, A., and Schuster, H. G. (1985). “Real and Apparent Divergencies in Low-Frequency Spectra of Nonlinear Dynamical Systems”, *Phys. Rev.* **A 31**, 1830.
- Dutta, P., and Horn, P. M. (1981): “Low-Frequency Fluctuations in Solids”, *Rev. Mod. Phys.* **53**, 497.
- Manneville, P. (1980): “Intermittency, Self-Similarity and $1/f$ -Spectrum in Dissipative Dynamical Systems”, *J. Phys. (Paris)*, **41**, 1235.
- Procaccia, I., and Schuster, H. G. (1983): “Functional Renormalization Group Theory of Universal $1/f$ -Noise in Dynamical Systems”. *Phys. Rev.* **28 A**, 1210.
- Wolf, D. (1978): *Noise in Physical Systems*. Series in Electrophysics Vol. 2. Springer, Heidelberg-New York.

Experiments in which intermittency has been observed:

- Berge, P., Dubois, M., Manneville, P., and Pomeau, Y. (1980): “Intermittency in Rayleigh-Bénard Convection”, *J. Phys. (Paris) Lett.* **41**, L-344.
- Dubois, M., Rubio, M. A., and Berge, P. (1983): “Experimental Evidence of Intermittencies Associated With a Subharmonic Bifurcation”, *Phys. Rev. Lett.* **51**, 1446.
- Jeffries, C., and Perez, J. (1982): “Observation of a Pomeau–Manneville Intermittent Route to Chaos in a Nonlinear Oscillator.”, *Phys. Rev.* **26 A**, 2117.

- Pomeau, Y., Roux, J. C., Rossi, A., Bachelart, S., and Vidal, C. (1981): “Intermittent Behavior in the Belousov–Zhabotinsky Reaction”, *J. Phys. (Paris) Lett.* **42**, L-271.
- Yeh, W. J. and Kao, Y. H. (1983): “Intermittency in Josephson Junctions”, *Appl. Phys. Lett.* **42**, 299.

Chapter 6: Strange Attractors in Dissipative Dynamical Systems

Introduction and definition of strange attractors:

- Eckmann, J. P. (1981): “Roads to Turbulence in Dissipative Dynamical Systems”, *Rev. Mod. Phys.* **53**, 643.
- Eckmann, J. P., and Ruelle, D. (1985): “Ergodic Theory of Chaos and Strange Attractors“, *Rev. Mod. Phys.* **57**, 617.
- Hénon, M. (1976): “A Two-Dimensional Map With a Strange Attractor”, *Commun. Math. Phys.* **50**, 69.
- Lanford, O. E. (1977): “Turbulence Seminar”, in P. Bernard and T. Rativ (eds.): *Lecture Notes in Mathematics* **615**. Springer, Heidelberg-New York, p. 114.
- Lorenz, E. N. (1963): “Deterministic Nonperiodic Flow”, *J. Atmos. Sci.* **20**, 130.
- Mandelbrot, B. (1982): *The Fractal Geometry of Nature*. Freeman, San Francisco.
- Ott, E. (1981): “Strange Attractors and Chaotic Motions of Dynamical Systems”, *Rev. Mod. Phys.* **53**, 655.
- Ruelle, D. (1980): “Strange Attractors”, *Math. Intelligencer* **2**, 126.

The Poincaré–Bendixson theorem is proved in:

- Hirsch, M. W., and Smale, S. (1965): *Differential Equations, Dynamic Systems and Linear Algebra*. Academic Press, New York.

The area-preserving and the dissipative baker’s transformation are discussed, together with the Kaplan–Yorke conjecture, in:

- Kaplan, J. and Yorke, J. (1979) in H. O. Peitgen and H. O. Walther (eds.): *Functional Differential Equations and Approximation of Fixed Points*. Springer, Heidelberg-New York.
- Lebowitz, J. L., and Pentrose, O. (1973): “Modern Ergodic Theory”, *Phys. Today* **23** (2).
- Russel, D. A., Hansen, J. D., and Ott, E. (1980): “Dimension of Strange Attractors”, *Phys. Rev. Lett.* **45**, 1175.
- Shaw, R. S. (1981): “Strange Attractors, Chaotic Behavior and Information Flow“, *Z. Naturforsch.* **36 a**, 80.

The Kolmogorov entropy and the computation of Liapunov exponents are treated in:

- Arnold, V. I., and Avez, A. (1974): *Ergodic Problems of Classical Mechanics*. Benjamin, New York.
- Farmer, J. D. (1982 a), “Information Dimension and the Probabilistic Structure of Chaos”, *Z. Naturforsch.* **37 a**, 1304.

- Kolmogorov, A. N. (1959): *Dokl. Akad. Nauk. USSR* **98**, 527.
- Pesin, Ya. B. (1977): *Usp. Mat. Nauk.* **32 (4)** 55; engl. transl.: *Math. Surveys* **32 (4)** 55.
- Shannon, C. E., and Weaver, W. (1949): *The Mathematical Theory of Information*. University of Illinois Press, Urbana.
- Shimada, I., and Nagashima, T. (1979): “A Numerical Approach to Ergodic Problems of Dissipative Dynamical Systems”, *Progr. Theor. Physics* **61**, 1605.
- Wolf, A., and Vestano, J. A. (1986): “Intermediate Length Scale Effects in Liapunow Exponent Estimation”, in G. Mayer-Kress (ed.): *Springer Series in Synergetics* **39**. Springer, Berlin-Heidelberg-New York-Tokyo.

References about the generalized dimensions and entropies of strange attractors are:

- Ben-Mizrachi, A., Procaccia, I., and Grassberger, P. (1984): “The Characterization of Experimental (noisy) Strange Attractors”, *Phys. Rev.* **29 A**, 975,
- Eckmann, J. P., and Procaccia, I. (1986): “Fluctuation of Dynamical Scaling Indices in Non-Linear Systems”, *Phys. Rev.* **34 A**, 659.
- Eckmann, J. P., and Ruelle, D. (1985): “Ergodic Theory of Chaos and Strange Attractors”, *Rev. Mod. Phys.* **57**, 617.
- Farmer, J. D. (1982 b), “Dimension, Fractal Measure and Chaotic Dynamics”, in H. Haken (ed.): *Evolution of Order and Chaos*. Springer, Heidelberg-New York.
- Fraser, A. M., and Swinney, H. L. (1986): “Independent Coordinates for Strange Attractors from Mutual Information”, *Phys. Rev.* **33 A**, 1134.
- Grassberger, P., and Procaccia, I. (1983 a), “On the Characterization of Strange Attractors”, *Phys. Rev. Lett.* **50**, 346.
- Grassberger, P., and Procaccia, I. (1983 b). “Estimation of the Kolmogorov Entropy From a Chaotic Signal”, *Phys. Rev.* **29 A**, 2591.
- Grassberger, P., and Procaccia, I. (1983 c), “Measuring the Strangeness of Strange Attractors”, *Physica* **9 D**, 189.
- Halsey, T. C., Jensen, M. H., Kadanoff, L. P., Procaccia, I., and Schraiman, B. I. (1986): “Fractal Measures and Their Singularities: the Characterization of Strange Sets”, *Phys. Rev.* **33 A**, 1141.
- Liebert, W., Schuster, H. G. (1989): “Proper Choice of the Time Delay for the Analysis of Chaotic Time Series”, *Phys. Lett. A* **142**, 107.
- Mayer-Kress, G. (ed.) (1986): *Dimensions and Entropies in Chaotic Systems* (Springer Series in Synergetics **32**). Springer, Berlin-Heidelberg-New York-Tokyo.
- Pawelzik, K., and Schuster, H. G. (1987): “Generalized Dimensions and Entropies From a Measured Time Series”, *Phys. Rev.* **35 A**, 481.
- Rössler, O. E. (1976): “An Equation for Continuous Chaos”, *Phys. Lett.* **57 A**, 397.
- Takahashi, Y., and Oono, Y. (1984): “Towards the Statistical Mechanics of Chaos”, *Progr. Theoret. Phys.* **71**, 851.

The reconstruction of an attractor from a time sequence is treated in:

- Farmer, J. D. (1982 c), “Chaotic Attractors of an Infinite-Dimensional System”, *Physica* **4 D**, 366.

- Mackey, M. C., and Glass, L. (1977): *Science* **197**, 287.
- Packard, N., Crutchfield, J. P., Farmer, J. D., and Shaw, R. S. (1980): “Geometry From a Time Series”, *Phys. Rev. Lett.* **45**, 712.
- Takens, F. (1981): *Lecture Notes in Math.* **898**, Springer, Heidelberg-New York.

Pictures of strange attractors and fractal boundaries:

- Brolin, H. (1965): “Invariant Sets Under Iteration of Rational Functions“, *Ark. for Math.* **6**, 103.
- Cvitanovic, P., and Myrheim, J. (1983): “Universality for Period- n Tuplings in Complex Mappings”, *Phys. Lett.* **94 A**, 329.
- Devaney, R. L. (1986): *An Introduction to Chaotic Dynamical Systems*. Benjamin-Cummings, Menlo Park.
- Douady, A., and Hubbard, J. H. (1982): “Iterations des Polynomes Quadratiques Complexes“, *Compt. Rend.* **294**, 93.
- Fatou, P. (1919): *Bull. Soc. Math. France* **47**, 161; **48**, 33, 208 (1920).
- Glass, L., Guevara, M. R., and Shrier, A. (1983): “Bifurcation and Chaos in a Periodically Stimulated Cardiac Oscillator”, *Physica* **7D**, 89; Copyright 1981 by A.A.A.S. Science, Vol. 214, pp. 1350–1353, 18. Dec. 1981.
- Gumowski, I., and Mira, C. (1980): “Recurrences and Discrete Dynamic Systems”, *Lect. Notes in Mathematics* **809**, Springer, Berlin-Heidelberg-New York.
- Hofstadter, D. R. (1979): *Gödel, Escher, Bach: an Eternal Golden Braid*. Basic Books, New York.
- Julia, G. (1918): “Memoire Sur L’Iteration des Fonctions Rationnelles”, *J. Math. Pures et Appl.* **4**, 47.
- Kawakami, H. (1984): *Strange Attractors in Duffing’s Equation – 50 Phase Portraits of Chaos*, available from Univ. of Tokushima, Dept. of Electronics.
- Klinker, T., Meyer-Ilse, W., and Lauterborn, W. (1984): “Period Doubling and Chaotic Behavior in a Driven Toda Oscillator”, *Phys. Lett.* **101 A**, 371.
- Lauterborn, W., and Cramer, E. (1981): “Subharmonic Route to Chaos Observed in Acoustics”, *Phys. Rev. Lett.* **47**, 1145.
- Mandelbrot, B. B. (1980): “Fractal Aspects of the Iteration of $z \rightarrow \lambda z(1 - z)$ for Complex λ and z ”, *Ann. N. Y. Acad. Sci.* **357**, 249.
- Martin, S., Leber, H., and Martienssen, W. (1984): “Oscillatory and Chaotic States of the Electrical Conduction in BSN Crystals”, *Phys. Rev. Lett.* **53**, 303.
- Peitgen, H. O., and Richter, P. H. (1984): *Harmonie in Chaos und Kosmos*, and *Morphologie komplexer Grenzen; Bilder aus der Theorie dynamischer Systeme*. Both catalogues can be obtained from: Forschungsschwerpunkt: Dynamische Systeme, Universität Bremen, D-2800 Bremen, F.R.G.
- Peitgen, H. O., and Richter, P. H. (1986): *The Beauty of Fractals*. Springer, Berlin-Heidelberg-New York-Tokyo.
- Pfister, G. (1984): “Period Doubling in Rotational Taylor–Couette Flow”, *Proc. 2nd Int. Symp. on Appl. of Laser Anemometry to Fluid Mechanics*. Lisboa.
- Prüfer, M. (1984): “Turbulence in Multistep Methods for Initial Value Problems”, to be published in SIAM, *Journal of Appl. Math.*

- Ruelle, D. (1980): “Strange Attractors”, *Math. Intelligencer* **2**, 126.
- Widom, M., Bensimon, D., Kadanoff, L. P., and Shenker, S. J. (1983): “Strange Objects in the Complex Plane”, *J. Stat. Phys.* **32**, 443.

Chapter 7: The Transition from Quasiperiodicity to Chaos

The onset of turbulence is discussed in:

- Berge, P. (1982): “Study of the Phase Space Diagrams Through Experimental Poincaré Sections in Prechaotic and Chaotic Regimes”, *Physica Scripta* **T 1**, 71.
- Brandstater, A., Swift, J., Swinney, H. L., Wolf, A., Farmer D., Jen, E., and Crutchfield, P. (1983): “Low-Dimensional Chaos in a Hydrodynamic System”, *Phys. Rev. Lett.* **51**, 1442.
- Curry, J. H., and Yorke, J. A. (1978): “A Transition From Hopf Bifurcation to Chaos”. *Lect. Notes in Math.* **668**, 48. Springer, New York.
- Dubois, M., Berge, P., and Croquette, V. (1982): “Study of the Steady Convective Regimes Using Poincaré Sections”, *J. Phys. (Paris) Lett.* **43**, L 295.
- Grebogi, C., Ott, E., and Yorke, J. A. (1983 a), “Are Three-Frequency Quasi-Periodic Orbits to be Expected in Typical Nonlinear Systems?” *Phys. Rev. Lett.* **51**, 339.
- Hopf, E. (1942): “Abzweigungen einer periodischen Lösung von einer stationären Lösung eines Differentialgleichungssystems”, *Math. Naturwiss. Klasse, Sächs. Akademie der Wissenschaften, Leipzig*, **94**, 1.
- Landau, L. D. (1944): “On the Nature of Turbulence”, *C. R. Dokl. Acad. Sci. USSR* **44**, 311.
- Landau, L. D., and Lifshitz, E. M. (1959): *Fluid Mechanics*. Pergamon, Oxford.
- Libchaber, A., Fauve, S., and Laroche, C. (1983): “Two-Parameter Study of the Routes to Chaos”, *Physica* **7D**, 73.
- Marsden, L., and McCracken, M. (eds.) (1971): *The Hopf Bifurcation Theorem and its Applications*. Springer, Heidelberg-New York.
- Martin, S., Leber, H., and Martienssen, W. (1984): “Oscillatory and Chaotic States of the Electrical Conduction in BSN Crystals”, *Phys. Rev. Lett.* **53**, 303.
- Newhouse, S., Ruelle, D., and Takens, F. (1978): “Occurrence of Strange Axiom-A Attractors near Quasiperiodic Flow on t^m , $m \geq 3$ ”, *Commun. Math. Phys.* **64**, 35.
- Ruelle, D., and Takens, F. (1971): “On the Nature of Turbulence”, *Commun. Math. Phys.* **20**, 167.
- Smale, S. (1967): “Differentiable Dynamical Systems”, *Bull. Am. Math. Soc.* **13**, 747.
- Swinney, H. L., and Gollub, J. P. (1978): “The Transition to Turbulence”, *Phys. Today* **31** (8), 41.
- Swinney, H. L., and Gollub, J. P. (1979): *J. Fluid Mech.* **94**, 103.
- Swinney, H. L., and Gollub, J. P. (1980): *Hydrodynamic Instabilities and the Transition to Turbulence*. Springer, Heidelberg-New York.

The universal features in the transition from quasiperiodicity to chaos are investigated in the following articles:

- Arnold, V. I. (1965): “Small Denominators, I. Mappings of the Circumference Onto Itself”, *Trans. of the Am. Math. Soc.* **42**, 213.

- Bak, P., Bohr, T., Jensen, M. H., and Christiansen, P. V. (1984): “Josephson Junctions and Circle Maps”, *Solid State Commun.* **51**, 231.
- Bak, P., and Jensen, M. H. (1985): “Mode Locking and the Transition to Chaos in Dissipative Systems”, *Physica Scripta* **T 9**, 50.
- Cvitanovic, P. (1984): *Universality in Chaos*. Adam Hilger, Bristol.
- Cvitanovic, P., and Soderberg, B. (1985 a), “Scaling Laws for Mode Lockings in Circle Maps”, *Physica Scripta* **32**, 263.
- Cvitanovic, P., Jensen, M. H., Kadanoff, L. P., and Procaccia, I. (1985 b), “Renormalization, Unstable Manifolds and the Fractal Structure of Mode Locking”, *Phys. Rev. Lett.* **55**, 343.
- Guevara, M. R., Glass, L., and Shrier, A. (1981): “Phase Locking, Period Doubling Bifurcations and Irregular Dynamics in Periodically Stimulated Cardiac Cells”, *Science* **214**, 1350.
- Feigenbaum, M. J., and Haslacher, B. (1982): “Irrational Decimation and Path Integrals for External Noise”, *Phys. Rev. Lett.* **49**, 605.
- Feigenbaum, M. J., Kadanoff, L. P., and Shenker, S. J. (1982): “Quasiperiodicity in Dissipative Systems: A Renormalizations Group Analysis”, *Physica* **5D**, 370.
- Fein, A. P., Heutmaker, M. S., and Gollub, J. P. (1985): “Scaling at the Transition From Quasiperiodicity to Chaos in a Hydrodynamic System”, *Phys. Scr.* **T9**, 79.
- Greene, M. J. (1979): “A Method for Determining a Stochastic Transition”, *J. Math. Phys.* **20**, 1183.
- Hardy, G. H., and Wright, E. M. (1938): *Theory of Numbers*. Oxford Univ. Press, Oxford.
- Helleman, R. H. G. (ed.) (1980): “Proc. of the 1979 Int. Conf. on Nonlinear Dynamics”, *Ann. N. Y. Acad. Sci.* **603**.
- Hentschel, H. G. E., and Procaccia, I. (1983): “The Infinite Number of Generalized Dimensions of Fractals and Strange Attractors”, *Physica* **8D**, 435.
- Hu, B. (1983). “A Simple Derivation of the Stochastic Eigenvalue Equation in the Transition From Quasiperiodicity to Chaos”, *Phys. Lett.* **98A**, 79.
- Jensen, M. H., Bohr, T., Christiansen, P., and Bak, P. (1983 a), “Josephson Junctions and Circle Maps”, *Solid State Commun.* **51**, 231.
- Jensen, M. H., Bak, P., and Bohr, T. (1983 b), “Complete Devil’s Staircase, Fractal Dimension and Universality of Mode-Locking Structures”, *Phys. Rev. Lett.* **50**, 1637.
- Jensen, M. H., Bak, P., and Bohr, T. (1984): “Transition to Chaos by Interaction of Resonances in Dissipative Systems I, II”, *Phys. Rev. A* **30**, 1960, 1970.
- Jensen, M. H., Kadanoff, L. P., Libchaber, A., Procaccia, I., A Libchaber, and Stavans, J. (1985): “Global Universality at the Onset of Chaos: Results of a Forced Rayleigh–Bénard Experiment”, *Phys. Rev. Lett.* **55**, 2798.
- Martin, S., and Martienssen, W. (1986): “Circle Maps and Mode Locking in the Driven Electrical Conductivity of Barium Sodium Niobate Crystals”, *Phys. Rev. Lett.* **56**, 1522.
- Rand, D., Ostlund, S., Sethna, J., and Siggia, E. D. (1982): “Universal Transition From Quasiperiodicity to Chaos in Dissipative Systems”, *Phys. Rev. Lett.* **49**, 132, and *Physica* **8D**, 303 (1983).
- Shenker, S. J. (1982): “Scaling Behavior in a Map of a Circle Into Itself: Empirical Results”, *Physica* **5D**, 405.

- Vul, E. B., and Khanin, K. M. (1982): “On the Unstable Manifold of the Feigenbaum Fixed Point”, *Usp. Math. Nauk.* **37**, 173.
- Yeh, W. H., He, D. R., and Kao, Y. H. (1984): “Fractal Dimension and Self-Similarity of the Devil’s Staircase in a Josephson Junction Simulator”, *Phys. Rev. Lett.* **52**, 480.

Additional transition scenarios are discussed in:

- Campbell, D., and Rose, H. (eds.) (1983): “Order in Chaos: Proceedings of the International Conference in Los Alamos”, *Physica* **7D**.
- Gollub, J. P., and Benson, S. V. (1979): “Phase Locking in the Oscillations Leading to Turbulence”, in H. Haken (ed.): *Pattern Formation and Pattern Recognition*. Springer, Heidelberg-New York.
- Grebogi, C., Ott, E., and Yorke, J. A. (1983 b), “Crises, Sudden Changes in Chaotic Attractors and Transients to Chaos”, *Physica* **7D**, 181.
- Swinney, H. L. (1983): in D. Campbell and H. Rose (eds.): “Order in Chaos. Proceedings of the International Conference in Los Alamos”. *Physica* **7D**, 1.

Chapter 8: Regular and Irregular Motion in Conservative Systems

Besides the classic books by Poincaré (1982), Arnold and Avez (1968), Moser (1973), and Balescu (1975), which we mentioned (together with the article by Lorenz (1963) on dissipative systems) in the list of references for the introduction, there are several other excellent reviews and monographs on the irregular behavior of Hamiltonian systems:

- Arnold, V. I. (1978): *Mathematical Methods of Classical Mechanics*. Springer, Heidelberg-New York.
- Berry, M. V. (1978): in S. Jorna (ed.), “Topics in Nonlinear Dynamics”, *Am. Inst. Phys. Conf. Proc.*, Vol. **46**.
- Helleman, R. H. G. (1980): “Self-Generated Chaotic Behavior in Nonlinear Mechanics”, in E. G. D. Cohen (ed.): *Fundamental Problems in Statistical Mechanics*, Vol. 5. North-Holland Publ., Amsterdam.
- Lichtenber, A. J., and Liebermann, M. A. (1982): *Regular and Stochastic Motion*. Springer, Heidelberg-New York.

The KAM theorem is proved in:

- Arnold, V. I. (1963): “Small Denominators II, Proof of a Theorem of A. N. Kolmogorov on the Preservation of Conditionally-Periodic Motions Under a Small Perturbation of the Hamiltonian”, *Russ. Math. Surveys* **18**, 5.
- Kolmogorov, A. N. (1954): “On Conservation of Conditionally-Periodic Motions for a Small Change in Hamilton’s Function”, *Dokl. Akad. Nauk. USSR* **98**, 525.
- Moser, J. (1967): “Convergent Series Expansions of Quasi-Periodic-Motions”, *Math. Ann.* **169**, 163.

More references on this topic can be found in the book by Lichtenberg and Liebermann (1982).

Moser's twist map is discussed in:

- Moser, J. (1973): *Stable and Random Motions in Dynamical Systems*. Princeton University Press.

The Poincaré–Birkhoff theorem can be found in:

- Birkhoff, G. D. (1935): “Nouvelles Recherches Sur les Systems Dynamiques”, *Mem. Pont. Acad. Sci. Novi Lyncaei* **1**, 85.

Some applications and examples are given in:

- Anosov, D. V. (1969): “Geodesic Flows on Closed Riemannian Manifolds With Negative Curvature”, *Am. Math. Soc.*
- Arnold, V. I. (1964): “Instability of Dynamical Systems With Several Degrees of Freedom”, *Sov. Math. Dokl.* **5**, 581. In this article the so-called Arnold diffusion is introduced.
- Aubry, S., and Andre, C. (1980): in: *Proceedings of the Israel Physical Society*, Vol. **3**, p. 133.
- Benettin, G., and Streleyn, J. M. (1978): “Numerical Experiments on the Free Motion of a Point Mass, Moving in a Plane Convex Region: Stochastic Transition and Entropy”, *Phys. Rev.* **17A**, 773.
- Bunimovich, L. A. (1979): “On the Ergodic Properties of Nowhere Dispersing Billiards”, *Commun. Math. Phys.* **65**, 295.
- Gustavson, F. (1966): “On Constructing Formal Integrals of a Hamiltonian System Near an Equilibrium Point”, *Astron. J.* **71**, 670.
- Hénon, M., and Heiles, C. (1964): “the Applicability of the Third Integral of the Motion: Some Numerical Experiments”, *Astron. J.* **69**, 73.
- Sinai, Y. G. (1970): “Dynamical Systems With Elastic Reflections”, *Russ. Math. Surv.* **25**, 137.

The universal behavior of period doubling for two-dimensional conservative maps is treated in the review article by Helleman, which is mentioned under the general sources of the introduction and in:

- Bountis, T. C. (1981): “Period-Doubling Bifurcations and Universality in Conservative Systems”, *Physica* **3D**, 577.
- Greene, J. M., McKay, R. S., Vivaldi, F., and Feigenbaum, M. J. (1981): “Universal Behavior of Area-Preserving Maps”, *Physica* **3D**, 468.

There is a rapidly growing number of articles on renormalization schemes for area-preserving maps, some examples are:

- Escande, D. F., and Doveil, F. (1981): “Renormalization Method of Computing the Threshold of the Large Scale Stochastic Instability in Two Degrees of Freedom Hamiltonian Systems”, *J. Stat. Phys.* **26**, 257.
- Kadanoff, L. P. (1981): “Scaling for a Critical K.A.M. Trajectory”, *Phys. Rev. Lett.* **47**, 1641.
- McKay, R. S. (1983): “A Renormalization Group Approach to Invariant Circles in Area-Preserving Maps”, *Physica* **7D**, 283.

- McKay, R. S., Meiss, J. D., and Percival, I. C. (1984): “Stochasticity and Transport in Hamiltonian Systems”, *Phys. Rev. Lett.* **52**, 697.
- Shenker, S. J. and Kadanoff, L. P. (1982): “Critical Behavior of a K.A.M. Trajectory: I. Empirical Results”, *J. Stat. Phys.* **27**, 631.

More on the classification of chaos in conservative systems can be found in:

- Lebowitz, J. L. (1972) in S. A. Rice, K. F. Freed, J. C. Light (eds.), *Proc. of the Sixth IUPAP Conf. on Statistical Mechanics*. Univ. of Chicago Press, Chicago.
- Lebowitz, J. L., and Penrose, O. (1973): “Modern Ergodic Theory”, *Phys. Today* **26**(2).

Chapter 9: Chaos in Quantum Systems?

The problem of quantization of classical chaotic systems was already recognized by:

- Einstein, A. (1917): “Zum Quantensatz von Sommerfeld und Epstein”, *Verh. Dtsch. Phys. Ges.* **19**, 82.

There are several excellent reviews on the problem of stochasticity in quantum systems:

- Berry, M. V. (1983): in R. H. G. Helleman, and G. Ioos (eds.): *Chaotic Behavior of Deterministic Systems. Les Houches Summer School 1981*. North-Holland, Amsterdam.
- Casati, G. (1982): in H. Haken (ed.): *Evolution of Order and Chaos*. Springer, Heidelberg-New York.
- Chirikov, B. V. (1979): “A Universal Instability of Many-Dimensional Oscillator Systems”, *Phys. Rep.* **52**, 463.
- Zaslavsky, G. M. (1981): “Stochasticity in Quantum Systems”, *Phys. Rep.* **80**, 157.

More on laser photochemistry can be found in:

- Ben Shaul, A., Haas, Y., Kompa, K. L., and Levine, R. D. (1981): *Laser and Chemical Change*. Springer, Heidelberg-New York.

The quantized version of Arnold’s cat map was first studied by:

- Hannay, J. H., and Berry, M. V. (1980): “Quantization of Linear Maps on a Torus, Fresnel Diffraction by a Periodic Grating”, *Physica* **1D**, 267.

The quantum particle in a stadium was investigated by:

- McDonald, S. W., and Kaufman, A. N. (1979): “Spectrum and Eigenfunction for a Hamiltonian With Stochastic Trajectories”, *Phys. Rev. Lett.* **42**, 1189.

The kicked quantum rotator is discussed in the following articles:

- Casati, G., Chirikov, B. V., Izraelev, F. M., and Ford, J. (1977): in G. Casati, and J. Ford (eds.): *Stochastic Behavior in Classical and Quantum Hamiltonian Systems. Lecture Notes in Physics* **93**, Springer, Heidelberg-New York.

- Grempel, D. R., Fishman, S., and Prange, R. E. (1982): “Localization in an Incommensurate Potential: An Exactly Solvable Model”, *Phys. Rev. Lett.* **49**, 833.
- Fishmann, S., Grempel, D. R., and Prange, R. E. (1982): “Chaos Quantum Recurrences and Anderson Localization”, *Phys. Rev. Lett.* **49**, 509.
- Hogg, T., and Huberman, B. A. (1982): “Recurrence Phenomena in Quantum Dynamics”, *Phys. Rev. Lett.* **48**, 711.
- Hogg, T., and Huberman, B. A. (1983): “Quantum Dynamics and Nonintegrability”, *Phys. Rev.* **28 A**, 22.
- Izraelev, F. M., and Shepelyanskii, D. L. (1980): “Quantum Resonance for a Rotator in a Nonlinear Periodic Field”, *Theor. Math. Phys.* **43**, 417.
- Peres, A., (1982): “Recurrence Phenomena in Quantum Dynamics”, *Phys. Rev. Lett.* **49**, 1118.
- Schuster, H. G. (1983): “Absence of Quasiperiodicity in a Kicked Quantum Rotator and a New Delocalization Transition”, *Phys. Rev.* **28 B**, 381.

The electron localization problem has been investigated for the general case by:

- Anderson, P. W. (1958): “Absence of Diffusion in Certain Random Systems”, *Phys. Rev.* **103**, 1492.

and especially for the one-dimensional case by:

- Ishii, K. (1973): “Localization of Eigenstates and Transport Phenomena in One-Dimensional Disordered Systems”, *Progr. Theor. Phys. Suppl.* **53**, 77.

Some more recent references on the question of chaos in quantum systems are:

- Berry, M. V., and Tabor, M. (1977): “Level Clustering in the Regular Spectrum”, *Proc. Roy. Soc. (London)* **A 356**, 375.
- Blümel, R., and Smilansky, U. (1984): “Quantum Mechanical Suppression of Classical Stochasticity in the Dynamics of Periodically Disturbed Surface Electrons”, *Phys. Rev. Lett.* **52**, 137.
- Bohigas, O., Giannoni, M. J., and Schmit, C. (1984): “Characterization of Chaotic Quantum Spectra and Universality of Level Fluctuation Laws”, *Phys. Rev. Lett.* **52**, 1.
- Casati, G., (ed.) (1985): *Chaotic Behavior in Quantum Systems. Proc. 1983 Como Conf. on Quantum Chaos*. Plenum Press, New York.
- Gutzwiller, M. C. (1983): “Stochastic Behavior in Quantum Scattering”, *Physica* **7D**, 341.
- Gutzwiller, M. C. (1990): “Chaos in Classical and Quantum Mechanics”, Springer, New York.
- Haake, F. (1991): “Quantum Signatures of Chaos”, Springer, New York.
- Reichl, L. E. (1992): “The Transition to Chaos in Conservative Systems: Quantum Manifestations”, Springer Verlag, New York.
- Seligmann, T. H., and Nishioka, H. (eds.) (1986): *Quantum Chaos and Statistical Nuclear Physics*. Springer, Berlin-Heidelberg-New York.
- Stöckmann, H. J. (1993): “Mikrowellenbillards: Chaos in der Quantenmechanik”, *Phys. uns. Zeit* **24**, 200.

- Stöckmann, H. J., and Stein, J. (1990): “Quantum’ Chaos in Billiards Studied by Microwave Absorption”, *Phys. Rev. Lett.* **64**, 2215.
- Stein, J., and Stöckmann, H. J. (1991): “Experimental Determination of Billiard Wave Functions”, *Phys. Rev. Lett.* **68**, 2867.
- Stöckmann, H. J. (1999): *Quantum Chaos : an Introduction*. Cambridge University Press, Cambridge.

Chapter 10: Controlling Chaos

General references concerning control problems:

- Chen, C.-T. (1999): *Linear System Theory and Design*. Oxford University Press.
- Dyson, F. (1988): *Infinite in All Directions*, p. 183. Harper and Row, New York.
- Farquhar, R., Muhonen, D., and Church, L. C. (1985): “Trajectories and Orbital Manœuvres for the ISEE-3/ICE Comet Mission”, *J. Astronaut. Sci.* **33**, 235.
- Schuster, H. G. (ed.) (1999): *Handbook of Chaos Control*. Wiley–VCH, Weinheim-Berlin.
- Slotine, J.-J. E. and Li, W. (1991): *Applied Nonlinear Control*. Prentice Hall, New York.

The OGY scheme and related aspects are discussed in:

- Hübinger, B., Doerner, R., and Martienssen, W. (1993): “Local Control of Chaotic Motion”, *Z. Physik* **B 90**, 103.
- Schuster, H. G., Niebur, E., Hunt, E. R., Johnson, G. A., and Löcher, M. (1996): “Parametric Feedback Resonance in Chaotic Systems” *Phys. Rev. Lett.* **76**, 400.
- Ott, E., Grebogi, C., and Yorke, J. A. (1990): “Controlling Chaos”, *Phys. Rev. Lett.* **64**, 1196.
- Petrov, V., Gaspar, V., Masere, L., and Showalter, K. (1993): “Controlling Chaos in the Belousov–Zhabotinsky Reaction”, *Nature* **361**, 240.
- Shinbrot, T., Grebogi, C., Ott, E., and Yorke, J. A. (1993): “Using Small Perturbations to Control Chaos”, *Nature* **363**, 411.

More details concerning time-delayed feedback schemes and their application can be found in:

- Kittel, A., Parisi, J., and Pyragas, K. (1995): “Delayed Feedback Control of Chaos by Self-Adapted Delay Time”, *Phys. Lett.* **198 A**, 433
- Pyragas, K. (1992): “Continuous Control of Chaos by Self-Controlling Feedback”, *Phys. Lett.* **170 A**, 421.
- Pyragas, K. (2001): “Control of Chaos via an Unstable Delayed-Feedback Controller”, *Phys. Rev. Lett.* **86**, 2265.
- Schuster, H. G., and Stemmler, M. B. (1997): “Control of Chaos by Oscillating Feedback”, *Phys. Rev. E* **56**, 6410.
- Socolar, J. E. S., Sukow, D. W., and Gauthier, D. J. (1994): “Stabilizing Unstable Periodic Orbits in Fast Dynamical Systems”, *Phys. Rev. E* **50**, 3245.

- Just, W., Benner, H., and Schöll, E. (2003): “Control of Chaos by Time-Delayed Feedback: a Survey of Theoretical and Experimental Aspects”, in B. Kramer (ed.): *Advances in Solid State Physics*, Vol. **43**, Springer, Heidelberg .

Experimental realizations of time-delayed feedback control are described in:

- Benner, H., and Just, W. (2002): “Control of Chaos by Time-Delayed Feedback in High Power Ferromagnetic Resonance Experiments”, *J. Kor. Phys. Soc.* **40**, 1046.
- Bielawski, S., Derozier, D., and Glorieux, P. (1993): “Experimental Characterization of Unstable Periodic Orbits by Controlling Chaos”, *Phys. Rev. A* **47**, R2492.
- Bielawski, S., Derozier, D., and Glorieux, P. (1994): “Controlling Unstable Periodic Orbits by a Delayed Continuous Feedback”, *Phys. Rev. E* **49**, R971.
- Gauthier, D. J., Sukow, D. W., Concannon, H. M., and Socolar, J. E. S. (1994): “Stabilizing Unstable Periodic Orbits in a Fast Diode Resonator Using Continuous Time-Delay Autosynchronization”, *Phys. Rev. E* **50**, 2343.
- Hall, K., Christini, D. J., Tremblay, M., Collins, J. J., L. Glass, L., J. Billette, J. (1997): “Dynamic Control of Cardiac Alternans”, *Phys. Rev. Lett.* **78**, 4518.
- Lüthje, O., Wolff, S., and Pfister, G. (2001): “Control of Chaotic Taylor–Couette Flow With Time-Delayed Feedback”, *Phys. Rev. Lett.* **86**, 1745.
- Parmananda, P., Madrigal, R., Rivera, M., Nyikos, L., Kiss, I. Z., and Gáspár, V. (1999): “Stabilization of Unstable Steady States and Periodic Orbits in an Electrochemical System Using Delayed-Feedback Control”, *Phys. Rev. E* **59**, 5266.
- Pierre, T., Bonhomme, G., and Atipo, A. (1996): “Controlling the Chaotic Regime of Nonlinear Ionization Waves Using Time-Delay Autosynchronization Method”, *Phys. Rev. Lett.* **76**, 2290.

Unstable Periodic Orbits:

- Poincaré, H. (1892): *Les methodes nouvelles de la mécanique céleste*, Gauthier Villers, Paris.
- Ruelle, D. (1978): *Statistical Mechanics, Thermodynamic Formalism*, Addison Wesley, Reading Massachusetts.
- Artuso, R., Aurell, E., and Cvitanovich, P. (1990): “Recycling of Strange Sets I, II”, *Nonlinearity* **3**, 325.
- Kadanoff, L. P., and Tang, C. (1984): “Escape from strange repellers”, *Proc. Natl. Acad. Sci. USA* **81**, 1276.
- Edwards, H. M. (1974): *Riemann’s Zeta Function*, Academic Press, New York.

Chapter 11: Synchronization of Chaotic Systems

An excellent and extensive introduction into the subject of synchronization:

- Pikovsky, A., Rosenblum, M., and Kurths, J. (2001): *Synchronization: A universal Concept in Nonlinear Sciences*, Cambridge University Press, Cambridge UK.

References concerning on–off intermittency and Milnor attractors:

- Fujisaka, H. and Yamada, Y. (1985): “A new Intermittency in Coupled Dynamical Systems” *Prog. Theor. Phys.* **74**, 918.
- Glendinning, P. (2001): “Milnor Attractors and Topological Attractors of a Piecewise Linear map”, *Nonlin.* **14**, 239.
- Heagy, J. F., Platt, N., and Hammel, S. M. (1994): “Characterization of on–off Intermittency”, *Phys. Rev. E* **49**, 1140.
- Ott, E., Alexander, J. C., Kan, I., Sommerer, J. C., and Yorke, J. A. (1994): “The Transition to Chaotic Attractors With Riddled Basins”, *Physica* **76 D**, 384.
- Pikovsky, A. S., and Grassberger, P. (1991): “Symmetry Breaking of Coupled Chaotic Attractors”, *J. Phys. A* **24**, 4587.
- Yamada, Y. and Fujisaka, H. (1986): “Intermittency Caused by Chaotic Modulation. I. Analysis With a Multiplicative Noise Model” *Prog. Theor. Phys.* **76**, 582.

References concerning synchronization of chaos in master–slave configurations, generalized synchronization, and strange nonchaotic attractors:

- Cuomo, K. M. and Oppenheim, A. V. (1993): “Circuit Implementation of Synchronized Chaos With Applications to Communications”, *Phys. Rev. Lett.* **71**, 65.
- Ding, W. X., Deutsch, H., Dinklage, A., and Wilke, C. (1997): “Observation of a Strange Nonchaotic Attractor in a Neon Glow Discharge”, *Phys. Rev. E* **55**, 55.
- Ditto, W. L., Spano, M. L., Savage, H. T., Rauseo, S. N., Heagy, J., and Ott, E. (1990): “Experimental Observation of a Strange Nonchaotic Attractor”, *Phys. Rev. Lett.* **65**, 533.
- Grebogi, C., Ott, E., Pelikan, S., and Yorke, J. A. (1984): “Strange Attractors That are not Chaotic”, *Physica* **13D**, 261.
- Prasad, A., Mehra, V., and Ramaswamy, R. (1998): “Strange Nonchaotic Attractors in the Quasiperiodically Forced Logistic map”, *Phys. Rev. E* **57**, 1576.
- Pecora, L. M. and Carroll, T. L. (1990): “Synchronization in Chaotic Systems”, *Phys. Rev. Lett.* **64**, 821.
- Rulkov, N. F., Sushchik, M. M., Tsimring, L.S, and Abarbanel, H. D. I. (1995): “Generalized Synchronization of Chaos in Directionally Coupled Chaotic Systems”, *Phys. Rev. E* **51**, 51

Chapter 12: Spatiotemporal Chaos

Theory of spatiotemporally complex models:

- Aranson, I. S. and Kramer, L. (2002): “The World of the Complex Ginzburg–Landau Equation”, *Rev. Mod. Phys.* textbf74, 99.
- Chazottes, J.-R. and Fernandez, B. (2005): “Dynamics of Coupled map Lattices and of Related Spatially Extended Systems”, (in preparation).
- Cross, M. C. and Hohenberg, P. C. (1993): “Pattern-Formation Outside of Equilibrium”, *Rev. Mod. Phys.* **65**, 851.
- Eckmann, J.-P., and Ruelle, D. (1985): “Ergodic Theory of Chaos and Strange Attractors”, *Rev. Mod. Phys.* **57**, 1115.

- Kaneko, K (1989): “Pattern Dynamics in Spatiotemporal Chaos”, *Physica* **34 D**, 1.
- Kaneko, K (1993): “Theory and Applications of Coupled map Lattices”, Wiley, Chichester.
- Kuramoto, Y. (1984): “Chemical Oscillations, Waves and Turbulence”, Springer, Berlin.
- Gielis, G. and R. S. MacKay, R. S. (2000): “Coupled map Lattices With Phase Transition”, *Nonlin.* **13**, 867.
- Kuramoto, Y. and Tsuzuki T. (1976): “Persistent Propagation of Concentration Waves in Dissipative Media Far From Thermal Equilibrium”, *Prog. Theor. Phys.* **55**, 356.
- Radons, G (2004): “Disordered Dynamical Systems”, in Radons G., Just, W., and Häussler, P. (eds.): *Collective Dynamics of Nonlinear and Disordered Systems*, Springer, Berlin.
- Strogatz, S. H. (2001): “From Kuramoto to Crawford: Exploring the Onset of Synchronization in Populations of Coupled Oscillators”, *Physica* **143 D**, 1.
- Yanagita, T. and Kaneko, K. (1995): “Rayleigh–Bénard Convection Patterns, Chaos, Spatiotemporal Chaos and Turbulence” *Physica* **82 D**, 288.

References concerning spatiotemporal Liapunov analysis:

- Deissler, R. J. and Kaneko, K. (1987): “Velocity-Dependent Liapunov Exponents as a Measure of Chaos for Open-Flow Systems”, *Phys. Lett.* **119 A**, 397.
- Kaneko, K. (1992): “Propagation of Disturbances, co-Moving Liapunov Exponent and Path Summation”, *Phys. Lett.* **170 A**, 210.
- Lepri, S., Politi, A., and Torcini, A. (1997): “Chronotopic Liapunov Analysis: II. Toward a Unified Approach”, *J. Stat. Phys.* **88**, 31.
- Politi, A. and Torcini, A. (1992): “Periodic Orbits in Coupled Hénon Maps: Liapunov and Multi-fractal Analysis”, *Chaos* **2**, 293.

Applications of spatiotemporal chaos:

- Bohr, T., van Hecke, M., Mikkelsen, R., and Ipsen, M. (2001): “Breakdown of Universality in Transitions to Spatiotemporal Chaos”, *Phys. Rev. Lett.* **86**, 5482.
- Chaté, . and Manneville, P. (1988): “Spatio-Temporal Intermittency in Coupled map Lattices”, *Physica* **32 D**, 409.
- Forster, C., Hirschl, R., Posch, H. A., and Hoover, W. G. (2004): “Perturbed Phase-Space Dynamics of Hard-Disk Fluids”, *Physica* **187 D**, 294.
- Frisch, U. (1995): “Turbulence: the Legacy of A. N. Kolmogorov”, Cambridge Univ. Press, Cambridge.
- Kaneko, K. (1985): “Spatiotemporal Intermittency in Coupled map Lattices”, *Prog. Theor. Phys.* **74**, 1033.
- Posch, H. A. and Forster, C. (2004): “Disordered Dynamical Systems”, in Radons G., Just, W., and Häussler, P. (eds.): *Collective Dynamics of Nonlinear and Disordered Systems*, Springer, Berlin.
- Ruelle, D. (1999): “Smooth Dynamics and New Theoretical Ideas in Nonequilibrium Statistical Mechanics”, *J. Stat. Phys.* **95**, 393.

Outlook

General:

- Abraham, N. B., Gollub, J. P., and Swinney, H. L. (1984): “Testing Nonlinear Dynamics”, *Physica* **11D**, 252.
- Benedek, G., Bilz, G., and Zeyher, R. (1984): “Statics and Dynamics of Nonlinear Systems”, *Springer Series in Solid-State Sciences* **47**, Springer, Berlin-Heidelberg-New York.
- Berry, M. V. (1978): in S. Yorna (ed.), “Topics in Nonlinear Dynamics”, *Am. Inst. Phys. Conf. Proc.*, Vol. **46**.
- Kaneko, K. (1986): *Collapse of Tori and Genesis of Chaos in Dissipative Systems*. World Scientific Publishing Co., Singapore.
- Schuster, H. G. (2002): *Complex Adaptive Systems*. Scator Verlag, Saarbrücken.

Coupled Systems:

- Bishop, A. R., Fesser, K., Lomdahl, P. S., Kerr, W. C., Trullinger, S. E., and Williams, M. B. (1983): “Coherent Spatial Structures Versus Time Chaos in a Perturbed Sine–Gordon System”, *Phys. Rev. Lett.* **50**, 1095.
- Kuramoto, Y. (1977): “Chemical Waves and Chemical Turbulence”, in H. Haken (ed.): *Synergetics*. Springer, Berlin-Heidelberg-New York.
- Vidal, C., and Pacault, A. (1981): *Nonlinear Phenomena in Chemical Dynamics*. Springer, Berlin-Heidelberg-New York.
- Winfree, A. T. (1980): “The Geometry of Biological Time”, *Biomathematics* **8**, Springer, Berlin-Heidelberg-New York.

Turbulence:

- Frisch, U. (1995): *Turbulence : the Legacy of A. N. Kolmogorov*. Cambridge University Press, Cambridge.
- Ruelle, D. (1983): “Five Turbulent Problems”, *Physica* **7D**, 40.
- Sacharov V. E., L'vov V. S., Falkovich, G. (1992): *Kolmogorov Spectra of Turbulence*, in Springer Series in Nonlinear Dynamics. Springer, Berlin.

Quantum Systems:

- Ackerhalt, J. R., Milonni, P. W., and Shih, M. L. (1985): “Chaos in Quantum Optics”, *Phys. Rep.* **128**, 207.
- Graham, R. (1984): “Chaos in Lasers”, in E. Frehland (ed.): *Synergetics – From Microscopic to Macroscopic Order*. Springer, Berlin-Heidelberg-New York.
- Elgin, J. N., and Sarkar, S. (1984): “Quantum Fluctuations and the Lorenz Strange Attractor”, *Phys. Rev. Lett.* **52**, 1215.
- Misra, B., and Prigogine, I. (1980): “One the Foundations of Kinetic Theory”, *Suppl. Progr. Theor. Physics* **69**, 101.

Random Numbers:

- De Long, H. (1970): *Randomness and Gödel's Incompleteness Theorem*. Addison-Wesley, Reading, MA.

Biology:

- Hess, B., and Markus, M. (1984): "Time Pattern Transitions in Biochemical Processes", in E. Frehland (ed.): *Synergetics – From Microscopic to Macroscopic Order*. Springer, Berlin-Heidelberg-New York.
- Schuster, P. (ed.) (1984): "Stochastic Phenomena and Chaotic Behavior in Complex Systems", *Springer Series in Synergetics* **21**, Springer, Berlin-Heidelberg-New York.

Cellular Automata:

- Wolfram, S. (1985): "Undecidability and Intractability in Theoretical Physics", *Phys. Rev. Lett.* **54**, 735.
- Frisch, U., Hasslacher, B., and Pomeau, Y. (1986): "Lattice-Gas Automata for the Navier–Stokes Equation", *Phys. Rev. Lett.* **56**, 1505.
- Farmer, D., Toffoli, T., and Wolfram, S. (1984): "Cellular Automata", *Physica* **10D**.

Nonlinear Dynamics and Statistical Mechanics:

- Beck C., Schlögl F. (1995): *Thermodynamics of Chaotic Systems: an Introduction*. Cambridge University Press, Cambridge.
- Dorfman, R. (1999): *An Introduction to Chaos in Nonequilibrium Statistical Mechanics*. Cambridge University Press, Cambridge.
- Gaspard P. (1998): *Chaos, Scattering and Statistical Mechanics*. Cambridge University Press, Cambridge.
- Hoover, W. G. (1999): *Time Reversibility, Computer Simulation, and Chaos*. World Scientific, Singapore.

Applied Nonlinear Dynamics and Time Series Analysis:

- Abarbanel, H. D., Rabinovich, M. I., Sushchik, M. M. (1993): *Introduction to Nonlinear Dynamics for Physicists*, World Scientific, Singapore.
- Kantz H., Schreiber T. (1999): *Nonlinear Time Series Analysis*. Cambridge University Press, Cambridge.

Textbooks on Nonlinear Stochastic Systems:

- Gardiner, C. W. (1985): *Handbook of Stochastic Methods for Physics, Chemistry and the Natural Sciences*. Springer, Berlin.
- Horsthemke, W., Lefever, R. (1984): *Noise-Induced Transitions : Theory and Applications in Physics, Chemistry and Biology*. Springer, Berlin.
- Moss F., McClintock P. V. E. (Eds.) (1989): *Noise in Nonlinear Dynamical Systems, Vol. 1–3*. Cambridge University Press, Cambridge.

- Risken, H. (1989): *The Fokker–Planck Equation : Methods of Solution and Applications*. Springer, Berlin.

Graduate and Undergraduate Textbooks on Nonlinear Dynamics:

- Abraham, R. H., and Shaw, C. D. (1983): *Dynamics: The Geometry of Behavior*, Aerial Press Santa Cruz, C. A.
- Barnsley, M. F. (1988): *Fractals Everywhere*, Academic Press, Orlando, FL.
- Cvitanovich, P. (ed.) (1989): *Universality in Chaos*, 2nd ed., Adam Hilger, Bristol.
- Devaney, R. L. (1989): *An Introduction to Chaotic Dynamical Systems*, 2nd ed., Addison Wesley, Redwood City, CA.
- Falconer, K. (1990): *Fractal Geometry: Mathematical Foundations and Applications*, Wiley, Chichester, England.
- Feder, J. (1988): *Fractals*, Plenum N.Y.
- Glass, L., and MacKey, M. C. (1990): *From Clocks to Chaos*, Princeton Univ. Press, Princeton, N.J.
- Gutzwiller, M. C. (1990): *Chaos in Classical and Quantum Mechanics*, Springer, New York.
- Hao, Bai-Lin (ed.) (1990): *Chaos I, II*, World Scientific, Singapore.
- Haake, F. (1991): *Quantum Signatures of Chaos*, Springer, New York.
- Jackson, E. A. (1990): *Perspectives of Nonlinear Dynamics, Vols. 1 and 2*, MIT Press, Cambridge MA.
- Lichtenberg, A. J., and Liebermann, M. A. (1992): *Regular and Chaotic Dynamics*, Springer, New York.
- Manneville, P. (1990): *Dissipative Structures and Weak Turbulence*, Academic Press, Boston.
- Moon, F. C. (1992): *Chaotic and Fractal Dynamics: An Introduction for Applied Scientists and Engineers*, Wiley, New York.
- Ott, E. (1993): *Chaos in Dynamical Systems*, Cambridge Univ. Press.
- Reichl, L. E. (1992): *The Transition to Chaos in Conservative Systems: Quantum Manifestations*, Springer Verlag, New York.
- Sagdeev, R. Z., Usikov, D. A., and Zaslavsky, G. M.: *Nonlinear Physics*, Harwood Acad. Publ., NY.
- Schroeder, M. (1991): *Fractals, Chaos, Power Laws*, Freeman, N.Y.
- Strogatz, S. H. (1994): *Nonlinear Dynamics and Chaos*, Addison Wesley, Reading MA.
- Weiss, C. O., and Vilaseca, R. (1991): *Dynamics of Lasers*, VCH, Weinheim, Germany.
- Winfree, A. T. (1987): *When Time Breaks Down*, Princeton University Press, Princeton, N.J.

Index

- action-angle variables, 163
- almost periodic function, 192
- Arnold diffusion, 171
- Arnold's tongues, 138
- arrowhead curve, 49
- aspect ratios, 157, 235
- asteroid distribution, 174
- attractor, 38, 121
 - Feigenbaum, 49, 55, 113
 - Hénon, 95, 111, 112, 119
 - Lorenz, 90, 111
 - strange, 89–125, 134, 135
- autocorrelation function, 10, 12, 177
- autonomous differential equation, 14, 16

- backfolding, 20, 92
- baker's transformation, 92, 120, 178, 211
- barium-sodium-niobate (BSN), 132, 133, 153
- basins of attraction, 91, 92, 122
- Belousov–Zhabotinsky reaction, 11, 12, 196
- Bénard instability, 9–11, 233–235
 - Feigenbaum route, 65
 - intermittency, 86, 88
 - quasiperiodicity → chaos, 156
 - strange attractors, 129, 134
 - three-frequency quasiperiodicity, 132
- Bernoulli shift, 19–21
- bifurcations, 248
 - blow-out, 209
 - crises, 158
 - Hopf, 127
 - pitchfork, 37
 - tangent, 70
- birefringence pattern, xiii
- blow-out bifurcation, 209
- boundaries of basins, xiv, 122–125
- Brownian motion, 29

- bursts, 69
- butterfly effect, 2

- canonical transformation, 163
- cantor set, 49
- cardiac cells, 154, 199
- Cassini division, xiii, 174
- cat map, 174
 - open, 188
 - quantum version, 184
- cavitation noise, xiii, 66, 67
- cellular automata, 218
- chain rule, 22, 248
- chaos, 1
 - characterization, 21
 - criteria for, 10, 13
 - mechanism, 20–21
 - spatiotemporal, 221
- chaotic bands, 59
- chemical reactions, 10–12
- chronotopic analysis, 225
- circle map, 137–141
 - experiments, 150–157
- coarse graining, 15, 183
- coexistence of regular and irregular motion, 163–174
- complex Ginzburg–Landau equation, 220
- conservative systems, 161
- continued fractions, 142
- control parameters, 14, 132, 157
- control theory, 196
- controlling chaos, 193–203
- correlation dimension, 111
- correlation function, 10, 12, 27
 - classical systems, 177
 - intermittency, 80
 - logistic map, 63
 - triangular map, 28

- correlation integral, 110, 118
- correlation length, 238, 239
- coupled chaotic systems, 207
- coupled oscillators, 218
- coupled map lattice, 217
- crisis, 158
- critical exponents, *see* scaling
 - surface, 62
 - temperature, 62
- cycles, 14, 40, 145
 - primitive, 255

- decimation method, 55, 240–243
- defect chaos, 220
- deterministic chaos, 1
 - diffusion, 29, 187
- devil's staircase, 140, 149, 153
- dimensions of strange attractors, 102
- dissipation scale, 221, 226
- dissipative maps, 14, 92
 - flows, 14, 89
- distribution of fractal dimensions, 109, 114
- doubling transformation, 34
 - circle maps, 145
 - intermittency, 75
 - modified version, 147, 148
 - quadratic maps, 41, 145
- Duffing oscillator, 123

- eigenvalues, 44, 45, 146, 236
 - cat map, 174
 - elliptic fixed point, 247
 - Frobenius–Perron operator, 250
 - Hopf bifurcations, 128
 - hyperbolic fixed point, 246
 - intermittency, 70, 77, 87
 - Liouville operator, 178–179
 - Schrödinger equation, 184, 186
 - time-evolution operator, 186, 189
- embedding dimension, 104, 112
- entropy, 96
- ergodicity, 5, 162
 - mechanism, 20
 - on a torus, 165
 - spectrum of the Liouville operator, 177

- Farey tree, 140
- feedback, 33
- Feigenbaum attractor, 49, 55
 - constants, 36, 249
 - route, 33–37
- Fibonacci numbers, 142
- fixed point, 14, 23
 - doubling operator, 42, 62, 76, 146, 148
 - elliptic, 162, 169, 247
 - hyperbolic, 169, 246
 - stability of, 23, 37, 236
 - unstable, 194
- Floquet multiplier, 199
- flows, 89
- Fourier modes, 221
- fractals, 49, 56
- Frobenius–Perron equation, 26

- Gaussian correlations, 29, 52, 240
- generalized Bernoulli maps, 222
- generalized dimensions, 106–114
 - entropies, 103
- generalized synchronization, 212
- generating function, 165
- geodesic motion, 180
- Ginzburg–Landau functional, 62
- golden mean, 142

- Hamilton–Jacobi equation, 165
- harmonic oscillator, 163, 179
- Hausdorff dimension, 48, 106, 120, 135
 - baker's transformation, 93
 - Feigenbaum attractor, 48, 55
 - Hénon map, 95
 - Lorenz attractor, 91
- Hénon attractor, 95
 - Heiles system, 12–13, 173
 - map, 17, 94–95
- hierarchy of classical chaos, 176
 - of levels of description, 15
- Hilbert transform, 214
- homoclinic point, 170–171
- Hopf bifurcation, 127

- inertial range, 221, 226
- information capacity, 243
 - dimension, 107
 - gain, 244
 - loss, 22
- integrable systems, 163
- integral scale, 221, 226
- intermittency corrections, 226

- intermittency route, 69
- invariant measure, 25
 - classical systems, 179
 - logistic map, 60
 - triangular map, 27
- Ising model, 238
- iterates of the logistic map, 35

- Josephson junctions, 2
- Julia set, 122

- K-systems, 177, 180
- KAM theorem, 4, 166–170
- Kaplan–Yorke conjecture, 120
- Koch’s curve, 49
- Kolmogorov entropy, 96–100, 135
 - fluctuations around, 115
 - Liapunov exponents, 97–100
 - lower bound, 118
- Kuramoto–Sivashinsky equation, 220

- laminar region, 70
 - distribution of, 82, 84–86
 - length of, 73
- Landau’s route, 128
- laser, 2
- Lebesgue spectrum, 177
- Legendre transformation, 102, 225
- level clustering, 186
 - repulsion, 186
- Li–Yorke theorem, 59
- Liapunov exponent, 21, 97, 135
 - baker’s transformation, 120
 - circle map, xiv, 153
 - computation, 99
 - conditional, 211
 - K-entropy, 97–100
 - Kaplan–Yorke conjecture, 121
 - logistic map, 35, 53, 62
 - Lorenz model, 101
 - pendulum, xiv, 153
 - scaling behavior, 54, 243
 - spectrum, 222, 228
 - triangular map, 25
 - vectors, 222, 229
 - velocity-dependent, 223
- limit cycle, 121, 127–131
- Liouville operator, 26, 178, 186
- Liouville’s theorem, 161

- localization problem, 189, 191
- logistic map, 17, 33–60, 194–196
 - and intermittency, 72
 - in the complex plane, 122–125
- Lorenz attractor, 90
 - model, 10, 233

- Mackey–Glass equation, 103
- magnetization, 55, 62
- Mandelbrot’s set, xiv, 125
- maps, 14, 92
 - Arnold’s cat, 174
 - Chirikov, 18, 187–188
 - circle, 137–141
 - Hénon, 17, 94–95, 245
 - logistic, 17, 33–60, 72, 122, 194–196
 - Moser’s twist, 168
 - periodic, 29
 - piecewise linear, 19
 - quadratic, 33–60
 - tent, 115
 - triangular, 23
- mechanism for chaos, 20–21
 - for intermittency, 69–74
- mixing, 175
- mode locking, 136, 139, 151
- Moser’s twist map, 168

- Navier–Stokes equation, 15, 225
- Newton’s algorithm, 122
- nodal curves, 187
- noise, 34
 - $1/f$, 79–84
 - intermittency, 79
 - logistic map, 52–55, 240
 - renormalization group, 240
 - separation from deterministic chaos, 112
- nonlinear systems, 2, 14

- on-off intermittency, 209
- order parameter, 25, 62
- oscillator
 - driven electronic, xiii, 64, 87
 - Duffing, 123
 - harmonic, 163, 179

- P–Manneville route, 69
- pairing rule, 228
- parameter space, 62

- partial synchronization, 219
- particle accelerator, 2
- path integrals, 55, 240–243
- pendulum, 7, 151
- period doubling, 39, 194
 - in conservative systems, 171, 246
 - parallels to phase transitions, 61–63
- phase portrait, xiii, 65
- phase synchronization, 214
- phase transitions, 62, 219, 227, 238
- phase turbulence, 220
- phase variable, 213
- photochemistry, 184
- pitchfork bifurcation, 37, 237
- plasmas, 2
- Poincaré map, 13, 136, 168
 - Bénard experiment, 134
 - Hénon Heiles system, 95, 173
 - intermittency, 71, 85, 87
 - Taylor experiment, 135
- Poincaré map, 15
- Poincaré–Bendixson theorem, 91, 130
- Poincaré–Birkhoff theorem, 169
- Pomeau–Manneville route, 74
- population dynamics, 33
- power spectrum, 9, 10, 12
 - $1/f$ noise, 79–84
 - BSN crystal, 133
 - Bénard experiment, 10, 64, 129, 132
 - cavitation noise, 66, 67
 - circle map, 144
 - electronic oscillator, 66
 - logistic map, 50–52, 64–66
- Prandtl number, 235
- prediction time, 100
- primitive cycles, 255
- propagation of signals, 223
- Pyragas scheme, 199
 - experimental, 203
 - extended, 201
- quantum chaos, 183–192
 - resonance, 190
- quasiperiodicity, 136–150
 - and period doubling, 145
- random forces, 20
- Rayleigh number, 9, 235
- reconstruction of an attractor, 103–106
- recurrent motion, 186
- relevant eigenvalue, 46, 61
- renormalization group
 - circle map, 141–150
 - external noise, 240–243
 - intermittency, 75–79, 82
 - Ising model, 238
 - logistic map, 41–46
 - phase transitions, 62
- resonances, 166, 215
- Reynolds number, 225
- rhythmic control, 200
- riddled basins, 210
- rings of Saturn, xiii, 174
- Rössler model, 213
- rotator, 16, 187
- routes of chaos, 157
- Ruelle zeta function, 256
- Ruelle–Takens–Newhouse route, 129–131, 158
- saddle point approximation, 109, 241
- Sarkovskii’s theorem, 59
- scaling behavior
 - global, 146–150
 - local, 141–146
- scaling for
 - area-preserving maps, 249
 - circle map, 143
 - correlation function, 63
 - diffusion, 31
 - external noise, 52, 54, 243
 - KAM-trajectory, 167
 - laminar length, 74, 78, 87
 - Liapunov exponent, 54, 62, 243
 - quadratic maps, 36–37, 52
- scaling indices, 102, 114
- Schwarzian derivative, 40, 236
- secure communication, 211
- self-similarity, xiv, 46, 48, 49, 61, 124, 170
- sensitive dependence on initial conditions, 2, 20, 21, 91, 97, 100, 171, 193
- sensitive parameter dependence, 55
- Shannon’s measure of information, 243
- shift from tangency, 78
- Sierpinski sponge, 49
- Sinai’s billiard, 181
- slaving principle, 15
- space-craft, 193

- spatiotemporal intermittency, 227
- stability criterion, 24, 236, 246
- stable manifold, 62, 197
- stadium problem, 180, 186
- stimulated heart cells, xiii, 2, 154
- strange attractor, 89–125
 - definition, 89
 - dimensions, 102
 - examples, 90, 92, 95, 134, 135
 - nonchaotic, 212
 - onset of turbulence, 127
 - periodic orbit expansion, 250
- stretching, 20, 92
- stroboscopic picture, 17
- strong synchronization, 210
- structural universality, 57
- subharmonics, 50–52, 64–66
- supercycles, 40
- synchronization, 207–215
 - generalized, 212
 - partial, 219
 - phase, 214
 - strong, 210
 - weak, 210
- tangent bifurcation, 71, 158
- Taylor instability, xiii, 134
- three-body problem, 193
- three-frequency quasiperiodicity, 131
- time-evolution operator, 186, 189
- torus, 164, 166, 167, 171, 175, 185
- transient chaos, 158
- translations on a circle, 178
- turbulence, 4, 127–136, 221, 225
- unimodal map, 236
- universality, 3, 46–52, 61, 79
 - global, 146
 - local, 141
 - metric, 59
 - structural, 57
- unstable direction, 62
 - manifold, 148
- unstable fixed point, 194
- varactor diode, 66
- weak synchronization, 210
- Wenckebach phenomenon, 156
- winding number, 136, 140, 214